University of Strathclyde
Department of Mechanical and Aerospace Engineering

ON THE EVALUATION OF CYCLIC BEHAVIOUR FOR A MECHANICAL STRUCTURE UNDER VARIABLE MECHANICAL AND THERMAL LOADS

Weihang Chen

A thesis presented in fulfilment of the requirements for the degree of Doctor of Philosophy

2012

COPYRIGHT DECLARATION

Signed:

Date:

ACKNOWLEDGMENTS

First and foremost, my deepest thanks go to Dr Haofeng Chen my primary supervisor, who not only provided me with a sound backdrop of academic and engineering experience and knowledge, but also, genuine, guidance and encouragement.

I gratefully acknowledge the support and help of Dr Robert Hamilton my second supervisor, who has provided me useful comments and suggestions, at the various stages of the work.

Acknowledgements go to my sponsors, Engineering and Physical Sciences Research Council (EPSRC-EP/G038880/1) and the Overseas Research Scholarship (ORS), for the financial support of the work.

I am thankful to my parents and Dongqing for their continuous encouragement throughout my life.

Finally, I would like to thank my beloved wife Rezana and my son Zilong, to whom I feel completely indebted to. They have provided me with so much love, continuous support and encouragement. I am really sorry for leaving my wife and our son to themselves for three years.

Table of contents

Table of contents

Table of contents

Table of contents

Table of contents

Table of contents

Table of contents

List of figures

CHAPTER 1

CHAPTER 2

CHAPTER 3

CHAPTER 4

List of figures

List of figures

CHAPTER 5

CHAPTER 6

List of figures

CHAPTER 7

List of figures

List of figures

CHAPTER 8

List of figures

List of figures

CHAPTER 9

List of figures

List of figures

CHAPTER 10

List of figures

List of tables

CHAPTER 3

CHAPTER 4

CHAPTER 6

CHAPTER 7

CHAPTER 8

CHAPTER 9

List of tables

CHAPTER 10

ABSTRACT

This thesis investigates and develops computational procedures for the assessment of the structural integrity and lifetime of mechanical structures subjected to cyclic variable loads.

The Linear Matching Method (LMM), which has been used in design and life assessment calculations for a number of years, is adopted for investigating the above problems. In order to produce sequences of linear solutions with spatially varying linear moduli, LMM matches the behaviours of a non-linear material to that of a linear material. The developed iterative programming algorithms, when implemented within the finite element scheme, ABAQUS, generate a monotonically reducing sequence of upper bounds that ultimately converges to the least upper bounds.

There are three main objectives of the present study. The first is to investigate the overall response of mechanical structures under the combined actions of mechanical and thermal loads without the presence of creep. Shakedown and ratchet limit interaction diagrams of different types of mechanical structures identifying the regions of shakedown, reverse plasticity, ratchetting and plastic collapse mechanism are presented and parametric studies of different types of defective component are investigated. The results for different types of mechanical structures shown in the parametric studies, confirm the applicability of LMM on complex structures under cyclic loadings without the effect of creep.

The second objective is to bridge the gap between Continuum Mechanics and Fracture Mechanics through the LMM by calculating the cyclic J-integral (ΔJ). The derivation of ΔJ based on the potential energy expression for a single edge cracked plate subjected to cyclic uniaxial loading and cyclic bending moment conditions using LMM is formulated in this study. The results of the proposed model have been compared to the cases obtained from the Reference Stress Method for a single edge cracked plate. They indicate that the estimates provide a relatively easy method for estimating ΔJ considering the complete accumulated cycle effects.

The last objective is to further develop the current LMM for the evaluation of the cyclic behaviour for mechanical structures when the effect of creep is taken into consideration. The creep strain and plastic strain range are obtained to be used in creep damage and fatigue assessments, respectively. A benchmark example of a Bree cylinder subjected to cyclic thermal load and constant mechanical load is analysed to verify the applicability of the LMM in creep fatigue damage case. The cyclic responses for different loading conditions and dwell time periods within the Bree boundary are obtained. In order to show the efficiency and effectiveness of LMM method for defective structures, a three dimensional plate with a hole and a welded pipe subjected to cyclic thermal loads and constant mechanical loads are analysed. The results of both examples show that the presence of creep changes significantly the cyclic responses. The LMM procedure provides a general purpose technique for the evaluation of cyclic behaviour and the determination of the plastic strain range and creep strain for the creep fatigue damage assessment with creep fatigue interaction.

CHAPTER 1. INTRODUCTION

1.1 Introductory Remarks

Imperfections in structures can arise in the initial production process, or during the heat-treatment of the component, particularly during welding processes. These defects or flaws are unavoidable within structure components, and they do not generally lead to an immediate failure. Imperfections also occur during the operating cycle of a component or structure. One example of these imperfections or local defects is a part-through slot in a pipeline which may appear due to existing surface cracks or from corrosion during operating times. Failure modes occurring from these part-through slots are different from industry to industry, but mostly such failures result from the application of cyclic loading with high temperature often aided by environmental degradation.

The power generation industry can also be given as an example here since it is trying to meet the criteria for clean and sustainable energy production by increasing efficiency and simultaneously decreasing levels of pollutants. Improving the efficiency of a conventional steam and gas turbine power plant by increasing the operating temperature, may reduce the fuel consumption and the levels of harmful emissions. Advanced numerical modelling together with analytical and experimental methods are needed to ensure operational safety and efficiency of current and future conventional or nuclear plants. The trend of higher operating temperatures and the necessity to extend the life of existing power plant components, is leading to research to develop more accurate and reliable numerical approaches. In the power generation industry these numerical approaches are used to primarily estimate the creep-fatigue damage as a structure's response to operate at high temperatures, under cyclic loads for a specific operational period.

In general, the lifetimes of these components, operating at elevated temperatures, depend on the nature of plastic deformation and fracture failures they experience. The first failure mode is mainly concerned with the excessive plastic deformations associated with the phenomenon of plastic collapse, shakedown and

ratchetting, while the second is concerned with the crack growth/crack propagation behaviour. The ability to accurately model these phenomenon, in components subjected to steady, cyclic and variable loading conditions, would provide a means of assessing the remaining life of the structural components. Thus, the elastic-plastic response of a structure needs to be well understood when using it as a design condition. The elastic-plastic response is load path dependent and usually simulated by an incremental Finite Element Analysis (FEA). This allows the investigation of any type of loading cycle but also requires a detailed load history and involves significant computational effort.

To avoid such difficulties, one of the failure criteria of structures operating at elevated temperatures is based upon design codes and rule based methods, such as R5 [1], the design life and assessment procedure used by British Energy in the UK. The main objective of R5 is to provide a comprehensive assessment procedure that can easily be used by both designers and practitioners.

In recent years, another alternative approach has been developed. It involves the application of numerical methods [2][3][4][5][6][7] for addressing the structural response in structures subjected to both severe mechanical and thermal loads. The assessments, provided from these new methods, have the potential of providing results that combine the accuracy of non-linear FEA simulation methods [8][9] with the efficiency of rules-based methods [10][11]. These are direct methods based upon a programming technique. Direct methods were incorporated into finite element analysis in order to evaluate the shakedown limit. The material model is considered to be elastic perfectly plastic, and the load domain including all the possible load paths eliminates the necessity to know the detailed load history. Such direct methods include; the mathematical programming methods [12][13][14], the Generalized Local Stress Strain (GLOSS) r-node method [15], the Elastic Compensation Method (ECM) [16][17], and the Linear Matching Method (LMM) [5][6][18][19].

Among these direct methods, the Linear Matching Method (LMM) is recognized as one of the most powerful methods. The LMM is distinguished from other simplified methods by ensuring that equilibrium and compatibility are satisfied at each stage [3][5][20][21]. In addition to the shakedown analysis method [20], the

LMM has been extended beyond the range of most other direct methods by including the evaluation of ratchet limit and plastic strain range [4][5][21][22]. Moreover, the extensions of LMM have resulted in the application of the method to high temperature creep behaviour including the effect of elastic follow-up [19], i.e. the evaluation of local creep damage due to the relaxation of stress during creep dwell times. In all these cases, the methods rely upon the standard set of material data used in rules-based methods, i.e. elastic moduli, yield stress, steady state creep deformation and simple descriptions of creep strains during relaxation, fatigue and creep-fatigue data. Since the LMM ABAQUS user subroutines [23] have also been consolidated by the R5 [24] research programme of EDF energy to the commercial standard, LMM could be regarded as the most amenable direct method in practical engineering applications involving complicated thermo-mechanical load histories.

This thesis is concerned with the investigation and development of the LMM in context of its application in mechanical structures with or without defects. In the field of plastic deformation failure without the presence of creep, the focus is on the identification of limits loads, shakedown and ratchet limits in mechanical structures subjected to cyclic histories of thermal and mechanical loads. In the presence of creep, the interest focuses on the investigation of understanding the stable cyclic response of a mechanical structure under creep and creep-fatigue conditions. In fracture failures, a cyclic J-integral model is introduced to be correlated with the crack growth rate using LMM.

This thesis also aims to generate standard solutions to typical problems, where the interaction diagrams developed would provide assistance in making an intelligent assessment of the operational safety of the structure under consideration.

In the following sections, the structure's response to cyclic loading with or without the effect of creep is discussed in more detail. An overview of the thesis is also included, at the end, stating the investigations conducted in each chapter.

1.2 Structural Response to Cyclic Loading without the Effect of Creep

The limit load is one of the most critical areas of interest in deformation failures, which has been the focus of research for many years in industry. The limit load is the maximum load that a structure assuming a perfectly plastic material can sustain. The implication of this phenomenon in a structure lies in the fact that the application of a proportional load beyond the limit load, would lead to plastic collapse. The accurate identification of the limit load is essential to the design and life assessment of mechanical structures.

In circumstances where structures are subjected to cyclic loading histories, the relative variations of the induced mechanical and thermal stresses have serious implications on the life span of the structural components. In the analysis of structures subjected to cyclic loading histories with elastic–plastic materials, the component will experience either elastic/plastic shakedown or ratchetting depending upon the applied load level. The elastic shakedown limit is the highest cyclic load under which a material shakes down to an elastic response after the first few load cycles. When the elastic shakedown limit is exceeded, the structure may experience either alternating plasticity (plastic shakedown) or ratchetting. Ratchetting should be avoided at all costs since it leads to intolerable deformation and eventual collapse of the structure. Reverse-plasticity can be endured provided low cycle fatigue is taken into consideration. Hence, in the design of structures, it must be ensured that any inelastic strain accumulation is avoided or restricted to the number of cycles within a designed limit so that they will not damage the structure.

1.3 Structural Response to Cyclic Loading with the Effect of Creep

In the presence of creep, the response of the structure to cyclic loading changes significantly. Interaction of plasticity and creep is the key feature of creep-fatigue mechanism under cyclic loading condition with creep. Assessments must be

carried out to ensure avoidance of creep-fatigue failure by, creep rupture and cyclically enhanced creep. The term cyclically enhance creep refers to the threat of gross section creep failure due to the accumulation of creep strains arising from the cyclic loading.

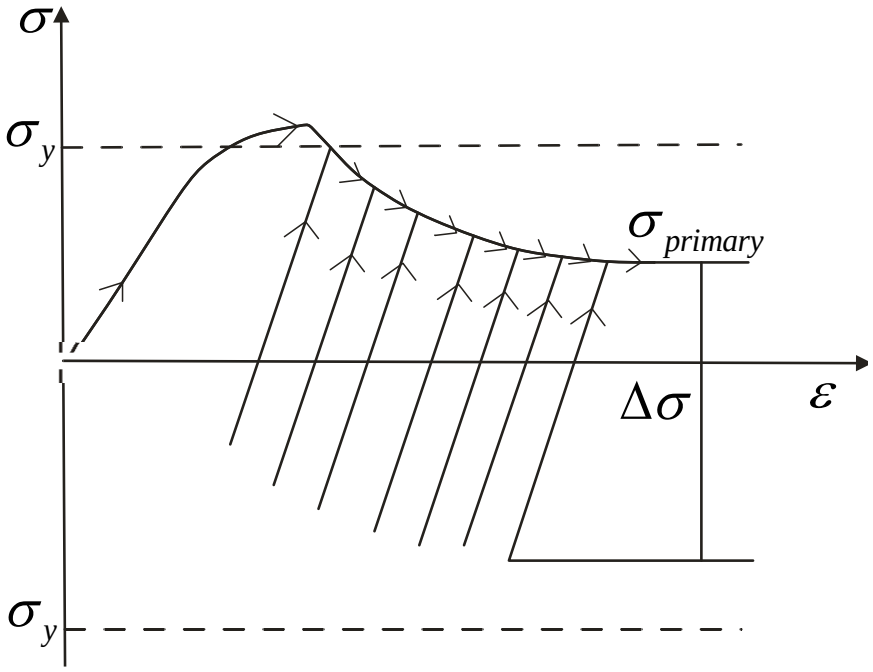

Figure 1.1 Stress strain cyclic histories with the effect of creep (In steady state the failure mode for this case is creep rupture) [1][24]

Briefly, a structure subjected to cyclic loading with creep can present different asymptotic behaviours, such as:

1) No stress relaxation is taking place, the accumulation of creep strain is due to primary loads only during each load cycle. Because the creep strains are driven by the primary loads alone, the situation is similar to that of a monotonic loading. This phenomenon can be explained in Figure 1.1. It is observed from Figure 1.1 that the dwell stress on each successive cycle just as if the load cycles did not occur. However, the stress cannot relax below the primary stress level $\sigma_{primary}$ in steady state case. Thus, the accumulation of creep strain is due to primary loads only during each load cycle and the failure mode for this case will be creep rupture.

2) The stress relaxation process introduces a residual stresses field so that there is a tendency for regions of the component material to yield during unloading.

Thus, a hysteresis loop is generated. On re-loading for the next cycle, the effect of creep and cyclic plasticity on the residual stress field causes the cyclic stress to reset on each load cycle, and the start of the dwell stress exceeds the primary stress, $\sigma_{primary}$. And a non-closed hysteresis loop due to creep strain is appeared. This phenomenon can be explained in Figure 1.2, and the failure behaviour for this case is called Cyclically Enhance Creep [24].

Therefore in an integrity assessment of components subjected to the cyclic load and under creep conditions, the above mechanisms need to be addressed.

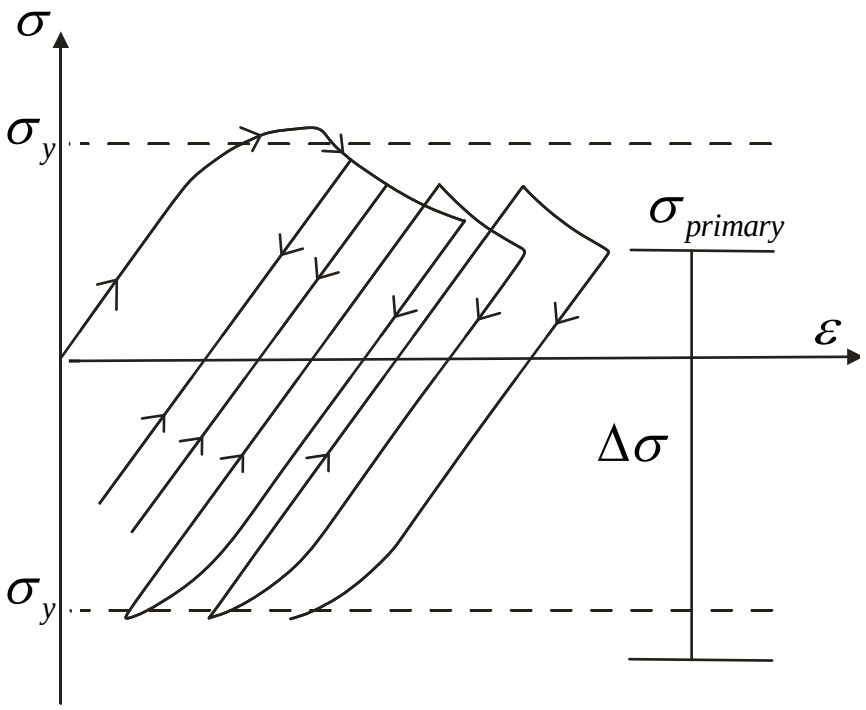

Figure 1.2 Stress strain cyclic histories with the effect of creep (In steady state the deformation failure will be due to cyclically enhanced creep) [1][24]

1.4 Overview of the Thesis

This thesis is divided into eleven main chapters, with each chapter focusing on the particular aspect of the problems identified in Section 1.2 and 1.3. In Chapter 1 the subjects of interest were introduced and the main objectives of the thesis are given. This was then followed by describing the possible structural response of

components subjected to cyclic histories of loads with and without the effect of creep in a defective or defect-free structure.

In Chapter 2, a general literature survey on limit, shakedown, ratchet and creep-fatigue interaction analysis by various experimental and numerical methods is discussed. From this literature survey, the methodology with the best prospect for investigating the behaviour of mechanical structures under the prescribed loading histories was then identified as the Linear Matching Method (LMM).

In Chapter 3, the application of the LMM in elastic shakedown analysis is discussed. It begins with brief statements on the lower and upper bound elastic shakedown theorems. This is then followed by the description and discussion of the foundation of the LMM, as an iterative upper and lower bound elastic shakedown analysis method. Its implementation within ABAQUS is then described, and a benchmark numerical example of a plate with a central hole subjected to cyclic loading is provided.

In Chapter 4, a parametric study is carried out to obtain upper and lower bound elastic shakedown boundaries for a composite cylinder with a cross-hole subjected to constant internal pressure and a cyclic thermal gradient. The effects of temperature-dependent yield stress, material discontinuities, composite cylinder thickness and the existence of the cross-hole on the shakedown limits are discussed for different geometry parameters. Finally, a safety shakedown envelope is created by formulating the shakedown limit results of different composite materials and cylinder thickness ratios with different cross-hole sizes.

In Chapter 5, the theory behind the LMM for plastic shakedown (reverse plasticity) analysis is discussed in depth. For structures loaded in excess of elastic and plastic shakedown, extended theorems for the identification of ratchet limits are also explained. These numerical methods are then applied to the plate with a central hole problem, under constant mechanical load and cyclic thermal load, enabling distinctions between the regions of elastic shakedown, reverse-plasticity and ratchetting to be identified.

In Chapter 6, a parametric study for a defective pipeline subjected to constant internal pressure and a cyclic thermal gradient is carried out. Shakedown and ratchet limit interaction diagrams of the defective pipeline identifying the regions of shakedown, reverse plasticity, ratchetting and plastic collapse mechanism are presented and parametric studies involving different types and dimensions of part-through slot in the defective pipeline are investigated.

In Chapter 7, another parametric study for a centre cracked plate subjected to cyclic tensile loading and cyclic bending moment is undertaken. The effect of circular holes drilled in the region of the crack tip on the ratchet limit and crack tip plastic strain range is studied. Parametric studies involving hole diameter and location are investigated. The optimum hole location for reducing the crack tip plastic strain range with the least reduction in ratchet limit is identified.

In Chapter 8, a cyclic J-integral model used to correlate with the crack growth rate using LMM is proposed. The derivation of the cyclic J-integral based on the potential energy expression for a single edge cracked plate subjected to cyclic uniaxial loading and cyclic bending moment condition using LMM is presented. To extend the analysis, so that it can be incorporated into other plasticity models, material Ramberg-Osgood hardening constants are also adopted. The results of the proposed model have been compared to results obtained from the Reference Stress Method (RSM) for a single edge cracked plate. These indicate that the estimates provide a relatively straight forward method for estimating cyclic J-integral which describes the crack growth rate behaviour by considering the complete accumulated cycle effects.

In Chapter 9, a new approach for the direct evaluation of cyclic behaviour with creep effects of structures subjected to a general load condition in the steady cyclic state using LMM technique is presented. The creep strain and plastic strain range to be used in creep damage and fatigue assessments, respectively, are obtained. A benchmark example of a Bree cylinder subjected to cyclic thermal load and constant mechanical load is analysed to verify the applicability of this new LMM to deal with the creep fatigue damage. The cyclic responses for different loading conditions and dwell time periods within the Bree boundary are obtained. To

demonstrate the efficiency and effectiveness of the method for more complex structures, a 3D plate with a central hole model subjected to cyclic thermal loads and constant axial tension is analysed. The results of both examples show that with the presence of creep, the cyclic responses change significantly.

In Chapter 10, a parametric study on the geometric effect of a heterogeneous welded pipe is carried out, to demonstrate the accuracy of the numerical procedure mentioned in Chapter 9. The steady state, creep, creep-fatigue behaviour of the heterogeneous weld-related material zones, investigating the importance of the weld and its effect on the design life are discussed in this chapter.

Finally, in Chapter 11, conclusions to the objectives outlined in this thesis are presented, including a summary of the results generated. Suggestions on the possible future research areas to be conducted are also enclosed.

CHAPTER 2. LITERATURE SURVEY

2.1 Introduction

Cyclic loading at high temperatures is what many structural components or elements of modern engines and power plants are subjected to, during their operations. This would mean that at high temperatures numerous failures must be considered in the design or integrity assessment process. This thesis is concerned with the development of the numerical method in the context of its application in mechanical structures subjected to cyclic histories of loads and temperatures with and without the effect of creep. In cases where creep is not effective, the focus is on the identification of limit loads, shakedown limits and ratchet limits. With the presence of cyclic loading histories operating at elevated temperatures with dwell period, structural failure causes are dominated by creep, fatigue and creep-fatigue interaction.

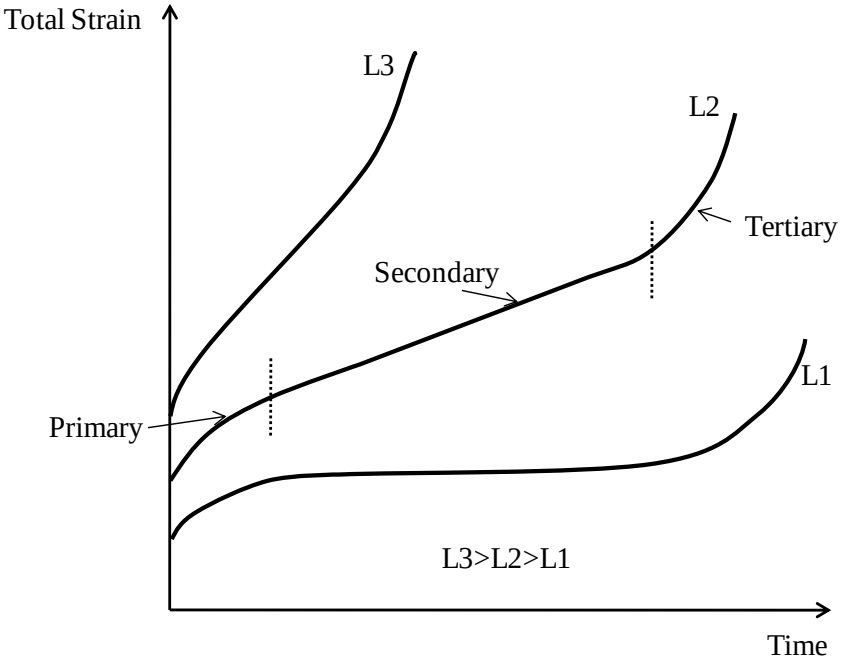

Figure 2.1 Typical creep curves for different constant load, L, and temperature (this curve is taken from Boyle & Spence [25] directly).

At elevated temperatures, in metallic structures continuous significant viscoplastic strains will appear due to creep, and this eventually causes failure. Under such operating conditions, the creep level and the time when the structure will fail depend on the material, the operating temperature, the applied stress history and the geometry of the component. Although creep for materials such as lead, copper and mild steel occurs even at room temperatures, for most metallic structures it is usually experienced at high temperatures greater than 40% of the absolute melting temperature of a metal [26].

Creep for a metallic structure starts with time with the accumulation of creep strain at a given stress and temperature. There are three distinct stages of creep and they are shown in Figure 2.1 [25]. Initial elastic strain occurs as an instant effect of the applied load and after this, a region of increasing creep strain with decreasing creep strain rate will be formed. This is the primary creep stage and it is followed, by a secondary creep region where the creep strain rate is constant. The secondary creep region alternatively is also named as the steady-state creep stage. The first two stages are followed by the third and the final stage where strain rate increases progressively. This is the tertiary creep stage and in this region the creep strain rate increases rapidly causing after some time, the material failure due to creep fracture or rupture [25][27]. These three stages are described below in some detail:

- Primary creep is a period of work-hardening in which the creep rate decreases with time resulting to the material becoming harder to deform as the internal stress increases with the dislocation density.
- Secondary creep**,** or the steady-state creep, is a period of balance between work-hardening and thermal softening which is a recovery process activated by the energy from the dislocation structure. This process results in a constant creep rate zone, where the material becomes neither harder nor softer. For structures at elevated temperatures with cyclic loading applications, where creep is effective, this stage is normally used as a base of the engineering design and life assessment, since it usually dominates the region over the design life of the components.

- Tertiary creep results from necking, cracking and metallurgical instability. This region usually is characterised by an increasing creep strain rate peaking in fracture.

The creep response of a material changes with the stage that dominates for a particular stress or temperature combination [28]. However the basic shape of the creep curve does not change. As an example for this can be given the CrMoV alloys which are used in steam piping systems for fossil-fuelled power plants. These alloys are generally under stresses lower than l00MPa and they experience temperatures around 550°C. In such examples the secondary creep stage is longer than the primary and tertiary creep stages. In Figure 2.2 [29] the creep behaviour for 1/2Cr1/2Mo1/4V alloy is shown at a temperature of 640 °C. From Figure 2.2 one can see that the secondary creep rate is decreasing with the decreasing stress resulting in an increase of the structure life before failure. Observing each curve, it can be concluded that the primary creep stage can be neglected. While the secondary creep stage dominates among the other stages, the creep curve and the tertiary creep stage are substantial for all the three stress levels, but their importance reduces for lower stresses. However, the secondary creep stage dominates in each of the creep curves in the graphic, and since the secondary creep stage (or steady state creep stage) is almost 70% of the material's creep life, for simplicity the numerical examples presented in this thesis are mostly focused on this stage when the creep is presented.

In this study, the author will summarize the most updated methods for the structural analysis under cyclic loading conditions with and without the presents of creep. This work might also be beneficial for other researchers who are interested on related research projects. In this Chapter, a brief literature review on structural response of mechanical components under cyclic loading conditions by various methods will be carried out.

2.2 Structural Response of an Elastic-Plastic Structure under Cyclic Loading

There are various ways an elastic-plastic structure responds to the cyclic loading, as shown in Figure 2.3 It can be seen from the figure that the response of

such structures to sufficiently small load levels is purely elastic with no permanent strains, and after each load application the structure will go back to its original state. However, as observed from Figure 2.3, this situation changes when the load level is higher than the elastic limit load. This time the structure will have permanent plastic strains and the response of it for the subsequent loading cycles is not the same with the first cycle. This is occurring since such load cycles will induce residual stress in the structure and the geometry with the material properties will also change when such loads are applied. According to the load levels there are three long term responses for a structure when the applied load is greater than its elastic limit. A structure 'shakes down' to elastic action if after a few load applications the residual stresses and changing material properties lead to a purely elastic structural response and the permanent plastic strain does not increase any further. Shakedown to elastic response may not necessarily occur at higher load levels. At this point the permanent strains may settle into a closed cycle, a state this named as "cyclic" or "alternating plasticity", or they may increase indefinitely, a condition known as "ratchetting".

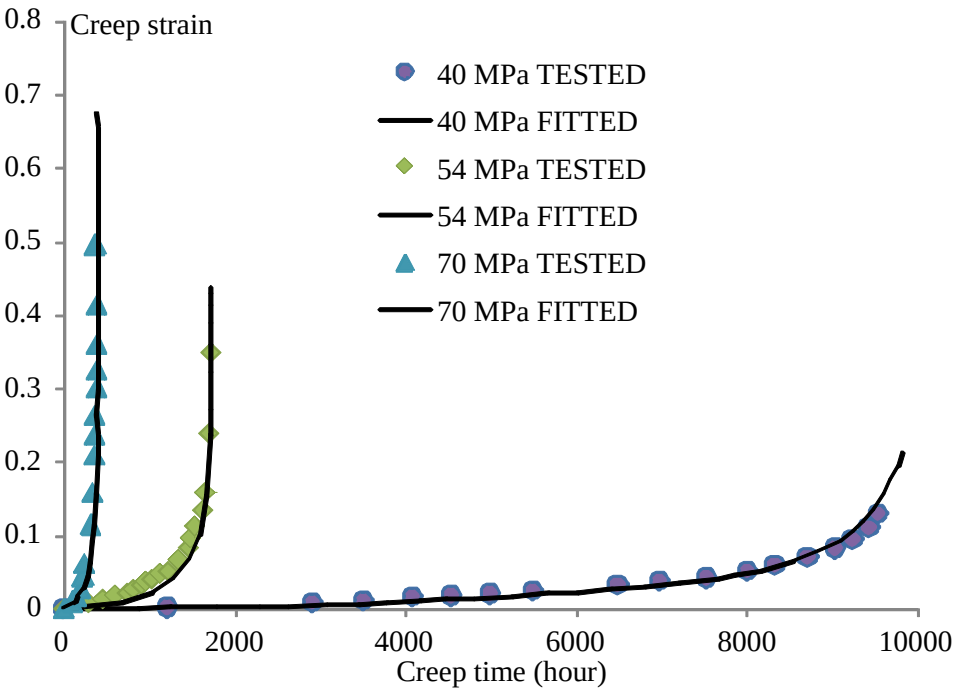

Figure 2.2 Creep curves for three different stress levels for a Y2Cr1/lMovV alloy at 640°C (this curve is taken from Hyde & Sun [29] directly).

One well-known illustration defining the boundaries of the elastic/plastic shakedown and ratchetting phenomenon under cyclic load history is Bree interaction diagram [30][31]. Bree [30][31] developed theoretical solutions for a simplified 2-dimensional model of a nuclear reactor fuel can. In his model, constant pressure stress and cyclic temperature gradient was applied across the can wall during start-up and shutdown. These theoretical solutions were illustrated on Bree interaction diagram in order to provide different modes of material behaviour for different cyclic loading conditions. These diagrams with various cyclic loading combinations are helping the designers especially in their early stages of design.

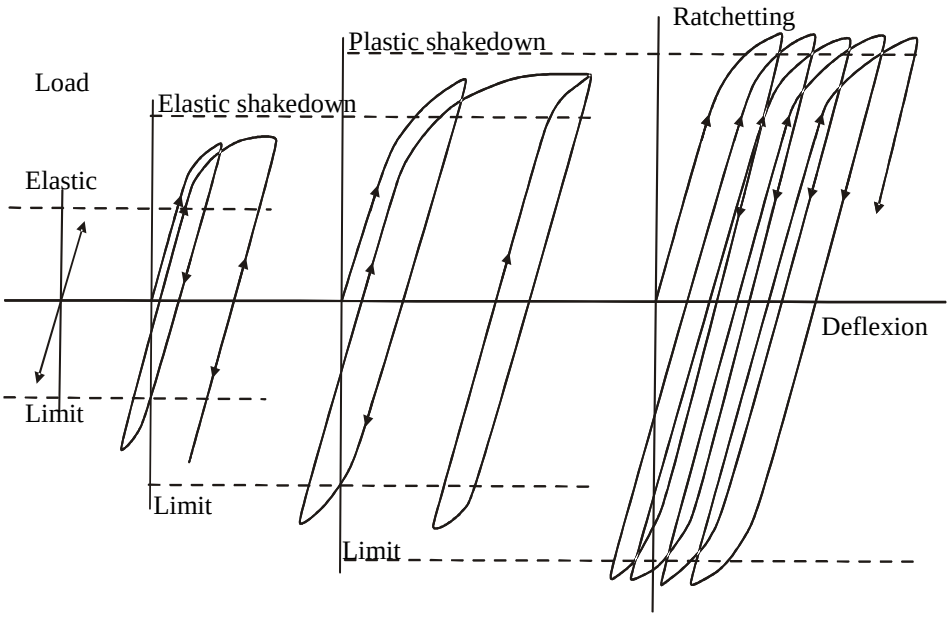

Figure 2.3 Possible responses of an elastic-plastic structure to cyclical load history

Figure 2.4 is the Bree diagram [30][31], illustrating the responses for the case of a fuel can subject to cyclic through-wall thermal stress and a constant internal pressure. The ordinate and abscissa give normalised values of pressure and thermal stress respectively, where the stresses have been normalised against the yield stress of the material.

The distinct feature on the interaction diagram is the separation of the different modes of material behaviour. In this particular analysis, the diagram is divided into four main regions, namely;

Pure Elastic Region: In this region, it was found that the load is lower than the first yield load of the structure, the response is wholly elastic but the structure may ultimately fail after a number of load cycles due to high-cycle fatigue.

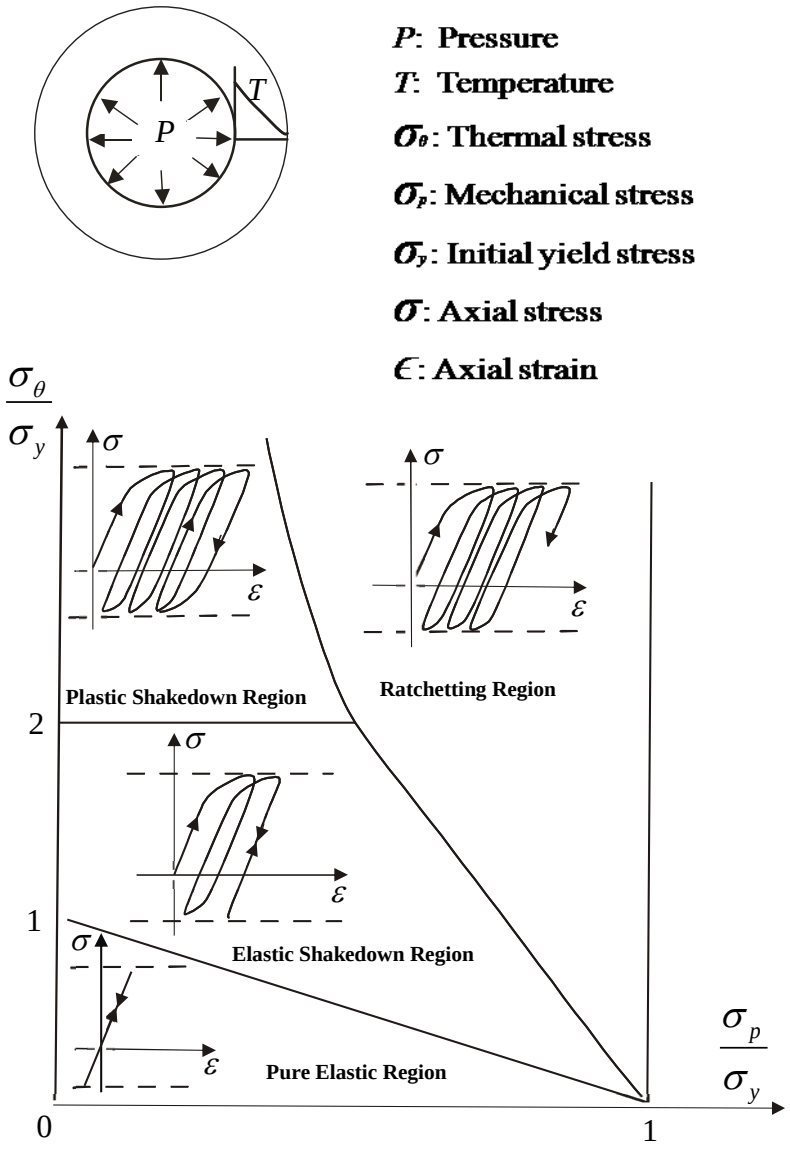

Figure 2.4 Bree diagram for pressurized tube and thermal loading [30][31]

(this curve is taken from [32] directly).

Elastic Shakedown Region: In this region, the stresses are exceeding the yield stress at the first few load cycles, which give rise to constant residual stress in the structure such that in subsequent load cycles only elastic deformation occurs. The constant residual stress field has caused the redistribution of the stresses within the

structure. This effectively has the effect of pulling the stress fields, the sum of the elastic and residual stresses in to the yield surface.

Reverse Plasticity/Plastic Shakedown Region: The transition to this region occurs when the effective elastic stresses exceed twice the yield stress. This was made possible with the accommodation of the time-varying residual stress field, causing the stress distribution at the outer fibre of the plate, to exceed twice the yield stress. When the structure exhibits reverse plasticity over each cycle, the positive plastic strain in the first half of the load cycle followed by equal magnitude negative strain in the second half, such that there is no accumulation of plastic strain during load cycle. And the failure mechanism for plastic shakedown is low-cycle fatigue.

Ratchetting Region: This region is best characterized by the breakdown of the elastic, shakedown and reverse-plasticity conditions. In each cycle, plastic strains accumulate over a significant volume of the plate, leading to immediate structural failure from the accumulation of plastic deformation during each load cycle and eventually incremental plastic collapse.

2.3 The Shakedown Theorems

Shakedown and ratchetting are two phenomena that have caught the interest of scientists and engineers and there is a broad research and modelling work on them. Although being a complex problem, in cyclic plasticity, significant advances has been achieved in recently in order to characterise the different responses. However, the designing process for a shakedown analysis is a difficult task. The advanced analysis methods require specific programs which may not be available or which often are impractical due to the time required to compute in 3-D structures design. Due to this, in order to ensure a safety margin to prevent ratchetting, during the design of shakedown sufficient design factors are incorporated on simple solid mechanics' models. This approach gives a safe shakedown design if used appropriately but, it often leads to excessive conservative designs, difficult to tackle technically and economically. That is why shakedown load is calculated during the design procedure and the safety conditions are specified accordingly during the operation.

The term shakedown was pointed out for the first time by Gruning [33] who proved the static shakedown theorem for a system of "*I*" beams. In 1936, Melan [34] presented a more general theorem and later [35] extended it to the general case of a continuum, providing the necessary criteria for which the structure will shakedown as follows: *"For a given load set P, if any distribution of self-equilibrium residual stresses can be found such that superposition with elastically calculated stresses, constitute a system of stresses within the yield limit, then P is a lower bound shakedown load set and the structure will shakedown"*. This theorem is referred to as the static and lower bound shakedown theorem. The lower bound shakedown theorem therefore requires specification or calculation of a constant residual stress field where the yield condition is not violated for any combination of cyclic elastic and residual stresses in order to define a lower bound shakedown limit. Then Koiter [36] presented a kinematic or upper bound shakedown theorem. The form of Koiter's upper bound shakedown theorem states: *"For a prescribed load set P(t) with cyclic period T, if any kinematically admissible strain rate* $\dot{\varepsilon}$*, can be found during a time interval (0,T) such that the strain field is compatible with a displacement field u (that satisfies the applied displacement boundary conditions) and*

$$\int_0^T \sum P\dot{u} \geq \int_0^T \int_v \dot{D} dv dt \qquad (2.1)$$

where $\dot{D}$ *is the rate of plastic dissipation per unit volume (corresponding to the admissible strain rate* $\dot{\varepsilon}$*), then shakedown has not occurred."*. Thus, the upper bound shakedown theorem requires the definition of a kinematically determinate mode of deformation for the component (that is, compatible sets of displacement and strain increments).

These lower and upper bound theorem provided sufficient criteria for shakedown of elastic-perfectly plastic structures. Both criteria presume the existence of a convex yield surface and the validity of the normality rule for the plastic strain rates.

Closed form solutions of shakedown problems are very limited due to the complexity of the analysis [37]. More complex problems may be solved by applying

plasticity bounding theorems to determine lower and upper bound shakedown loads. Thus, in analysing the behaviour of structures, such as Bree's interaction diagram, subjected to cyclic histories of loads and temperatures, there are a number of different computer based and experimental methods available at the present time. A summary of these methods is presented below.

2.4 Experimental Methods

A typical shakedown experiment can be described as follows. A model of a structure is subjected to cyclic loading usually consisting of concentrated forces. Meaningful displacements are measured after each cycle, so that their divergence in time (i.e. gradual increase of residual displacements, whose increments are differences between the values measured at two subsequent unloaded situations) or their stabilization reveal in-adaptation or shakedown, respectively. By performing tests at various level of amplifications of the same loading program (sometimes including straining effects such as temperature changes, simulated by imposed displacements at constraints), the safety factor with respect to incremental collapse is estimated experimentally. Experiments of this type have been performed and discussed for continuous beams in steel, e.g. [38][39] steel beam grids [40][41], reinforced concrete portal frames [42] and two-bay frames [43], two-story steel frames, steel plates [44], a pressure vessel consisting of an axisymmetric shell [45].

The CEA/DEMT employees [46] have suggested a procedure for accumulating the experimental results, a method which searches the response of a real scale structure subjected to mechanical and thermal loadings. The test can also be performed by taking into consideration a scaled model and its scaled loadings. According to this method when subsequent results are obtained they are organized and analysed, in plots of non-dimensionalised graphs. These graphics are named as Efficiency Diagrams, and the boundaries of the critical limits in creep and plasticity are identified to make comparisons with solutions obtained from numerical methods. This method is used for problems experienced in the Liquid Metal Cooled Fast Breeder Reactors (LMFBR) [47]. From the results it was observed that in specific

conditions, the shakedown and ratchetting limits of CEA/DEMT solutions give favourable results. However in other circumstances they do not, and this leads to the need in conducting experiments for different structural problems, under various load history and structural geometries.

There are several experimental results that have been presented on fatigue and creep-fatigue situations. Marie and Delaval [48] presented a creep-fatigue experiment for 316-stainless steel for a wide cracked plate subjected to cyclic bending loads at 650 degree. Kim, Chang and Ryu [49] conducted a creep-fatigue test with 10 minutes hold times at tensile maximum strain at 600 degree for type 316 L and type 316 LN stainless steels containing nitrogen contents 0.04% and 0.10%. They discovered that the creep-fatigue life was less than the fatigue life for both alloys. The fatigue and creep-fatigue life and saturation stress were increased with the addition of nitrogen. Shi Duoqi et.al [50] conducted a creep-fatigue test on nickel-based super alloy DZ125 at 850 and 980 degree to study the creep-fatigue interaction behaviour of alloy with different dwell time. They concluded that the life of creep-fatigue decreases as dwell time increases, but the life of this alloy was almost unchanged when dwell time exceeds a critical value at 850 degree. During the experiments mentioned above, the forces, the inclination of the levers and the deflection were recorded. And the experimental results were compared with known numerical results. Here, the practicality of performing different arrays of experiments is debatable as these incur excessive cost, which also need to be justified by being compared to other inexpensive available methods. Besides, the ability in conducting these experiments is also dependent upon the technological advances made in the field in question.

Due to the drawbacks of the experimental methods many numerical methods have been presented for estimating the structural responses under cyclic loading conditions with and without the presents of creep. R5, and Computer Based Methods are the most commonly used approach in conjunction with the Finite Element Modelling for estimating cyclic structural responses.

2.5 R5 Method

One method for assessing structural integrity of mechanical components with and without the effect of creep is R5 [24], the design life and assessment procedure used by British Energy. The main objective of R5 is to provide an assessment procedure for structural integrity that can be easily used by both designers and practitioners. In addressing the effect of shakedown, the current R5 procedures adopted Melan's [34] classical shakedown theorem. As mentioned before, this theorem requires the identification of a constant residual stress field, such that the sum of the applied linear elastic stress and the time independent residual stresses, are brought under yield. In assessing the creep-fatigue effect for defect free and defective structures, the volumes 2/3 and 4/5 from R5 are used, respectively.

Although the collaboration concluded that the R5 current shakedown and creep-fatigue assessment procedures are safe, the over conservatism of the solutions produced is a concern. Besides, there are no existing procedures within R5 for the identification of boundary between the reverse plasticity and ratchetting regions.

2.6 Computer Based Methods

Modern computers used in structural analyses have made it possible to analyse many complex structure problems. By taking into account stress, strain, deformation and material property changes, precise descriptions of structures' behaviours operating at elevated temperatures and cyclic loadings can be done using the modern computers. Due to the achievements in Finite Element Analysis (FEA) codes, computer based methods are being on the focus of interest recently. Finite Element Analysis is considered to be the foundation of computer solution methods for structural analyses. The reliability of numerical analyses, when used with contemporary high performance computers, has enabled a complete inelastic analysis to be performed together with the comprehensive deformation and material data obtained from the classical constitutive plasticity/creep equations. This is achieved even for very complex design shapes.

Today, there is a wide range of commercial software, which is using the numerical method of Finite Elements. One of them is ANSYS [8], a simulation program that can do simple linear elastic analyses but also challenging non-linear simulations. Another general-purpose software package is ABAQUS [9], used for numerical solutions of mechanical or thermal problems in structures. There are also other computer software, however they are used within specific industries. CASTEM 2000, developed by the Mechanical Department and Technology (DMT) of the French police, is one of such examples.

To sum up, computer solution methods have the advantageous capability to solve the structural problems, regardless of their geometries or loading conditions. FEA can solve many types of failure problems, whether the structures in question are defect free or defective. With this recent advances in the finite element technique, Incremental elastic-plastic FEA Methods and Direct Methods have been developed for calculating the cyclic structural responses (the phenomenon of shakedown and ratchetting). These two computer based methods are summarized as below.

2.6.1 Incremental Elastic-Plastic FEA Methods

Incremental elastic-plastic FEA recently is a widely used method for pressure vessel designs since software FEA programs provide a wide spectrum of analysis options. Structures plastically deformed respond in a non-linear form. In elastic-plastic FEA, the loading is applied in a number of discrete load steps or increments. This allows the program to simulate the initiation and growth of plastic zones and modify the structural stiffness and hence response accordingly. When a structure experiences large deformations, its global stiffness might be depending on the geometry. This, can also be simulated using non-linear FEA. Generally Cyclic Incremental FEA and Direct Cycle Analysis are two methods used to calculate structures' cyclic response in the context of incremental elastic-plastic FEA.

2.6.1.1 Cyclic Incremental FEA

The application of a number of recurrent loading cycles on an elastic-plastic structure may result in stable state of shakedown. In such a stabilized condition the

hysteresis relationship of stress and strain remains unchanged for every successive cycle. The traditional way to get the response of an elastic-plastic structure is by cyclically applying the periodic loading until the structure reaches the stable state. In cyclic incremental FEA, the critical condition for a structure can be located by following the entire deformation history. This method can be also used for complex models of structures with elastic-plastic materials. On the other hand, step-by-step inelastic numerical calculations have their disadvantages. One of these disadvantages is that until the structure gives a stable state response a great number of loading cycles must be applied, making the approach expensive to use. If the problem in question has a greater size, solving the nonlinear equations becomes very time consuming, especially for visco-plasticity problems and structures under very complex loadings. Another disadvantage is that in order to obtain the desired material, in a detailed cyclic-inelastic FEA basic material models which often are not on hand are needed. Despite the fact that most of the finite element software packages include basic plasticity and inelastic creep models, the access to their required material parameters is not easy. The material parameters are not easy to generate for a specific basic model and they depend on the accessibility of suitable test data. Finally, in inelastic step-by-step calculations correct boundary conditions and appropriate time step are necessary to obtain the convergent result. In certain cases the solution might fail as a result of a sensitive mesh, nonlinearities in the structure's material or due to the incrementation scheme. As a result, it can be said that cyclic incremental finite element calculations can be very time consuming for routine assessments in structural design, especially for producing diagrams similar to Bree's Diagram. These problems have caused the interest to shift toward methods from which the convergence information is obtained without the need of a complete stress and strain history. Direct Cyclic Analyses enter to such methods categories since they can directly calculate the stabilized state without the need to compute the transient cycles [51][52][53].

2.6.1.2 Direct Cyclic Analysis

Lately, Direct Cyclic Analysis (DCA) [23] is implemented into ABAQUS to calculate the stabilized cyclic behaviour. A modified Newton's method combined

with the solution and the residual vector represented in Fourier, is used in direct cyclic algorithm to get the stabilized cyclic response directly. The displacement coefficients are updated and employed in the following iteration step in order to get the displacements at each time increment, this process continued until convergence is reached. Going through each complete load cycle can be considered as a separate iteration of the solution for a nonlinear problem. Being a quasi-static analysis, the DCA uses the Fourier series in conjunction with time integration of the nonlinear material behaviour to get, in an iterative way, the stabilized cyclic response of the structure. This method avoids a significant numerical calculation time spent in transient analysis, thus it can be suitable for problems in which many load cycles must be applied to get the stabilized response. The DCA is also used for the assessment of the local plastic deformation in low cycle fatigue calculation and it can calculate the plastic ratchetting as well. In this method the assumptions made are; that the structure is showing linear geometrical behaviour, there is elastic stiffness and the contact conditions are fixed. In the direct cyclic algorithm, modified Newton's method is used. According to this method, a constant elastic stiffness is used as the Jacobian during the analysis. Due to the modified Newton's method, interface nonlinearities, such as contact or friction are not considered. Interface nonlinearities are severe and may lead to divergence. This is why they are not included in the direct cyclic algorithm. The elastic shakedown is identified in a straight forward way by DCA due to the absent iterations; plastic strains or zero incremental displacements. Ratchetting behaviour can be seen easily from the non-converging residual force related to the constant term in Fourier series representing the time-dependent cyclic displacements in DCA. However the certain identification of reverse plasticity is a harder task [54] because heavy cyclic loading above shakedown is characterized by very slowly converging solutions which also do not demonstrate clearly the divergence of the constant residual force term. In DCA, if plastic cyclic solution cannot be calculated directly then reverse plasticity is difficult to distinguish from ratchetting in most structures accept for some very simple examples. This tool can still be used for the assessment of the cyclic behaviour. The DCA method, same as the incremental FEA, cannot directly foresee the shakedown or ratchetting boundary but it can only show whether elastic shakedown, plastic

shakedown or ratchetting will take place. In order to calculate the concrete shakedown or ratchet limit, several simulations at various load levels are needed to determine the limit between the shakedown behaviour from the non-shakedown one.

As a conclusion, it can be said that DCA are not suitable for ratchetting cases. This is more obvious when ratchetting remains as a high part of deformation [55]. There are also other methods used to determine the convergence; such as the Direct Methods. Direct Methods basically are founded on static and kinematic shakedown theorems. Their aim as described in the following sections is to define the boundary between the elastic or plastic shakedown and ratchetting.

2.6.2 Direct Methods

Direct Methods do not follow the change of a structural system for a given history of external loading but directly evaluate the critical, final states and provide only essential information, without following the step-by-step inelastic structural responses. The interest on them arises from their ability to implement in standard finite element codes, and to give the potential for generally applicable methods available for design use. The main drive for developing Direct Methods has been to provide facilities for industries involved in the design of complex metallic structures subjected to severe cyclic loading, and sometimes operating at high temperatures. Another significant reason of using direct methods is that they save computational time, compared to other computer solution methods. With recent advances in the finite element technique and mathematical optimization theory, the simplified shakedown and limit analysis methods have been developed rapidly. Such methods include Mathematical Programming Method, Elastic Compensation Method (ECM) and Linear Matching Method (LMM) etc.

Current direct solution methods available are focused on ultimate limit conditions that lead to plastic collapse. Linear elastic analysis was modified to be used for the development of simple lower bound limit load methods by Jones [56] and Marriot [57]. Their methods were called the Reduced Modulus Methods and it was Mackenzie and Boyle [58] who extended them in their Elastic Compensation Method [16][17] for including in the analysis both upper and lower bounds. On the

other hand, Seshandri has developed the R-node method and the GLOSS method [15], both of them giving a great grasp for the structural behaviour. All these methods are practical but they lack a firm theoretical basis. There is no guarantee of convergence and even upper and lower bounds are obtained according to the rules of limit analysis and shakedown, they may not be optimal. Moreover, according to the kinematic finite element methods the lower bounds cannot be reached, and they sometimes are only the lower bounds of the optimal upper bound corresponding to the finite element mesh.

Following this work has been the attempts by the Ponter *et al* [3][5][59] to derive strictly convergent direct methods using linear solutions with spatially varying linear moduli. This has resulted in a class of methods referred to as Linear Matching Methods which arose originally from an attempt to prove the convergence of the Elastic Compensation Method [17].

The literature survey for the Mathematical Programming Method , Elastic Compensation Method and Linear Matching Method are summarized in the following sections. From this literature survey, Linear Matching Method (LMM) was selected as a numerical procedure in this thesis to address cyclic problems of mechanical components subjected to cyclic histories of mechanical and thermal loads with or without the presents of creep.

2.6.2.1 Mathematical Programming Method

Mathematic programming is applied to the shakedown load bound theorems as an optimization problem. Recently, this method was recognized as the most common method for shakedown analysis of complex structures. Both lower and upper bound shakedown limits can be used by mathematical programming processes based on the static and kinematic theorems of shakedown analysis [60] [61]. The FEM of the upper bound shakedown analysis may be formulated as a nonlinear mathematical programming problem subjected to a number of constraints. The objective function is to minimize plastic dissipation energy. According to this optimizing function an upper bound shakedown load is obtained. The lower bound shakedown analysis is alike as the upper bound for solving the nonlinear objective

function with the inequality constraint controlled by the yield condition and the equality constraint induced by the equilibrium equation. With such a formation a number of self-equilibrating residual stress fields is produced.

There are many existing solution techniques for mathematical programming problems which cannot be used [62], because of the nonlinearity and non-smoothness of the objective function in the upper bound procedure and the strong physical nonlinearity and unidirectionality of the constraints in lower bound analysis. Zhang et al.[63] and Liu et al.[12] have overcome the numerical difficulties caused by the nonlinearity and non-smoothness of the objective function for the upper bound procedure, however their methods are mainly presented for simple 2D structures. The shakedown analysis methods for more complex structures, such as 3D structures, need further studies and development. Some methods for loosening the nonlinear constraints have been proposed to overcome the numerical difficulties in the lower bound procedure, , such as the linearization of the yield condition [64]. However, most of these methods are very time-consuming. This time consumption is because of the huge number of constraint equations and degrees of freedom induced to construct a statically admissible stress field of the structure while conducting the lower bound analysis. This is one of the main reasons why classical lower bound analysis is so difficult to use in engineering analysis for complex 3-D structures. Hence, the complexity of this method has restricted its application in many fields of practical engineering, including pressure vessel designs.

2.6.2.2 Elastic Compensation Method

In recent years, repeated elastic techniques have been proposed and implemented using the finite element method in order to evaluate lower and upper bound shakedown loads rapidly [15] [57][65]. These approaches begin with an initial homogeneous elastic solution which is adapted in an iterative manner, through a series of linear elastic finite element solutions, to redistribute stresses within the component by varying the elastic modulus of elements. The iteration process stops when a meaningful equilibrium solution is reached. Both the ECM and the LMM are utilized for the repeated elastic techniques to calculate the cyclic structural responses.

The Elastic Compensation Method [16][17] [66] generalized and developed Marriot's method through application of plasticity bounding theorems in order to calculate upper and lower bounds for the limit and shakedown loads of complex structures modelled in either solid, shell or beam elements. In the theory of plasticity it is well known that if a technique is available for the estimation of limit loads, then this same method can be used with little modification to calculate shakedown loads [67] [68]. This fact has been used to adapt the ECM to the estimation of shakedown loads.

The ECM is able to operate to the issue of shakedown and ratchetting by using the theorems of lower and upper bound shakedown [16] [17] [66]. These methods were applied in ANSYS for 2D and 3D solid element models. The publications related to the ECM were mostly focused on the benchmark of plane stress and axisymmetric configurations for which another shakedown solution existed. The lower and upper bounds obtained by the ECM are compared to the solution given by Leckie and Penny [69] and the ASME 3Sm curve. To extend the ECM for a complex 3D structure, the same user routines are used.

Despite practical applications ECM lacks a firm theoretical basis. There is no guarantee of convergence for the upper and lower bounds. Besides, according to the rules of shakedown analysis, the obtained lower and upper bounds may not be optimal [59]. This may be due to the nature of the FEM, specifically in the displacement method, where the stress fields are not in equilibrium either within elements or across element boundaries (e.g. mixed FE formulations), so there is no guarantee that the lower bound ECM will produce monotonic convergence. Then Ponter & Carter address the convergence problem correctly by matching the state of incompressibility with the plastic state. Their studies showed that this could have a considerable effect on the rate of 'convergence' of the upper bound.

From their study of shakedown analysis [59], a more accurate version and theoretical justification of modified elastic modulus scheme has been proposed by Ponter and Carter [59][70].

This justification is theoretical, since an approximate FE analysis is used. For the finite element displacement method, the upper bound solutions reduce monotonically to a least upper bound, corresponding to the specific finite element formulation used.

The ECM procedure was implemented as a non-linear programming technique into the commercial FE code ABAQUS by Ponter, Fuschi and Engelhardt [71]. On the basis of this research, a new simplified and generalized analysis method, the LMM has subsequently been developed by Ponter and Chen[4][5] [6][19][22][72][73][74].

So far, the reviews in the solution methods, described in the previous sections, showed a wide variety of available procedures, capable of analysing the behaviour of mechanical structures subjected to cyclic histories of loads and temperatures. Each of these methods approaches the problems differently, with some more capable in implementation, while others having the advantage of being cost and time effective. Upon careful consideration into each of the method's features, the methodology with the best potential, for further exploration, was identified as the LMM.

2.6.2.3 Linear Matching Method

The LMM forms the foundation of the analyses conducted in this thesis. It is a nonlinear programming technique, developed from the Elastic Compensation Method. The LMM combines the convenience and efficiency of rule based methods and the accuracy of simulation techniques. It involves the matching of the non-linear material behaviour to a linear material and forms a basis for a powerful upper bound programming method that may be applied to a significant class of direct methods. The basis of the LMM is through the simple idea of representing histories of stress and inelastic strain as the solution of a linear problem where the linear moduli are allowed to vary both spatially and in time. Hence, effective elastic-plastic stiffness is matched with the stiffness of a fictitious elastic material at each point in the structure. A sequence of linear problems is defined that give strain rate histories that give rise to equilibrium residual stress fields. Sequentially, the correct non-linear constitutive assumptions are imposed. This is achieved by posing the problem as a minimum

problem where the desired solution is the minimum of a functional of the strain rate history. Expressed in this way the method has the character of a non-linear programming method, with each step involving the solution of a linear problem that has most of the characteristics of problem to be solved. When implemented in a finite element code the method seeks out the solution that provides the minimum amongst the class of displacement fields described by the finite element mesh. In this way, methods of great efficiency and flexibility can be devised where convergence proofs exist.

The LMM, distinguishes among other direct methods by ensuring that equilibrium and compatibility are satisfied at each stage [75][76]. In addition to the shakedown analysis method [20], the LMM has been extended beyond the range of most other direct methods by including the evaluation of ratchet limit and plastic strain range [76] and high temperature material behaviour [22]. Besides, LMM has the capability to combine the flexibility of the computer solution methods as well as the simplicity associated with the direct methods. This means that it can perform structural analysis, accurately for less time and cost of the full step-by-step inelastic analysis calculations. Lytwyn et.al [77] provided a direct comparison study between the LMM and the Direct Cyclic Analysis to calculate the ratchet boundary. The study showed that the computational efficiency of the LMM over the DCA was that in LMM it was not necessary to consider the entire cyclic load history of the component in question, avoiding the need to search for the ratchet boundary, as this is obtained directly. All these advantages became the choice of using the LMM in addressing the structural response for mechanical structures subjected to cyclic histories of loads and temperatures with and without the effect of creep.

2.7 Conclusions

The Linear Matching Method and ABAQUS Direct Cyclic Analysis appear to be the two methods most amenable to practical engineering applications involving complex cyclic thermo-mechanical load conditions. Both are computationally efficient in comparison with traditional cycle to cycle elastic plastic FE analysis for the prediction of stabilised cyclic behaviour, in which either elastic shakedown,

alternating plasticity or ratchetting may occur. However, as the DCA only shows whether elastic shakedown, alternating plasticity or ratchetting occurs in the stabilised cyclic response, the LMM may be the best method to generate Bree-like diagrams in engineering practice.

The LMM can presently be used for a range of different types of analysis and has the potential to be developed into a general tool for limit, shakedown, ratchetting and creep design and assessment.

In order to further justify the selection of this method the application of the LMM, to complex structures (defective and defect free structures) subjected to cyclic loading histories with and without the effect of creep will be posed in the coming chapters.

CHAPTER 3. LINEAR MATCHING METHOD ON ELASTIC SHAKEDOWN ANALYSIS

3.1 Introduction

Several types of structures and structural elements, such as the design of nuclear reactor components [78], are exposed to complex cyclic mechanical and thermal loads. The elastic plastic response to cyclic loading may imply structural failure either by low cycle fatigue or by incremental plastic collapse. The low cycle fatigue phenomenon corresponds to the existing alternating plastic strains which eventually induce local material failure. The incremental collapse phenomenon which has a rather global nature consists of a gradual divergence of the deformed configuration and eventually results in local failure or in excessive displacements causing in-serviceability.

Elastic shakedown represents the safe occurrence, alternative to the above undesirable events. The elastic shakedown limit is the highest cyclical load that allows a structure to shake down to an elastic response in the first few cycles of load. When the elastic shakedown limit is exceeded, the structure may experience either plastic shakedown or ratchetting. In many applications for conservative reason, it is allowable for a structure to be within the elastic shakedown limit, but plastic shakedown (alternating plasticity), under which a local low cycle fatigue failure mode occurs, and ratchetting that ultimately leads to incremental plastic collapse, are not permitted.

The elastic-plastic behaviour of the structure needs to be well understood when the elastic shakedown design condition is used since the elastic-plastic reaction is load path dependent and is typically simulated by nonlinear incremental Finite Element Analysis (FEA). This allows the investigation of any type of load cycle but also requires a detailed load history and can involve significant computational effort Research interest in elastic shakedown analysis methods is mainly due to their apparent advantage over step-by-step inelastic analysis methods [8][9]. Thus, uncomplicated, cost effective and efficient methods capable to predict whether a

structural system will elastic shakedown or not, are attracting more and more attention in structural engineering.

Direct methods are incorporated into finite element analysis in order to evaluate the elastic shakedown limit. The model's material is considered to be elastic perfectly plastic, and the load domain including all the possible load paths eliminates the necessity to know the load history particularities in detail. Such methods include; the mathematical programming methods [12][13][14], the Generalized Local Stress Strain (GLOSS) r-node method [15], the Elastic Compensation Method (ECM) [16][17], and the Linear Matching Method (LMM) [18][19]. As discussed in Chapter 2, among these direct methods, the Linear Matching Method (LMM) is recognized as one of the most powerful methods. In addressing the effect of elastic shakedown, the LMM approach involves the employment of elastic shakedown analysis methods, developed using the classical lower and upper bound elastic shakedown theorems of Melan [34] and Koiter [36]. The utilization of such procedures [6] has enabled elastic shakedown limit to be accurately and efficiently evaluated in many structural components.

In this chapter, the foundation behind the Linear Matching Method (LMM), employed in the identification of the elastic shakedown limit is discussed. A summary of its implementation for the upper and lower bound elastic shakedown theorems is presented. The application of the LMM is then investigated on a 3D plate with a central hole problem.

3.2 Elastic Shakedown Analysis

Figure 3.1 shows the general problem considered in the analysis. It consists of a body of volume, V, having a surface area, S. The surface is divided into two parts S_u and S_T, where S_u is the part with constraints and S_T is the part on which loads are applied. Let this body be subjected to a cyclic history of varying temperature $\lambda_\theta \theta(x_i,t)$ within the volume of the structure and surface loads $\lambda_p P(x_i,t)$ acting over part of the structure's surface S_T be considered. The variation is considered to be over

a typical cycle $0 \le t \le \Delta t$. Here λ_p and λ_θ denotes a load parameter, allowing a whole class of loading histories to be taken into account. X_i is the integration point in the body. On the remainder of the surface S_u, the displacement is $u_i = 0$. The body is made up of an elastic-perfectly plastic material with a uniaxial yield stress, σ_y, satisfying the von-Mises yield condition,

$$f\left(\sigma_{ij}\right) = \bar{\sigma}\left(\sigma_{ij}\right) - \sigma_y = 0 \tag{3.1}$$

where $\bar{\sigma}\left(\sigma_{ij}\right) = \sqrt{\frac{3}{2}\sigma_{ij}^{'}\sigma_{ij}^{'}}$ is the von-Mises effective stress and $\sigma_{ij}^{'} = \sigma_{ij} - \frac{1}{3}\sigma_{ij}\delta_{ij}$ are the deviatoric stresses.

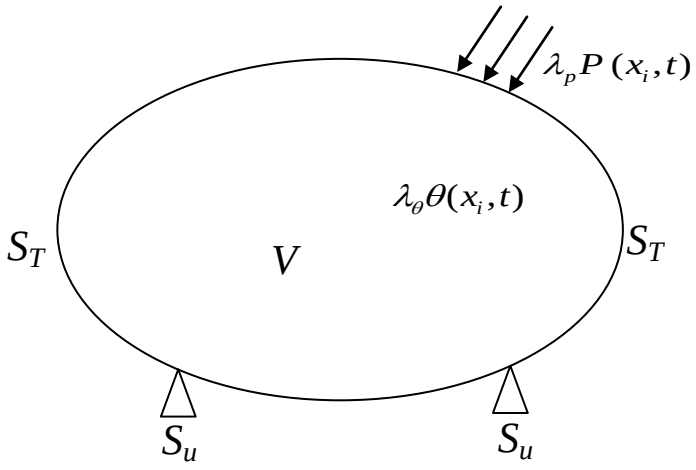

Figure 3.1 Schematic of the problem

Under conditions of small strains, the total strain is the sum of a elastic and plastic component,

$$\varepsilon_{ij} = \varepsilon_{ij}^{e} + \varepsilon_{ij}^{p} \tag{3.2}$$

where the plastic strains are associated with a strictly convex yield condition which satisfies the condition of (3.1). The plastic strain rate, $\dot{\varepsilon}_{ij}^{p}$, at yield are given by the associated flow rule,

$$\dot{\varepsilon}_{ij}^{p} = \dot{\alpha}\frac{df\left(\sigma_{ij}\right)}{d\sigma_{ij}^{'}} \tag{3.3}$$

where $\dot{\alpha}$ is the constant of proportionality. This can be expressed as the Prandtl-Reuss equation, given by,

$$\dot{\varepsilon}_{ij}^{p} = \frac{3}{2}\frac{\bar{\dot{\varepsilon}}}{\bar{\sigma}\left(\sigma_{ij}\right)}\sigma_{ij}' \tag{3.4}$$

where $\bar{\dot{\varepsilon}}$ is the associated effective strain rate. In stress space, $\dot{\varepsilon}_{ij}^{p}$ forms a normal vector to the yield surface and for the von-Mises yield condition, it implies that the plastic strain rates, $\dot{\varepsilon}_{ij}^{p}$, and the associates deviatoric stress at yield, σ_{ij}', are proportional to each other. Corresponding to the loading histories described in Figure 3.1, a linear elastic solution history is obtained:

$$\hat{\sigma}_{ij} = \lambda_{\theta}\hat{\sigma}_{ij}^{\theta} + \lambda_{p}\hat{\sigma}_{ij}^{p} \tag{3.5}$$

where $\hat{\sigma}_{ij}^{p}$ and $\hat{\sigma}_{ij}^{\theta}$ are the linear elastic stress solutions corresponding to mechanical load $P\left(x_i,t\right)$ and thermal load $\theta\left(x_i,t\right)$, respectively. In the following, the linear elastic stress solutions are chosen such that the load parameter $\lambda \geq 0$. In addition, the elastic moduli are assumed to be independent of temperature.

Defining λ_{E} and λ_{S} as the elastic limit multiplier and elastic shakedown limit multiplier respectively, then purely elastic or elastic shakedown behaviour can be described as:

Elastic region--- $0 \leq \lambda \leq \lambda_{E}$, where $f\left(\lambda\hat{\sigma}_{ij}\right) \leq 0$ though out the volume *V*.

Elastic Shakedown region--- $\lambda_{E} \leq \lambda \leq \lambda_{S}$, where $f\left(\lambda\hat{\sigma}_{ij} + \bar{\rho}_{ij}\right) \leq 0$, $\bar{\rho}_{ij}$ is a constant residual stress field and plastic strain rate history $\dot{\varepsilon}_{ij}^{p} = 0$. However, in the analysis of structures having complex geometries and loading conditions, the exact shakedown limits are hard to achieved. Therefore, an upper bound or lower bound shakedown limit theorems [67] [79] is often employed to simulate the exact elastic shakedown limit.

3.2.1 Upper Bound Shakedown Theorem

Koiter's [36] theorem states: "*a structure under cyclic loadings would shakedown if the external work done by the loads is less than or equal to the internal*

work dissipated for all admissible strain rate cycles, $\dot{\varepsilon}_{ij}^{c}$ ". Koiter's theorem is also referred to as the upper bound shakedown theorem.

In Koiter's theorem, the concept of an incompressible and kinematically admissible strain rate history is introduced. This admissible strain rate history, $\dot{\varepsilon}_{ij}^{c}$, does not need to be compatible but is associated with a compatible strain increment, $\Delta\varepsilon_{ij}^{c}$, such that,

$$\int_{0}^{\Delta t} \dot{\varepsilon}_{ij}^{c} = \Delta\varepsilon_{ij}^{c} \tag{3.6}$$

This satisfies the strain-displacement relations,

$$\Delta\varepsilon_{ij}^{c} = \frac{1}{2}\left(\frac{\partial \Delta u_i^c}{\partial x_j} + \frac{\partial \Delta u_j^c}{\partial x_i} \right) \tag{3.7}$$

Then the upper bound shakedown theorem is given by,

$$\lambda_{UB} \int_{v} \int_{0}^{\Delta t} \hat{\sigma}_{ij} \dot{\varepsilon}_{ij}^{c} dt dv = \int_{v} \int_{0}^{\Delta t} \sigma_{ij}^{c} \dot{\varepsilon}_{ij}^{c} dt dv \tag{3.8}$$

where λ_{UB} is the upper bound shakedown limit and σ_{ij}^{c} denotes a state associated with $\dot{\varepsilon}_{ij}^{c}$ at yield. Then $\lambda_{UB} \geq \lambda_{S}$, with the equality achieved, if and only if, the exact deformation mechanism is chosen. Equation (3.8) could be rewritten as,

$$\lambda_{UB} = \frac{\int_{v} \int_{0}^{\Delta t} \sigma_{ij}^{c} \dot{\varepsilon}_{ij}^{c} dt dv}{\int_{v} \int_{0}^{\Delta t} \hat{\sigma}_{ij} \dot{\varepsilon}_{ij}^{c} dt dv} \tag{3.9}$$

Considering the von-Mises yield condition,

$$\bar{\sigma}\left(\sigma_{ij}\right) = \sqrt{\frac{3}{2} \sigma_{ij}^{'c} \sigma_{ij}^{'c}} = \sigma_{y} \tag{3.10}$$

where $\sigma_{ij}^{'c}$ can be expressed as,

$$\sigma_{ij}^{'c} = \sqrt{\frac{2}{3}} \sigma_{y} \frac{\dot{\varepsilon}_{ij}^{c}}{\sqrt{\dot{\varepsilon}_{ij}^{c} \dot{\varepsilon}_{ij}^{c}}} \tag{3.11}$$

Equation (3.9) is obtained such as,

$$\lambda_{UB} = \frac{\int_{v}\int_{0}^{\Delta t} \sigma_y \bar{\dot{\varepsilon}}\, dt dv}{\int_{v}\int_{0}^{\Delta t} \hat{\sigma}_{ij}\dot{\varepsilon}_{ij}^{c} dt dv} \tag{3.12}$$

where $\sigma_{ij}^{c}\dot{\varepsilon}_{ij}^{c} = \sigma_y \bar{\dot{\varepsilon}}$ and $\bar{\dot{\varepsilon}} = \sqrt{\frac{2}{3}\dot{\varepsilon}_{ij}\dot{\varepsilon}_{ij}}$.

3.2.2 Lower Bound Shakedown Theorem

Melan [34] developed the shakedown theorem using the static approach to determine whether shakedown would occur or not, in an elastic-perfectly plastic structure subjected to a combination of loads. Melan's theorem [34] states: "*If a time constant residual stress field* $\bar{\rho}_{ij}(x)$ *exists such that superposition with induced elastic stresses* $\lambda_{LB}\hat{\sigma}_{ij}(x,t)$ *forms a safe state of stress everywhere in the structure, i.e.*

$$f\left(\lambda_{LB}\hat{\sigma}_{ij}(x_i,t) + \bar{\rho}_{ij}(x_i)\right) \le 0 \tag{3.13}$$

then $\lambda_{LB} \le \lambda_S$." where λ_{LB} is the lower bound load parameter.

Melan's theorem can also be referred to as lower bound shakedown theorem or static shakedown theorem. On the basis of Melan's lower bound shakedown theorem, a lower bound of shakedown limit can be constructed by maximizing the lower bound load parameter λ_{LB} under the condition where for any potentially active load/temperature path, the stresses resulting from the superposition of this constant residual stress field $\bar{\rho}_{ij}$ with the thermal-mechanical elastic stress $\lambda_{LB}\hat{\sigma}_{ij}$ nowhere will violate the yield condition.

3.3 Elastic Shakedown Analysis Using Linear Matching Method

As mentioned before, elastic shakedown refers to the behaviour of a structure subjected to a history of cyclic loading when it shakes down to an elastic response

after a few load cycles. Associated with this phenomenon is a constant residual stress field and the associated deformation strain field.

The elastic shakedown analysis using LMM was first developed by Ponter et al [59]. In order to identify the elastic shakedown limit, LMM is capable of determining the constant residual stress field, $\bar{\rho}_{ij}(x_i)$, which causes the redistribution of stresses within the body, and the associated strain field ε. The sections below show the numerical procedures how LMM identifies the elastic shakedown limit using upper and lower bound shakedown theorem and how it incorporate into ABAQUS.

3.3.1 Upper Bound Shakedown Analysis using Linear Matching Method

In general, the LMM involves the definition of a sequence of linear problems $\hat{\sigma}_{ij}$, where the linear coefficients, μ are identified so that they match the yield condition, σ_y. Thus, corresponding to an initial kinematically admissible strain rate history, this linear coefficient-shear modulus μ is found by matching the linear material to that of a perfectly plastic material so that they both give the same effective stress,

$$\frac{3}{2}\mu\bar{\dot{\varepsilon}}^{i} = \sigma_y \tag{3.14}$$

The iterative procedure for defining the sequence of shear modulus, μ, can be best understood from the construction shown in Figure 3.2. The iterative method begins with a linear elastic stress solution, having an initial effective stress, $\bar{\sigma}\left(\sigma_{ij}^{k}\right)$ (Figure 3.2) and an associated strain rate field, $\bar{\dot{\varepsilon}}^{0}$, with an initial uniform shear modulus μ^{k}. A new distribution of shear moduli, μ^{k+1}, is then evaluated, so that, for fixed $\bar{\dot{\varepsilon}}^{0}$, the stress point would be brought to the yield surface. Thus, the new linear stress solution constructed would be an improvement to the previous iterative solution, provided they are related by the following relationship,

$$\mu^{k+1} = \mu^{k}\frac{\sigma_y}{\bar{\sigma}\left(\hat{\sigma}_{ij}^{k}\right)} \tag{3.15}$$

where *k* is the iterative number in an iterative process. This process is then continued until convergence occurs. At each iterative step, the upper bound elastic shakedown limit is then evaluated.

For subsequent linear problems, a new kinematically admissible strain rate history, $\dot{\varepsilon}_{ij}^{f}$, is now defined, such that,

$$\dot{\varepsilon}_{ij}^{f\prime} = \frac{1}{\mu}\left(\lambda_{UB}^{i}\hat{\sigma}_{ij}{}' + \bar{\rho}_{ij}^{f\prime}\right), \qquad \dot{\varepsilon}_{kk}^{f} = 0 \tag{3.16}$$

where $\bar{\rho}_{ij}^{f}$ is a time independent constant residual stress field. It is important to note that the superscripts, *i* and *f*, corresponds to the initial and final states respectively. Integrating the loading history, (3.16) becomes,

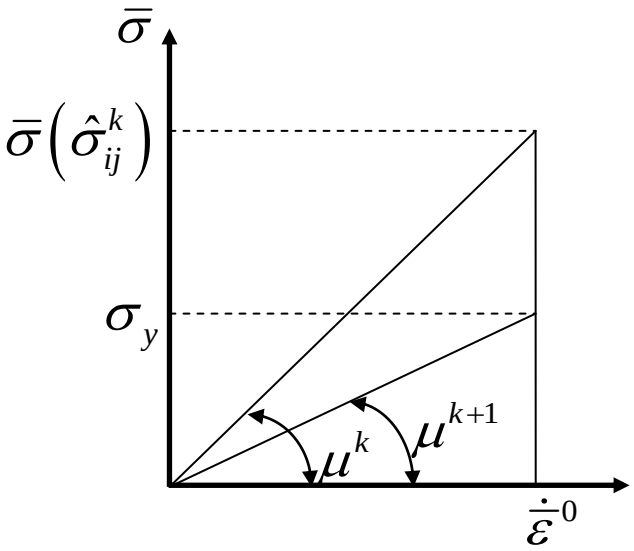

Figure 3.2 The linear matching process

$$\Delta\varepsilon_{ij}^{f\prime} = \frac{1}{\bar{\mu}}\left(\sigma_{ij}^{in\prime} + \bar{\rho}_{ij}^{f\prime}\right) \tag{3.17}$$

where

$$\frac{1}{\bar{\mu}} = \int_{0}^{\Delta t}\frac{1}{\mu(t)}dt \tag{3.18}$$

and

$$\sigma_{ij}^{in\prime} = \bar{\mu}\left(\int_{0}^{\Delta t}\frac{1}{\mu(t)}\lambda_{UB}^{i}\hat{\sigma}_{ij}{}'(t)\,dt\right) \tag{3.19}$$

A new upper bound, λ_{UB}^{f}, is generated when $\dot{\varepsilon}_{ij}^{f}$ is substituted into (3.12). The existence of the convergence proofs [3] [59] shows that $\lambda_{UB}^{f} \leq \lambda_{UB}^{i}$, with equality occurring, if and only if, $\dot{\varepsilon}_{ij}^{f} \equiv \dot{\varepsilon}_{ij}^{i}$. This procedure, when repeated, would generate a monotonically reducing sequence of upper bounds, converging to the least upper bound shakedown limit.

The above mentioned equations ((3.16)-(3.19)) give rise to a programming method. The application of this programming method-the LMM, as an iterative upper bound elastic shakedown limit analysis method, combines the convenience of using linear elastic stress solutions with the capability of non-linear programming method and is implemented within the FEA code, ABAQUS.

3.3.1.1 Implementation the LMM into ABAQUS

ABAQUS [9], is a product of HKS, and being a powerful engineering simulation program based on FEA methods, it is applied in this study. This general-purpose software is commonly used to analyse engineering problems in various areas of stress/strain analysis, heat transfer, or thermal-electrical analyses. ABAQUS has an wide library of elements, with a very large list of material models. It has the ability to incorporate new customised material behaviour by using user subroutines and option blocks, which makes it ideal choice for using it together with LMM.

There are three distinct stages in a standard ABAQUS analysis. The first one is the pre-processing stage. In this stage a model of the physical problem is defined and an input file is created. In ABAQUS analyses generally it is sufficient for the user to implement the engineering data such as the geometry of the structural, material behaviour, loading, and boundary conditions, but in the proposed procedures, based on the LMM the material's behaviour is user-defined, thus user subroutines such as UMAT need to be incorporated at this stage. The first stage is then followed by simulation. This stage involves solving the numerical problem defined in the input file and the results obtained are evaluated in the post-process stage by using the output files generated. When the LMM is used for the shakedown analysis, in ABAQUS some characteristics must be re-defined and re-interpreted,

according to the requirements related to this method. These modifications are done according to the user subroutines (UMAT, URDFIL) provided by ABAQUS in the analysis. In order to show how LMM works with ABAQUS, the functions of these subroutines are discussed as follows:

Subroutine UMAT:

UMAT subroutine is used to specify complex material properties, which cannot be defined by simple constitutive models using the Young's modulus, E, and Poisson's ratio, ν. It is accessed at each material gauss point, where the *USER MATERIAL* option is prescribed. The user must then define the Jacobian matrix, [*J*], which is the relationship between the incremental stresses and incremental strains,

$$\Delta\sigma_{ij} = [J]\Delta\varepsilon_{ij} \tag{3.20}$$

Once this matrix is defined, it allows the computation of the incremental stresses from equation (3.20), using the incremental strains calculated by ABAQUS. These incremental stresses would then be updated and added after each increment, ultimately providing the total stress solution.

Subroutine URDFIL:

This subroutine is where the results files can be found during the analysis. At the end of each increment, the user requested results are sent to the result files where they would be stored, extracted and updated as the analysis goes on. This subroutine is also used as a terminating mechanism for the analysis process according to the satisfaction of certain convergence criteria or the specified number of iterations.

While implementing the LMM into ABAQUS UMAT subroutine, it was observed that the procedure changes according to the way ABAQUS solves non-linear problems by diving them into linear increments and solving linearly each increment. Thus the solution from ABAQUS UMAT is the sum of stress and strain increments at the end of the analysis.

In LMM, the incremental values are viewed differently. Each of these increments is seen as a part of a separate linear solution. This implies that the material definition in UMAT, normally used to define the relationship between the incremental stresses and strains ($\Delta\sigma_{ij} = [J]\Delta\varepsilon_{ij}$), now in LMM defines the relationship between the iterative stress and strain of a linear solution ($\sigma_{ij} = [J]\varepsilon_{ij}$).

3.3.1.2 Iterative and Numerical Procedure for Upper Bound Shakedown Analysis

For the problem in Figure 3.1 two load types are solved at an arbitrary integration point X_i, then the varying surface loads and temperature loads at this point can be represented as, $P(t_n)$ and $\theta(t_n)$ respectively, where n represents the time load instance and range from $1 \le n \le N$, in a load space, where N represents the total number of time instants. For a strictly convex yield condition, which includes the von-Mises yield condition in deviatoric stress space, the loading histories describe sequences of straight line paths between sets of extreme points in a load space. Similarly, the linear elastic stress histories, $\hat{\sigma}_{ij}^{P}(t_n)$ and $\hat{\sigma}_{ij}^{\theta}(t_n)$, would also describe sequences of linear paths in the stress space. This implies that the only instants when plastic strains can occur are at the vertices of the stress history, $\hat{\sigma}_{ij}(t_n)$. The strain rate history then becomes the sum of increments of plastic strain:

$$\Delta\varepsilon_{ij}^{c} = \sum_{n=1}^{N} \Delta\varepsilon_{ij}(t_n) \tag{3.21}$$

Then equation (3.18) and (3.19) are modified as

$$\frac{1}{\bar{\mu}} = \sum_{n=1}^{N} \frac{1}{\mu(t_n)} \qquad where \qquad \mu(t_n) = \frac{\sigma_y}{\bar{\varepsilon}\left(\Delta\varepsilon_{ij}(t_n)\right)} \tag{3.22}$$

and

$$\sigma_{ij}^{in\prime} = \bar{\mu}\left(\sum_{n=1}^{N} \frac{1}{\mu(t_n)} \lambda\hat{\sigma}_{ij}{}'(t_n)\right) \tag{3.23}$$

The iteration procedure which is given in Chen and Ponte [6] in ABAQUS thought the user subroutine UMAT and URDFIL would be summarized as:

The first iteration (*k*=1) in the analysis procedure is the initialisation of the material model within UMAT. The shear moduli, $\mu(t_n)$, at *n* vertices of the loading history, is assigned to a constant value arbitrarily (normally with the value of the material Young's Modulus). The loads are applied though external linear elastic stress solution, $\hat{\sigma}_{ij}(t_n)_{ext}$, associated with *n* vertices of the load history. These solutions are solved separately beforehand and written to a formatted direct access file, in terms of the stress components for each element at each gauss integration point x_i. The load files are extracted and incorporated into UMAT for constructing extreme elastic stresses with $\hat{\sigma}^1_{ij}(t_n) = \lambda^1_{UB}\hat{\sigma}_{ij}(t_n)_{ext}$, where $\lambda^1_{UB} = 1$ for the first iteration. Therefore, the applied loads in UMAT are set to zero, so that the stress fields generated from this computation is now the residual stress field. These initialisation values are then written to files accessible via URDFIL, which allow the Jacobian to be updated via shared data blocks.

The following iteration (*k*=*k*+*1*), let $\lambda^{k+1}_{UB} = \lambda^k_{UB}$, and the shear moduli, at each integration point will then be updated by,

$$\mu(t_n)^{k+1} = \frac{\sigma_y}{\bar{\varepsilon}\left(\Delta\varepsilon^k_{ij}(t_n)\right)} \tag{3.24}$$

and

$$\frac{1}{\bar{\mu}^{k+1}} = \sum_{n=1}^{N}\frac{1}{\mu_n^{k+1}} \tag{3.25}$$

Then the Jacobian matrix, $[J]^{k+1}$, which relates increments of stress and strain in UMAT, is obtained from the calculated values of $\bar{\mu}^{k+1}$ as,

$$[J]^{k+1} = \frac{\bar{\mu}^{k+1}(1-\upsilon)}{(1+\upsilon)(1-2\upsilon)}\begin{bmatrix} 1 & \frac{\upsilon}{1-\upsilon} & \frac{\upsilon}{1-\upsilon} & 0 & 0 & 0 \\ \frac{\upsilon}{1-\upsilon} & 1 & \frac{\upsilon}{1-\upsilon} & 0 & 0 & 0 \\ \frac{\upsilon}{1-\upsilon} & \frac{\upsilon}{1-\upsilon} & 1 & 0 & 0 & 0 \\ 0 & 0 & 0 & \frac{1-2\upsilon}{2(1-\upsilon)} & 0 & 0 \\ 0 & 0 & 0 & 0 & \frac{1-2\upsilon}{2(1-\upsilon)} & 0 \\ 0 & 0 & 0 & 0 & 0 & \frac{1-2\upsilon}{2(1-\upsilon)} \end{bmatrix} \tag{3.26}$$

where ν is the Poisson's ratio. For the case of incompressibility, $\nu = 0.5$ and the volume strain rate, $\dot{\varepsilon}_{kk} = 0$.

This Jacobian enabling,

$$\sigma_{ij}^{ink+1} = \bar{\mu}^{k+1}\left(\sum_{n=1}^{N}\frac{1}{\mu\left(t_n\right)^{k+1}}\hat{\sigma}_{ij}^{k+1}\left(t_n\right)\right) \tag{3.27}$$

to be evaluated. Then, the constant residual stress can be calculated by,

$$\bar{\rho}_{ij}^{k+1} = \left[J\right]^{k+1}\Delta\varepsilon_{ij}^{k+1} - \sigma_{ij}^{ink+1} \tag{3.28}$$

which provides information for the strain rate associated with *n* vertices of the load history to be computed,

$$\Delta\varepsilon_{ij}^{k+1}\left(t_n\right) = \left[C\right]_n^{k+1}\left(\bar{\rho}_{ij}^{k+1} + \hat{\sigma}_{ij}^{k+1}\left(t_n\right)\right) \tag{3.29}$$

where $\left[C\right]_n^{k+1}$ is the stiffness matrix derived from μ_n^{k+1}. Before the calculation of coming iteration, ABAQUS will call upon subroutine URDFIL, and the terms of $\left(\sigma_y\sum_{n=1}^{N}\bar{\varepsilon}\left(\Delta\varepsilon_{ij}^{k+1}\left(t_n\right)\right)\right)$ and $\left(\sum_{n=1}^{N}\Delta\varepsilon_{ij}^{k+1}\left(t_n\right)\hat{\sigma}_{ij}^{k+1}\left(t_n\right)\right)$ for each Gauss integration point in the structure are then calculated. The iterative upper bound shakedown limit, derived from equation (3.12), is determined as,

$$\lambda_{UB}^{k+1} = \frac{\int_v \sigma_y\sum_{n=1}^{N}\bar{\varepsilon}\left(\Delta\varepsilon_{ij}^{k+1}\left(t_n\right)\right)dv}{\int_v\sum_{n=1}^{N}\Delta\varepsilon_{ij}^{k+1}\left(t_n\right)\hat{\sigma}_{ij}^{k+1}\left(t_n\right)dv} \tag{3.30}$$

This is then returned to subroutine UMAT as a scaling factor on the linear elastic solutions in the next iteration. The iteration procedure ends when the stopping criteria is satisfied. The overall organization of this method could be further understood by examining the block diagram in Figure 3.3.

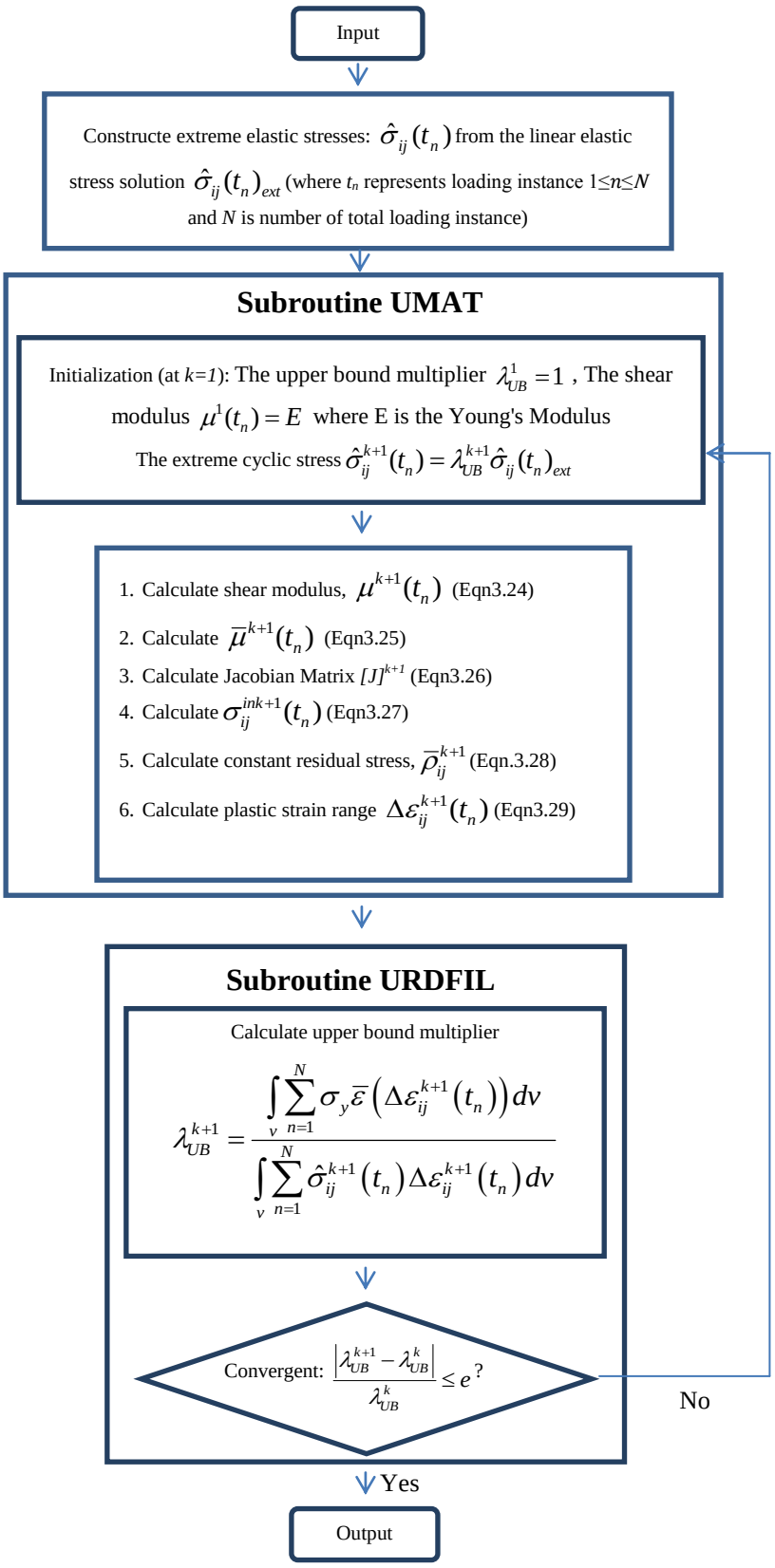

Figure 3.3 Flow chart for the upper bound shakedown limit using LMM

3.3.2 Numerical Procedure for the Lower Bound Shakedown Analysis

According to Melan's theorem mentioned in section 3.2.2, a lower bound of shakedown limit can be constructed using a similar procedure as upper bound by maximizing the lower bound load parameter λ_{LB} under the condition where for any potentially active load/temperature path, the stresses resulting from the superposition of this constant residual stress field $\overline{\rho}_{ij}$ with the thermal-mechanical elastic stress $\lambda_{LB}\hat{\sigma}_{ij}$ nowhere will violate the temperature-dependent yield condition. Hence, as the above upper bound iterative process provides a sequence of residual stress fields in (3.28), it is possible to evaluate an analogous lower bound at each step of the iteration by scaling the elastic solution so that $\lambda_{LB}\hat{\sigma}_{ij} + \overline{\rho}_{ij}$ satisfies the yield condition everywhere. The lower bound of shakedown limit multiplier can be written as: $\lambda_{LB}^{s} = \max\ \lambda_{LB}$.

The utilization of this shakedown method to limit analysis problems is made possible due to the similarities existing between the iterative processes associated with limit analysis and shakedown. This is easily demonstrated by assuming that the load and temperature remains constant with time at any loading histories *n*. With this change, the above procedure becomes the limit analysis. This shows that limit analysis is a special case of shakedown analysis, with the only exception which is the need to consider load cycles in shakedown calculations rather than a static load.

3.4 Benchmark Example

3.4.1 Geometry and Loading Condition

To demonstrate the numerical procedures, discussed in Sections 3.3, upper and lower bound shakedown limit calculations are reproduced [20] for a 3-D square plate with a hole subjected to a cyclic thermal load and constant mechanical load. The geometry of the structure and its finite element mesh are shown in Figure 3.4a and Figure 3.4b, respectively. The ABAQUS 20-node solid isoparametric element with reduced integration is adopted [80]. The ratio between the diameter *D* of the hole and the length *L* of the plate is 0.2 and the ratio of the depth of the plate to the

length L of the plate is 0.05. The plate is subjected to a temperature difference $\Delta\theta$ between the edge of the hole and the edge of the plate and the uniaxial tension P acts along one side (Figure 3.4a). The model of the 3D plate is assumed elastic perfectly plastic with the following material properties: Yield Stress σ_y=360MPa, Poisson's Ratio, ν=0.3, Young's Modulus, E= 200 GPa, Coefficient of Thermal Expansion, α=1.0x10^{-5}.

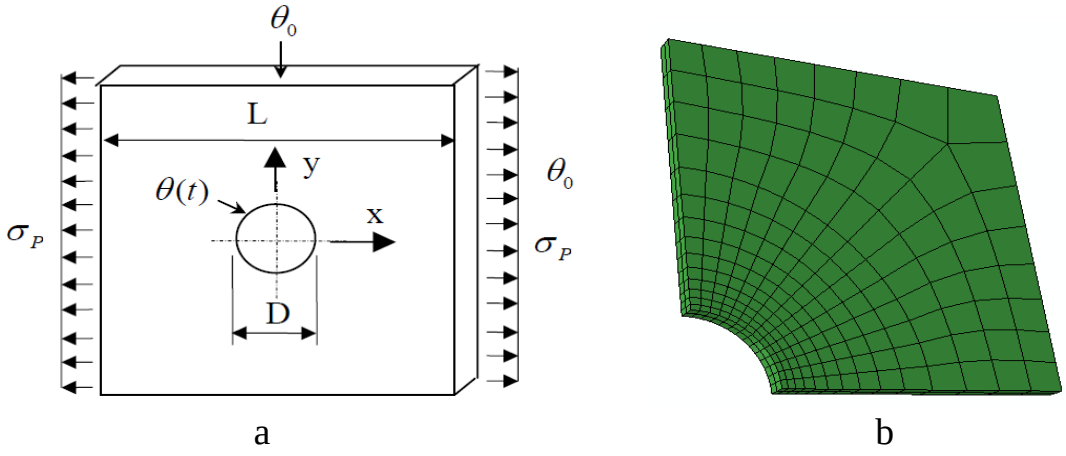

Figure 3.4 (a) Geometry of the square plate with a hole subjected to varying thermal load and constant tensile load (D/L=0.2) (b) Finite Element Mesh

The detailed temperature history at the inner bore of the hole is given in Figure 3.5, where $\theta(t)$ varies between θ_0 and $\theta_0+\Delta\theta$. When the ambient temperature θ_0 remains at $0^{\circ}C$, the magnitudes of the maximum thermo elastic stresses for the above thermal loading extremes can be determined by the maximum temperature difference $\Delta\theta$ between the bore of the hole and the edge of the plate. Hence the cyclic thermal load and constant mechanical load can be characterized by the maximum temperature difference $\Delta\theta$ and the uniaxial tension σ_p, respectively. The reference constant elastic mechanical stress can be calculated by the axial tension $\sigma_p=\sigma_{p0}=100MPa$ while the reference temperature difference $\Delta\theta=\Delta\theta_0=100^{\circ}C$ determines the reference cyclic elastic thermal stress. When the temperature-dependent yield stress $\sigma_y(T)$ is adopted, the actual load factor is updated in an iterative way during the calculation using equation (3.31).

$$\sigma_y(T)=\sigma_y^0-0.4\left(MPa/{}^0C\right)\times T \tag{3.31}$$

Where σ^0_y=360 MPa, and T is the temperature in Degree Celsius.

Two thermal stress extremes with two load instances are adopted for this cyclic load history:

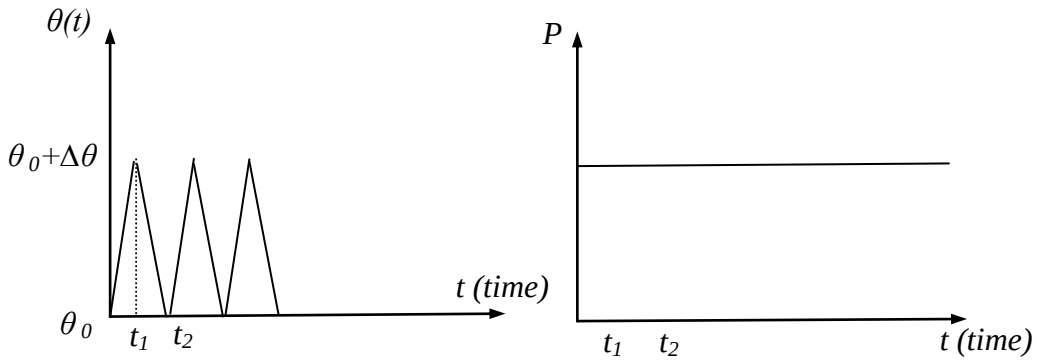

Figure 3.5 Load history for plate with hole under cyclic temperature variation and constant mechanical load

---Load instance (1): The temperature distribution and axial tension are applied (at time t_1 in Figure 3.5).

---Load instance (2): The temperature load is removed and the constant axial tension remains applied (at time t_2 in Figure 3.5).

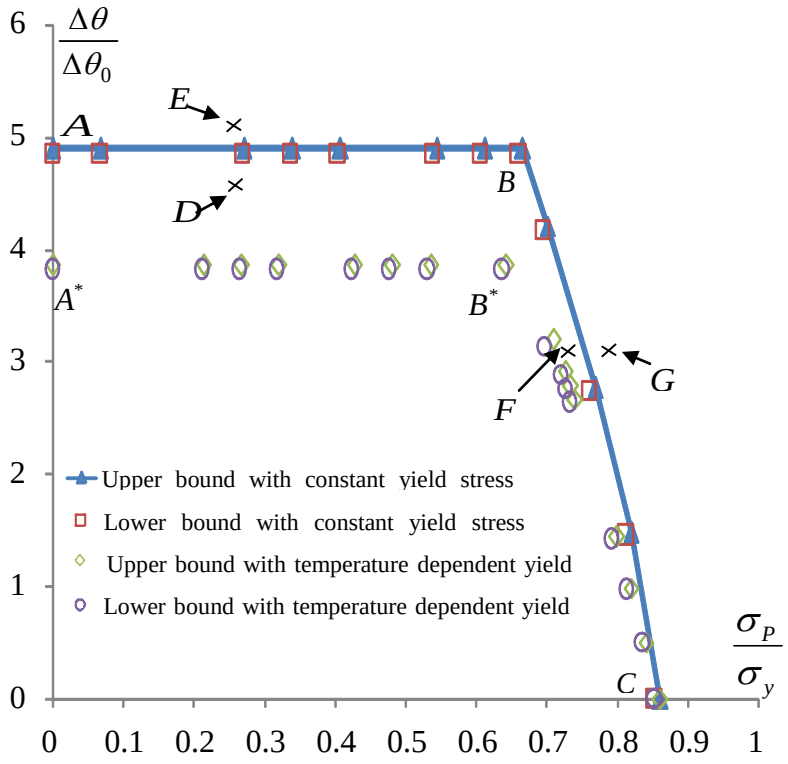

Figure 3.6 Upper and lower bounds shakedown limit interaction curves of the plate with a hole

3.4.2 Upper and Lower Bound Elastic Shakedown Boundary with Temperature Dependent and Independent Yield Stresses

Based upon the kinematic theorem of Koiter [36], the LMM procedure gives highly accurate upper bound [6] and lower bound shakedown limits [20]. The converged values of both upper and lower bounds elastic shakedown limits for the plate with hole are shown in Figure 3.6. Using various load combinations of cyclic $\Delta\theta$ and steady load P, the elastic shakedown load was calculated using the LMM method. A total of lower and upper bound results for non-temperature dependent and temperature dependent are tabulated in Table 3.1 and 3.2, respectively. From these tabulated results, an interaction diagram of shakedown limit for different ratios of varying thermal load and constant mechanical load is also presented in Figure 3.6. The applied pressure in X-axis is normalized with respect to the yield stress, σ_y, while the thermal load in Y-axis is normalized by using the reference temperature difference $\Delta\theta=\Delta\theta_0=100^{\circ}C$.

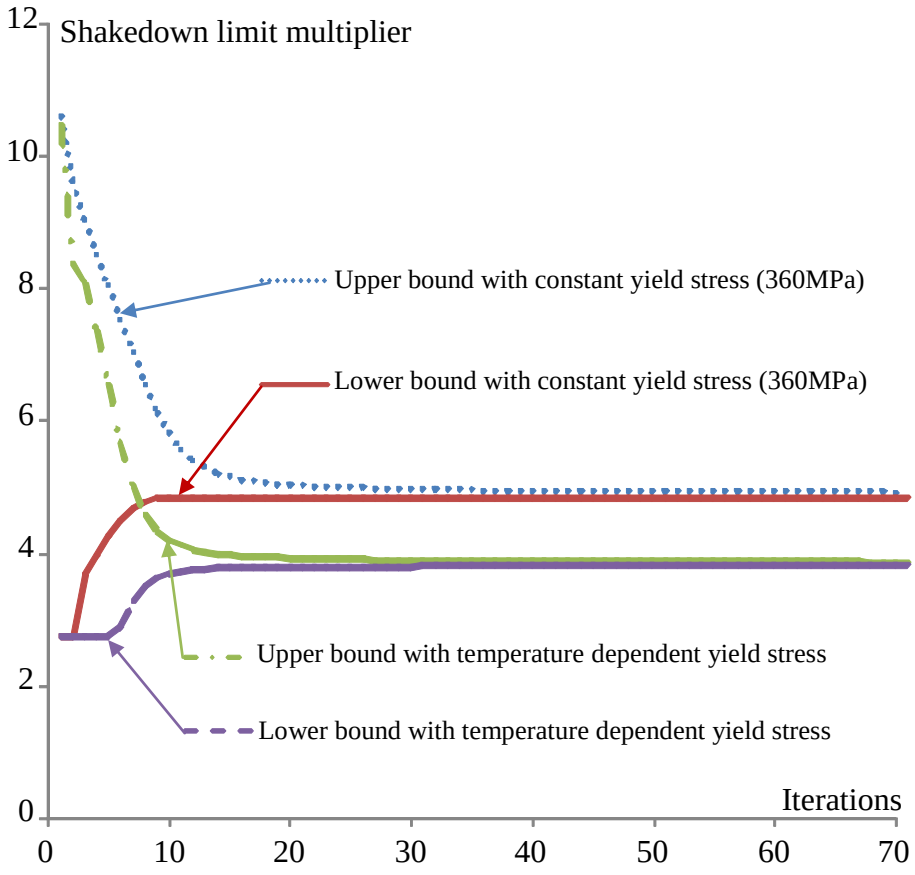

Figure 3.7 The convergence condition of iterative processes for shakedown analysis (point A and A*, subjected to cyclic thermal loads only)

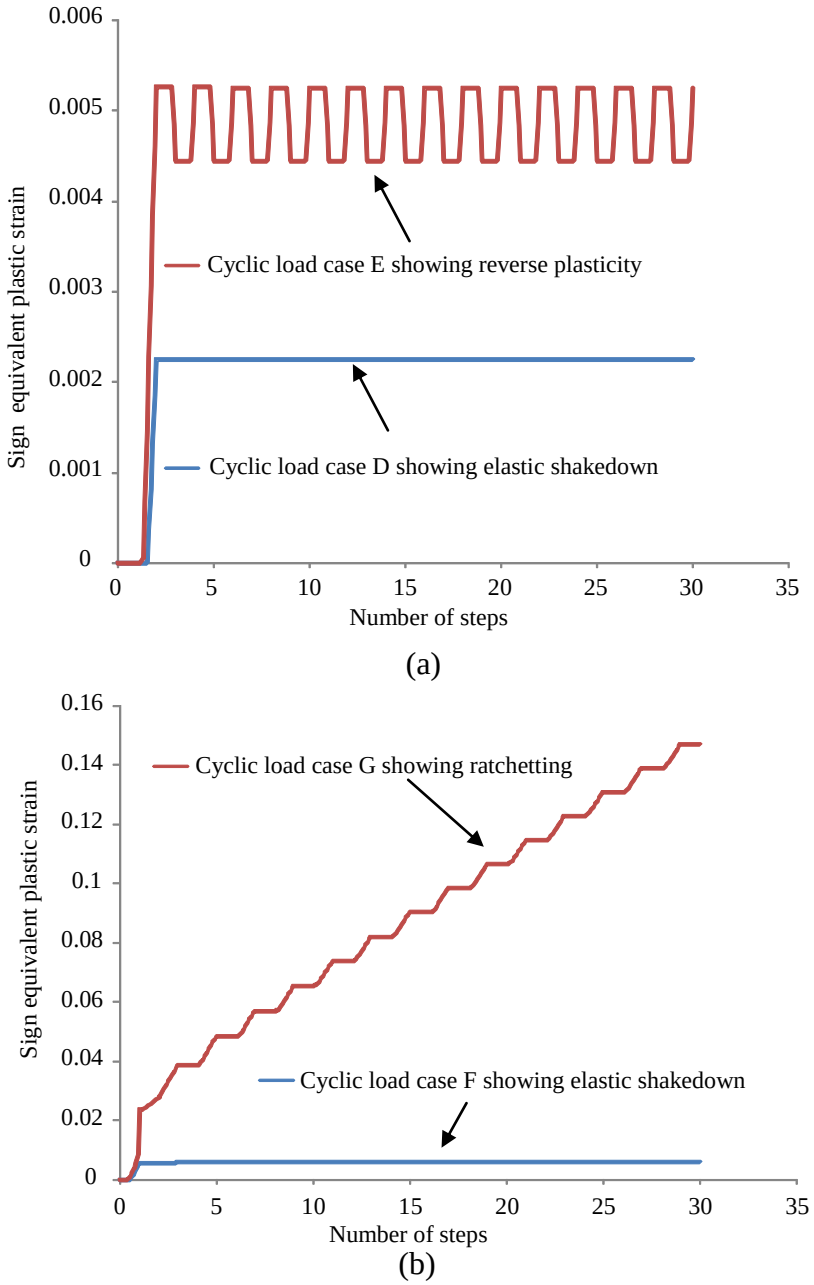

Figure 3.8 ABAQUS verification using step by step non-linear analysis for (a) the reverse plasticity limit (b) the ratchet limit

This diagram is divided into two regions separated by lines, which signify the transition from elastic shakedown behaviour to reverse plasticity (AB or A*B*) and the transition from elastic shakedown behaviour to ratchetting (BC or B*C). These lines on the interaction diagram are usually called the reverse plasticity limit (AB or A*B*), and ratchet limit (BC or B*C). Elastic shakedown will not occur if the load applied surpasses the reverse plasticity limit AB/A*B*. In this case the permanent strains settle into a closed cycle, a condition also known as “cyclic” or “alternating

plasticity". These permanent plastic strains will increase indefinitely if the applied cyclic load level is beyond the ratchet limit BC/B*C. This is known as "ratchetting" or "incremental plastic collapse". The point C corresponds to the limit load for the applied mechanical load acting alone with no cyclic temperature load. There are significant differences between the reverse plasticity limit A*B* assuming a temperature-dependent yield stress and the reverse plasticity limit AB considering a temperature-independent yield stress. Hence it is important to adopt temperature-dependent yield stress for a structure assessment under high temperature variations. However, in order to simplify the calculations, the temperature-independent yield stress can be adopted when the variation of operating temperature approaches to zero or the temperature varies within a limited range. The temperature effects on the yield stress may be ignored in such conditions.

The results of typical lower and upper bound sequences converging after 70 iterations for load point A (Figure 3.6) considering temperature-independent yield stress, and for load point A*(Figure 3.6) considering temperature-dependent yield stress are tabulated in Appendix I, respectively. These tabulate results are presented in Figure 3.7. It can be observed from Figure 3.7 that both the upper bound and lower bound converge to the exact shakedown limit proving that LMM produces highly accurate upper bound and lower bound shakedown limit results.

In order to verify the accuracy of the LMM, four load cases (labelled D, E, F and G in Figure 3.6) with cyclic and constant loads of D($\frac{\Delta\theta}{\Delta\theta_0}=4.7, \frac{\sigma_p}{\sigma_{p0}}=0.28$), E($\frac{\Delta\theta}{\Delta\theta_0}=5.1, \frac{\sigma_p}{\sigma_{p0}}=0.28$), F($\frac{\Delta\theta}{\Delta\theta_0}=3.1, \frac{\sigma_p}{\sigma_{p0}}=0.72$) and G($\frac{\Delta\theta}{\Delta\theta_0}=3.1, \frac{\sigma_p}{\sigma_{p0}}=0.81$) respectively, have been performed using ABAQUS step-by-step analyses to verify the elastic shakedown limit "ABC" (Figure 3.6). The signed equivalent plastic strain histories for the cyclic loading cases D, E, F and G are shown in Figure 3.8. The term signed equivalent plastic strain refers to the usual formulation of effective plastic strain, but with a sign equal to that of the principal plastic strain of greatest magnitude [1]. Load cases D (Figure 3.8a) and F (Figure 3.8b) exhibit elastic shakedown behaviour as the calculated equivalent plastic strain stop changing after 3

load cycles. The calculated sign equivalent plastic strain for the load case E (Figure 3.8) converges to a closed cycle after about 4 load cycles giving reverse plasticity behaviour, and the load case G (Figure 3.8b) shows strong ratchetting behaviour, with the sign equivalent plastic strain increasing at every cycle. Thus, the results in Figure 3.8 obtained using ABAQUS step-by-step analysis confirm the accuracy of the predicted elastic shakedown limit by the LMM. Further benefits of the LMM can be found considering the computing time necessary to generate the elastic shakedown interactive diagram. The time that the LMM needed to generate the points on the elastic shakedown and ratchetting boundary was less than 10% of that needed for the above four load cases to complete using the ABAQUS step-by-step analysis.

3.5 Conclusions

The capability of the identification of the elastic shakedown boundary using Linear Matching Method (LMM) is discussed in this chapter. The introduction of the fundamental shakedown theorems for a general problem, the numerical procedure, and the implementation for the upper and lower bound shakedown theorem [2], was then described for a problem of a plate with a central hole. The solutions showed that the LMM-based methodologies were capable of generating accurate elastic shakedown limit, within a finite number of iterations.

In Chapter 4, in order to demonstrate the efficiency and effectiveness of the LMM for more complex structures, a parametric study of a composite cylinder made of steel and aluminium with a cross hole subjected to cyclic thermal loads and constant pressure is analysed.

Table 3.1 Elastic shakedown loads for temperature independent σ_y

$\frac{\sigma_p}{\sigma_{p0}}$	$\frac{\Delta\theta}{\Delta\theta_0}$ (Upper bound)	$\frac{\Delta\theta}{\Delta\theta_0}$ (Lower bound)
0	4.897	4.848
0.245	4.897	4.848
0.979	4.897	4.848
1.224	4.897	4.848
1.469	4.897	4.848
1.959	4.897	4.848
2.203	4.896	4.848
2.399	4.896	4.848
2.524	4.207	4.165
2.768	2.768	2.737
2.952	1.476	1.461
3.099	0	0

Table 3.2 Elastic shakedown loads for temperature dependent σ_y

$\frac{\sigma_p}{\sigma_{p0}}$	$\frac{\Delta\theta}{\Delta\theta_0}$ (Upper bound)	$\frac{\Delta\theta}{\Delta\theta_0}$ (Lower bound)
0	3.857	3.819
0.771	3.857	3.819
1.543	3.857	3.819
1.929	3.857	3.819
2.314	3.857	3.819
2.554	3.193	3.138
2.616	2.907	2.878
2.642	2.781	2.753
2.666	2.666	2.639
2.879	1.440	1.425
2.952	0.984	0.976
3.025	0.504	0.501
3.099	0	0

CHAPTER 4. ELASTIC SHAKEDOWN ANALYSIS OF A COMPOSITE CYLINDER WITH A CROSS-HOLE

4.1 Introduction

Chapter Three described the numerical procedure for the Linear Matching Method to identify the upper and lower bound elastic shakedown limits. This method was then applied to the problem of a square plate with a hole. In this chapter, a further examination on a real industrial problem will be conducted; in this case a composite cylinder manufactured from steel and aluminium.

Innovations in materials have largely been responsible for the performance improvements in many areas of structures technology. The continuous development of computational structures technology and the advanced composite materials have improved structural performance, reduced operational risk, and shortened production time [81]. On the other hand, one of the most important reasons for using composite materials is the reduction of weight [82].

With the achievements in aerospace industry, the strength-to-weight ratio of engineering components has become a very important design criterion since a high strength-to-weight ratio results in a better performance and greater shear strength. The lower weight results in lower fuel consumption and emissions.

Strength-to-weight ratio is able to increase when the elastic limit of materials is surpassed and the allowable accumulated plastic strain constraints are assigned. In this way the design of composite pressure cylinder subjected to cyclic mechanical and thermal loads can be achieved. The investigations of the elastic and elastic-plastic behaviour of a uniform cylinder with a cross-hole under constant internal pressure and cyclic thermal loads are presented by the well-known Bree-like diagram in [83] and [84].

The local stress concentration is redistributed around the material boundaries for composite cylinders under cyclic thermal loads. This changes the fatigue life and elastic shakedown limits of the cylinder. As mentioned in Chapter 3, the elastic shakedown limit is the highest cyclical load at which a structure shakes down to an elastic response in the first few cycles of load. When the elastic shakedown limit is exceeded, the cylinder may experience either plastic shakedown or ratcheting. In many applications, it is allowable for a structure to be within the elastic shakedown limit, but plastic shakedown and alternating plasticity, under which a local low cycle fatigue failure mode occurs, and ratcheting that ultimately leads to incremental plastic collapse, are not permitted. Consequently the elastic shakedown limit is a particularly important design condition to the pressure cylinder.

In this chapter, in order to demonstrate the efficiency and effectiveness of LMM in the calculation of the elastic shakedown loads for more complex structures, the numerical procedure described in Chapter Three is applied to the problem of a composite cylinder. Specifically a cylinder, manufactured from steel and aluminium with a cross-hole subjected to a constant internal pressure and cyclic thermal loads. The Bree-like shakedown limit diagrams of the composite cylinders are plotted for different composite materials and thickness ratios with and without cross-holes. Three cross-hole sizes are considered, all relatively small in comparison with the other cylinder dimensions. The objective of the investigation is to formulate a safety shakedown limit region for industrial design purposes using the calculated shakedown limit results with different geometry parameters. This work has been published in the International Journal of Pressure Vessel Technology in 2010.

4.2 Composite Cylinder Geometry

The geometrical shape and the material properties of the composite cylinder with a cross-hole are as shown in Figure 4.1 and Table 4.1, respectively. The composite thick cylinder has an inner layer of steel and an outer layer of aluminum. R_i, R_m, R_o are the inner radius, middle radius, and outer radius of the composite cylinder, respectively.

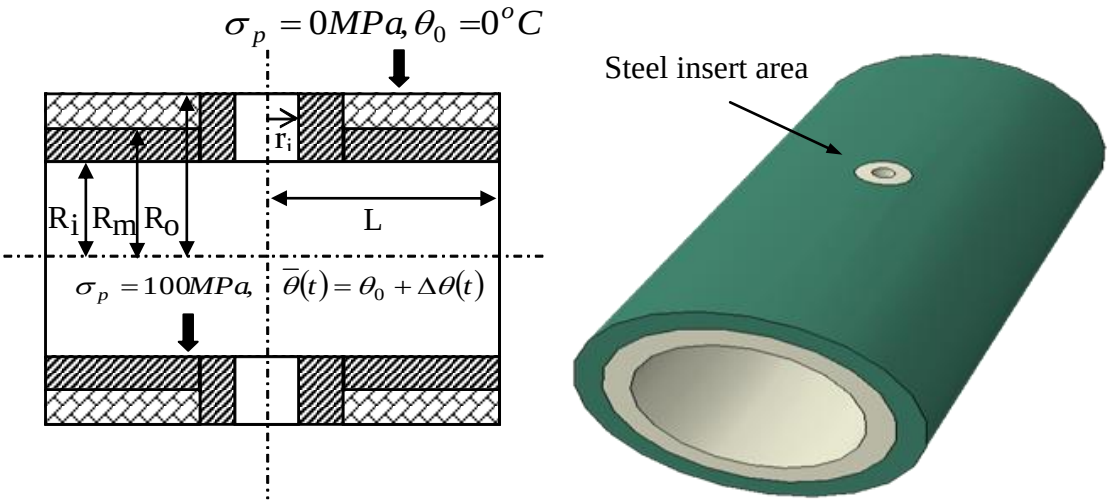

Figure 4.1Geometrical shape of the composite cylinder

The area surrounding the hole, which can be an instrumentation tapping or a port for the fluid entry or exit, is expected to be the most critical region since this is a structure discontinuity causing the rise of the local stress concentration. To improve the mechanical performance of this critical region, the material surrounding the hole is selected to be the same high performance steel as the inner portion of the composite cylinder. The thickness of the cylindrical shape steel insert is equal to the half thickness of the composite cylinder $\frac{R_o - R_i}{2}$.

Table 4.1 Material property parameters for the steel and aluminum

Type	Young's modulus E (GPa)	Poisson's ratio ν	Coefficient of thermal expansion α ($^\circ C^{-1}$)	Yield stress σ_y (MPa)	Thermal Conductivity k (W/mK)	Density (Kg/mm^3)
Steel	200	0.3	1.4×10^{-5}	360	20	7.85×10^{-6}
Aluminium	72	0.33	2.36×10^{-5}	100	250	2.7×10^{-6}

The shakedown results are obtained for three different radius ratios: $R_o/R_i = 1.5, 1.75, 2.0$. Three cross-hole radius ratios are also modelled: $r_i/R_i = 0.1, 0.2, 0.3$. The maximum radius ratios $\frac{r_i}{R_i} = 0.3$ defined in this study meets

the requirement of ASME B&PV Code Section VIII Division 2, in which the limitation of $\frac{r_i}{R_i}$ should be less or equal to 1/2 for perforated cylindrical shells [10]. The analysis is performed for three composite material ratios: $V_s/V_A = \frac{1}{3}, 1, 3$, where V_s and V_A stand for the volume of steel and aluminum, respectively. For better comparison of results, in all the cases the inner radius is chosen to be $R_i = 300mm$ while length is $L = 900mm$.

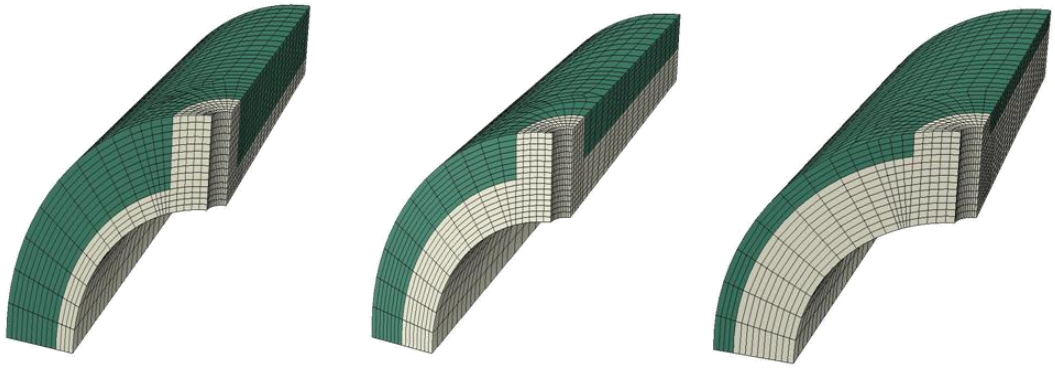

(a) $\frac{V_s}{V_A} = \frac{1}{3}$ (b) $\frac{V_s}{V_A} = 1$ (c) $\frac{V_s}{V_A} = 3$

Figure 4.2 Quarter finite element models for different material ratios

4.3 Finite Element Modelling

Table 4.2 Temperature-dependent yield stress for aluminum

Temperature (°C)	0	100	200	300	400	500	525	550	600
$\sigma_y(T)$ (MPa)	100	90	72.7	43.9	31.8	27.3	23.2	19.3	15.1

The composite cylinders were analysed using ABAQUS type C3D20R 20 node quadratic brick elements with a reduced integration scheme. The composite cylinders with cross-holes have three planes of symmetry. Hence, to minimize the size of the model, these symmetry boundary conditions are applied to a quarter section of the model. A 3D view of a composite cylinder with cross-hole is shown in

Figure 4.2. The main cylinder bore and the hole bore are under constant internal pressure. The cut end of the cylinder is constrained (by using ABAQUS constrained equation) in order to keep the plane section plane during loading. The closed-end boundary condition is achieved by applying uniform axial thrust ($T_N = \sigma_p R_i^2 \big/ \left(R_o^2 - R_i^2\right)$) to the end of the cylinder, where σ_p is the internal pressure. The holes are assumed to have open-ended boundary condition. The applied cyclic thermal loading is produced by assuming that the outside surface of the cylinder is at ambient temperature while the internal surface temperature is fluctuating from ambient to higher values. Three thermal stress extremes are adopted for this cyclic load history:

Firstly, according to different thermal conductivities of the steel and aluminum, a thermal stress is produced by the most significant nonlinear thermal gradient along the thickness. This most significant thermal load is calculated by a steady-state thermal analysis;

Secondly, a thermal stress occurring at the highest uniform temperature is applied due to the material mismatch. This thermal stress is produced because thermal expansions between the steel and aluminum are significantly different;

Finally, a zero thermal stress field is selected to simulate a uniform ambient temperature for the whole cylinder.

When the ambient temperature θ_0 remains at $0^o C$, the magnitudes of the maximum von-Mises effective thermo elastic stresses for the above thermal loading extremes can be determined by the maximum temperature difference $\Delta\theta$ between the inner surface and outer surface of the composite cylinder. Hence these thermal and mechanical load path extremes can be characterized by the maximum temperature difference $\Delta\theta$ and the internal pressure σ_p. The reference constant elastic mechanical stress can be calculated by the internal pressure $\sigma_p = \sigma_{p0} = \sigma_y^{\text{aluminum}} = 100 MPa$ while the reference temperature difference $\Delta\theta = \Delta\theta_0 = 100^o C$ determines the reference cyclic thermal elastic stresses. When the temperature-dependent yield stress $\sigma_Y(T)$ is adopted, the actual load factor is updated in an iterative way during the calculation. The adopted temperature-

dependent yield stress is given in equation (4.1) for steel and presented in Table 4.2 for aluminum:

$$\sigma_y(T) = \sigma_y^0 - 0.4\left(MPa/{}^0C\right)\times T \tag{4.1}$$

4.4 Results and Discussions

4.4.1 Upper and Lower Bound Results with Temperature Dependent and Independent Yield Stresses

Based upon the kinematic theorem of Koiter [36], the LMM procedure has proved to produce highly accurate upper bound [6] and lower bound shakedown limits [20]. The converged values of both upper and lower bounds shakedown limits for the composite cylinder are shown in Figure 4.3 where material ratios, cylinder and cross-hole radius ratios are $\frac{V_s}{V_A}=1$, $\frac{R_o}{R_i}=1.75$, $\frac{r_i}{R_i}=0.1$, respectively. In Figure 3.7 it is observed that the converged solution is reached after 20 iterations while in Figure 4.3 the convergence is obtained after 60 iterations. This is due to the initial value of the chosen shear modulus, since the speed of the convergence depends on how close the chosen shear modulus is to the convergent solution during the linear matching process. An interaction diagram consisting of shakedown limit for different ratios of varying thermal load and constant mechanical load is also presented. This limit is divided into two regions; the reverse plasticity limit AB or A*B*, and the ratchet limit BC or B*C. Elastic shakedown will not occur if the load applied surpasses the reverse plasticity limit AB/ A*B*. In this case the permanent strains settle into a closed cycle, a condition also known as “cyclic” or “alternating plasticity”. These permanent plastic strains will increase indefinitely if the applied cyclic load level is beyond the ratchet limit BC/ B*C. This is known as “ratchetting” or “incremental plastic collapse”. The point C corresponds to the limit load for the applied mechanical load. There are significant differences between the reverse plasticity limit A*B* adopting temperature-dependent yield stress and the reverse plasticity limit AB considering temperature-independent yield stress. Hence it is important to adopt temperature-dependent yield stress for a structure assessment under high temperature variations. However, in order to simplify the calculations, the

temperature-independent yield stress can be adopted when the variation of operating temperature approaches to zero or the temperature varies within a limited range. The temperature effects on the yield stress may be ignored in such conditions.

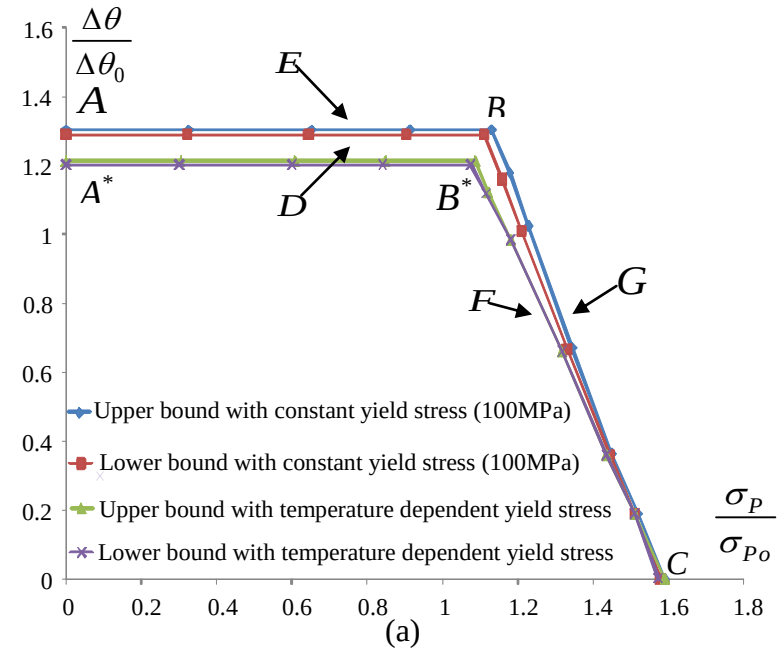

(a)

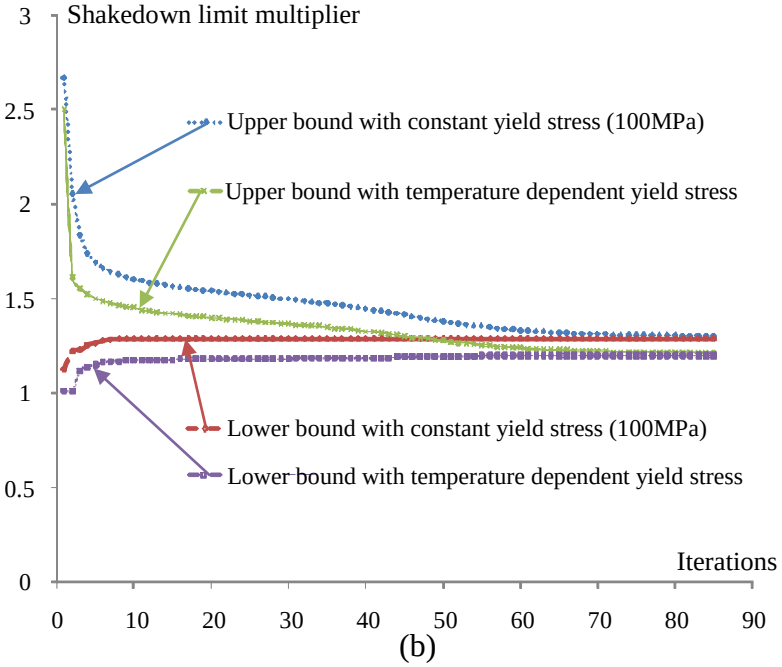

(b)

Figure 4.3 a) Upper and lower bounds shakedown limit interaction curves of the composite cylinder b) the convergence condition of iterative processes for shakedown analysis (point A and A*, subjected to cyclic thermal loads only) ($\frac{V_s}{V_A}=1$, $\frac{R_o}{R_i}=1.75$, $\frac{r_i}{R_i}=0.1$)

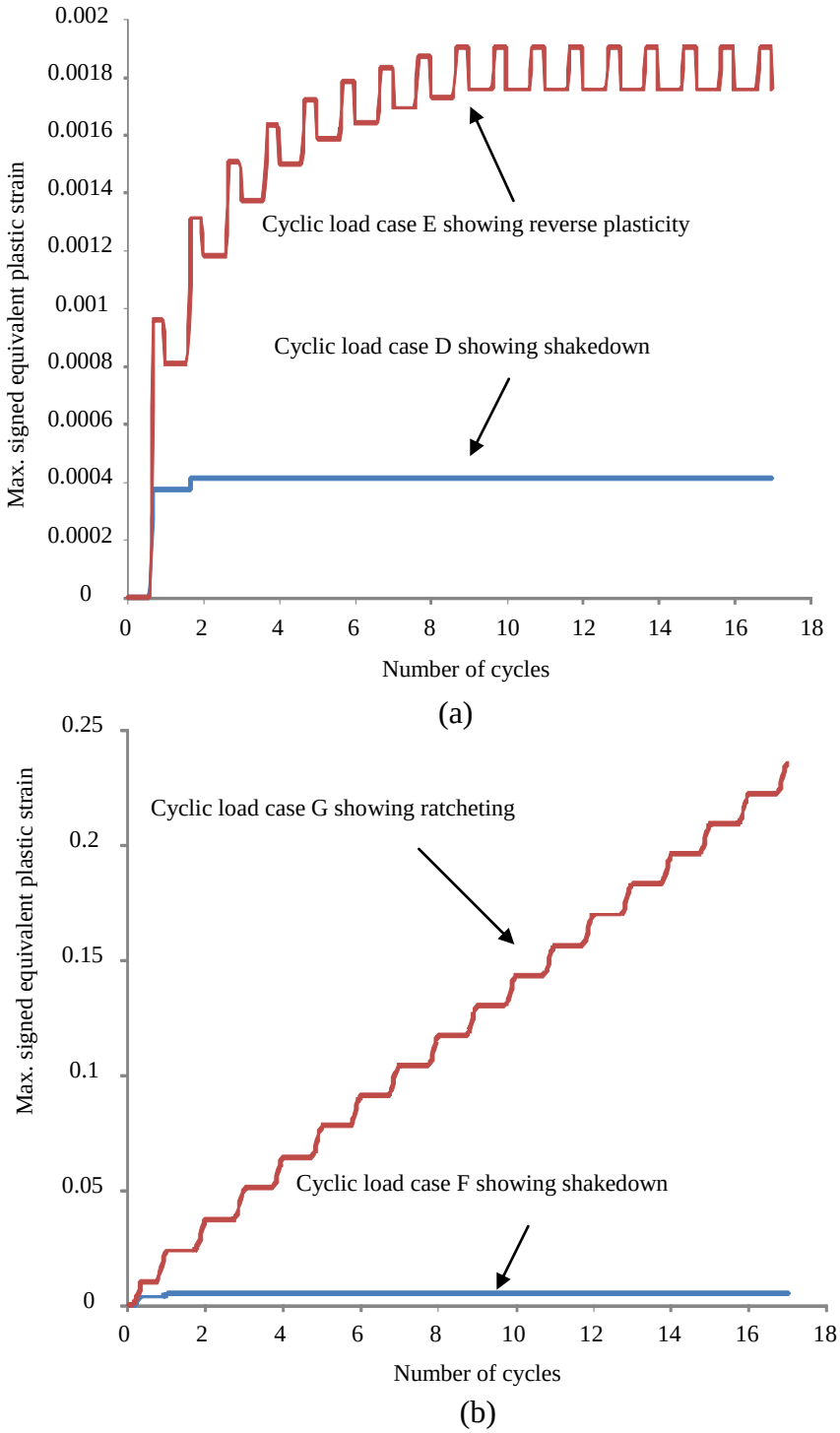

Figure 4.4 ABAQUS verification using step by step analysis for (a) the reverse plasticity limit (b) the ratchet limit

Figure 4.3b shows typical upper and lower bound sequences converging after 70 iterations for load point A (Figure 4.3a) considering temperature-independent yield stress, and for load point A*(Figure 4.3a) considering temperature-dependent yield stress. It can be observed that both the upper bound and lower bound converge

to an exact shakedown limit proving that LMM produces highly accurate upper bound and lower bound shakedown limit results. For the simplification of discussion, the results in the next section only show the upper bound shakedown limit for the temperature-independent yield stress.

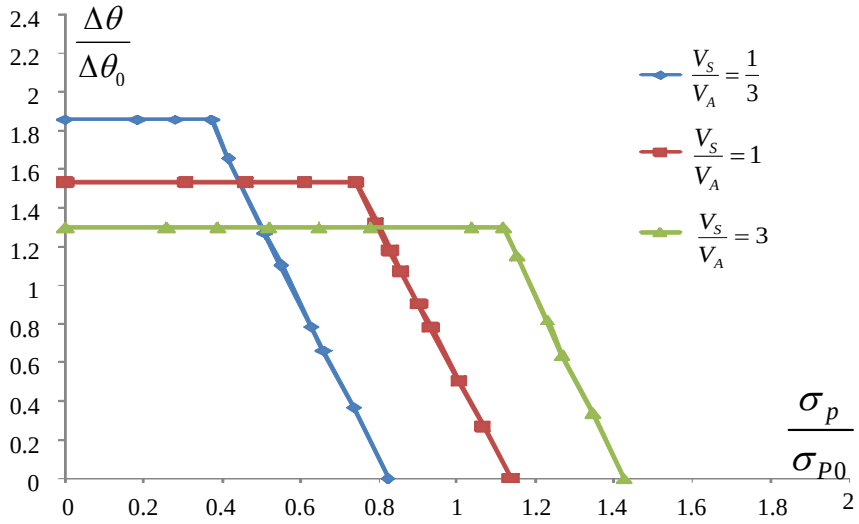

Figure 4.5 Shakedown limit interaction curves of the composite cylinder for different composite material ratios without cross-hole

In order to verify the accuracy of the LMM, four load cases (labelled D, E, F and G in Figure 4.3a) with cyclic thermal loads of $\frac{\Delta\theta}{\Delta\theta_0}=1.25$, $\frac{\Delta\theta}{\Delta\theta_0}=1.35$, $\frac{\Delta\theta}{\Delta\theta_0}=0.7$ and $\frac{\Delta\theta}{\Delta\theta_0}=0.7$ respectively, have been performed using ABAQUS step-by-step analyses. The plastic strain histories representing the maximum plastic strain range for the cyclic loading cases D, E, F and G are shown in Figure 4.4. Load cases D (Figure 4.4a) and F (Figure 4.4b) exhibit elastic shakedown mechanism as the calculated maximum signed equivalent plastic strain stop changing after two load cycles. The calculated maximum signed equivalent plastic strain for the load case E (Figure 4.4a) converges to a closed cycle after about nine load cycles showing a reverse plasticity mechanism, and the load case G (Figure 4.4b) shows a strong ratchetting mechanism, with the maximum signed equivalent plastic strain increasing at every cycle. Thus, the results in Figure 4.4 obtained using ABAQUS step-by-step analysis confirm the accuracy of the predicted shakedown limits by the LMM. Further benefits of the LMM can be found considering the computing time necessary to generate the

shakedown curves. The total time that the LMM needed to generate the points on the ratcheting boundary was less than 10% of that needed for the above four load cases to complete using the ABAQUS step-by-step analyse methodology.

4.4.2 Effect of the Composite Material Ratio

The upper bound temperature independent shakedown limit interaction curves of a composite cylinder with varying material ratio configurations (Figure 4.2) are presented in Figure 4.5. The applied pressure σ_p, in X-axis is normalized with respect to the reference internal pressure σ_{p0} while the thermal load $\Delta\theta$, in Y-axis is normalized by using the reference temperature difference $\Delta\theta_0 = 100^o C$.

Figure 4.5 shows that the limit load of the composite cylinder reduces when the volume of steel material is decreasing, whereas the reverse plasticity limit is increased with smaller $\frac{V_s}{V_A}$. The reduction in the limit load is approximately in proportion to the loss of steel material. The increasing reverse plasticity limit is due to the difference in thermal conductivities of the steel and aluminum. As the volume of aluminum increases, a larger proportion of the cylinder will have larger thermal conductivity, which leads to a lower thermal elastic stress range. Hence, when the volume of aluminum increases the reverse plasticity limit increases. Shakedown limit interaction curves of the composite cylinder ($\frac{R_o}{R_i} = 1.5$) with cross-hole for different composite material ratios and different cross-hole ratios are presented in Figure 4.6 which shows that with the addition of a cross-hole, the general trend of the shakedown curves is similar to Figure 4.5. Both figures show a decreasing limit load and increasing reverse plasticity limit for decreasing volume of steel. It is worth noting that for the pure material cases, the reverse plastic limit is determined by the maximum thermal stress due to the temperature gradient while the reverse plastic limit for the composite material is defined by the maximum thermal stress due to the material mismatch. The addition of a hole gives rise to a local stress concentration. This is shown to have little effect on the limit load for any material configuration when the hole diameter is small. A detailed discussion of the effects of the hole diameter is given in section 4.4.3.

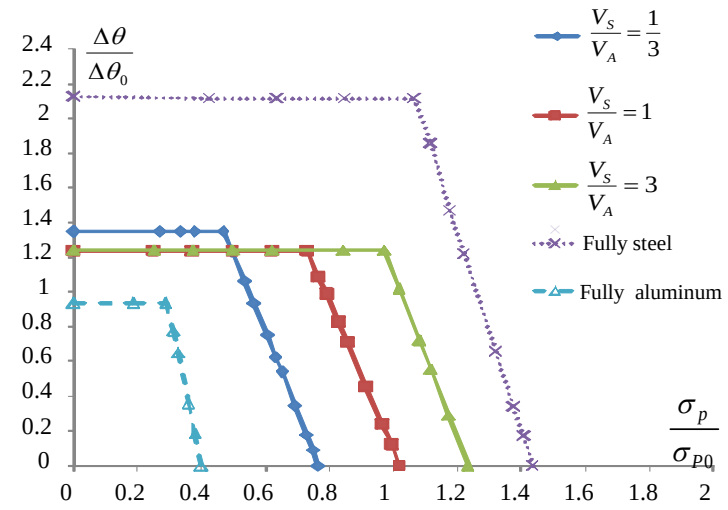

(a)

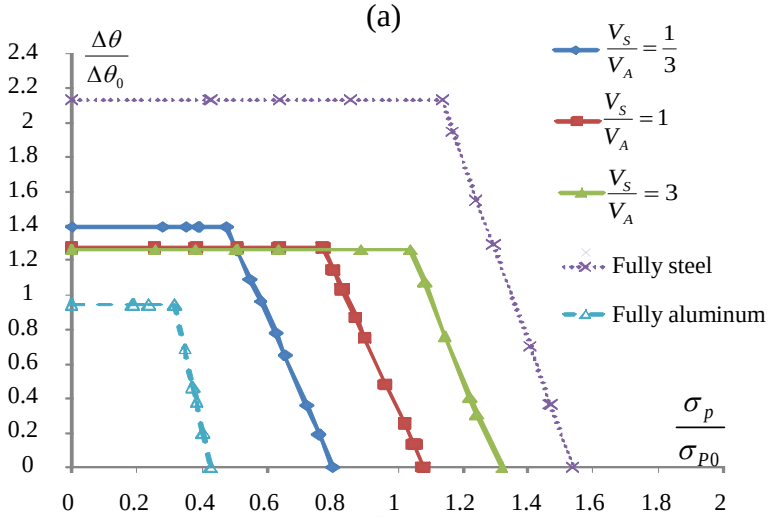

(b)

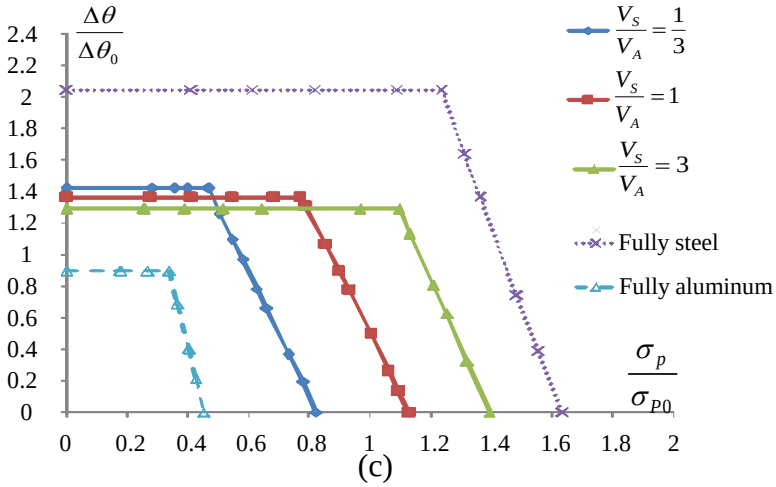

(c)

Figure 4.6 Shakedown limit interaction curves of the composite cylinder ($\frac{R_o}{R_i}=1.5$) for different composite material ratio with different cross-hole ratio: a) $\frac{r_i}{R_i}=0.3$ b) $\frac{r_i}{R_i}=0.2$ c) $\frac{r_i}{R_i}=0.1$

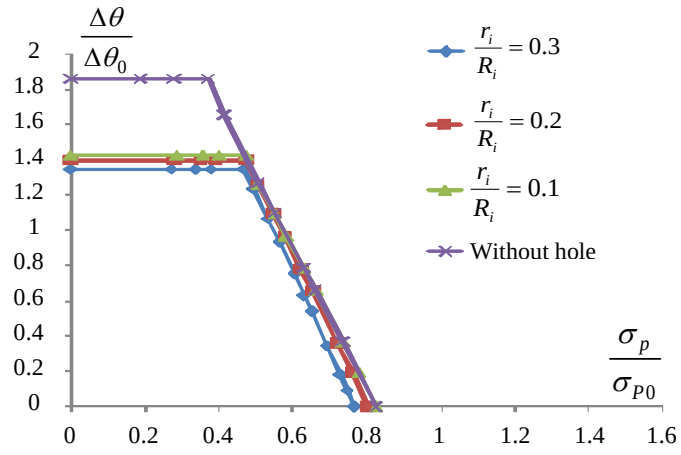

(a)

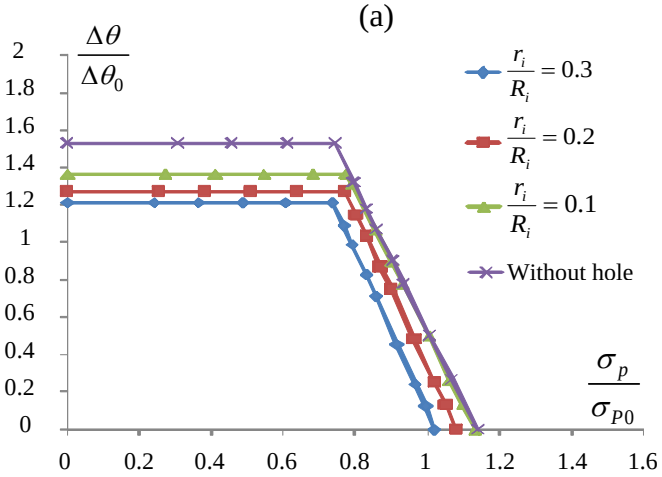

(b)

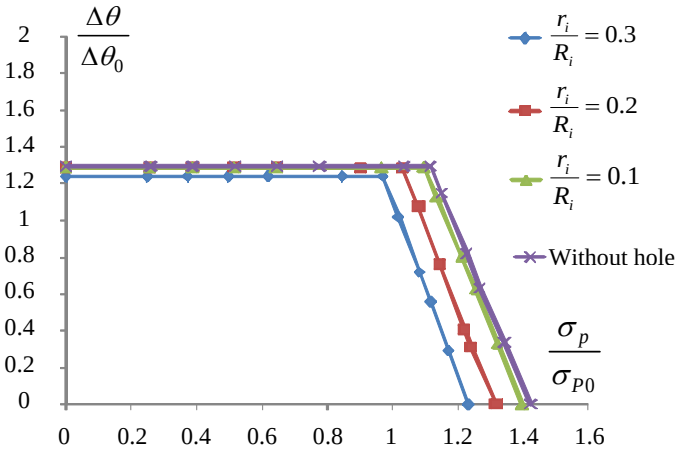

(c)

Figure 4.7 Shakedown limit interaction curves of the composite cylinder ($\frac{R_o}{R_i}=1.5$) with different hole radius ratios and different composite material ratios: a) $\frac{V_s}{V_A}=\frac{1}{3}$ b) $\frac{V_s}{V_A}=1$ c) $\frac{V_s}{V_A}=3$

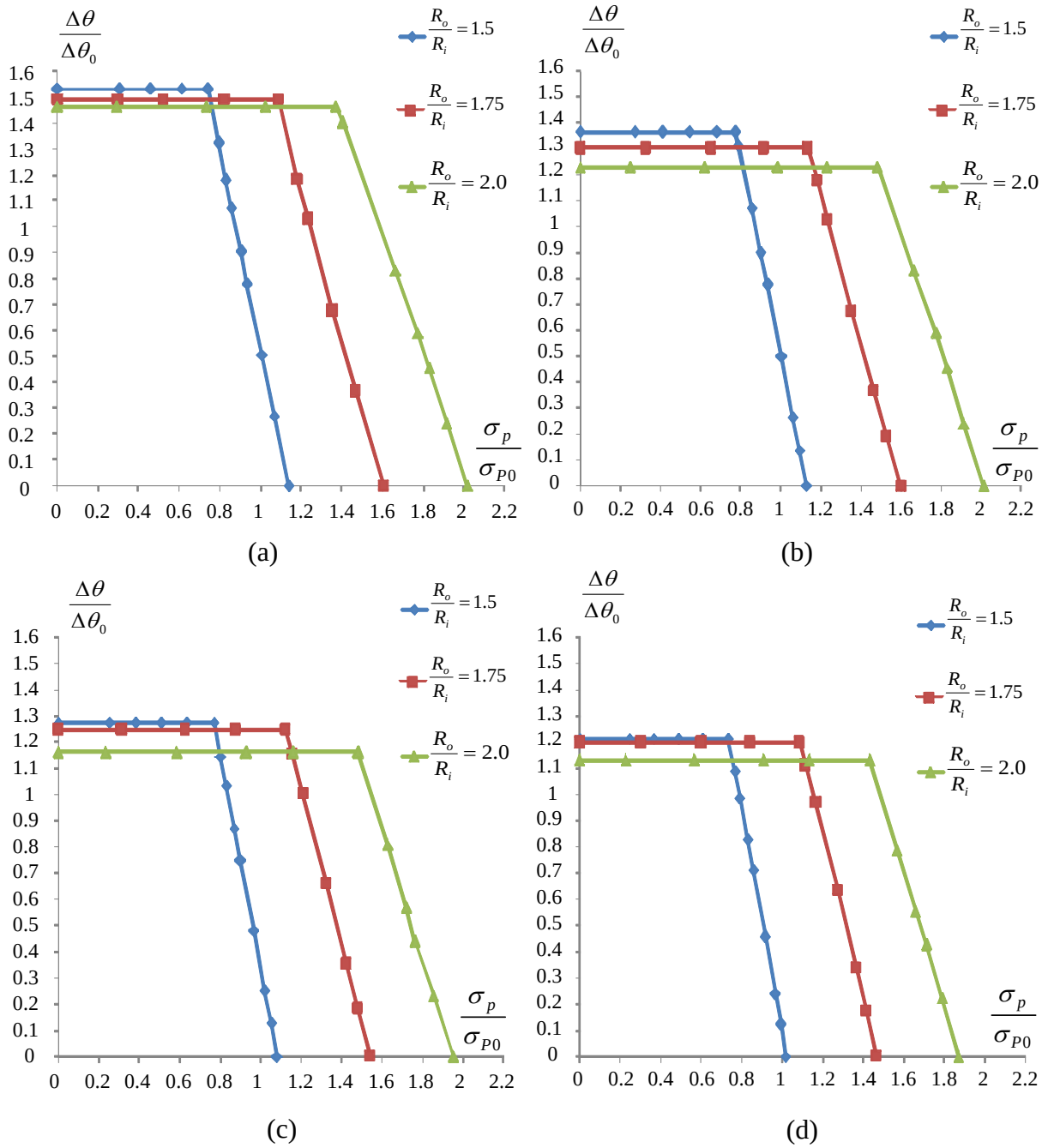

Figure 4.8 Shakedown limit interaction curves for the composite cylinder ($\frac{V_s}{V_A}=1$) with different thickness radius ratios and different hole radius ratios: a) without hole b) $\frac{r_i}{R_i}=0.1$ c) $\frac{r_i}{R_i}=0.2$ d) $\frac{r_i}{R_i}=0.3$

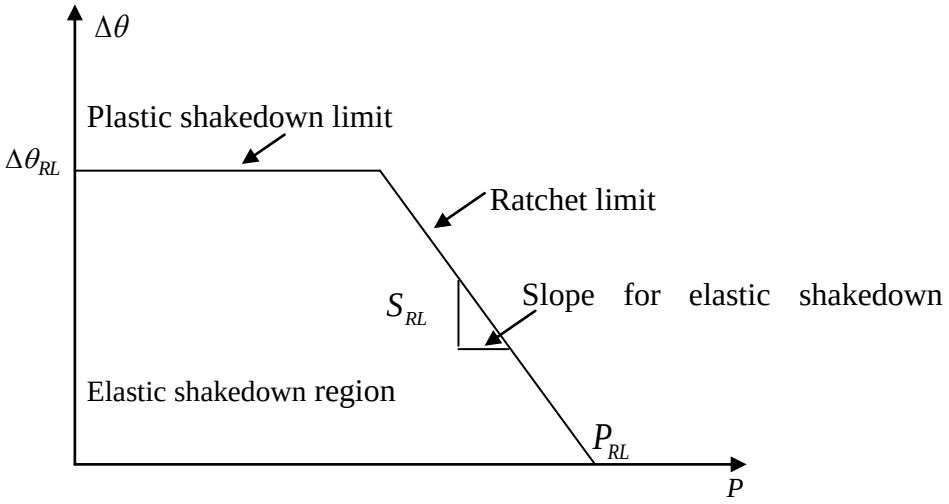

Figure 4.9 Elastic shakedown design regions for composite cylinders

4.4.3 Effect of the Hole Diameter

Cross-holes in composite cylinders are structural discontinuities which increase elastic stress due to local stress concentration. The influence of cross-hole size, $r_i/R_i = 0.1, 0.2, 0.3$ on the shakedown limit interaction curve is shown in Figure 4.7 for different material ratio configurations.

Figure 4.7a shows that for a material ratio of $\frac{1}{3}$, the addition of a hole has a large impact on the reverse plasticity limit, which demonstrates the dominance of this stress raiser to the mechanism. The addition of a hole is shown to have negligible effect on the limit load. When the material ratio $\frac{V_s}{V_A} = \frac{1}{3}$, the limit load is determined by the large proportion of the aluminum material due to its lower yield stress. The introduction of a hole has much less effect on the limit load than this small material ratio.

Figure 4.7b demonstrates that for a material ratio of 1, the addition of a hole has a sizable effect on the reverse plasticity limit, but impacts the limit load less significantly than Figure 4.7c for a material ratio of 3. This is because when the material ratio reduces to 1, the stress concentration from the hole becomes

comparable with the stress concentration due to the material mismatch. When the size of hole increases, both the limit load and reverse plasticity limit decreases.

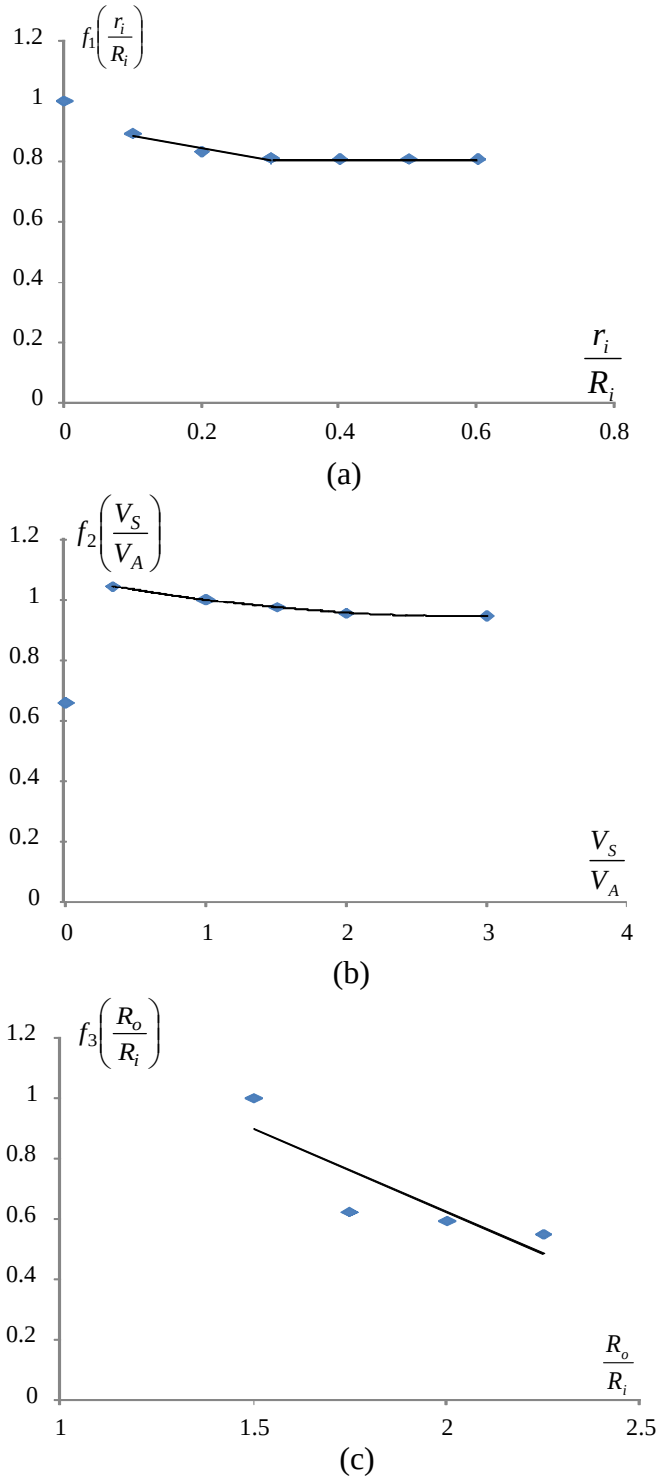

Figure 4.10 Influence functions for reverse plasticity limits against: a) cross-hole ratio b) steel to aluminum ratio c) thickness ratio

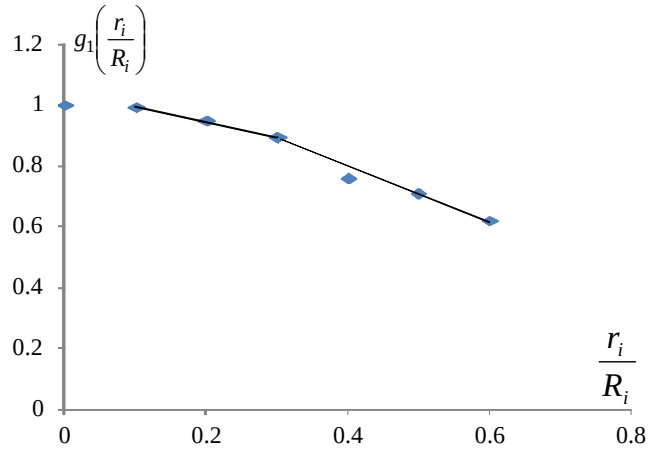

(a)

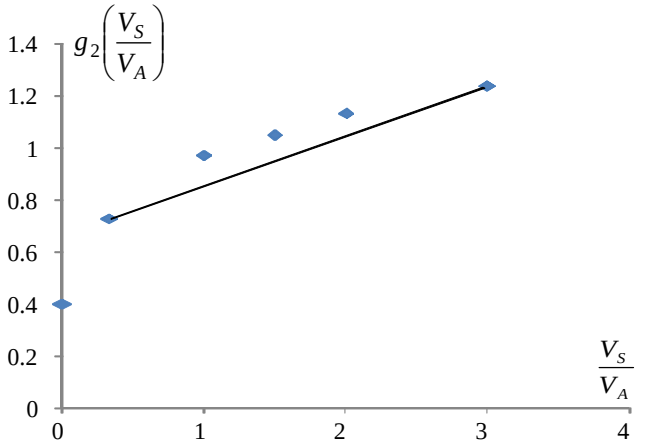

(b)

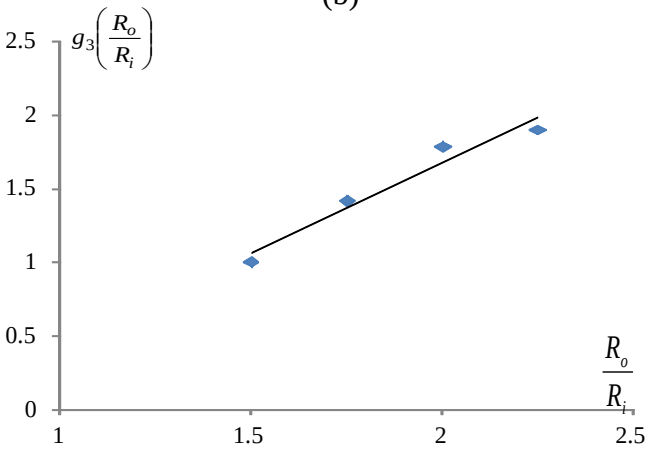

(c)

Figure 4.11 Influence functions for limit pressures against: a) cross-hole ratio b) steel to aluminum ratio c) thickness ratio

Figure 4.7c shows that for a material ratio of 3, the addition of a hole has little effect on the value of reverse plasticity limit, but causes a reduction in the limit load. The reduction in material by an increasing hole diameter is the cause of the reduction in limit load. There is little effect of the hole size on the reverse plasticity limit due to the dominance of the material boundary stress raiser, which has little interaction with the stress concentration caused by the hole.

4.4.4 Effect of the Composite Cylinder Thickness

Figure 4.8 presents the effects of the radius ratio $\frac{R_o}{R_i}$ on the shakedown limit interaction curve. Three different relative thicknesses $R_o/R_i = 1.5, 1.75, 2.0$ of the composite cylinder with a fixed material ratio of 1 were analyzed.

Increasing this radius ratio greatly increases the limit load and reduces the reverse plasticity limit. The increase in limit load is an obvious result, as effectively the thickness of the pipe is increased for the same inner radius. The reduction in the reverse plasticity limit is caused by the increased thickness of steel. This increase in thickness (which causes greater conductive temperatures in the steel) results in higher thermal stresses at the material boundary.

4.4.5 Formulated Shakedown Limit Design Region

In this section an elastic shakedown limit formulation for the composite cylinder is made for the purposes of safety in engineering design. A "theoretical" diagram of the elastic shakedown design regions for composite cylinders are shown in Figure 4.9, where $\Delta\theta_{RL}$ is the design temperature range corresponding to the reverse plasticity limit, P_{RL} is the design internal pressure representing the limit load and S_{RL} is the design slope of the ratchet limit curve. Figure 4.9 is the elastic shakedown region of a typical Bree interaction diagram [30]. In order to simplify the formulation, $\Delta\theta_{RL}$, P_{RL} and S_{RL} are assumed to be the product of three independent functions $f_1\left(\frac{r_i}{R_i}\right)$, $f_2\left(\frac{V_S}{V_A}\right)$, $f_3\left(\frac{R_o}{R_i}\right)$; $g_1\left(\frac{r_i}{R_i}\right)$, $g_2\left(\frac{V_S}{V_A}\right)$, $g_3\left(\frac{R_o}{R_i}\right)$, and $h_1\left(\frac{r_i}{R_i}\right)$, $h_2\left(\frac{V_S}{V_A}\right)$,

$h_3\left(\frac{R_o}{R_i}\right)$ respectively. In Figure 4.9 the X axis is the applied pressure P_{RL} and the Y axis is the applied temperature difference $\Delta\theta_{RL}$. Therefore, the design shakedown limits are formulated as

$$\Delta\theta_{RL} = \Delta\theta_L f_1\left(\frac{r_i}{R_i}\right) f_2\left(\frac{V_s}{V_A}\right) f_3\left(\frac{R_0}{R_i}\right) \tag{4.2}$$

$$P_{RL} = P_L g_1\left(\frac{r_i}{R_i}\right) g_2\left(\frac{V_s}{V_A}\right) g_3\left(\frac{R_o}{R_i}\right) \tag{4.3}$$

$$S_{RL} = S_L h_1\left(\frac{r_i}{R_i}\right) h_2\left(\frac{V_S}{V_A}\right) h_3\left(\frac{R_o}{R_i}\right) \tag{4.4}$$

Where $f_1\left(\frac{r_i}{R_i}\right)$, $f_2\left(\frac{V_S}{V_A}\right)$, $f_3\left(\frac{R_o}{R_i}\right)$, are the influence functions for the design temperature range corresponding to the reverse plasticity limit, $g_1\left(\frac{r_i}{R_i}\right)$, $g_2\left(\frac{V_S}{V_A}\right)$, $g_3\left(\frac{R_o}{R_i}\right)$ are the influence functions for the design internal pressure representing the limit load, and $h_1\left(\frac{r_i}{R_i}\right)$, $h_2\left(\frac{V_S}{V_A}\right)$, $h_3\left(\frac{R_o}{R_i}\right)$ are the influence functions for the design slope of the ratchet limit curve. $\frac{r_i}{R_i}$, $\frac{V_S}{V_A}$ and $\frac{R_o}{R_i}$ stand for the cross-hole ratio, steel to aluminum ratio and thickness ratio, respectively. $\Delta\theta_L$, P_L and S_L are constants standing for the calculated reverse plasticity limit, the limit internal pressure and the slope of the ratchet limit curve in case of $\frac{R_o}{R_i}=1.5$, $\frac{V_S}{V_A}=1$ without a cross-hole, where,

$$\Delta\theta_L = 153^0 C \tag{4.5}$$

$$P_L = 113.8 MPa \tag{4.6}$$

$$S_L = 3.873^0 C / MPa \tag{4.7}$$

In order to find these influence functions, the obtained reverse plasticity limits, limit internal pressure and the slope of the ratchet limit curve are replotted in graphs of functions *f*, *g* and *h* against $\frac{r_i}{R_i}$, $\frac{V_S}{V_A}$ and $\frac{R_o}{R_i}$ respectively as shown in Figure 4.10, Figure 4.11 and Figure 4.12. Trend lines are fitted to the data obtained from the shakedown limit results of different composite material ratio and cylinder thickness ratio with different cross-hole sizes to show the influence function. Equations (4.8)-(4.10), (4.11)-(4.13) and (4.14)-(4.16) are the obtained influence functions for the design temperature range corresponding to the reverse plasticity limit, the design internal pressure representing the limit load, and the design slope of the ratchet limit curve, respectively. Once $\Delta\theta_{RL}$, P_{RL} and S_{RL}, are defined, a safety shakedown envelope is created as shown in Figure 4.9.

$$f_1\left(\frac{r_i}{R_i}\right)=\begin{cases}1 & \left(\frac{r_i}{R_i}=0\right)\\ -0.411\left(\frac{r_i}{R_i}\right)+0.926 & \left(0.1\le\frac{r_i}{R_i}<0.3\right)\\ 0.803 & \left(0.3\le\frac{r_i}{R_i}<0.7\right)\end{cases} \tag{4.8}$$

$$f_2\left(\frac{V_S}{V_A}\right)=\begin{cases}0.659 & (\textit{pure}\ \text{aluminum})\\ 0.015\left(\frac{V_S}{V_A}\right)^2-0.087\left(\frac{V_S}{V_A}\right)+1.072 & \left(\frac{1}{3}\le\frac{V_S}{V_A}\le 3\right)\\ 1.495 & (\textit{pure steel})\end{cases} \tag{4.9}$$

$$f_3\left(\frac{R_o}{R_i}\right)=-0.659\left(\frac{R_o}{R_i}\right)+1.989 \qquad \left(1.5\le\frac{R_o}{R_i}\le 2.25\right) \tag{4.10}$$

$$g_1\left(\frac{r_i}{R_i}\right)=\begin{cases}1 & (\frac{r_i}{R_i}=0)\\ -0.494\left(\frac{r_i}{R_i}\right)+1.043 & (0.1\le\frac{r_i}{R_i}<0.3)\\ -0.872\left(\frac{r_i}{R_i}\right)+1.156 & (0.3\le\frac{r_i}{R_i}<0.7)\end{cases} \tag{4.11}$$

$$g_2\left(\frac{V_S}{V_A}\right)=\begin{cases}0.402 & (\textit{pure}\ \text{aluminum})\\ 0.173\left(\frac{V_S}{V_A}\right)+0.827 & (\frac{1}{3}\le\frac{V_S}{V_A}\le 3)\\ 1.433 & (\textit{pure steel})\end{cases} \tag{4.12}$$

$$g_3\left(\frac{R_o}{R_i}\right)=1.227\left(\frac{R_o}{R_i}\right)-0.84 \qquad (1.5\le\frac{R_o}{R_i}\le 2.25) \tag{4.13}$$

$$h_1\left(\frac{r_i}{R_i}\right)=\begin{cases}1 & (\frac{r_i}{R_i}=0)\\ -0.743\left(\frac{r_i}{R_i}\right)+1.061 & (0.1\le\frac{r_i}{R_i}<0.3)\\ -0.058\left(\frac{r_i}{R_i}\right)+0.855 & (0.3\le\frac{r_i}{R_i}<0.7)\end{cases} \tag{4.14}$$

$$h_2\left(\frac{V_S}{V_A}\right)=\begin{cases}1.988 & (\textit{pure}\ \text{aluminum})\\ 0.029\left(\frac{V_S}{V_A}\right)+0.971 & (\frac{1}{3}\le\frac{V_S}{V_A}\le 3)\\ 1.324 & (\textit{pure steel})\end{cases} \tag{4.15}$$

$$h_3\left(\frac{R_o}{R_i}\right)=-0.777\left(\frac{R_o}{R_i}\right)+2.165 \qquad (1.5\le\frac{R_o}{R_i}\le 2.25) \tag{4.16}$$

4.5 Conclusions

The Linear Matching Method has been verified by the step-by-step analysis, showing that it gives very accurate elastic shakedown limits for the composite cylinder with a cross hole. The result obtained using the LMM for the composite cylinder without a cross-hole shows that the limit load decreases with the reduction of the steel material, whereas the reverse plasticity limit increases with the decreasing volume of steel. With the cross-hole addition, the general trend of the shakedown curves is similar to the one without a cross-hole - a decreasing limit load and increasing reverse plasticity limit for decreasing volume of steel. For steel to aluminium ratio $\frac{V_s}{V_A}=3$, the existence of a hole has little effect on the value of reverse plasticity limit, but it causes a reduction in the limit load. For material ratio of 1, the existence of a hole has a sizable effect on the reverse plasticity limit, but impacts the limit load less significantly than for a material ratio of 3. For a material ratio $\frac{V_s}{V_A}=\frac{1}{3}$, the hole is shown to have negligible effect on the limit load. This implies that the size of the cross-hole raised the local stress concentration which will influence the fatigue life but will not greatly affect the global response when the limit load is determined by the low yield stress of the dominant aluminium material. Increasing the cylinder radius ratio $\frac{R_o}{R_i}$ highly increases the limit load and reduces the reverse plasticity limit. A safety shakedown envelope is created by formulating the elastic shakedown limit results of different composite material and cylinder thickness ratios with different cross-hole sizes.

In some applications, it is too conservative for a structure to be within the elastic shakedown limit. The industry is calling out for a direct method capable of predicting the boundaries between elastic shakedown, plastic shakedown (or reverse plasticity) and ratchetting. Therefore, in the coming chapter the identification of the corresponding plastic shakedown and ratchet limit using LMM will be discussed.

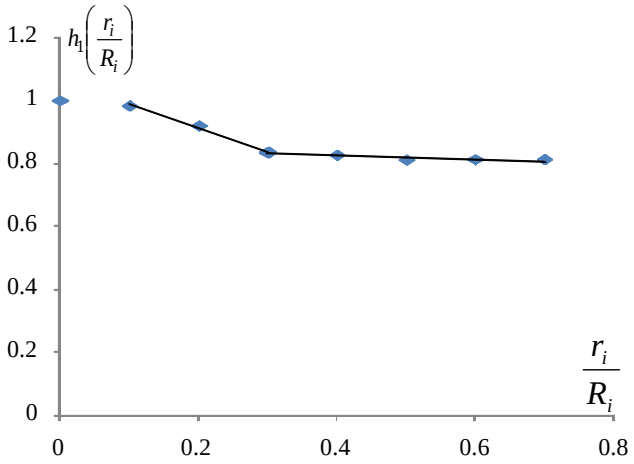

(a)

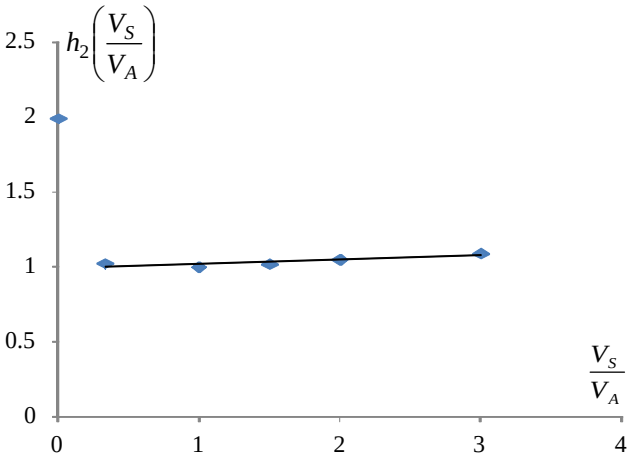

(b)

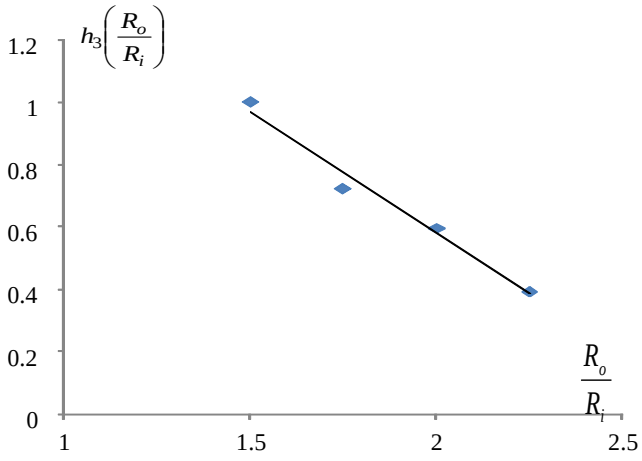

(c)

Figure 4.12 Influence functions for the design slope of the ratchet limit curve against: a) cross-hole ratio b) steel to aluminum ratio c) thickness ratio

CHAPTER 5. LINEAR MATCHING METHOD ON RATCHET ANALYSIS

5.1 Introduction

The iterative upper and lower bound elastic shakedown method mentioned in Chapter3 identifies a limit generally corresponding to structural deformation in either alternating plasticity or ratchetting. As mentioned in Chapter 3, elastic shakedown refers to one of the possible behavioural modes experienced by an elastic plastic body subjected to cyclic loading histories. If, during the loading process, plastic strains ceased to develop further and purely elastically behaviour is observed thereafter, then the structure is said to have elastic shaken down and is safe [34][36]. Basically, designing within this boundary is ideal, as long as small accumulations of plastic strains are accommodated during the initial loading cycles. The use of the elastic shakedown solutions is often realized in low temperature loading situations.

In applications with severe thermal mechanical loads, such as the operation of power plants, nuclear reactors, it is too conservative for the structure to be within the elastic shakedown limit [34]. The structural components usually ended up being designed beyond the elastic shakedown region. When the elastic shakedown limit is exceeded, an unlimited accumulation of plastic strains will lead to the structure failing by either low cycle fatigue due to alternating plasticity or incremental plastic collapse due to ratchetting [37]. In the alternating plasticity region, the amplitude of the variation of the elastic effective stress is higher than twice the yield stress. Thus, the cyclic plastic strain is developed, which alternates equally in tension and compression during the cyclic process. These developed plastic strains, without inducing any substantial plastic strain growth during the cyclic loading histories, forms a reverse plasticity mechanism in a structural component. This causes the sum of the elastic stresses, $\hat{\sigma}_{ij}(x,t)$, the time-independent constant residual stress field, $\bar{\rho}_{ij}(x)$ and the time-dependent varying residual stress field, $\rho_{ij}(x,t)$, to be kept within yield over the volume of the body.

Plastic shakedown or alternating plasticity, under which a local low cycle fatigue failure mode occurs, may be permitted, provided that during its design life the effect of low cycle fatigue is taken into consideration. Ratchetting, which ultimately leads to incremental plastic collapse, should be avoided, since it may lead to intolerable deformations. For this reason it is desirable to calculate the ratchet limit of a structure under cyclic load conditions. In addition, the evaluation of the ratchet limit is particularly useful for structures with stress raisers, such as cracks. In such structures, due to the presence of the elastic stress singularity at the crack tip the shakedown condition becomes invalid. Hence a finite shakedown limit does not exist anymore. However, the procedures for identifying the ratchet limit are still valid. This is due to the closed cycles of plastic strains occurring at the crack tip, enabling the evaluation of the finite ratchet limits. As a result, a method on the determination of the ratchet limit for cracked bodies is particularly desirable.

In the identification of the corresponding ratchet limits, not much work has been done. In filling this gap, Ponter et al [4][5] developed minimum theorems for an arbitrary cyclic state to calculate the ratchet limit for load history with two load instants. This minimum theorem is reduced to the classical elastic shakedown theorem when the loading histories lie within the shakedown limit. The minimisation theorem is further enhanced by Chen [21] with the recently developed finite element analysis codes, which are capable to evaluate the ratchet limits with multi-load instants case.

In the minimization theorem [4], for the component subjected to a predefined cyclic load history, the evaluation of an additional constant load that the component can withstand before ratchetting takes place, includes two sequential minimisation processes. The first stage involves the evaluation of a varying residual stress field and the corresponding closed cycles of plastic strains for the applied cyclic load condition. The second stage for the ratchet limit due to the additional constant load then becomes a conventional elastic shakedown calculation, with the cyclic elastic stress history augmented by the varying residual stress field.

In this chapter, the derivation of the minimization theorem using LMM-basic computational procedure [5] for the identification of the ratchet limit is discussed. A

summary of this numerical procedure is presented. The application of the minimization theorem is then investigated through a 3D plate with a central hole. To extend the theorem so that it can be incorporated to other plasticity models, the Ramberg-Osgood material model is also adopted.

5.2 General Cyclic Problem

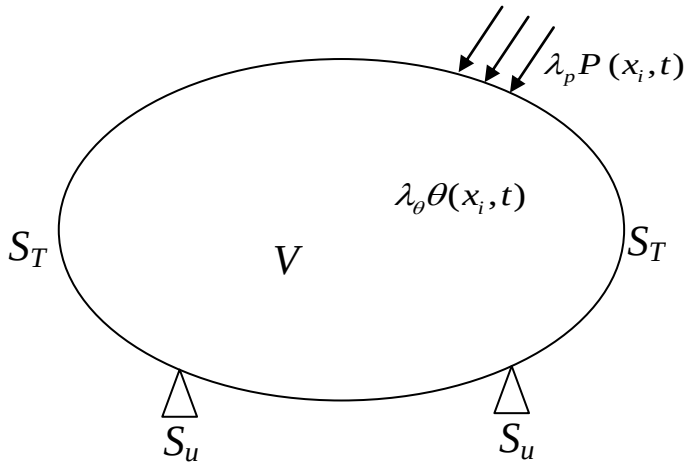

Figure 5.1 Schematic of the problem

Considering the cyclic problem in Figure 5.1, an elastic plastic body is subjected to a general cyclic load condition, where the material is isotropic, elastic-plastic and satisfies the von-Mises yield condition. The body is subjected to a cyclic history of varying temperatures $\lambda_p\theta(x_i,t)$ within the volume *V* and varying surface loads $\lambda_\theta P(x_i,t)$ acting over part of the body's surface S_T, where λ_p and λ_θ are reference load parameter, allowing a whole class of loading histories to be taken into account. On the remainder of the surface *S*, denoted by S_u, the displacement satisfies $u_i = 0$. The variation is considered to be over a typical cycle $0 \le t \le \Delta t$ in a cyclic state. For the problem defined above the stresses and strain rates will asymptote to a cyclic state where

$$\sigma_{ij}(t) = \sigma_{ij}(t+\Delta t), \qquad \dot{\varepsilon}_{ij}(t) = \dot{\varepsilon}_{ij}(t+\Delta t) \tag{5.1}$$

The corresponding linear elastic stress history is denoted by $\hat{\sigma}_{ij}(x_i,t)$ as,

$$\lambda \hat{\sigma}_{ij}\left(x_i,t\right)=\hat{\sigma}_{ij}^{\Delta}\left(x_i,t\right) \tag{5.2}$$

where

$$\hat{\sigma}_{ij}^{\Delta}\left(x_i,t\right)=\lambda_p \hat{\sigma}_{ij}^{P}\left(x_i,t\right)+\lambda_\theta \hat{\sigma}_{ij}^{\theta}\left(x_i,t\right) \tag{5.3}$$

$\hat{\sigma}_{ij}^{p}$ and $\hat{\sigma}_{ij}^{\theta}$ represent the linear elastic stress history corresponding to varying surface loads and temperature, respectively. The total strain is the sum of a linear elastic and perfectly plastic component,

$$\varepsilon_{ij}=\varepsilon_{ij}^{e}+\varepsilon_{ij}^{p} \tag{5.4}$$

where the elastic strains are $\varepsilon_{ij}^{e}=C_{ijmn}\sigma_{mn}$, and the tensor is C_{ijmn}, satisfying the usual symmetrical properties. The plastic strains are associated with a strictly convex yield condition satisfying the condition of (3.1) and the associated flow law of (3.3) and (3.4). Then the maximum work principle is,

$$\left(\sigma_{ij}^{c}-\sigma_{ij}^{*}\right)\dot{\varepsilon}_{ij}^{c}\geq 0 \tag{5.5}$$

where σ_{ij}^{c} denotes the stress at yield, $f\left(\sigma_{ij}^{c}\right)=0$, associated though (3.1) with the plastic strain rate $\dot{\varepsilon}_{ij}^{p}=\dot{\varepsilon}_{ij}^{c}$. σ_{ij}^{*} denotes any state of stress, which satisfies the condition of (3.1), $f\left(\sigma_{ij}^{*}\right)\leq 0$. For this general problem, the existence of the minimum theorems [75] allows the possibility of defining load histories lying within or beyond the elastic shakedown limit. Consider the function where λ is regarded as prescribed (here λ denotes a scalar load parameter),

$$I\left(\dot{\varepsilon}_{ij}^{c},\lambda\right)=\int_V\int_0^{\Delta t}\left(\sigma_{ij}^{c}-\lambda\hat{\sigma}_{ij}\left(x_i,t\right)\right)\dot{\varepsilon}_{ij}^{c}dtdV \tag{5.6}$$

where $\dot{\varepsilon}_{ij}^{c}$ is a kinematically admissible strain rate history such that the accumulated strain over the cycle,

$$\int_0^{\Delta t}\dot{\varepsilon}_{ij}^{c}=\Delta\varepsilon_{ij}^{c} \tag{5.7}$$

is compatible with a displacement field Δu_{ij}^{c}, which satisfies the displacement boundary conditions. According to [4][5], two additional conditions are now applied on the magnitude of $\dot{\varepsilon}_{ij}^{c}$.

Condition (i): Corresponding to $\dot{\varepsilon}_{ij}^{c}$, a cyclic history of residual stress, $\rho_{ij}^{c}\left(x_i,t\right)$, is defined such that it satisfies the relationship,

$$\dot{\varepsilon}_{ij}^{cT} = C_{ijmn}\rho_{ij}^{c} + \dot{\varepsilon}_{ij}^{c} \tag{5.8}$$

where $\dot{\varepsilon}_{ij}^{cT}$ is also a kinematically admissible strain rate history and it is compatible. And,

$$\rho_{ij}^{c}\left(x_i,0\right) = \rho_{ij}^{c}\left(x_i,\Delta t\right) \tag{5.9}$$

Condition (ii): Corresponding to $\rho_{ij}^{c}\left(x_i,t\right)$, there exists a constant residual stress field in equilibrium with zero traction on S_T, $\bar{\rho}_{ij}\left(x_i\right)$, on the absolute magnitude of $\dot{\varepsilon}_{ij}^{c}$. Thus, the general form of the stress solution for the cyclic problems involving cyclic (or changing) and constant residual fields is given by,

$$\sigma_{ij}\left(x_i,t\right) = \lambda\hat{\sigma}_{ij}\left(x_i,t\right) + \bar{\rho}_{ij}\left(x_i\right) + \rho_{ij}^{c}\left(x_i,t\right) \tag{5.10}$$

and (5.10) satisfies the yield condition,

$$f\left(\lambda\hat{\sigma}_{ij}\left(x_i,t\right) + \bar{\rho}_{ij}\left(x_i\right) + \rho_{ij}^{c}\left(x_i,t\right)\right) \le 0, \qquad for \qquad 0 \le t \le \Delta t \tag{5.11}$$

And (5.6) can be rewritten as,

$$I\left(\dot{\varepsilon}_{ij}^{c},\lambda\right) = \int_{V}\int_{0}^{\Delta t}\left\{\sigma_{ij}^{c}\dot{\varepsilon}_{ij}^{c} - \left[\lambda\hat{\sigma}_{ij}\left(x_i,t\right) + \rho_{ij}^{c}\left(x_i,t\right) + \bar{\rho}_{ij}\left(x_i\right)\right]\dot{\varepsilon}_{ij}^{c}\right\}dtdV \tag{5.12}$$

It was proven from [76] that for a prescribed load history (λ),

$$I\left(\dot{\varepsilon}_{ij}^{c},\lambda\right) \ge 0 \tag{5.13}$$

with the equality achieved, when,

$$\dot{\varepsilon}_{ij}^{c} = \dot{\varepsilon}_{ij}^{cr} \tag{5.14}$$

where $\dot{\varepsilon}_{ij}^{cr}$ is the exact cyclic solution.

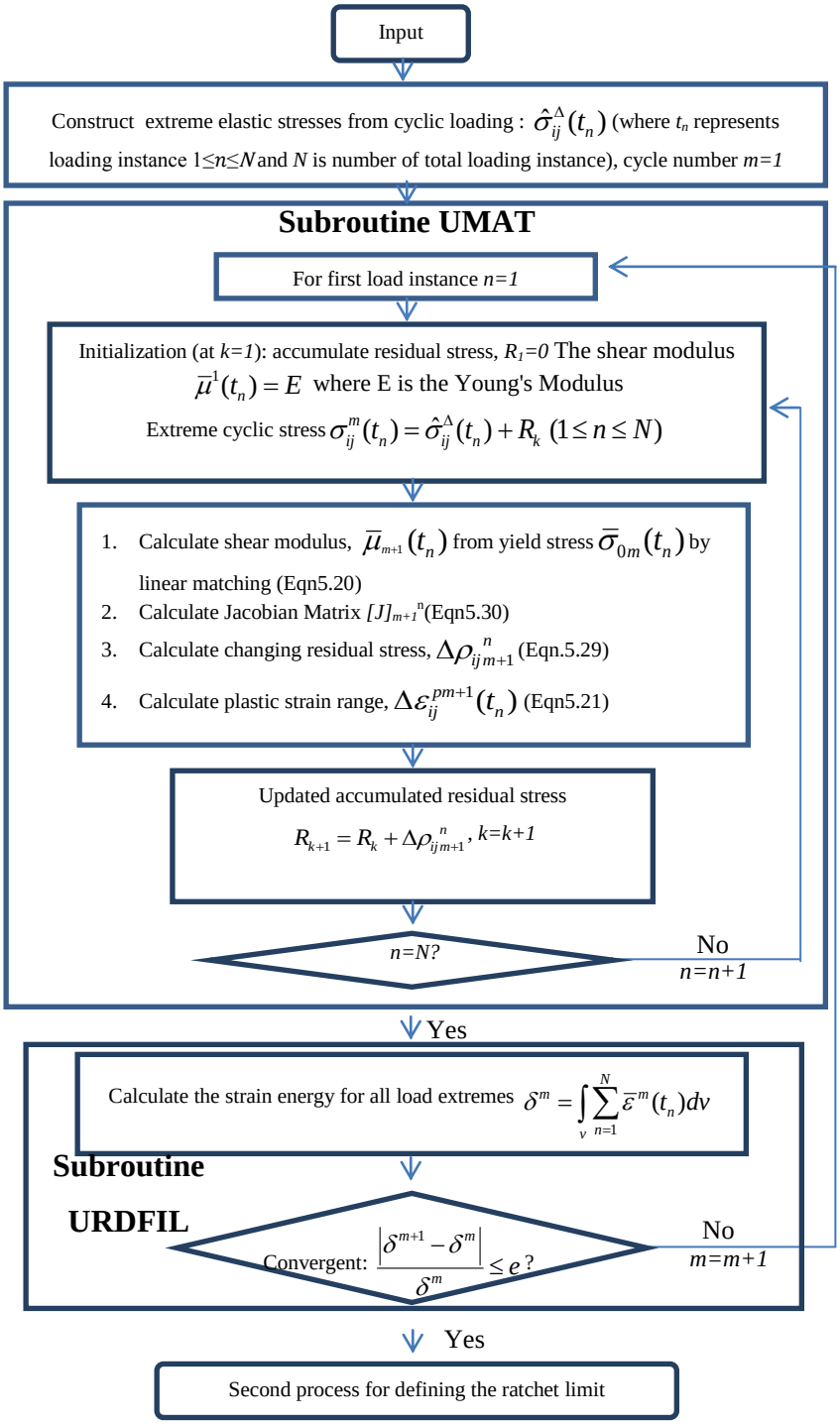

Figure 5.2 Flow chart for identifying changing residual stress and plastic strain range(LMM)

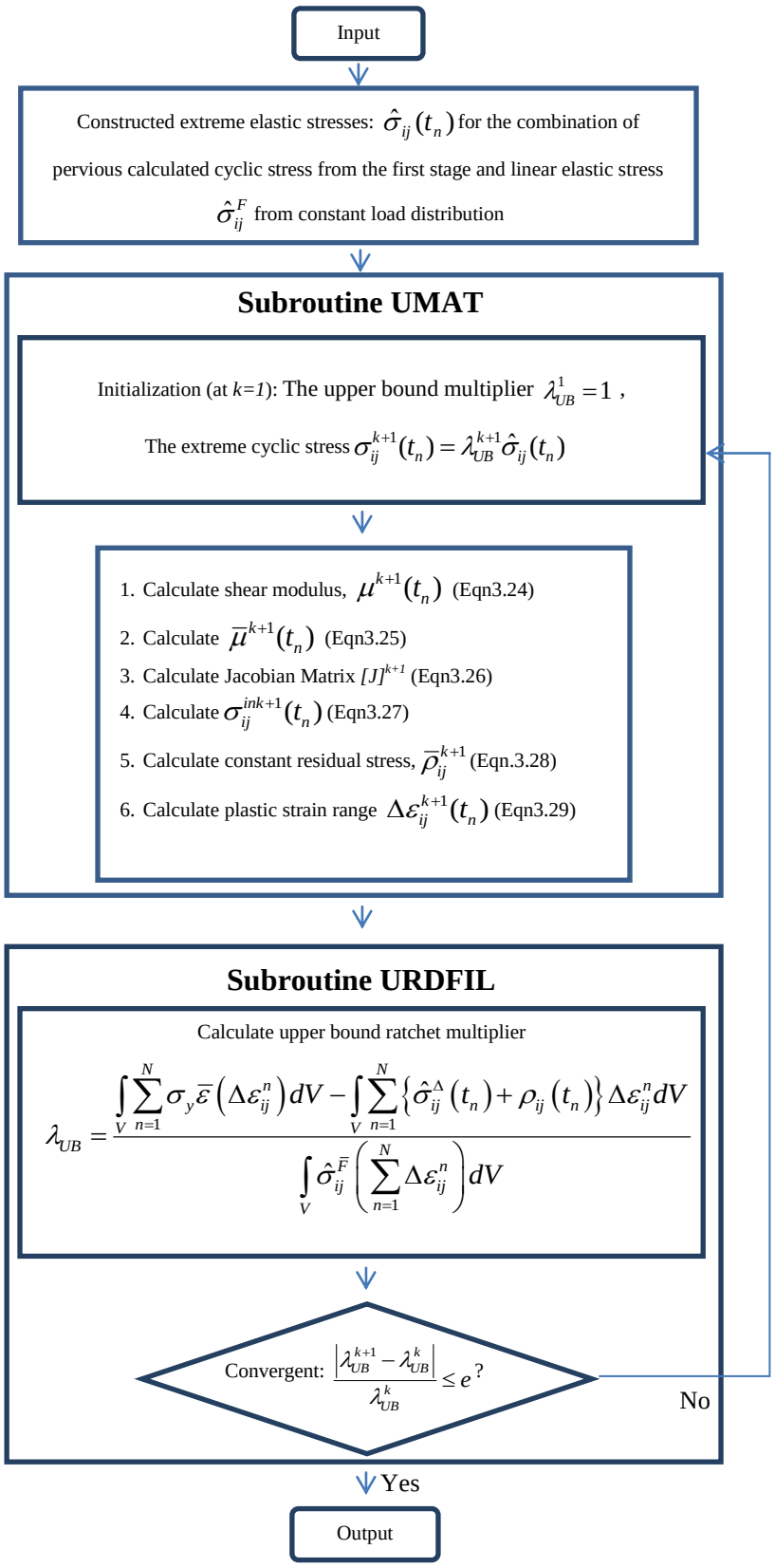

Figure 5.3 Flow chart for identifying the ratchet limit using LMM

5.3 Dual Minimization Process for Ratchet Analysis

As mentioned in the introduction, in the case of loading in excess of shakedown, the definition of the ratchet limits is required. This ratchet limits satisfied the requirement that plastic deformation takes place in the cycle, but there is no net accumulation of plastic strain. Associated with such loading histories, a changing residual stress field exists. If the changing residual stress field is calculated, then the analysis is reduced to a conventional elastic shakedown calculation where the loading history is augmented by the constant load.

Considering the same problem as Figure 5.1, a structure subjected to a general cyclic load condition, which can be decomposed into cyclic and constant components, and the corresponding linear elastic stress history is denoted by $\lambda\hat{\sigma}_{ij}\left(x_i,t\right)$ as,

$$\lambda\hat{\sigma}_{ij}\left(x_i,t\right)=\lambda\hat{\sigma}_{ij}^{\bar{F}}\left(x_i\right)+\hat{\sigma}_{ij}^{\Delta}\left(x_i,t\right) \tag{5.15}$$

where $\hat{\sigma}_{ij}^{\Delta}\left(x_i,t\right)$ is described as (5.3), $\hat{\sigma}_{ij}^{\bar{F}}$ represents the linear elastic stress history corresponding to a constant load distribution $\bar{F}\left(x_i\right)$.

Now, the entire numerical procedures for defining the ratchet boundary are performed in two minimization processes [21]. In the first minimization process, the varying residual stress field, associated with the applied varying loads, $\hat{\sigma}_{ij}^{\Delta}\left(x_i,t\right)$, is evaluated. The corresponding plastic strain ranges for the low cycle fatigue assessment is also calculated. The second minimization process is to define the location of the ratchet boundary due to the extra constant load, $\lambda\hat{\sigma}_{ij}^{\bar{F}}\left(x_i\right)$ as a conventional shakedown analysis (as mentioned in Chapter 3) where a time independent residual stress field is evaluated and the elastic stress history is augmented by the changing residual stress field calculated in the first minimization process. The implementations of these two numerical minimization processes [21], are summarized below.

5.3.1 Incremental Minimization Process for the Varying Residual Stress Field and Plastic Strain

Applying the same assumption as in section 3.3.5, for a strictly convex yield condition, which includes the von-Mises yield condition in a deviatoric stress space and for histories of elastic stress, which describe a sequence of straight line paths in stress space, the only instants when plastic strains can occur are at the vertices of the stress history $\hat{\sigma}_{ij}^{\Delta}(t_n)$, where *n* represents the loading histories and *n*=1 to *N*, in a load space.

It is assumed that plastic strains only occur at load extremes corresponding to *N* time instants, $t_1, t_2,$ ....., t_N ,where t_n corresponds to a sequence of time points in the cyclic history, which leads to $\Delta\varepsilon_{ij}^{c} = \sum_{n=1}^{N} \Delta\varepsilon_{ij}^{n}$, where $\Delta\varepsilon_{ij}^{n}$ is the increment of plastic strain that occurs at time t_n. Hence, the minimization function *I* in (5.12) is written as,

$$I\left(\dot{\varepsilon}_{ij}^{c}, \lambda\right) = \sum_{n=1}^{N} I^{n} \tag{5.16}$$

where

$$I^{n}\left(\Delta\varepsilon_{ij}^{n}, \lambda\right) = \int_{V} \left\{ \sigma_{ij}^{n} \Delta\varepsilon_{ij}^{n} - \left[\lambda\hat{\sigma}_{ij}\left(x_i, t_n\right) + \rho_{ij}\left(x_i, t_n\right) \right] \Delta\varepsilon_{ij}^{n} \right\} dV \tag{5.17}$$

and

$$\rho_{ij}\left(x_i, t_n\right) = \bar{\rho}_{ij}\left(x_i\right) + \sum_{l=1}^{n} \Delta\rho_{ij}\left(x_i, t_l\right) \tag{5.18}$$

where in (5.12) the term $\dot{\varepsilon}_{ij}^{c}$ is replaced by a sequence of increments of strain $\Delta\varepsilon_{ij}^{n}$ occurring at a sequence of *N* times t_n. The incremental minimization of $I^{n}\left(\Delta\varepsilon_{ij}^{n}, \lambda\right)$ assumes that the prior history of the residual stress is known and compatibility of the total elastic and plastic strain in the increment is used. $\bar{\rho}_{ij}(x_i)$ is the constant element of the changing residual stress $\rho_{ij}(t_n)$ and represents as,

$$\bar{\rho}_{ij}^{M} = \sum_{n=1}^{N} \Delta\rho_{ij1}^{\ n} + \sum_{n=1}^{N} \Delta\rho_{ij2}^{\ n} + \cdots + \sum_{n=1}^{N} \Delta\rho_{ijM-1}^{\ n} \tag{5.19}$$

where M represents the total number of cycles. The LMM methodology [5] requires the solution of a sequence of linear problems. For an initial estimate of the strain increment, $\Delta\varepsilon_{ij}^{n} = \Delta\varepsilon_{ijm}^{\ n}$, at *mth* cycle of iterations, a class of linear problems for a new estimate, $\Delta\varepsilon_{ij}^{n} = \Delta\varepsilon_{ijm+1}^{\ n}$, can be defined at the *(m+1)th* cycle of iterations.

In an iterative process, at an arbitrary point x_i, the repeated application of the algorithm produces a sequence of solutions for $\Delta\varepsilon_{ij}^{n}$, which converges to the absolute minimum of the minimization function. The entire iterative procedure requires a total number of cycles, *M*, where each cycle, *m*, contains *N* iterations associated with *N* load instances, where *n=1,2,...N* and *m=1,2,...M*. If two consecutive cycles, *m* and *m+1*, are now considered, then the linear coefficient $\bar{\mu}_{m+1}(t_n)$ is given by the linear matching as,

$$\bar{\mu}_{m+1}(t_n) = \bar{\mu}_m(t_n)\frac{\sigma_{0m}(t_n)}{\bar{\sigma}\left(\hat{\sigma}_{ij}^{\Delta}(t_n) + \rho_{ij}^{m}(t_n)\right)} \tag{5.20}$$

where $\sigma_{0m}(t_n)$ is the iterative von-Mises yield stress for Ramberg-Osgood material model or yield stress for the elastic perfectly plastic material model, $\bar{\mu}_m(t_n)$ is the iterative shear modulus. The new distribution of the strain increment, $\Delta\varepsilon_{ijm+1}^{\ n}$, is then characterized as the solution to the following problem,

$$\Delta\varepsilon_{ij\,m+1}^{T\,n\ \prime} = \frac{1}{2\mu}\Delta\rho_{ijm+1}^{\ n\ \prime} + \Delta\varepsilon_{ijm+1}^{\ n\ \prime}, \quad \Delta\varepsilon_{kk\,m+1}^{T\,n} = \frac{1}{3K}\Delta\rho_{kk\,m+1}^{\ n} \tag{5.21}$$

$$\Delta\varepsilon_{ijm+1}^{\ n\ \prime} = \frac{1}{2\bar{\mu}_m(t_n)}\left\{\hat{\sigma}_{ij}^{\Delta}(t_n) + \rho_{ij}^{\ m+1}(t_{n-1}) + \Delta\rho_{ijm+1}^{\ n}\right\}' \tag{5.22}$$

where the prior history of the residual stress is known as,

$$\rho_{ij}^{m}(t_{n-1}) = \bar{\rho}_{ij}^{m} + \Delta\rho_{ijm}^{\ 1} + \Delta\rho_{ijm}^{\ 2} + \ldots\ldots + \Delta\rho_{ijm}^{\ n-1} \tag{5.23}$$

Where $\Delta\rho_{ijm}^{\ n}$ is the evaluated changing residual stress for *nth* load instance at *mth* cycle of iterations, where n=1,2,...N and m=1,2,...M. The entire iterative procedure for the changing residual stress field and the plastic strain range with numbers of cycles is shown in Appendix II.

In equation (5.21) and (5.22) $\bar{\mu}$ is the iterative shear modulus. K and μ are the bulk modulus and the shear modulus, respectively, the values of which are obtained from materials data. And the term, $\hat{\sigma}_{ij}^{\Delta}$, is the cyclic solution from (5.3). Due to (5.22), equation (5.21) is rewritten as,

$$\Delta\varepsilon_{ij\,m+1}^{Tn\ \prime}=\left(\frac{1}{2\mu}+\frac{1}{2\bar{\mu}_m(t_n)}\right)\Delta\rho_{ij\,m+1}^{n\ \prime}+\frac{1}{2\bar{\mu}_m(t_n)}\left\{\hat{\sigma}_{ij}^{\Delta}(t_n)+\rho_{ij}^{m+1}(t_{n-1})\right\}' \tag{5.24}$$

Defining μ^{eff} and K^{eff} as:

$$\frac{1}{\mu^{eff}{}_m(t_n)}=\frac{1}{\mu}+\frac{1}{\bar{\mu}_m(t_n)} \tag{5.25}$$

$$\frac{1}{K^{eff}(t_n)}=\frac{1}{K(t_n)} \tag{5.26}$$

Then (5.24) and (5.21) can be rearranged as,

$$\Delta\rho_{ij\,m+1}^{n\ \prime}=2\mu_m^{eff}(t_n)\Delta\varepsilon_{ij\,m+1}^{Tn\ \prime}-\frac{\mu_m^{eff}(t_n)}{\bar{\mu}_m(t_n)}\frac{1}{2}\left\{\hat{\sigma}_{ij}^{\Delta}(t_n)+\rho_{ij}^{m+1}(t_{n-1})\right\}' \tag{5.27}$$

$$\Delta\rho_{kk\,m+1}^{n}=3K^{eff}(t_n)\Delta\varepsilon_{kk\,m+1}^{T\,n} \tag{5.28}$$

The solution of equation (5.27) and (5.28) is implemented in ABAQUS via subroutines UMAT and URDFIL. Solving the following equation in the standard ABAQUS form:

$$\Delta\rho_{m+1}^{n}=[J]_{m+1}^{n}\Delta\varepsilon_{m+1}^{Tn}-\Delta\sigma_{m+1}^{inn} \tag{5.29}$$

the Jacob matrix, for a 3-D solid is given by:

$$[J]_{m+1}^{n}=\frac{E(1-\upsilon)}{(1+\upsilon)(1-2\upsilon)}\begin{bmatrix}1 & \frac{\upsilon}{1-\upsilon} & \frac{\upsilon}{1-\upsilon} & 0 & 0 & 0\\ \frac{\upsilon}{1-\upsilon} & 1 & \frac{\upsilon}{1-\upsilon} & 0 & 0 & 0\\ \frac{\upsilon}{1-\upsilon} & \frac{\upsilon}{1-\upsilon} & 1 & 0 & 0 & 0\\ 0 & 0 & 0 & \frac{1-2\upsilon}{2(1-\upsilon)} & 0 & 0\\ 0 & 0 & 0 & 0 & \frac{1-2\upsilon}{2(1-\upsilon)} & 0\\ 0 & 0 & 0 & 0 & 0 & \frac{1-2\upsilon}{2(1-\upsilon)}\end{bmatrix} \tag{5.30}$$

where

$$\Delta\sigma^{innn}_{m+1} = \frac{\mu^{eff}_{m+1}(t_n)}{\bar{\mu}_{m+1}(t_n)} \frac{1}{2} \left\{ \hat{\sigma}^{\Delta}_{ij}(t_n) + \rho^{m+1}_{ij}(t_{n-1}) \right\}' \tag{5.31}$$

$$E = \frac{9K^{eff}(t_n)\mu^{eff}_{m+1}(t_n)}{3K^{eff}(t_n) + \mu^{eff}_{m+1}(t_n)} \quad and \quad \upsilon = \frac{3K^{eff}(t_n) - 2\mu^{eff}_{m+1}(t_n)}{2(3K^{eff}(t_n) + \mu^{eff}_{m+1}(t_n))} \tag{5.32}$$

5.3.2 Global Minimization Process

The numerical procedure, used in the identification of the ratchet limit, is similar to the existing methods of upper bound elastic shakedown analysis which is described in (Chapter 3.3.5). The main difference is the need to take into account the changing residual stress field calculated from the previous procedure (chapter 5.3.1). Thus the linear elastic solution becomes,

$$\lambda\hat{\sigma}_{ij}(x_i,t) = \lambda\hat{\sigma}^{\bar{F}}_{ij}(x_i) + \hat{\sigma}^{\Delta}_{ij}(x_i,t) + \rho_{ij}(x_i,t) \tag{5.33}$$

For the von-Mises yield condition and the associated flow rule, an upper bound ratchet limit multiplier can be obtained by,

$$\lambda_{UB} = \frac{\int_V \sum_{n=1}^{N} \sigma_y \bar{\varepsilon}\left(\Delta\varepsilon^n_{ij}\right) dV - \int_V \sum_{n=1}^{N} \left\{ \hat{\sigma}^{\Delta}_{ij}(t_n) + \rho_{ij}(t_n) \right\} \Delta\varepsilon^n_{ij} dV}{\int_V \hat{\sigma}^{\bar{F}}_{ij} \left(\sum_{n=1}^{N} \Delta\varepsilon^n_{ij} \right) dV} \tag{5.34}$$

The upper bound ratchet limit multiplier gives the capacity of the body subjected to a predefined cyclic load history $\hat{\sigma}^{\Delta}_{ij}(t_n)$ to withstand an additional constant load $\hat{\sigma}^{\bar{F}}_{ij}$ before ratchetting takes place.

Since the numerical formulation of the upper bound ratchet limit multiplier is similar to the one in upper bound elastic shakedown theorem, for the chosen class of displacement fields, the same iterative monotonically reducing sequence of upper bounds, converging to the least upper bound ratchet limit behaviour, is to be expected.

To this point, the usage of the numerical technique is based upon the assumption of a perfectly plastic material. It is a well-known fact that the cyclic strain amplitude in a reverse plasticity mechanism is sensitive to cyclic hardening. And the inclusion of hardening effect requires the development of a method based upon a constitutive equation, which predicts the required material's behaviour in the steady state. The numerical example in the coming section describes the inclusion of cyclic hardening effect for Ramberg-Osgood material model.

The overall organization of the dual minimization process (first and second processes) could be further understood by examining the block diagram in Figure 5.2 and Figure 5.3, respectively.

5.4 Benchmark Example

5.4.1 Geometry and Loading Condition

To demonstrate the numerical procedures, discussed in Sections 5.2 and 5.3, an upper bound ratchet limit calculations are performed for a 3-D plate with a central hole subjected to a cyclic thermal load and constant mechanical load. The same loading condition and geometry are adopted as the example in Figure 3.4 and Figure 3.5 (Chapter 3.4.1).

Two thermal stress extremes with two load instances are adopted for this cyclic load history:

---Load instance (1): The temperature distribution and axial tension are applied (at time t_1 in Figure 3.5).

---Load instance (2): The temperature load is removed and the constant axial tension remains applied (at time t_2 in Figure 3.5)..

For non-linear analysis, both the elastic perfectly plastic material model and Ramberg-Osgood material model are adopted in this study. The following Ramberg-Osgood type is adopted for the cyclic stress and strain range relationship [80]:

$$\Delta\varepsilon = \frac{\Delta\sigma}{E} + 2\frac{\alpha}{E}\left(\frac{\Delta\sigma}{2\sigma_0}\right)^{n^*}\sigma_0 \tag{5.35}$$

where $\Delta\sigma$ is the true stress range, $\Delta\varepsilon$ is the true strain range, E is the elastic modulus, σ_0 is reference stress usually taken as 0.2% yield stress (σ_y), and α and n^* are the Ramberg-Osgood plastic hardening constants. At the lower limit, n=1, the above equation represents a linear-elastic behaviour. At the upper limit, n=∞, it may be represent an elastic-perfectly plastic behaviour. The first term on the right-hand side of the above equation represents the elastic strain range and the second term corresponds to the plastic strain range.

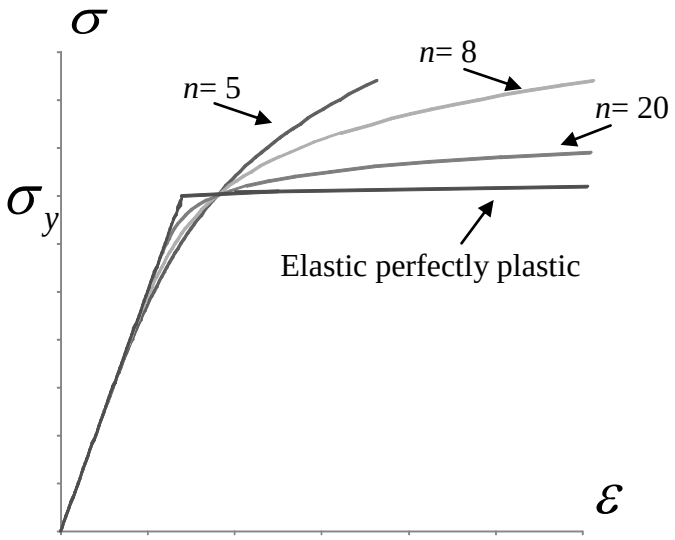

Figure 5.4 The curve of the constitutive relation for elastic perfectly plastic and Ramberg-Osgood material model with different hardening n

Then the plastic strain range from Equation (5.35) can be written as:

$$\Delta\varepsilon_p = 2\frac{\alpha}{E}\left(\frac{\Delta\sigma}{2\sigma_0}\right)^{n^*}\sigma_0 \tag{5.36}$$

and

$$\frac{\Delta\sigma}{2} = \left(\frac{\Delta\varepsilon_p E}{2\alpha}\sigma_0^{\,n^*-1}\right)^{\frac{1}{n^*}} \tag{5.37}$$

$$\alpha = \frac{\Delta\varepsilon_p E}{2\sigma_0}\left(\frac{2\sigma_0}{\Delta\sigma}\right)^{n^*} \tag{5.38}$$

In this study the reference stress (σ_0) is taken as 0.2% of yield stress (σ_y), where σ_y is defined as half stress range that results from a strain range of 0.2% in the steady state as:

$$\sigma_y = \frac{\Delta\sigma_{0.2\%}}{2} \qquad \Delta\varepsilon_p = 0.2\% \tag{5.39}$$

and α could be evaluated with the given yield stress (σ_y) as:

$$\alpha = \frac{0.2\%E}{2\sigma_0} \tag{5.40}$$

The same elastic perfectly plastic material properties as the one in Chapter 3 (Yield Stress σ_y=360MPa, Poisson's Ratio, ν=0.3, Young's Modulus, E= 200 GPa) are used also in this chapter. The Ramberg-Osgood material model with the power hardening exponents in equation (5.36) n*=5, 8, 20, and in order to compare the solution from elastic perfectly plastic material, a reference yield stress σ_0=360 are adopted for this study. Figure 5.4 shows the curves of the above mentioned material constitutive relations.

In LMM the iterative von-Mises stress σ_y from Ramberg-Osgood material model is obtained from equations (5.39), (5.37) and (5.22) as,

$$\sigma_y(t_n) = \left(\frac{\Delta\bar{\varepsilon}(\Delta\varepsilon_{ij}^n)E}{2\alpha}\sigma_0{}^{n^*-1}\right)^{\frac{1}{n^*}} \tag{5.41}$$

5.4.2 Ratchet Limit Boundary

The upper bound shakedown and ratchet limit interaction curve for a 3D plate with a central hole subjected to constant tensile load and a cyclic thermal gradient is shown in Figure 5.5. The applied tensile force in X-axis is normalized with respect to the material yield stress, while the thermal load in Y-axis is normalized by using the reference temperature difference $\Delta\theta=\Delta\theta_0=100^{\circ}C$. This interaction diagram consists of limit load, shakedown limit (Chapter Three) and ratchet limit for different ratios of varying thermal loads and constant mechanical loads. The diagram is divided into four zones; elastic shakedown, reverse plasticity or global shakedown, ratchetting and plastic collapse zone. Elastic shakedown will not occur if the load applied

surpasses the reverse plasticity limit "*AB*". In this case the permanent strains settle into a closed cycle, a condition also known as "alternating plasticity" and associated with a low cycle fatigue mechanism. The plastic strains will increase indefinitely if the applied cyclic load level is beyond the ratchet limit "*CD*". This is known as "ratchetting" or "incremental plastic collapse". The point "*D*" corresponds to the limit load for the applied mechanical load. Any applied cyclic load which exceeds the limit load line *DI* will cause plastic collapse.

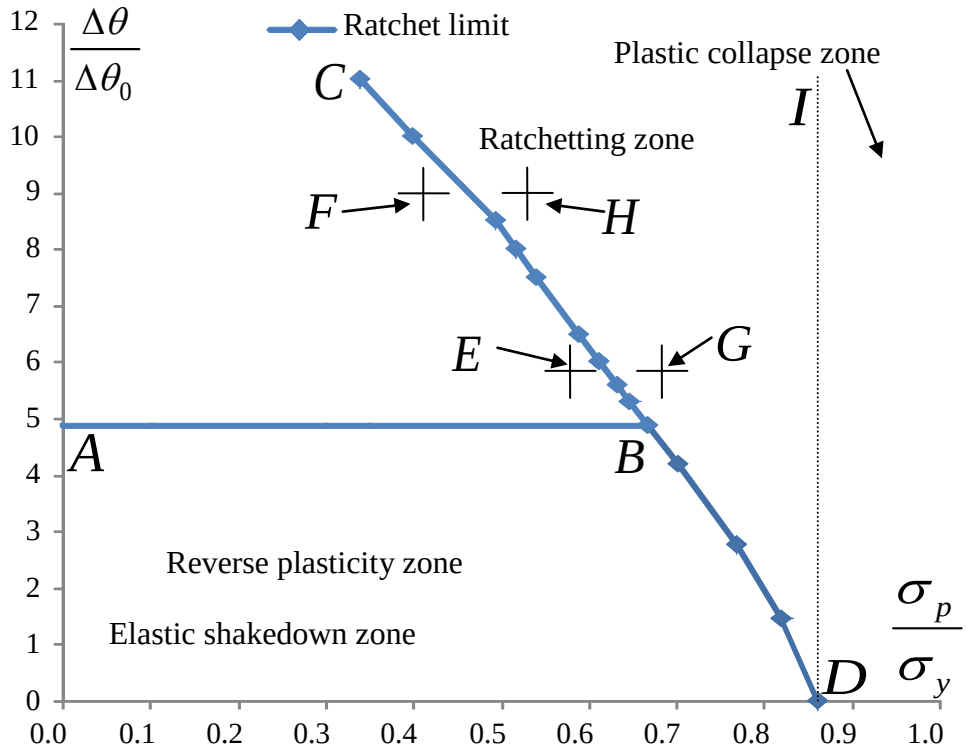

Figure 5.5 The ratchet limit boundary for 3D plate with a central hole

The solution of the elastic shakedown zone (curve "ABD") calculated by the LMM has been verified by the ABAQUS step-by-step inelastic analysis in Chapter 3. And for the verification of the ratchet limit boundary (curve "CB") calculated by the LMM, the cyclic load points $E(\Delta\theta=6.0\Delta\theta_0,\ \sigma_p=0.58\ \sigma_y)$, $F(\Delta\theta=9.0\ \Delta\theta_0,\ \sigma_p=0.42\ \sigma_y)$, and $G(\Delta\theta=6.0\Delta\theta_0,\ \sigma_p=0.69\ \sigma_y)$, $H(\Delta\theta=9.0\Delta\theta_0,\ \sigma_p=0.55\ \sigma_y)$, which are just below and above the calculated ratchet limit boundary (Figure 5.5), respectively, are chosen for

the step-by-step inelastic analysis by ABAQUS. The maximum signed equivalent plastic strain histories for the cyclic loadings *E,G* and *F,H* are shown in Figure 5.6a and Figure 5.6b, respectively. The term signed equivalent plastic strain refers to the usual formulation of effective plastic strain, but with a sign equal to that of the principal plastic strain of greatest magnitude [24]. From Figure 5.6a it is observed that the calculated maximum signed equivalent plastic strain for the load case *E* exhibits plastic shakedown (reverse plasticity) as the calculated signed equivalent plastic strain becomes stable after 18 load cycles, and the load case *G* shows a strong ratchetting mechanism, with the maximum signed equivalent plastic strain increasing at every cycle. A similar result is also obtained from Figure 5.6b, where the calculated maximum signed equivalent plastic strain for the load case *F* settles into a stable cycle after about 15 load cycles showing a reverse plasticity mechanism, and the load case *H* shows a strong ratchetting mechanism, with the maximum signed equivalent plastic strain increasing at every cycle. Thus, the results in Figure 5.6 obtained by ABAQUS step-by-step inelastic analysis confirm the accuracy of the predicted ratchet limits by the LMM.

5.4.3 The Effect of Different Material Models on the Plastic Strain Range

The plastic strain range concerning a fatigue crack initiation is a key factor in a low cycle fatigue assessment. The maximum equivalent plastic strain range against cyclic temperature history with $\Delta\theta=800^0C$ and varying constant internal pressure for different types of material model is plotted in Figure 5.7. It is observed from Figure 5.7 that the value of the maximum equivalent plastic strain range increases as the Ramberg-Osgood material data *n* is increased. This can be explained by Figure 5.4 which shows the elastic perfectly plastic material model causing larger plastic strain than Ramberg-Osgood model in the reverse plasticity zone, since the elastic perfectly plastic model does not suffer any cyclic hardening.

The results of Figure 5.7 also show that the cyclic loading history, with increasing constant internal pressure, has slight influence on the maximum equivalent plastic strain range for both perfectly plastic and Ramberg-Osgood type material models.

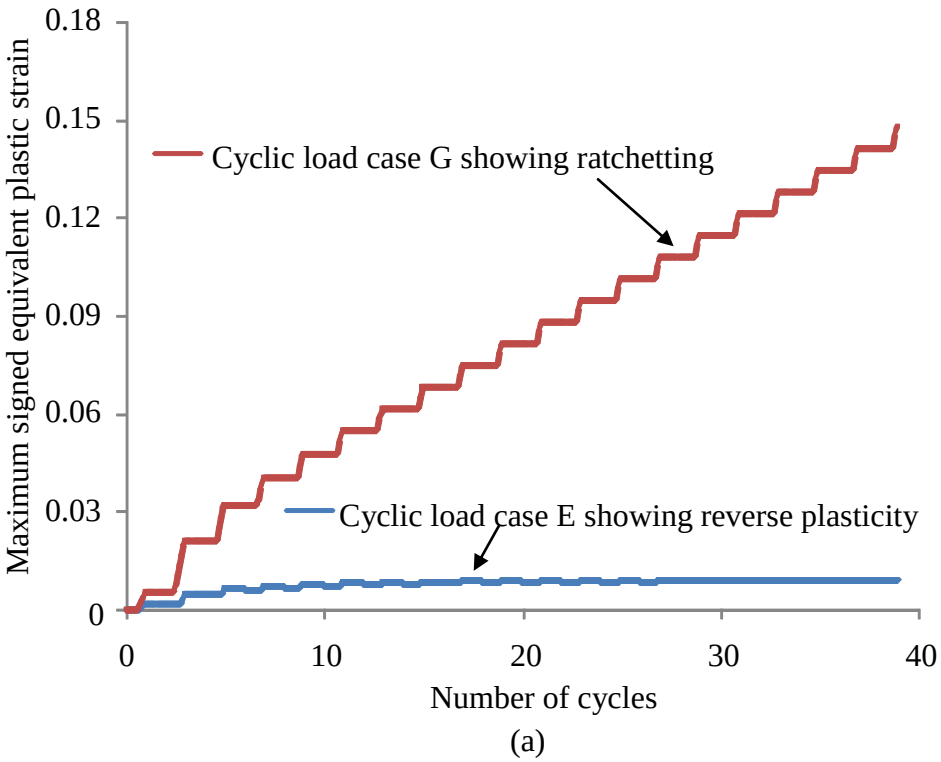

(a)

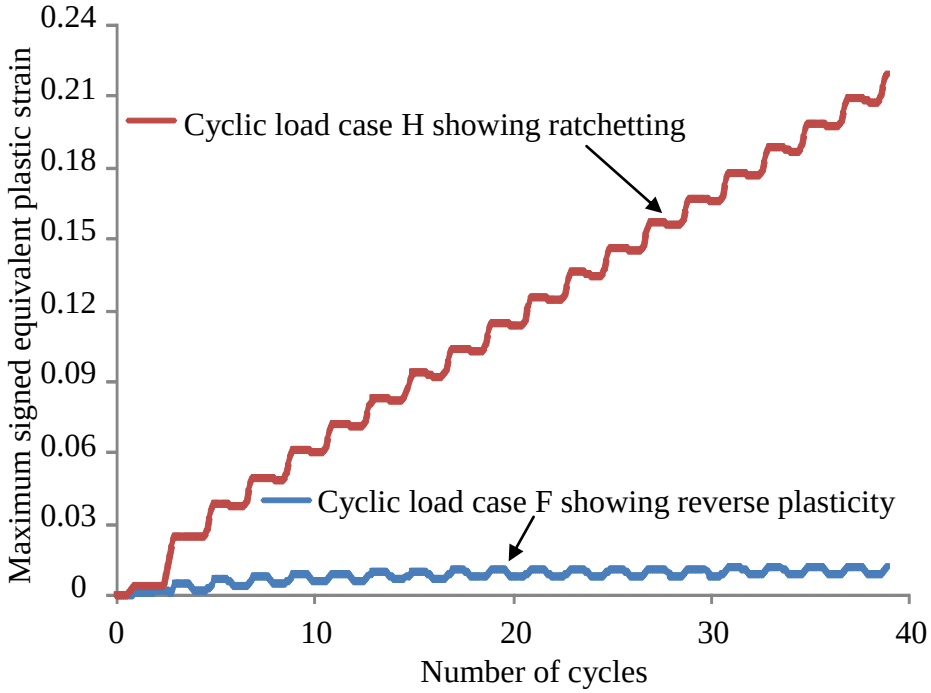

(b)

Figure 5.6 ABAQUS verification using step by step inelastic analysis for load cases (a) G and E (b) H and F

5.4.4 The Effect of Different Material Models on the Ratchet Boundary

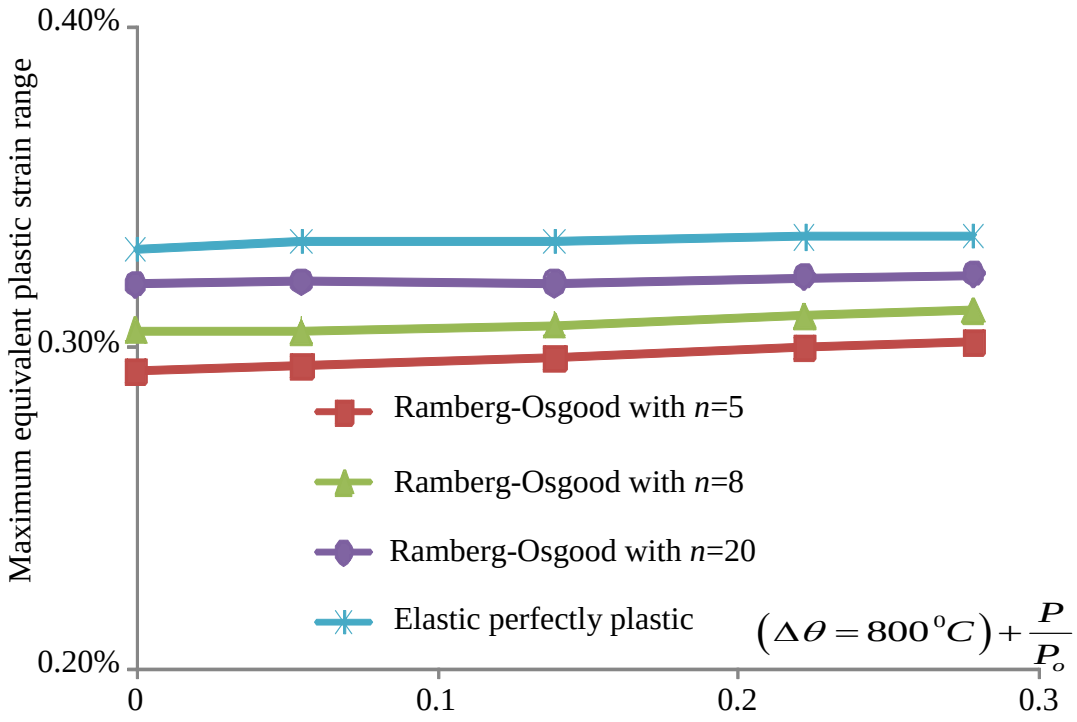

Figure 5.7 Maximum equivalent plastic strain range against the combination of cyclic thermal load and constant mechanical load for different material models

The ratchetting boundary for different types of inelastic material models is shown in Figure 5.8. It is observed from Figure 5.8 that the Ramberg-Osgood type material model considered in this chapter produced larger reverse plasticity boundary, when the cyclic loading is above the reverse plasticity limit *AB*, compared to the elastic perfectly plastic material model. And the size of the reverse plasticity region is increasing with decreasing Ramberg-Osgood material data *n*. This can be explained by Figure 5.4, which shows that the Ramberg-Osgood type material model has larger stress range than the elastic perfectly plastic material model above the reference yield stress.

The above phenomenon could be further explained by Figure 5.9 and Figure 5.10. Figure 5.9 shows the hardening von-Mises stress distribution due to cyclic thermal load with $\Delta\theta = 1000^{o}C$ (the first stage in minimization process) for

Ramberg-Osgood material with different parameter *n*. Figure 5.10 shows the failure pattern at the limit state with the additional constant tensile load (the second stage in minimization process) for both Ramberg-Osgood and perfectly plastic material model, where the lighter colour represents the failure pattern area.

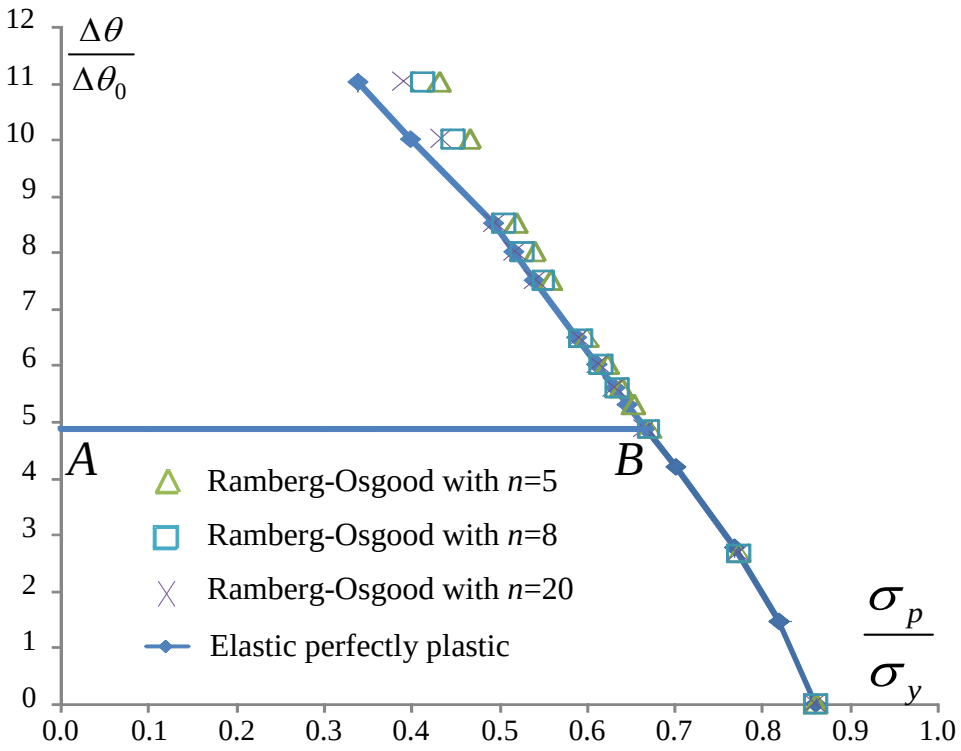

Figure 5.8 The ratchet limit boundary for different material models

It is observed from Figure 5.9 that the cyclic hardening von-Mises stress increases with decreasing parameter *n* and that hardening stress areas are surrounding the hole. Because the hardening stress distribution around the hole (Figure 5.9) is effecting a small portion of the failure area at the ratchet limit state (Figure 5.10), the ratchet boundary is slightly effected for the Ramberg-Osgood type material model (Figure 5.8) when the cyclic loading condition exceeds the reverse plasticity limit.

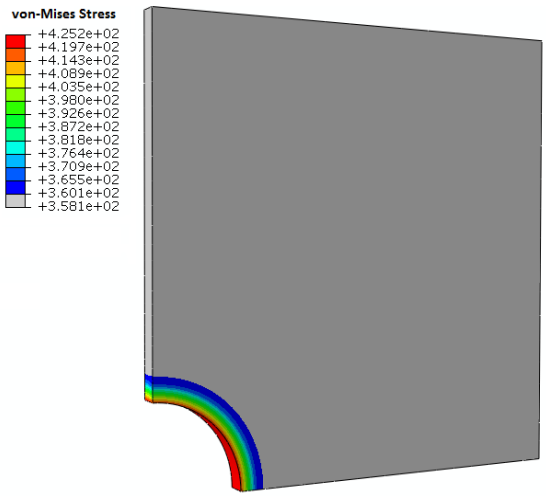

(a) *n*=5

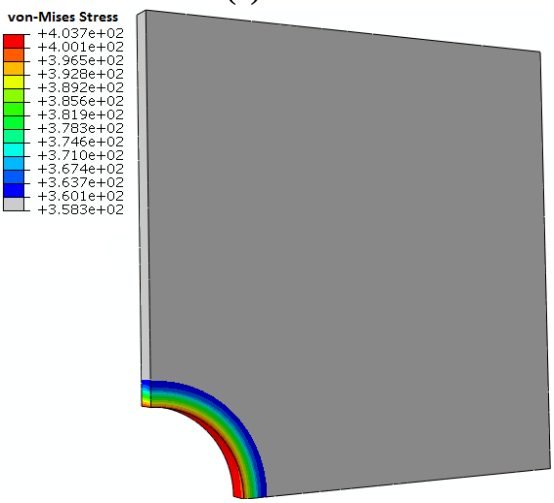

(b) *n*=8

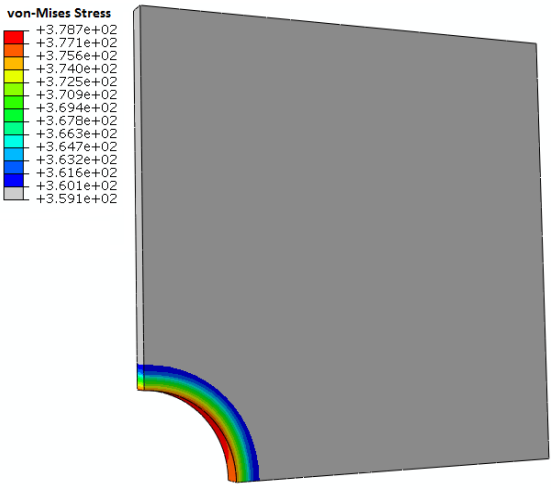

(c) *n*=20

Figure 5.9 Hardening von-Mises stress distribution (stress distribution that is greater than the reference yield stress $\bar{\sigma}\left(\sigma_{ij}\right) > \sigma_0$) with different Ramberg-Osgood material parameter *n* due to the cyclic thermal load (first stage of the minimization process) with $\Delta\theta = 1000^0 C$

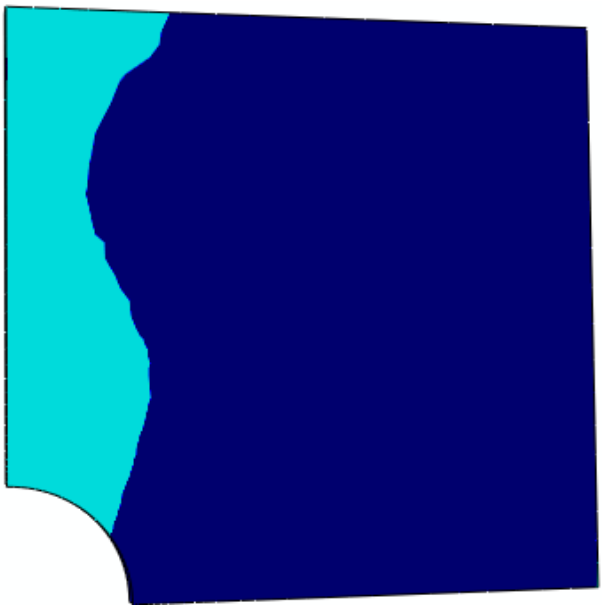

Figure 5.10 Failure pattern at the ratchet limit state due to the additional tensile force (second stage of the minimization process) with $\Delta\theta = 1000^0 C$ for Ramberg-Osgood type material and elastic perfectly plastic material model

5.5 Conclusions

The capability of the identification of the ratchetting boundary using Linear Matching Method (LMM) is discussed in this chapter. The associated numerical procedures [4], for the identification of ratchet limits in both elastic perfectly plastic and Ramberg-Osgood type hardening conditions, are presented.

The application of this numerical method was then examined on a 3D plate with a central hole problem. The solutions showed that the LMM-based methodologies were capable of generating accurate ratchet limits. The sensitivity of the solutions to cyclic hardening was also observed, as Ramberg-Osgood type material model increases the plastic strain range with increasing parameter *n*, and enlarges slightly the size of the reverse plasticity region with decreasing parameter *n*.

In the coming two chapters, a further examination on two complex defective structures will be conducted by using the numerical procedure mentioned in Chapters 3 and 5. In Chapter 6, the regions of shakedown, reverse plasticity, ratchetting and plastic collapse mechanism are identified for the defective pipeline under cyclic

thermal load and a constant mechanical load. In Chapter 7, the effect of circular holes on the ratchet limit and crack tip plastic strain range are investigated for a centre cracked plate.

CHAPTER 6. ON SHAKEDOWN, RATCHET AND LIMIT ANALYSES OF A DEFECTIVE PIPELINE

6.1 Introduction

Pipelines are widely used in various fields such as the petrochemical industry, energy and electric power engineering. During their operation, many local defects such as part-through slots can be produced by corrosion, mechanical damage or abrading surface cracks. These defects may jeopardize the integrity (i.e. reduce load-carrying capacity and low cycle fatigue life) of the pipelines and sometimes even lead to severe industrial accidents. The integrity assessment of defective pipelines is very important in the pipeline industry. The current testing codes and standards for the pipelines in service provide severe limitations to the allowable dimensions of part-through slots. Unnecessary welding treatments of part-through slots required by the codes are not only resource-consuming processes but can also produce more severe welding defects. Therefore, some serious and systematic attempts should be made to investigate the effects of part-through slots on the load-carrying capacity and fatigue life of pipelines under cyclic loading conditions. These attempts are expected to provide some more scientific and reasonable approaches for the defect assessment and treatment. Studies of the effects of part-through slots on the load-carrying capacity of pipelines under cyclic mechanical load have been carried out [85] [86] However, due to the lack of systematic theoretical analyses as well as enough experimental results, the effects of part-through slots on the shakedown and ratchet limit of pipelines under cyclic thermal load and a constant mechanical load are still unclear at present.

In the analysis of structures subjected to cyclic loading histories for an elastic–perfectly plastic material, the component will either shakedown or ratchetting. In many applications, it is too conservative for a structure to be within the elastic shakedown limit. Plastic shakedown or alternating plasticity, under which a local low cycle fatigue failure mode occurs, may be permitted, provided that during its design life the effect of low cycle fatigue is taken into consideration. Ratchetting,

which ultimately leads to incremental plastic collapse, should be avoided, since it may lead to intolerable deformations. And for this reason it is desirable to calculate the ratchet limit of a structure under cyclic load condition. In addition, the evaluation of the ratchet limit is particularly useful for structures with stress raisers, such as cracks. In such structures, due to the presence of the elastic stress singularity at the crack tip the shakedown condition becomes invalid, since a finite shakedown limit does not exist anymore.

In this chapter, a numerical procedure of LMM mentioned in Chapter 3 and 5 is used in the analysis of the defective pipeline subjected to constant internal pressure and a cyclic thermal gradient. The effect of part-through slots on the load carrying capacity, shakedown and ratchet limit is presented. Parametric studies involving different types and dimensions of part through slots are carried out. ABAQUS [80] step-by-step inelastic analyses are also carried out to verify the obtained shakedown and ratchet limits by the proposed method.

This work has been published in the International Journal of Pressure Vessel Technology in 2011.

6.2 3-D Defective Pipeline

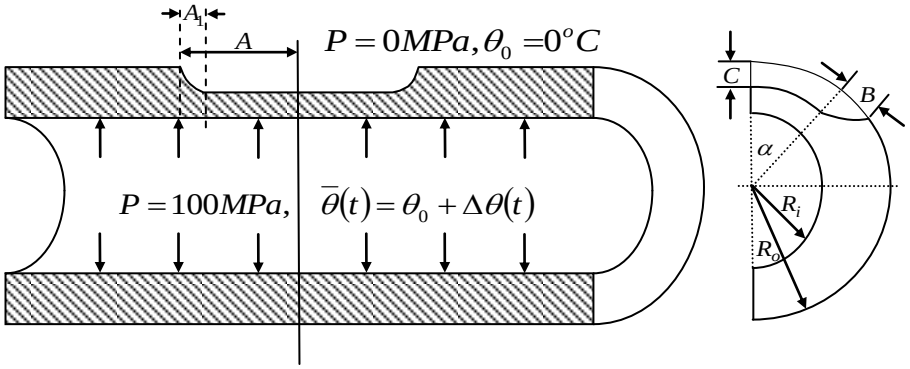

Figure 6.1 The geometry of a pipeline with part-through slot subjected to internal pressure and cyclic thermal load

6.2.1 Geometry

The geometry [85] and the material properties of a defective pipeline subjected to constant internal pressure and a cyclic thermal gradient are shown in Figure 6.1 and Table 6.1, respectively. R_i and R_0 are the inner radius and outer radius of the defective pipeline, respectively. The analysis is performed for different geometric parameters of a pipeline with different types of slots (Table 6.2). In all cases the inner radius and outer radius are chosen to be $R_i=17mm$ and $R_0=21mm$, respectively, while the length is $L=250mm$.

Table 6.1 Material properties of the steel

Type	Young's modulus E (GPa)	Poisson's ratio ν	Coefficient of thermal expansion α ($°C^{-1}$)	Yield stress σ_y (MPa)
Steel (S235H)	200	0.3	1.4×10^{-5}	360

Table 6.2 The pipeline shape parameters and dimensions with different defect types (shallow slot/deep slot) (mm/mm)

Defect type	α	A_1 (mm) Shallow/deep slot	A(mm) Shallow/deep slot	B(mm) Shallow/deep slot	C(mm) Shallow/deep slot
Small slot	0°	2mm/3mm	2mm/3mm	2mm/3mm	2mm/3mm
Circumferential slot	45°	2mm/3mm	2mm/3mm	2mm/3mm	2mm/3mm
Axial slot	0°	2mm/3mm	20mm	2mm/3mm	2mm/3mm
Large area slot	45°	2mm/3mm	20mm	2mm/3mm	2mm/3mm

6.2.2 Finite Element Model

The defective pipeline is analyzed using ABAQUS type C3D20R 20 node quadratic brick elements with reduced integration scheme. The defective pipeline has two planes of symmetry. Hence, to minimize the size of the model, these symmetry boundary conditions are applied to the half section of the model. A finite element model of a defective pipeline with four different types of slot is shown in Figure 6.2. The pipeline bore is under constant internal pressure. The free end of the pipeline is

constrained in order to keep the plane section plane during loading. The closed-end boundary condition is achieved by applying uniform axial thrust to the end of the pipe. The uniform axial thrust T_N induced by the internal pressure P is given by $T_N = PR_i^2/\left(R_o^2 - R_i^2\right)$. The applied cyclic thermal loading is produced by assuming that the outside surface of the pipeline is at ambient temperature while the internal surface temperature $\theta(t)$ is fluctuating from ambient to higher values. Two thermal stress extremes are adopted for this cyclic load history:

1. A thermal stress is produced by the linear thermal gradient along the thickness. This thermal load is calculated by a steady-state thermal analysis;

2. Then a zero thermal stress field is selected to simulate a uniform ambient temperature for the whole defective pipeline.

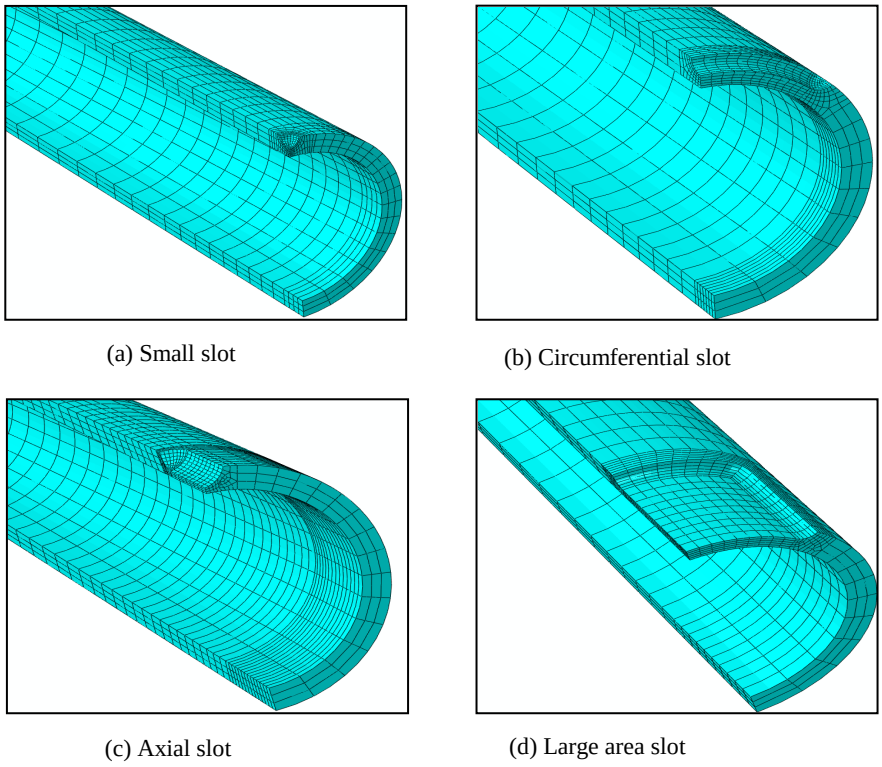

(a) Small slot (b) Circumferential slot

(c) Axial slot (d) Large area slot

Figure 6.2 The finite element mesh for a pipeline with part-through slot: (a) small slot; (b) circumferential slot; (c) axial slot and (d) large area slot

The detailed temperature history at the inner surface of the defective pipeline is given in Figure 6.3, where $\theta(t)$ varies between θ_0 and $\theta_0+\Delta\theta$. When the ambient

temperature θ_0 remains at $0^{\circ}C$, the magnitudes of the maximum thermo elastic stresses for the above thermal loading extremes can be determined by the maximum temperature difference $\Delta\theta$ between the inner surface and outer surface of the defective pipeline. Hence the cyclic thermal load and constant mechanical load can be characterized by the maximum temperature difference $\Delta\theta$ and the internal pressure P, respectively. The reference constant elastic mechanical stress can be calculated by the internal pressure $P=P_0=100MPa$ while the reference temperature difference $\Delta\theta=\Delta\theta_0=100^{\circ}C$ determines the reference cyclic elastic thermal stress.

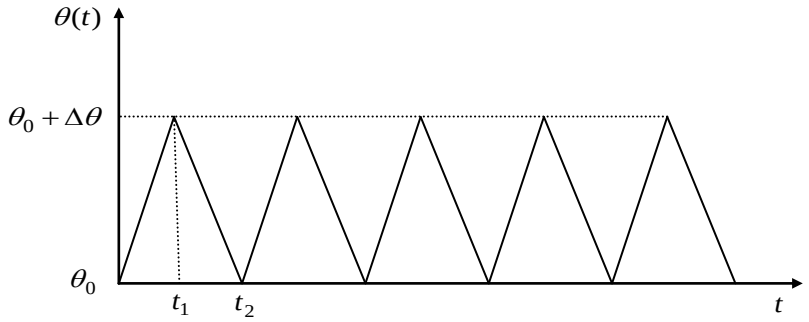

Figure 6.3 The cyclic thermal loading history for the defective pipeline

6.3 The Limit Load, Shakedown and Ratchet Limit Interaction Curve

The shakedown and ratchet limit interaction curve for a pipeline with small slot (shallow dimension) subjected to constant internal pressure and a cyclic thermal gradient is shown in Figure 6.4. The applied pressure in X-axis is normalized with respect to the reference internal pressure P_0, while the thermal load in Y-axis is normalized by using the reference temperature difference $\Delta\theta=\Delta\theta_0=100^{\circ}C$. This interaction diagram consists of shakedown limit, ratchet limit and limit load for different ratios of varying thermal load and constant mechanical load. The diagram is divided into four zones; shakedown, reverse plasticity, ratchetting and plastic collapse zone. Elastic shakedown will not occur if the load applied surpasses the reverse plasticity limit "*AB*". In this case the permanent strains settle into a closed cycle, a condition also known as "alternating plasticity" and associated with a low

cycle fatigue mechanism. The plastic strains will increase indefinitely if the applied cyclic load level is beyond the ratchet limit "*CD*". This is known as "ratchetting" or "incremental plastic collapse". The point "*D*" corresponds to the limit load for the applied mechanical load. Any applied cyclic load which exceeds the limit load line *DI* will cause plastic collapse.

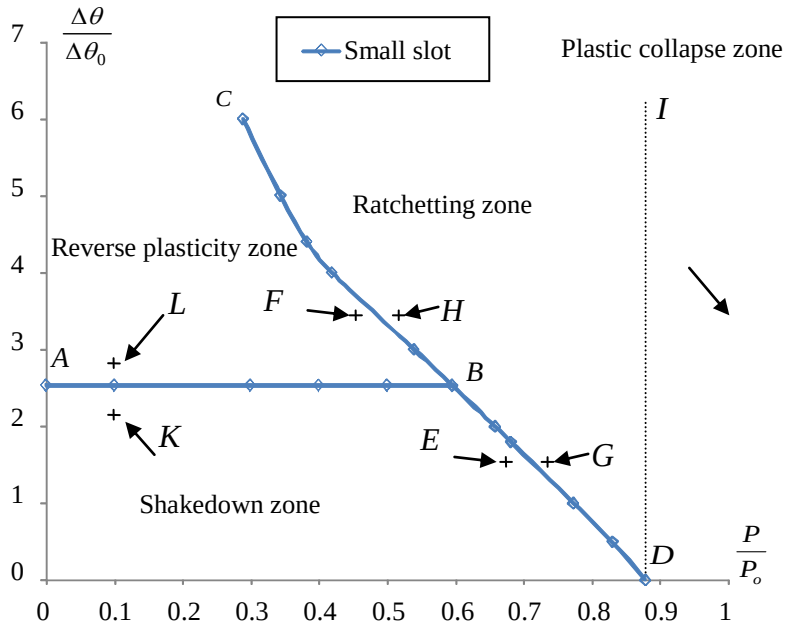

Figure 6.4 The ratchet limit boundary for small slot case

For the verification of the ratchet limit boundary calculated by the LMM, the cyclic load points $E(\Delta\theta=1.5\Delta\theta_0,\ P=0.68\ P_0)$, $F(\Delta\theta=3.5\Delta\theta_0,\ P=0.45P_0)$, and $G(\Delta\theta=1.5\Delta\theta_0,\ P=0.75P_0)$, $H(\Delta\theta=3.5\Delta\theta_0,\ P=0.55P_0$), which are just below and above the calculated ratchet limit boundary (Figure 6.4), respectively, are chosen for the step-by-step analysis by ABAQUS. The plastic strain histories for the cyclic loadings *E*, *G* and *F*, *H* are shown in Figure 6.5a and Figure 6.5b, respectively. From Figure 6.5a it is observed that the calculated maximum signed equivalent plastic strain for the load case *E* exhibits shakedown as the calculated maximum signed equivalent plastic strain stops changing after 3 load cycles, and the load case *G* shows a strong ratchetting mechanism, with the maximum signed equivalent plastic strain increasing at every cycle. A similar result is also obtained from Figure 6.5b, where the

calculated maximum signed equivalent plastic strain for the load case *F* settles into a stable cycle after about 10 load cycles showing a reverse plasticity mechanism, and the load case *H* shows a strong ratchetting mechanism, with the maximum signed equivalent plastic strain increasing at every cycle. For verifying the accuracy of the reverse plasticity limit "*AB*", the cyclic load points $K(\Delta\theta=2.3\Delta\theta_0,\ P=0.1P_0)$ and $L(\Delta\theta=2.7\Delta\theta_0,\ P=0.1P_0)$, which are just below and above the calculated reverse plasticity limit (Figure 6.4), respectively, are chosen for the step-by-step analysis by ABAQUS. Load point *K* (Figure 6.5c) exhibit shakedown mechanism as the calculated max signed equivalent plastic strain stops changing after 3 load cycles. The calculated maximum signed equivalent plastic strain for the load point *L* (Figure 6.5c) converges to a closed cycle after 3 load cycles showing a reverse plasticity mechanism. Thus, the results in Figure 6.5 obtained by ABAQUS step-by-step analysis confirm the accuracy of the predicted ratchet and shakedown limits by the LMM.

6.4 Results and Discussions

6.4.1 The Effect of the Part-through Slot on Limit Load

The loads causing plastic collapse on a defective pipeline with part-through slots and on defect-free pipeline under a constant internal pressure are shown in Table 6.3. From Table 6.3 it is observed that the calculated limit load for the defective pipeline with a small slot is identical to that for the defect-free pipeline. This reveals that the small slot does not affect the global failure mechanism of the defect-free pipeline. It can be seen from Table 6.3 that other types of slot cause a reduction in the limit load according to the volume of material removed. Despite removing the same volume of material, an axial slot will reduce the limit load more significantly than a circumferential slot. A thin walled pipe with closed ends subjected to internal pressure will have a hoop stress which is twice the axial stress, which makes an axial slot more dangerous than a circumferential slot. The calculated limit load for the defective pipeline with a large area slot has the least value, since the material loss for this type of slot is maximum.

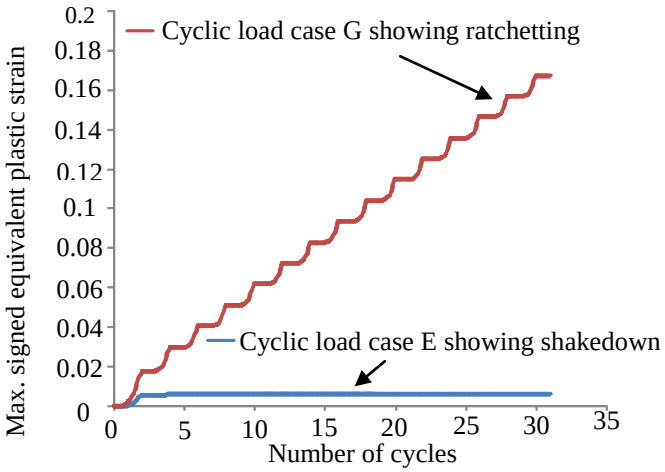

(a)

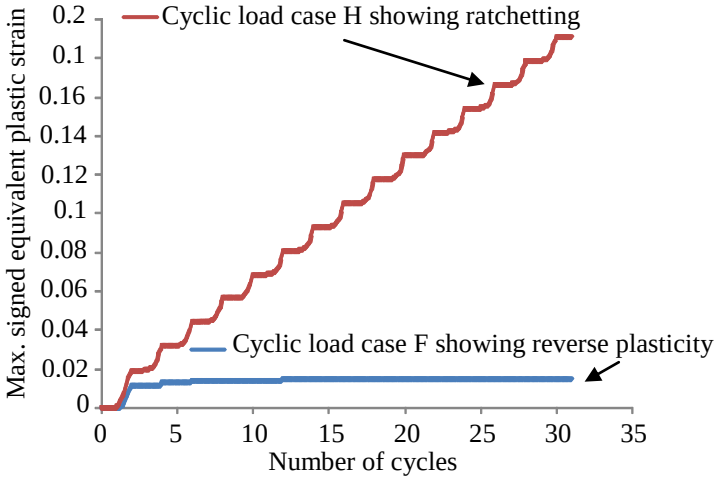

(b)

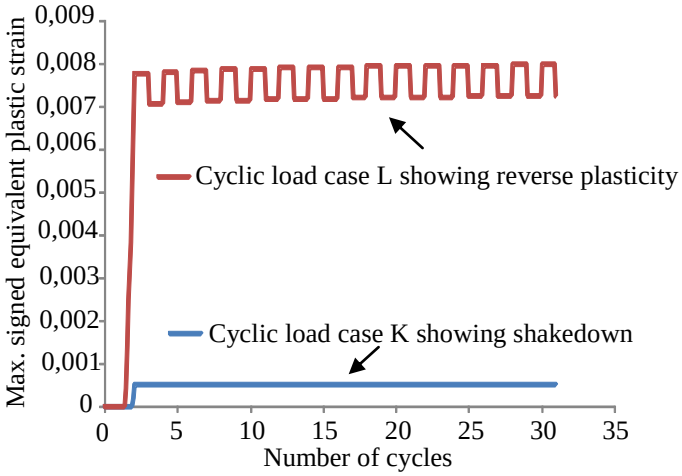

(c)

Figure 6.5 ABAQUS verification using step by step analysis for: (a) the shakedown and ratchet limit and (b) reverse plasticity and ratchet limit (c) reverse plasticity limit "*AB*"

Table 6.3 The limit loads for a pipeline with different defect types of slot under internal pressure P_0

Defect type	Limit Load for shallow type slot (MPa)	Limit Load for deep type slot (MPa)
Defect-free	87.8	87.8
Small slot	87.8	87.7
Circumferential slot	87.4	72.3
Axial slot	62.6	46.2
Large area slot	49.1	24.4

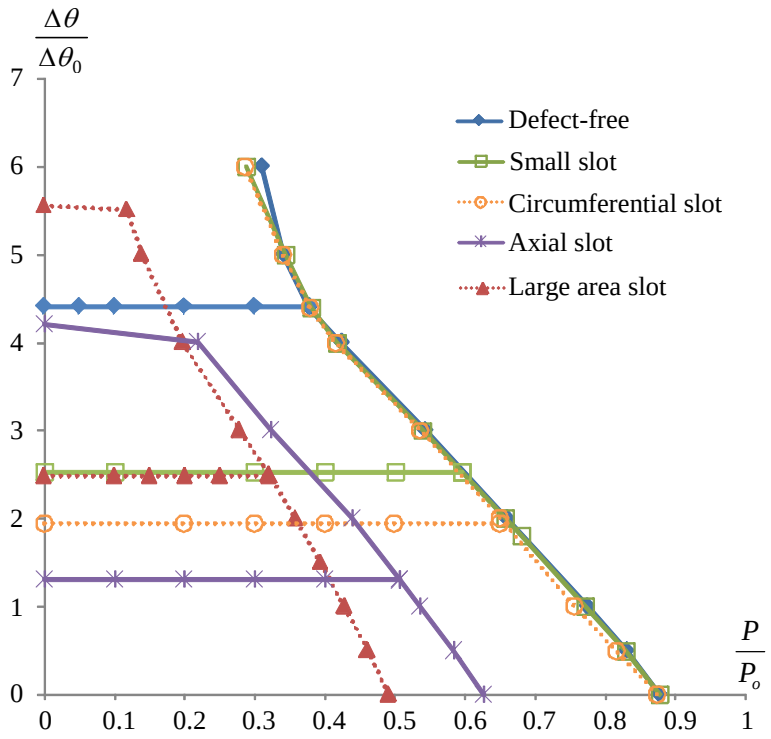

Figure 6.6 Shakedown and ratchet limit interaction curve for defective pipeline with shallow type slot

6.4.2 The Effect of the Part-through Slot on Shakedown Limit

The shakedown and ratchet limit interaction curve for a defective pipeline with different defect types of shallow slots is shown in Figure 6.6. The same interaction curve with shallow and deep type slot is shown in Figure 6.7. In both figures the applied pressure in the X-axis is normalized with respect to the reference internal pressure while the thermal load in the Y-axis is normalized by using the

reference temperature difference $\Delta\theta=\Delta\theta_0=100^{\circ}C$. Form Figure 6.6 it is observed that any part-through slot significantly reduces the reverse plasticity limit of the pipeline due to the stress concentration caused by the existence of the slot.

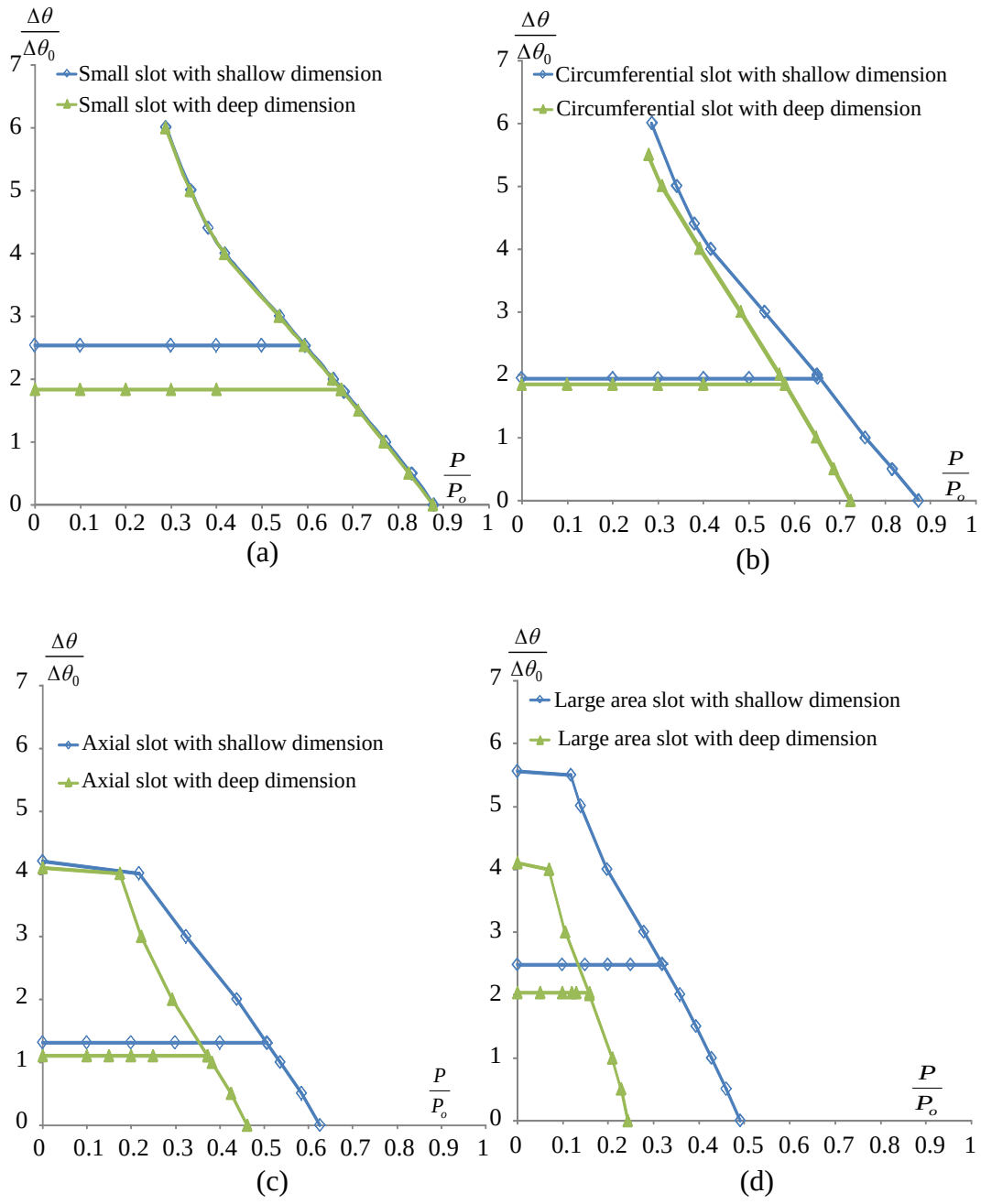

Figure 6.7 Shakedown and ratchet limit interaction curve of part-through slot with different dimensions: (a)small slot; (b) circumferential slot; (c) axial slot and (d) large area slot

For a pipeline with a small slot and a pipeline with a large area slot, the reverse plasticity limits are almost identical and have a greater value than a pipeline with circumferential and axial slot. A pipeline with an axial slot has the least reverse

plasticity limit due to the most significant stress concentration. In the same way as with the limit load, the axial slot has a larger impact on the hoop stress than a circumferential slot, and therefore has a larger reduction in the reverse plasticity limit. The stress concentration factor of a large area slot is less than that of an axial or circumferential slot and therefore has a larger reverse plasticity limit.

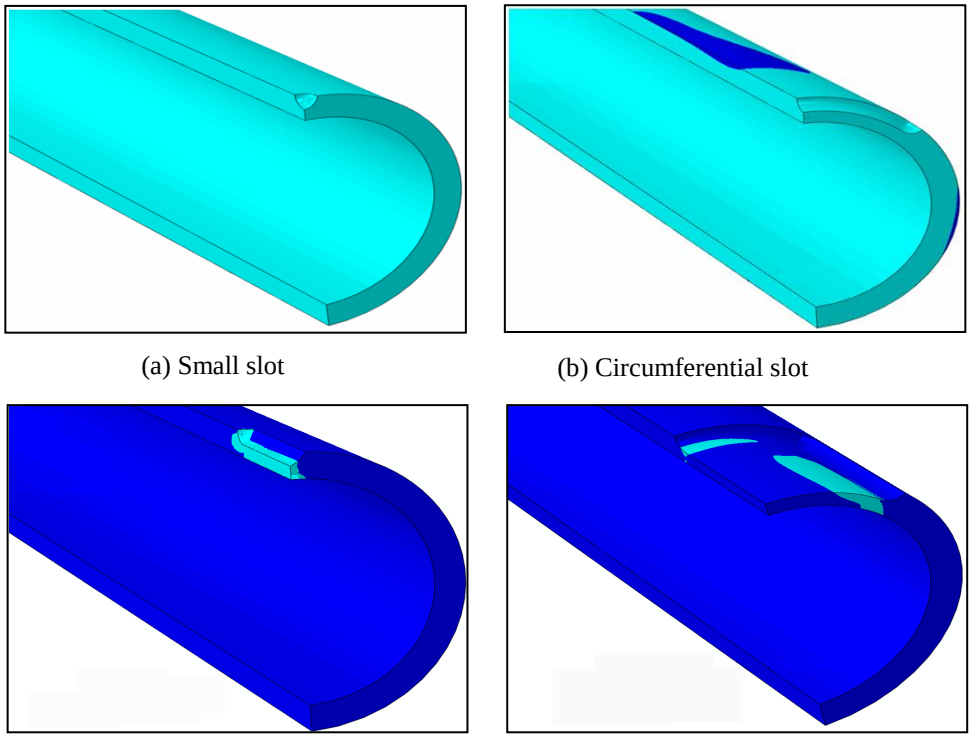

(a) Small slot (b) Circumferential slot

(c) Axial slot (d) Large area slot

Figure 6.8 Failure pattern at the limit state for defective pipeline: (a) small slot; (b) circumferential slot; (c)axial slot and (d)large area slot

Figure 6.7 shows that the reverse plasticity limit decreases when the slot gets deeper. The decreasing reverse plasticity limit is due to the increasing local stress concentration in the case of a deeper slot.

6.4.3 The Effect of the Part-through Slot on Ratchet Limit

From Figure 6.6 it is observed that at different levels of cyclic thermal loading the ratchet limit boundary decreases sharply for a defective pipeline with axial and large area slot and it remains almost constant for small and circumferential slot, compared to a defect-free pipeline. This phenomenon could be explained by Figure 6.8, which shows the failure pattern at the ratchet limit state for a defective

pipeline with a shallow slot subjected to constant internal pressure and a cyclic thermal gradient. Figure 6.8a and Figure 6.8b show that for a defective pipeline with small and circumferential slots the failure pattern appears almost in the whole body of the pipe, where the lighter colour represents the failure area. These failure pattern are a global response, which are similar to that of a defect-free pipeline. Hence the ratchet limit boundary for the pipeline with small and circumferential slots has almost the same magnitude as the defect-free pipeline. In the case of a defective pipeline with axial and large area slots (Figure 6.8c and Figure 6.8d), both failure areas appear locally around the slot, while the other parts of the pipe are unaffected. This explains why the ratchet limit boundary for the defective pipeline with axial and large area slot decreases significantly comparing to that of defect-free pipeline.

Figure 6.6 also shows that for the cases of axial and large area slots, the ratchet limit ends at cyclic thermal loading points $\Delta\theta$=4.1$\Delta\theta_0$ and $\Delta\theta$=5.5$\Delta\theta_0$, respectively, which indicates that when the cyclic thermal loading $\Delta\theta$ is beyond these cyclic thermal loading limits (4.1$\Delta\theta_0$ for axial slot and 5.5$\Delta\theta_0$ for large area slot), then any amount of constant internal pressure will result in ratchetting. This phenomena can be explained by Figure 6.8c-d, which indicates that at these cyclic thermal loading limits (4.1$\Delta\theta_0$ for axial slot and 5.5$\Delta\theta_0$ for large area slot) the failure regions (in light blue colour) all fell into reverse plasticity mechanism, therefore, any further mechanical load would cause the ratchetting of the component.

Similar to the limit load behaviour, the results in Figure 6.7a show that the deeper slot has no effect on the ratchet limit boundary for the small slot type. For the circumferential slot (Figure 6.7b), a deeper slot reduces the ratchet limit boundary slightly. When considering the axial and large area slots (Figure 6.7c-Figure 6.7d), a deeper slot causes greater reduction in the ratchet limit boundary.

6.4.4 The Effect of the Part-through Slot on Plastic Strain Range

The plastic strain range concerning a fatigue crack initiation is a key factor in a low cycle fatigue assessment. The maximum plastic strain range against temperature range for different types of shallow slot subjected to cyclic thermal loading only is plotted in Figure 6.9a. It is observed from Figure 6.9a that the

presence of part-through slot leads to an increase in the maximum plastic strain range. The axial slot causes a sharp increase in plastic strain range with increasing temperature compared to a defect free pipe. All other slot types cause only a small increase in comparison.

In order to investigate the effect of the constant mechanical load on the plastic strain range, three types of cyclic load histories are chosen as follows:

1) Cyclic temperature history ($\Delta\theta$) only,
2) Cyclic temperature history and constant internal pressure ($\Delta\theta$+0.1 P_0),
3) And cyclic temperature history and constant internal pressure ($\Delta\theta$+0.2 P_0).

The diagrams of maximum plastic strain range versus temperature range for a defect-free pipeline and a defective pipeline with different slot types are shown in Figure 6.9b-Figure 6.9f. It can be seen that the plastic strain range occurs when the applied temperature range exceeds the reverse plasticity limit. The results show that the cyclic loading history with additional constant internal pressure ($\Delta\theta$+0.1P_0) causes an increase in the maximum plastic strain range. The extra increase of the constant internal pressure from (0.1P_0) to (0.2P_0) does not result in further increase in the plastic strain range. For the axial and large area slots (Figure 6.9e-Figure 6.9f), when the maximum temperature range exceeds the level $\Delta\theta$=400°*C*, the component will exhibit ratchetting under this cyclic temperature load and the extra constant internal pressure ($\Delta\theta$+0.2P_0) (Figure 6.6). Thus, for these two slot cases, the maximum plastic range is plotted for the temperature ranges up to level $\Delta\theta$=400°*C*.

The location of the initiation of a fatigue crack, in different types of defective pipes occurring due to fatigue of the structure under cyclic loadings, is shown in Figure 6.10. From Figure 6.10b-Figure 6.10d it is observed that the location of the initiation of a fatigue crack in a defective pipe with circumferential, axial or large area slots, respectively, will occur along the slot surface direction. Whereas for the defective pipe with a small slot (Figure 6.10a) the initiation of a fatigue crack occurs in the inner bore of the pipe. Further investigation on this study shows that the location of the initiation of a fatigue crack for a defective pipeline is independent of the cyclic loading types considered in this chapter.

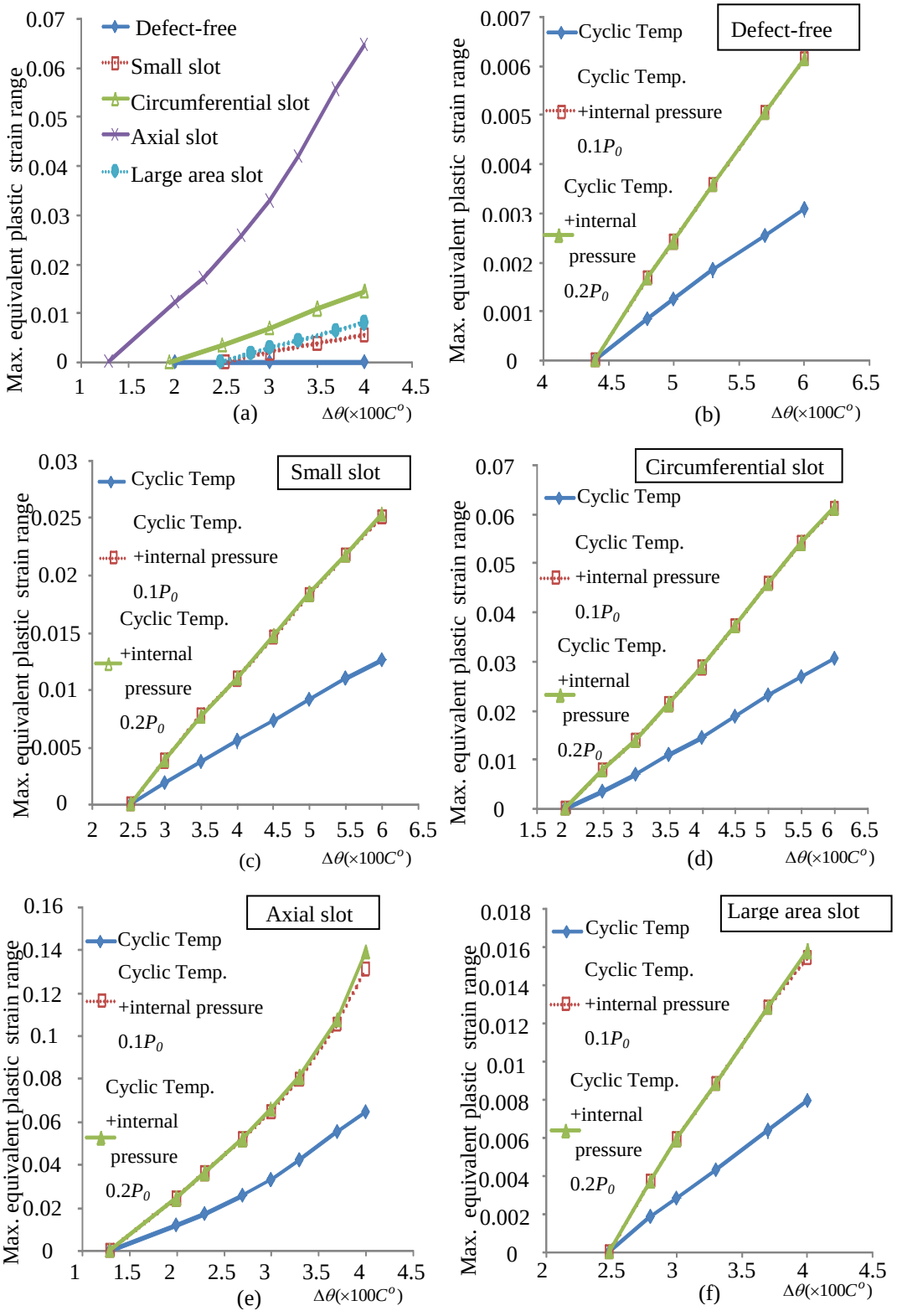

Figure 6.9 Maximum equivalent plastic strain range against temperature range for (a) Cyclic thermal load only (all defective pipeline); (b) Cyclic thermal and mechanical load (defect-free); (c) Cyclic thermal and mechanical load (small slot); (d) Cyclic thermal and mechanical load (circumferential slot); (e) Cyclic thermal and mechanical load (axial slot); (f) Cyclic thermal and mechanical load (large area slot)

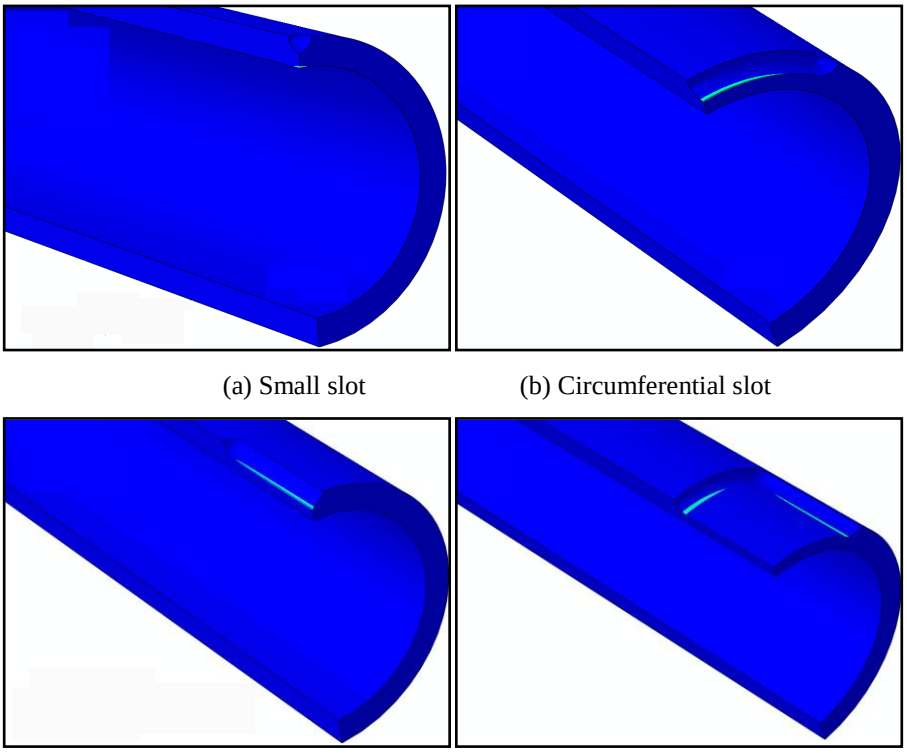

(a) Small slot (b) Circumferential slot

(c) Axial slot (d) Large area slot

Figure 6.10 The location of the initiation of a fatigue crack under cyclic thermal load and constant internal pressure (a)small slot; (b) circumferential slot; (c) axial slot

6.5 Conclusions

In the present study, the effect of part-through slots on limit loading, shakedown limit, ratchet limit and maximum plastic strain range has been investigated using the proposed LMM mention in Chapter 3,5 and the following observations have arisen:

1. The LMM has been verified by the step-by-step analysis, showing that it gives very accurate shakedown and ratchet limits for the defective pipelines with part-through slots.

2. A defective pipeline with a small slot and circumferential shallow slot greatly reduces the thermal load at which plastic shakedown occurs but does not affect the ratchet boundary and limit load. This implies that a small slot and circumferential shallow slot of the size studied in this chapter gives essentially a local stress concentration, which will affect the fatigue life of the pipeline but will

not influence the gross plastic deformation or the incremental plastic collapse behaviour.

3. The presence of a part-through slot leads to an increase in the maximum plastic strain range. The maximum plastic strain ranges obtained in this study give key information for the low cycle fatigue assessment.

4. The location of the initiation of a fatigue crack for a defective pipeline is independent of the cyclic loading types considered in this chapter.

As mentioned in the introduction, the evaluation of the ratchet limit is particularly useful for structures with stress raisers, such as cracks. In such structures, due to the presence of the elastic stress singularity at the crack tip, the shakedown condition becomes invalid, since a finite shakedown limit does not exist anymore. Therefore, in the coming chapter the effect of circular holes on the ratchet limit and crack tip plastic strain range in a centre cracked plate will be discussed.

CHAPTER 7. EFFECT OF CIRCULAR HOLES ON THE RATCHET LIMIT AND CRACK TIP PLASTIC STRAIN RANGE IN A CENTRE CRACKED PLATE

7.1 Introduction

In Chapter 5, the numerical procedure of the LMM was described to identify the ratchet limit. This method was then applied for the investigation of the defective pipeline under cyclic thermal load and a constant mechanical load. As mentioned previously in these chapters, the evaluation of the ratchet limit is particularly useful for structures with stress raisers, such as cracks. In such structures, the presence of the elastic stress singularity at the crack tip makes the shakedown condition invalid, since a finite shakedown limit does not exist anymore. For this reason, in this chapter the effect of the ratchet limit for a cracked structure under cyclic mechanical load will be investigated numerically.

Cracks, which develop during manufacturing or the service period of structures, affect the load capacity, residual strength, life and integrity of the structure. These cracks may grow and cause material, economical and human damages. Therefore, it is necessary to increase the residual strength and service life of the cracked structures by arresting crack growth. Several methods have been employed to arrest crack growth, such as external adhesive patching across the crack used in aircraft industry [87] [88], the method of pressing steel balls and drilling holes in front of the crack tip so that when the crack approaches the hole it will become blunted and be arrested. The method of drilling stop holes is well known to reduce the stress intensity factor and studies have been carried out in this area [89]. However, the effects of the location and diameter of circular holes on the ratchet limit and crack tip plastic strain range, which provides information concerning fatigue crack growth in a low cycle fatigue assessment, have not been undertaken.

In the analysis of structures subjected to cyclic loading histories for an elastic–perfectly plastic material, the component will either shakedown or ratchet. As mentioned in Chapters 5 and 6, for many applications, it is too conservative for a structure to be within the elastic shakedown limit. For this reason it is desirable to calculate the ratchet limit of a structure under cyclic load conditions. In addition, the evaluation of the ratchet limit is particularly useful for structures with stress raisers, such as cracks. In such structures, due to the presence of the elastic stress singularity at the crack tip the shakedown condition becomes invalid. Hence a finite shakedown limit does not exist anymore. However, the procedures for identifying the ratchet limit are still valid. This is due to the closed cycles of plastic strains occurring at the crack tip, enabling the evaluation of the finite ratchet limits. As a result, a method on the determination of the ratchet limit for cracked bodies is particularly desirable.

The aim of this chapter is to examine the evaluation of ratchet limit and plastic strain range for cracked bodies subjected to cyclic load conditions, and to analyse the effect of the circular hole on the ratchet limit and crack tip plastic strain range in a centre cracked plate using the LMM numerical procedure mentioned in Chapter 5. In this chapter, a centre cracked plate with symmetric holes subjected to two load conditions, cyclic uniaxial loading and cyclic bending moment with constant tensile loading, is considered by assuming plane strain condition. The effect of circular holes on the ratchet limit and crack tip plastic strain range, which is considered to be a better similitude parameter than the stress intensity range for the fatigue crack growth behaviour [90] in a stable cycle, is presented. Parametric studies involving the hole diameter and locations are carried out. The optimum location for reducing the crack tip plastic strain range with the least reduction in ratchet limit is identified considering the fact that reducing the plastic strain range will increase the component's fatigue life while an unchanged ratchet limit will keep the cyclic loading capacity of the cracked plate. An ABAQUS [80] step-by-step inelastic analysis is also carried out to verify the obtained ratchet limit by the LMM.

This work has been published in the International Journal of Fracture Mechanics in 2011.

7.2 Centre Cracked Plate with Circular Holes

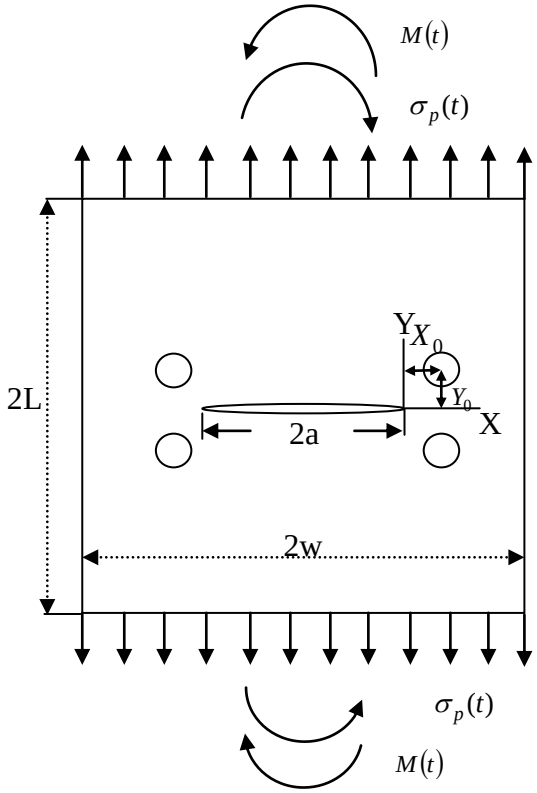

Figure 7.1 Centre cracked plate with symmetric holes subjected to cyclic tensile loading and cyclic bending moment

Table 7.1 Material properties of the steel

Young's modulus E (GPa)	Poisson's ratio ν	Coefficient of thermal expansion α ($°C^{-1}$)	Yield stress σ_y (MPa)
200	0.32	1.11×10^{-5}	360

7.2.1 Geometry

The geometrical shape and the material properties of the centre cracked plate with symmetric drilled holes are as shown in Figure 7.1 and Table 7.1, respectively. The half-crack length a is 500 mm and the ratios $\frac{W}{a}$ and $\frac{L}{a}$ are both 2. The hole locations are referred to a co-ordinate system X, Y, the origin of which is located at the crack tip. X_0 and Y_0 are the coordinates of the hole's centre according to the coordinate system placed at the crack tip as shown in Figure 7.1. Calculations are

made for hole diameters $D = 40$, 50, 100, 125, 150 mm with various symmetric drilled hole locations. The hole locations are defined by first drilling symmetric holes at various horizontal locations and keeping the vertical distance constant at $\frac{Y_0}{a} = 0.3$. Once the optimum horizontal location has been found, this is then held constant and holes are drilled for various vertical locations.

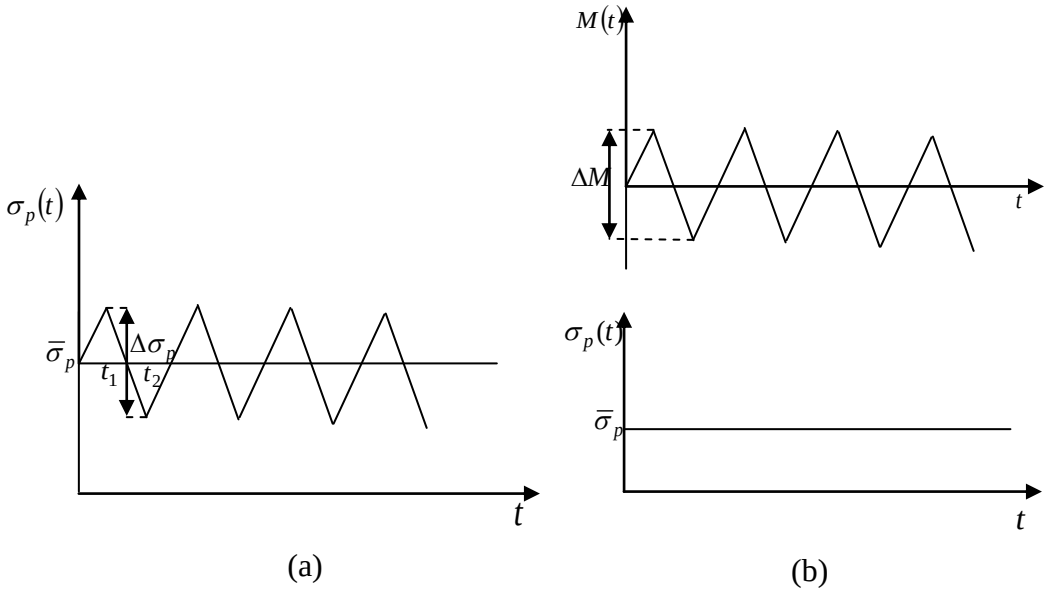

Figure 7.2 (a) The cyclic tensile loading history with mean tension $\bar{\sigma}_p$ and tension range $\Delta\sigma_p$ (b) The cyclic bending moment history with reversed bending moment range ΔM and constant tension $\bar{\sigma}_p$

7.2.2 Loading

The centre cracked plate is subjected to two different cyclic loading cases under plane strain condition. In the first case the plate is under cyclic tension loading with mean tension $\bar{\sigma}_p$, and in the second case a cyclic bending moment with reversed bending moment range ΔM and constant uniaxial tension $\bar{\sigma}_p$ is applied to the plate. The detailed cyclic loading histories are given in Figure 7.2, which show a cyclic loading history with two load extremes during each load cycle. For the cyclic tension case (Figure 7.2a), the two extremes of loading history can be formulated as $\sigma_p(t_1) = \bar{\sigma}_p + \Delta\sigma_p / 2$ and $\sigma_p(t_2) = \bar{\sigma}_p - \Delta\sigma_p / 2$, respectively, where $\bar{\sigma}_p$

represents the mean tensile loading and $\Delta\sigma_p$ represents the tension range. A similar loading history has also been modelled for the cyclic bending moment case (Figure 7.2b), by combining ΔM, the reversed bending moment range, and $\bar{\sigma}_p$, the constant tensile loading. The reference mean tensile loading and the reference constant uniaxial tension, $\bar{\sigma}_{po}$, with loading magnitude equal to 100MPa are used in both cases. A reference reversed bending moment range, $\Delta M_0 = 100N.mm$, is used for the cyclic bending moment case.

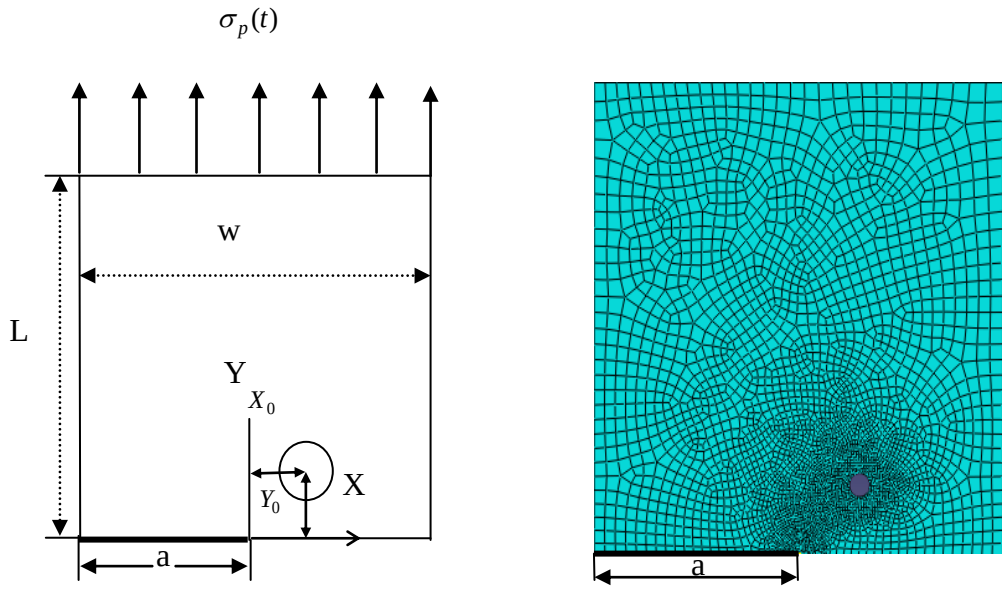

(a) (b)

Figure 7.3 (a) Quarter symmetry model for cyclic tensile loading case (b) Finite element model

7.2.3 Finite Element Model

In the Finite Element Modelling (FEM) the sizes of the models are minimized by applying symmetry boundary conditions to quarter- and half-models, accordingly. The cyclic tensile loading case has two planes of symmetry, and for the cyclic bending moment case one plane of symmetry is used. Thus, only quarter- and half-model is required for the cyclic tension and cyclic bending moment cases, as shown in Figure 7.3 and Figure 7.4, respectively. In both cases, along the symmetric axis, symmetric boundary conditions are imposed in the FEM. The analysis is performed

using ABAQUS type CPE8R 8 node quadratic quadrilateral elements with reduced integration scheme.

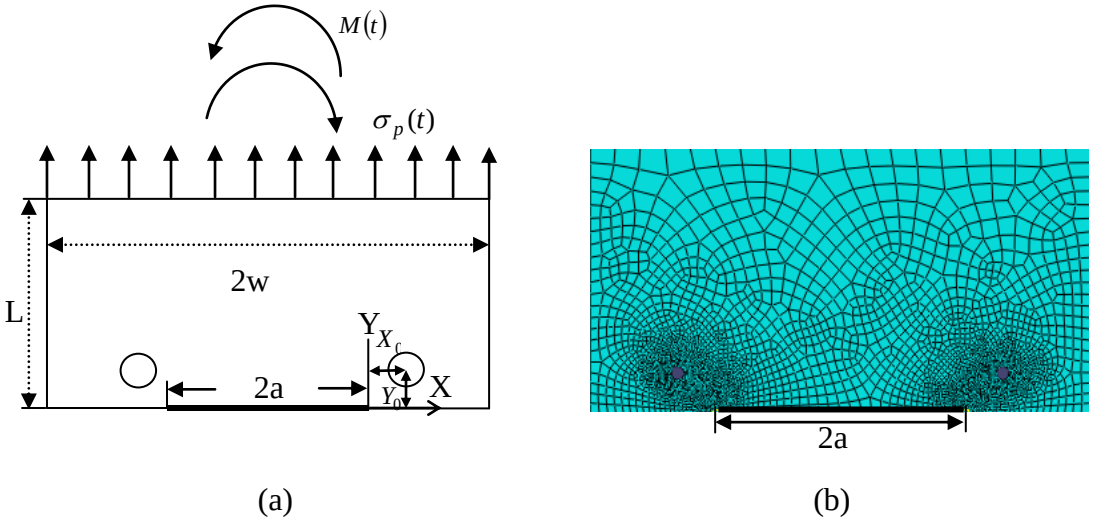

Figure 7.4 (a) Half symmetry model for cyclic bending moment case (b) Finite element model

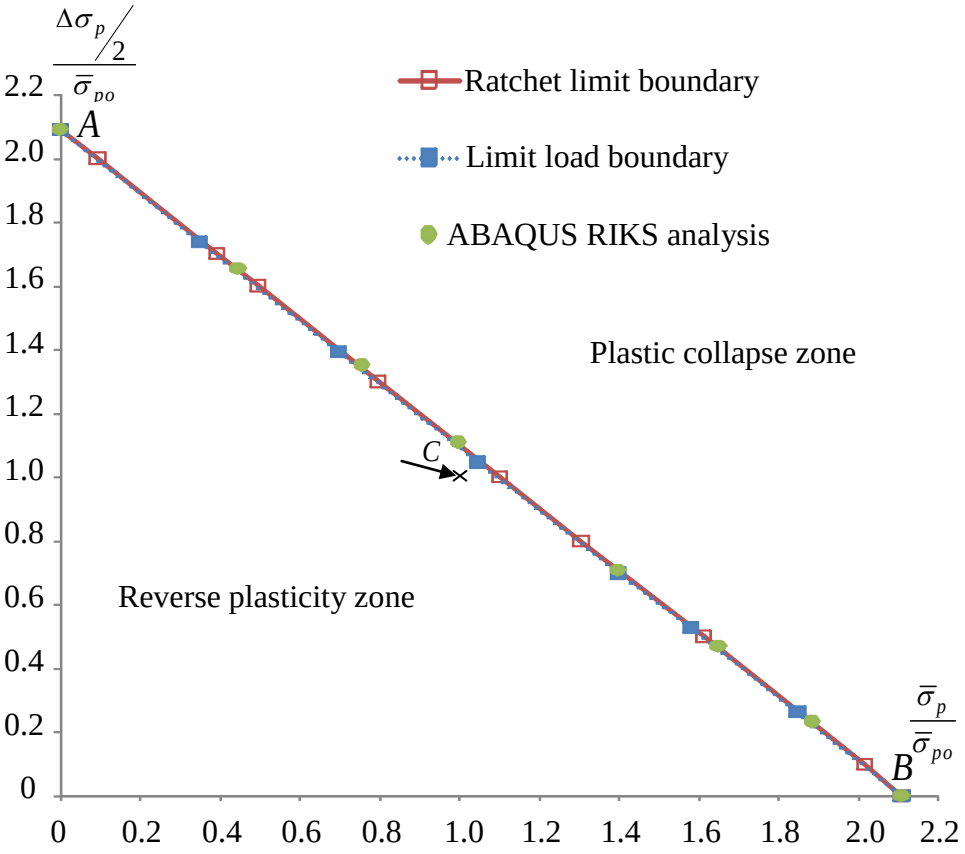

Figure 7.5 Ratchet limit interaction curve for the cyclic tensile loading case with hole location at $\frac{X}{a} = -0.1$, $\frac{Y}{a} = 0.3$ (D=100mm)

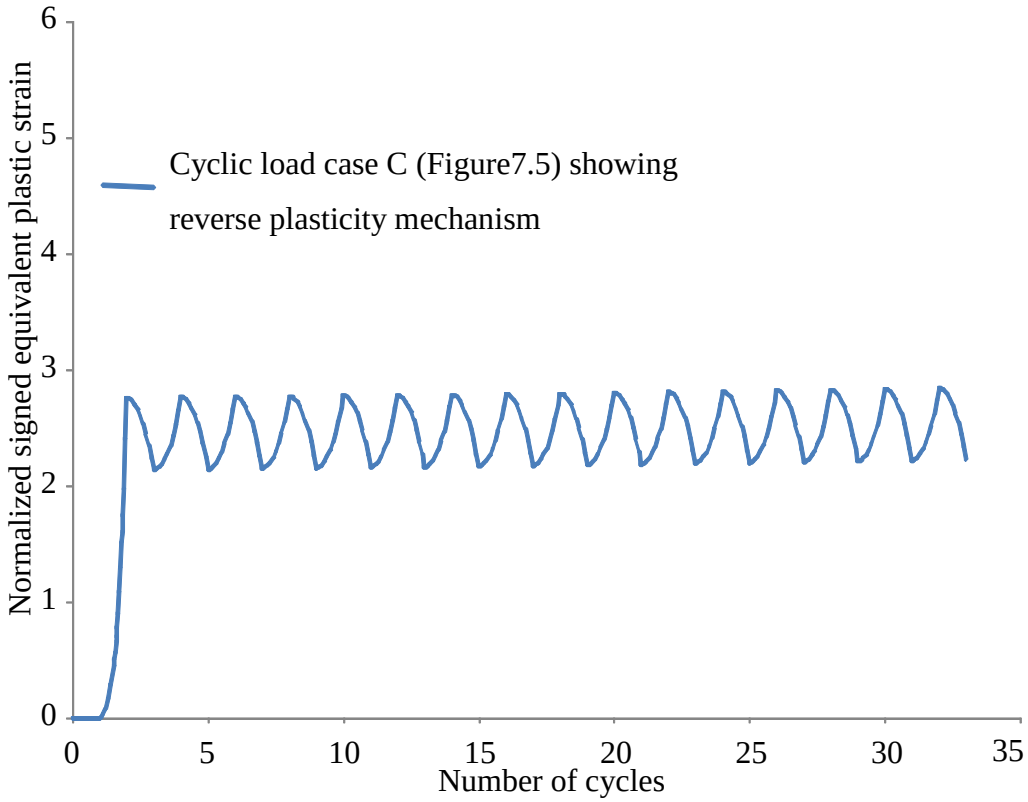

Figure 7.6 ABAQUS verification of the ratchet limit for the cyclic tensile loading case using detailed step by step analysis

7.3 Comparison of the Ratchet Limit with Limit Load Boundary

In order to illustrate the effectiveness of the ratchet limit method in cracked bodies, a centre cracked plate subjected to two different cyclic loading cases with a symmetrically located hole of diameter $D = 100mm$ is considered. The horizontal location, X_0, and the vertical location, Y_0, of the hole are kept at locations $\frac{X_0}{a} = -1$, $\frac{Y_0}{a} = 0.3$, respectively.

7.3.1 Cyclic Tensile Case

In the case of the cyclic tensile loading, the converged values of upper bound ratchet limits obtained from the LMM are shown in Figure 7.5 as an interaction diagram, composed of the limit for different ratios of varying tensile loading

amplitude and the mean tension. The applied mean tension, $\bar{\sigma}_P$, in X-axis and the tension amplitude $\Delta\sigma_P/2$ in Y-axis are normalized with respect to the reference tension $\bar{\sigma}_{po}$. Figure 7.5 shows that the ratchet limit boundary coincides with limit load boundary, which is also calculated by the LMM. This means that any cyclic tensile load which exceeds the ratchet limit will also exceed the limit load and cause plastic collapse in the first cycle (i.e. there will be no ratchetting or incremental plastic collapse which normally occurs due to the excessive cyclic loads). The coincidence of the ratchet limit and limit load boundaries is due to the fact that for both the ratchet limit analysis with the cyclic tensile load history, and the limit load analysis with static tensile load, the maximum tensile load during the cycle is dominant and leads to the same plastic collapse in both cases. The accuracy of the limit load boundary by the LMM has been verified by ABAQUS RIKS analysis, which provides the same limit load boundary as that calculated by the LMM. For the verification of ratchet limit boundary calculated by the LMM the cyclic load point C ($\Delta\sigma_p = 2\bar{\sigma}_{p0}, \bar{\sigma}_p = \bar{\sigma}_{p0}$), which is just below the calculated ratchet limit boundary (Figure 7.5), is chosen for the step-by-step analysis in ABAQUS. The plastic strain history at the crack tip for the cyclic loading C is shown in Figure 7.6, where the Y-axis represents the normalized maximum equivalent plastic strain for the cyclic load point C (Figure 7.5) with respect to maximum equivalent plastic strain at the crack tip for a centre cracked plate without holes under the action of the reversed tension ($\Delta\sigma_p = 2\bar{\sigma}_{p0}, \bar{\sigma}_p = 0$). As expected, Figure 7.6 shows a reverse plasticity mechanism under the cyclic load case C, where the maximum equivalent plastic strain calculated by the step-by-step analysis ceases to increase at about 3 load cycles and settles into a closed loop for the remaining cycles. This observation confirms the predicted ratchet limit curve.

7.3.2 Cyclic Bending Moment Case

The same procedure is also applied to the cyclic bending moment case, and the interaction diagram is shown in Figure 7.7, where the applied constant pressure in X-axis is normalized with respect to the reference uniaxial tension $\bar{\sigma}_{po}$, while the

cyclic bending moment in Y-axis is normalized using the reference cyclic bending moment ΔM_0. Unlike in the cyclic tensile loading case, the ratchet limit and the limit load curves do not coincide, which means that an increase in the loads beyond the ratchet limit will not automatically cause plastic collapse. Any combination of loads which lies between these two boundaries will result in ratchetting. The accuracy of the limit load boundary obtained by the LMM has been verified by ABAQUS RIKS analysis, which provides the same limit load boundary as that calculated by the LMM. For the verification of ratchet limit boundary calculated by the LMM the cyclic load points $D(\Delta M = 1.6\Delta M_0, \bar{\sigma}_p = \bar{\sigma}_{p0})$, and E $(\Delta M = 1.6\Delta M_0, \bar{\sigma}_p = 1.1\bar{\sigma}_{p0})$, which are just below and above the calculated ratchet limit boundary (Figure 7.7), respectively, are chosen for the step-by-step analysis in ABAQUS. The plastic strain history at the crack tip for the cyclic loading *D* and *E* are shown in Figure 7.8, where the Y-axis represents the normalized maximum equivalent plastic strain for the cyclic load points *D* and *E* (Figure 7.7) with respect to maximum equivalent plastic strain at the crack tip for a centre cracked plate without holes under the action of the reversed bending moment $(\Delta M = 1.6\Delta M_0, \bar{\sigma}_p = 0)$. The calculated maximum equivalent plastic strain for the load case D settles to a stable cycle after about 5 load cycles showing a reverse plasticity mechanism, and the load case E shows a strong ratchetting mechanism, with the maximum equivalent plastic strain increasing at every cycle. Thus, the results in Figure 7.8 obtained by ABAQUS step-by-step analysis confirm the accuracy of the predicted ratchet limits by the LMM for the cyclic bending moment case.

7.4 Results

The effect of the hole location and the hole size on ratchet limit and maximum plastic strain range for the centre cracked plate are analyzed in this study. Firstly, symmetric holes are drilled at various horizontal locations keeping the vertical distance constant at $\frac{Y_0}{a} = 0.3$. Once the optimum point is reached subsequent analyses are performed with varying vertical coordinates and fixed horizontal location.

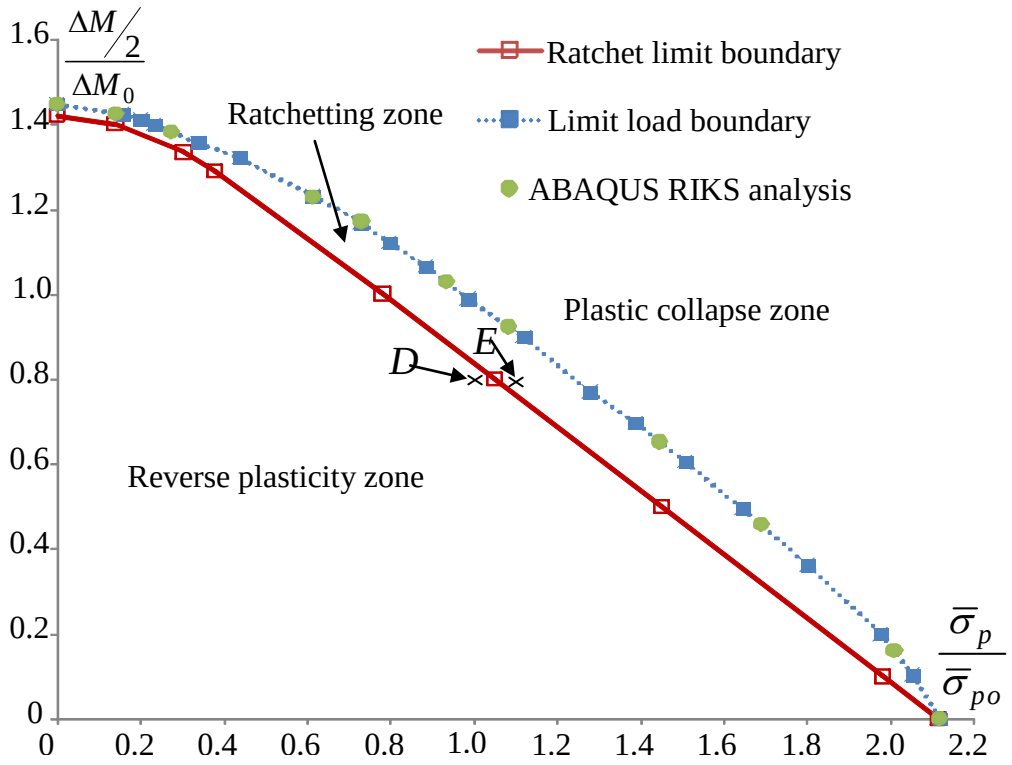

Figure 7.7 Ratchet limit interaction curve for the cyclic bending moment case with hole location at $\frac{X}{a} = -0.1$, $\frac{Y}{a} = 0.3$ (D=100mm)

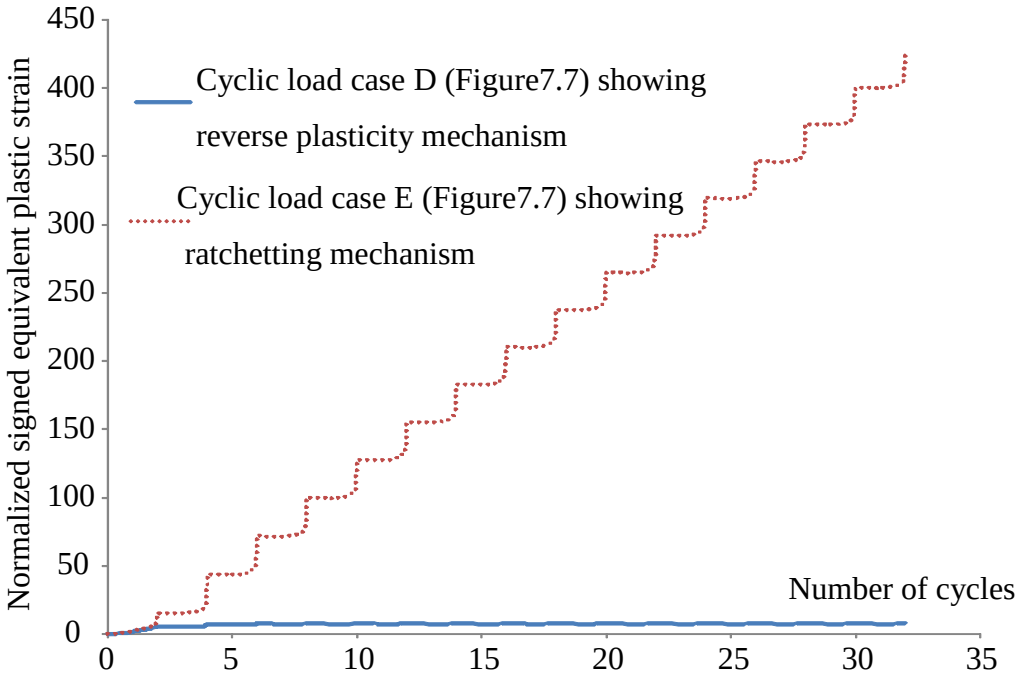

Figure 7.8 ABAQUS verification of the ratchet limit for the cyclic bending moment case using detailed step by step analysis

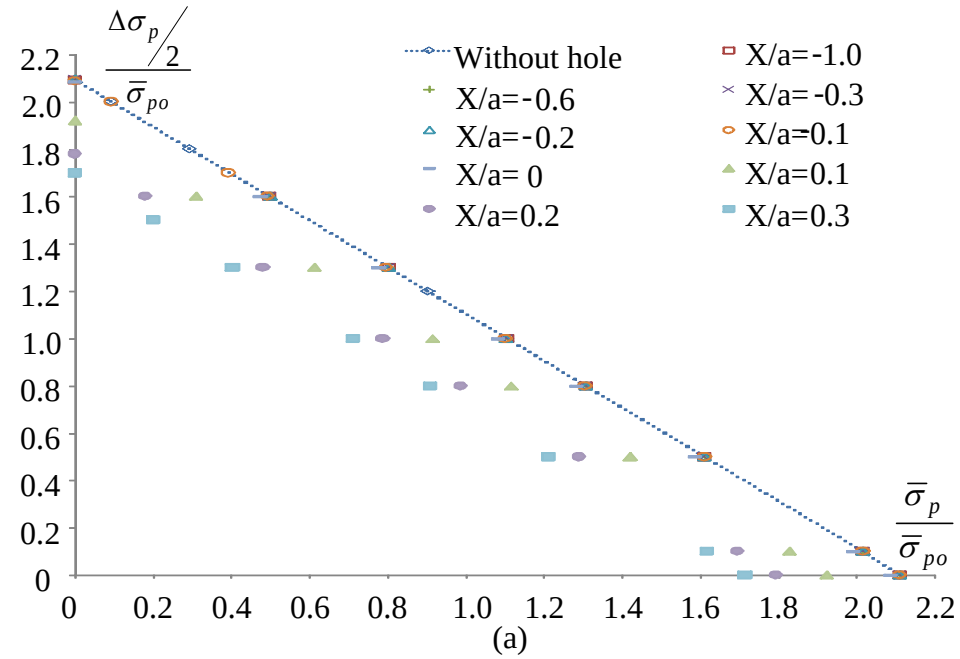

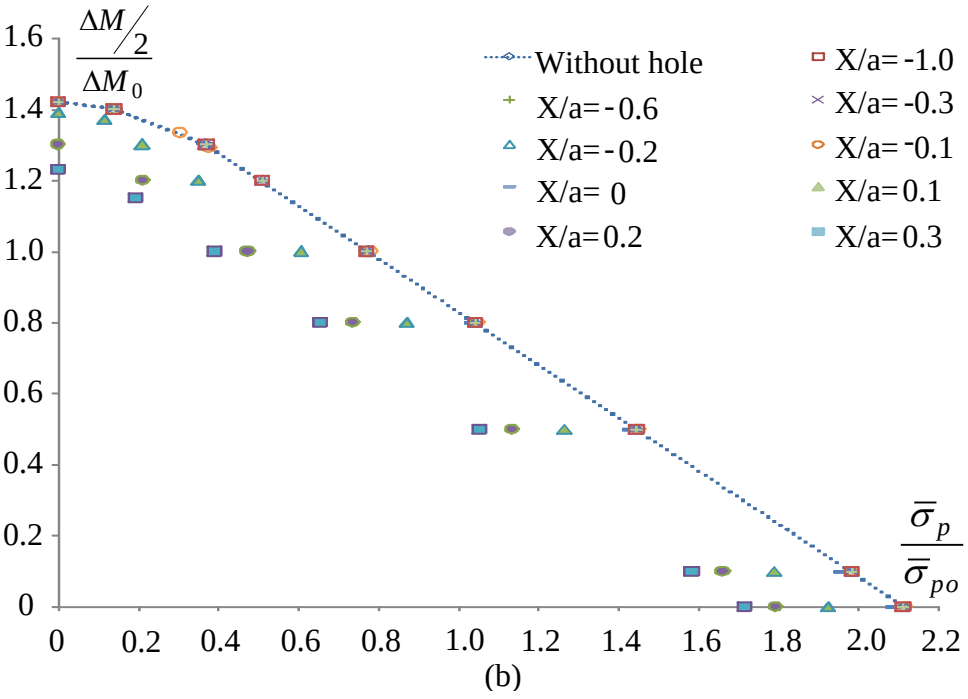

Figure 7.9 Ratchet limit interaction curve with varying horizontal hole location and fixed vertical location at $Y/a = 0.3$ (D=100m): (a) cyclic tensile loading case and (b) cyclic bending moment case

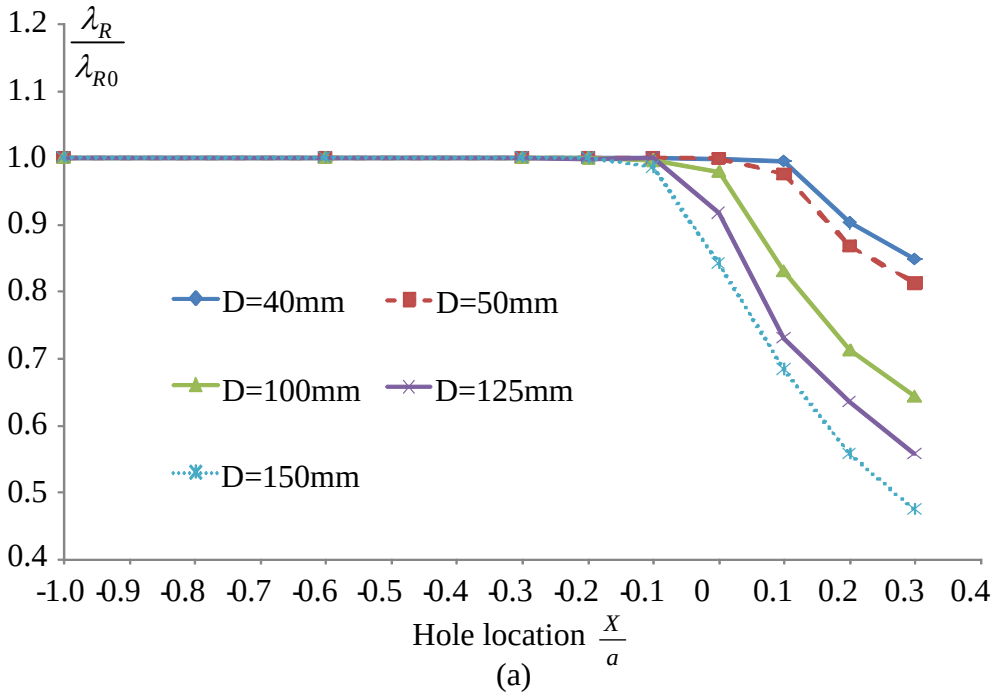

(a)

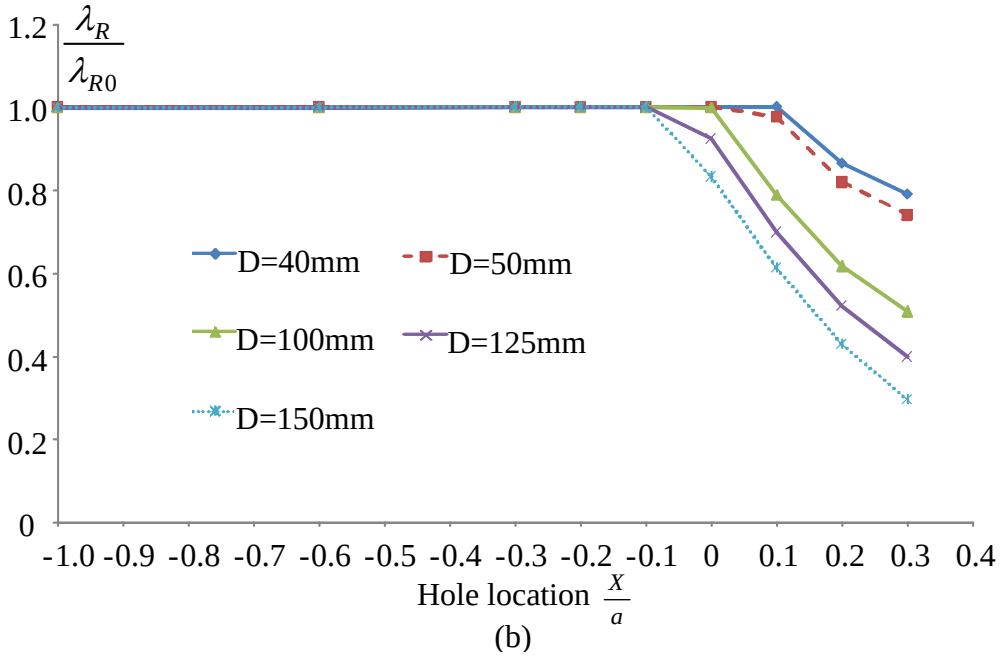

(b)

Figure 7.10 Variation of normalized ratchet limit multiplier with varying horizontal hole location at the fixed vertical location($Y/a=0.3$): (a) for cyclic tensile loading case $(\Delta\sigma_p/2)/\bar{\sigma}_{po}=1$ (Figure 7.9a) and (b) for cyclic bending moment case $(\Delta M/2)/\Delta M_0=1$ (Figure 7.9b)

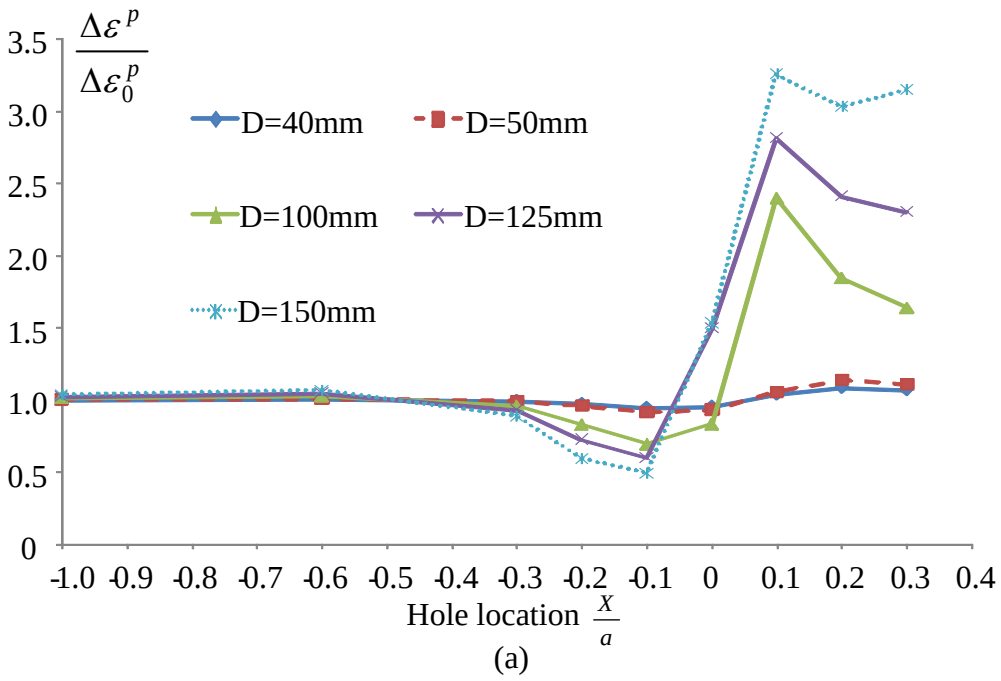

(a)

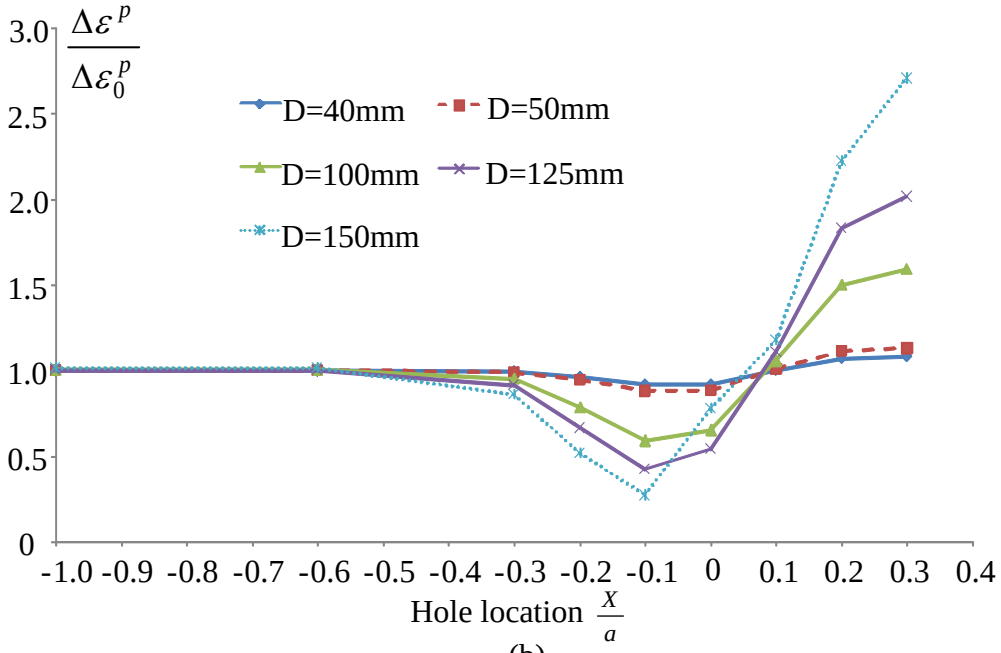

(b)

Figure 7.11 Variation of normalized maximum plastic strain range with varying horizontal hole location at the fixed vertical location ($Y/a = 0.3$): (a) for cyclic tensile loading case $(\Delta\sigma_p/2)/\bar{\sigma}_{po} = 1$ (Figure 7.9a) and (b) for cyclic bending moment case $(\Delta M/2)/\Delta M_0 = 1$ (Figure 7.9b)

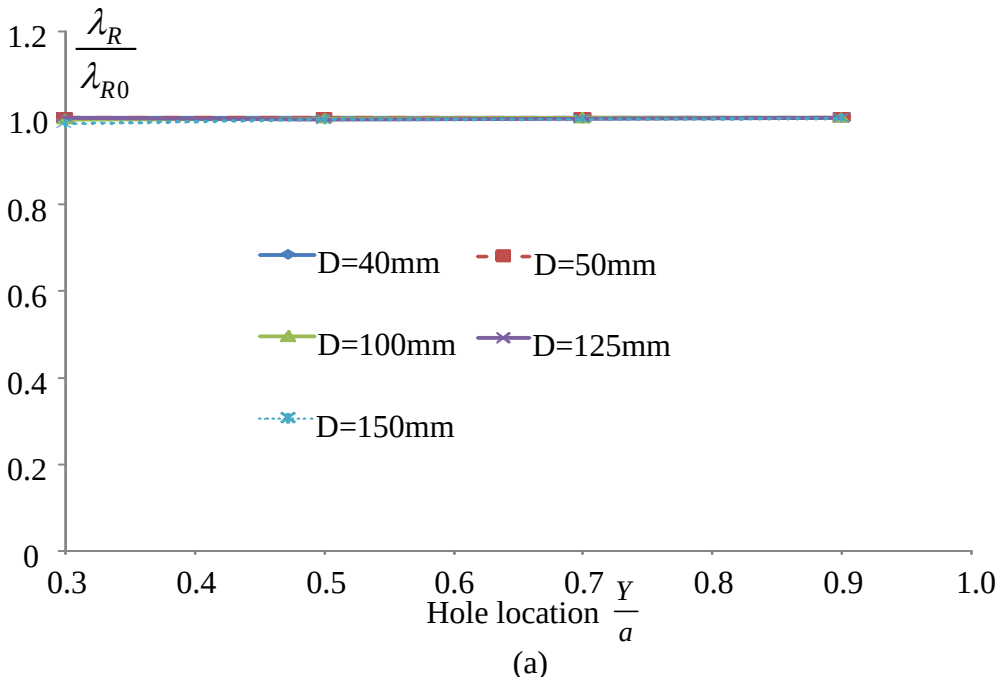

(a)

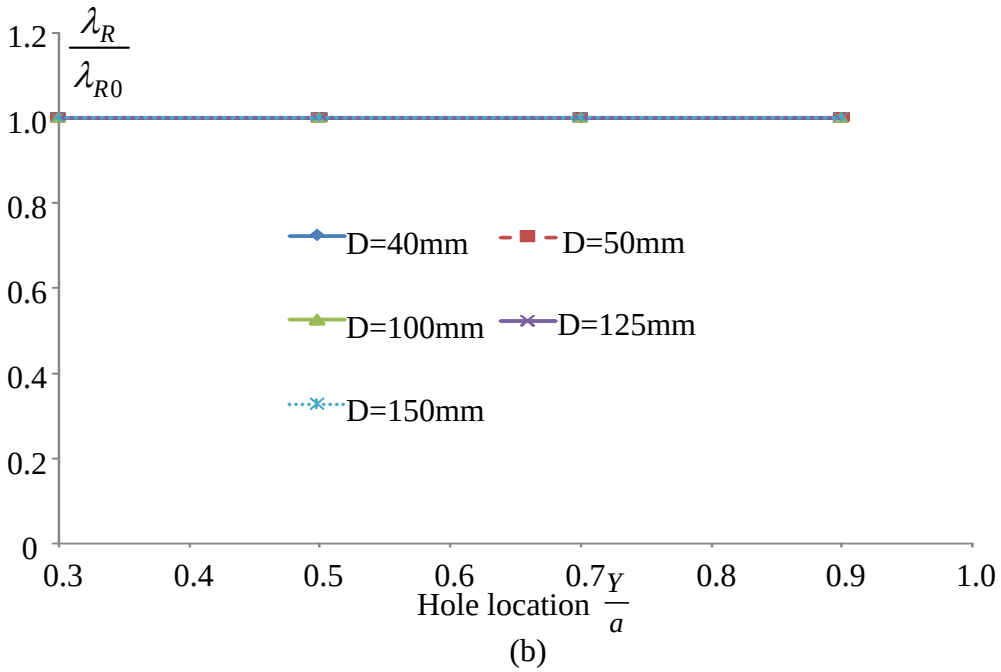

(b)

Figure 7.12 Variation of normalized ratchet limit multiplier with varying vertical hole location at fixed horizontal location ($X / a = -0.1$): (a) for cyclic tensile loading case $(\Delta\sigma_p / 2) / \overline{\sigma}_{po} = 1$ (Figure 7.9a) and (b) for cyclic bending moment case $(\Delta M / 2) / \Delta M_0 = 1$ (Figure 7.9b)

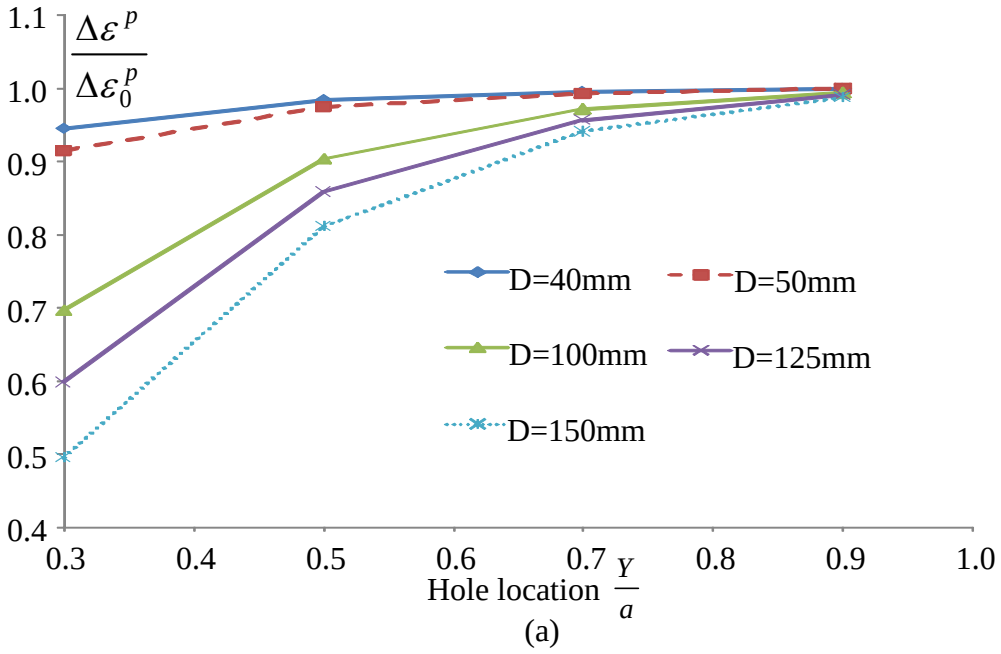

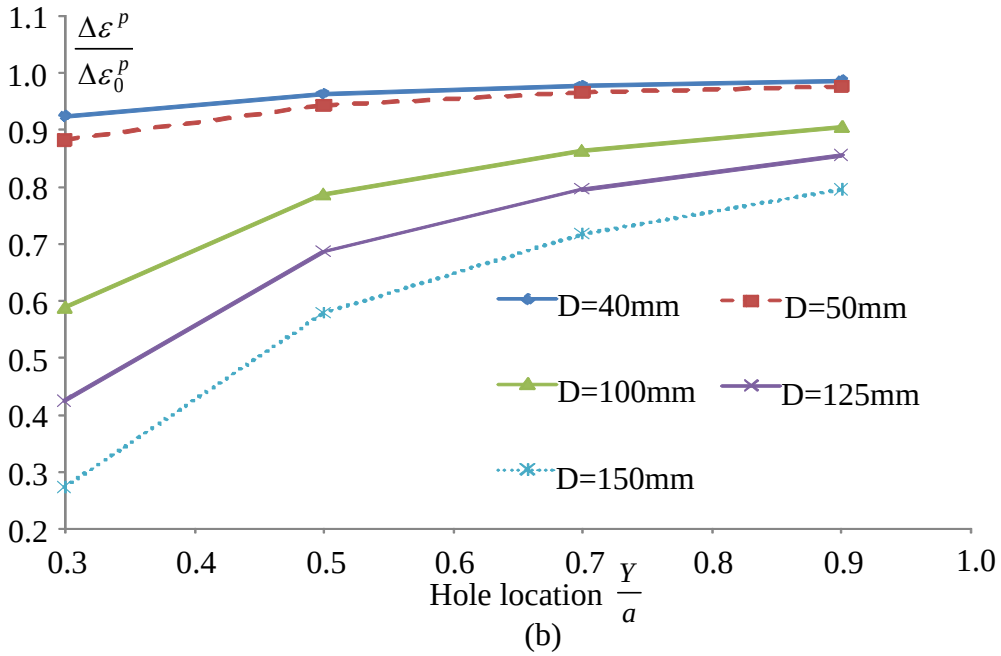

Figure 7.13 Variation of normalized maximum plastic strain range with varying vertical hole location at fixed horizontal location ($X/a = -0.1$): (a) for cyclic tensile loading case $(\Delta\sigma_p/2)/\overline{\sigma}_{po} = 1$ (Figure 7.9a) and (b) for cyclic bending moment case $(\Delta M/2)/\Delta M_0 = 1$ (Figure 7.9b)

7.4.1 The Effect of the Hole Location and Size on Ratchet Limit in Horizontal Direction

The ratchet limit interaction curve for a centre cracked plate with drilled holes of diameter *D*=100*mm* at different horizontal locations (keeping the vertical distance constant at $\frac{Y_0}{a}=0.3$) is shown in Figure 7.9 for both cyclic loading cases. It is observed from Figure 7.9 that at different levels of cyclic tension and bending moment the ratchet limit boundary will always show the trend to sharply decrease as the holes move toward the ligament side (from $\frac{X_0}{a}=0$ to $\frac{X_0}{a}=0.3$) and it will remain almost constant when the holes move from the crack tip to the centre of the plate (from $\frac{X_0}{a}=0$ to $\frac{X_0}{a}=-1$).

Since the above trend of results is valid for any cyclic loading point, in the coming discussions we only consider the results of the ratchet limit and maximum plastic strain range calculated at the cyclic loading point $(\Delta\sigma_p/2)/\bar{\sigma}_{po}=1$ for the cyclic tensile loading case and $(\Delta M/2)/\Delta M_0=1$ for the cyclic bending moment case. The variation of the normalized ratchet limit multiplier λ_R/λ_{R0} for various hole diameters and locations is shown in Figure 7.10a and Figure 7.10b, where the ratchet limit multiplier λ_R, in the Y direction, is normalized with respect to that of a centre cracked plate without holes, λ_{R0}.

It is observed in Figure 7.10a that from point $\frac{X_0}{a}=-1$ ($\frac{Y_0}{a}=0.3$), to point $\frac{X_0}{a}=-0.2$ ($\frac{Y_0}{a}=0.3$), all the ratchet limit multipliers for various hole sizes are nearly having the same value as that in the case without holes, therefore the ratchet limit is unaffected by the presence of the hole within the range of diameters considered here. From location $\frac{X_0}{a}=-0.2$ to location $\frac{X_0}{a}=-0.1$ the normalized ratchet limit multiplier decreases slightly. Beyond hole location $\frac{X_0}{a}=-0.1$ the normalized ratchet limit multiplier falls sharply. This decrease in the figure is shown up to point

$\frac{X_0}{a} = 0.3$. Between hole location $\frac{X_0}{a} = -0.2$ and $\frac{X_0}{a} = -0.1$ in Figure 7.10a, it is shown that the ratchet limit multiplier is decreasing less than 0.1% for diameters 40-50mm, and less than 2% for diameters 100-150mm compared to the case of a centre cracked plate without holes. From location $\frac{X_0}{a} = -0.1$ to location $\frac{X_0}{a} = 0.3$ the drop of the ratchet limit multiplier increases proportionally with the increasing hole diameter.

Figure 7.10b shows the variation of the normalized ratchet limit multiplier with moving holes in horizontal direction for the cyclic bending moment case. It is observed from Figure 7.10b that the holes start to show the effect on ratchet limit multiplier at location $\frac{X_0}{a} = -0.1$ while for the cyclic tensile loading case this effect is observed to start at point $\frac{X_0}{a} = -0.2$. From location $\frac{X_0}{a} = -0.1$ to location $\frac{X_0}{a} = 0.3$, more significant decrease in normalized ratchet limit multiplier is identified at the same hole location when compared with the cyclic tensile loading case.

7.4.2 Effect of Hole Location and Size on Plastic Strain Range in Horizontal Direction

The variation of calculated normalized maximum plastic strain range $\Delta\varepsilon_p / \Delta\varepsilon_{p0}$ for various hole diameters is shown in Figure 7.11, where the maximum plastic strain range $\Delta\varepsilon_p$ in the Y direction is normalized with respect to that of a centre cracked plate without holes, $\Delta\varepsilon_{p0}$.

It is observed in Figure 7.11a that from point $\frac{X_0}{a} = -1$ ($\frac{Y_0}{a} = 0.3$), to point $\frac{X_0}{a} = -0.3$ ($\frac{Y_0}{a} = 0.3$), the maximum plastic strain range is unaffected by the presence of the holes regardless of the hole size. From location $\frac{X_0}{a} = -0.3$ to location $\frac{X_0}{a} = -0.1$ the maximum plastic strain range falls sharply and reaches its minimum at location

$\frac{X_0}{a} = -0.1$. Beyond hole location $\frac{X_0}{a} = -0.1$ there is a drastic increase in the maximum plastic strain range and this increase reaches its maximum at point $\frac{X_0}{a} = 0.1$. Between hole location $\frac{X_0}{a} = -0.3$ and $\frac{X_0}{a} = -0.1$ in Figure 7.11a it is observed that greater reductions in the maximum plastic strain range are given by larger hole diameters. It is also observed in the figure that at location $\frac{X_0}{a} = -0.1$ a hole diameter of 40 or 50mm has little effect on the maximum plastic strain range (causing differences of 1% and 3% respectively). Larger hole diameters at this location have a more significant effect, with differences between 30% and 50% in the maximum plastic strain range observed for diameters between 100mm and 150mm. Beyond point $\frac{X_0}{a} = -0.1$ (as the hole is moving from the crack tip toward the ligament side), the bigger the hole diameter is, the greater the increase of the maximum plastic strain range will be.

Figure 7.11b shows the trend of the maximum plastic strain range for a plate with a hole moving in horizontal direction while the vertical direction is kept constant for the cyclic bending moment case. Compared to the cyclic tensile loading case, the moving holes show a similar effect on the maximum plastic strain range however the hole size has a more profound effect. As for the cyclic tensile case, diameters of 40-50mm show little effect on the maximum plastic strain range (1% and 2%, respectively). Larger hole diameters, however, show a greater effect, with reductions of 40-72% in the maximum plastic strain range resulting from hole diameters of 100-150mm.

It can be seen from Figure 7.10 and Figure 7.11 that the largest decrease in maximum plastic strain range is given by a hole at a distance of $\frac{X_0}{a} = -0.1$ from the crack tip. This hole location of $\frac{X_0}{a} = -0.1$ is considered to be the horizontal optimum location.

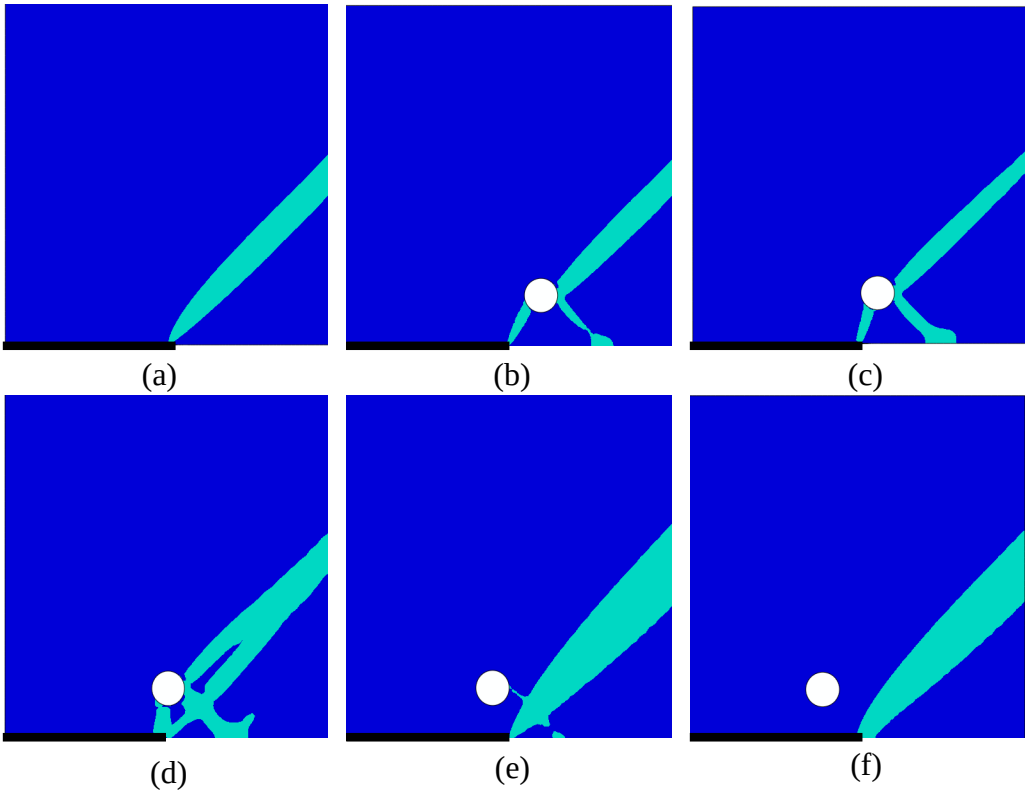

Figure 7.14 Fracture pattern at the limit state for cyclic tensile loading case with different horizontal hole location (fixed vertical location $Y/a = 0.3$) at: (a) without hole; (b) $X/a = 0.2$;(c) $X/a = 0.1$;(d) $X/a = 0$;(e) $X/a = -0.1$ and (f) $X/a = -0.2$

7.4.3 Effect of Hole Location and Size on Ratchet Limit in Vertical Direction

Keeping the horizontal optimum location ($\frac{X_0}{a} = -0.1$) constant, holes are drilled at various vertical locations. The variation of ratchet limit multiplier in different vertical positions for both cyclic loading cases is shown in Figure 7.12a-Figure 7.12b, where the ratchet limit multiplier λ_R in the Y direction is normalized with respect to that of a centre cracked plate without holes, λ_{R0}. It can be seen from these figures that at $\frac{X_0}{a} = -0.1$, the vertical height of the holes have no effect on the ratchet limit multiplier.

7.4.4 The Effect of the Hole Location and Size on Plastic Strain Range in Vertical Direction

The variation of maximum plastic strain range in different vertical positions for both cyclic loading cases is shown in Figure 7.13a-Figure 7.13b, where the maximum plastic strain range $\Delta\varepsilon_p$ in the Y direction is normalized with respect to the one in the case of a centre cracked plate without holes, $\Delta\varepsilon_{p0}$. It is seen in Figure 7.13a that as the holes move in the positive Y direction (Figure 7.1), the maximum plastic strain range increases for the cyclic tensile loading case. From hole location $\frac{Y_0}{a}=0.3$ to $\frac{Y_0}{a}=0.8$ it can be observed that larger hole sizes will give smaller maximum plastic strain range. The normalized value of maximum plastic strain range asymptotically approaches to unity irrespective of the hole size when the holes move away from the crack and after location $\frac{Y_0}{a}=0.7$ the difference between hole sizes becomes negligible. At location $\frac{Y_0}{a}=0.3\,(\frac{X_0}{a}=-0.1)$, the decrease in maximum plastic strain range is maximum, 1% and 3% for diameters 40-50 mm and 30% to 50% for diameters 100 mm to 150 mm. The similar but more significant behavior is observed in the cyclic bending moment case. At location $\frac{Y_0}{a}=0.3$ $(\frac{X_0}{a}=-0.1)$, the decrease in maximum plastic strain range is maximum, 1% and 2% for diameters 40-50 mm and 40% to 72% for diameters 100 mm to 150 mm.

7.4.5 The Optimum Hole Location and Size

It can be concluded from above discussions that the optimum location, where the decrease in maximum plastic range is maximum and the reduction in ratchet limit is minimum, is located at point $\frac{X_0}{a}=-0.1,\ \frac{Y_0}{a}=0.3$. It is also observed that from the hole diameters considered here, a 150mm diameter hole is shown to be the most beneficial. At this optimum hole location and size, the maximum decrease in plastic strain range is 50% and the corresponding ratchet limit is 2%, for the cyclic tensile

case. For cyclic bending, this hole diameter and location gives a 72% reduction in the maximum plastic strain range and does not reduce the ratchet limit.

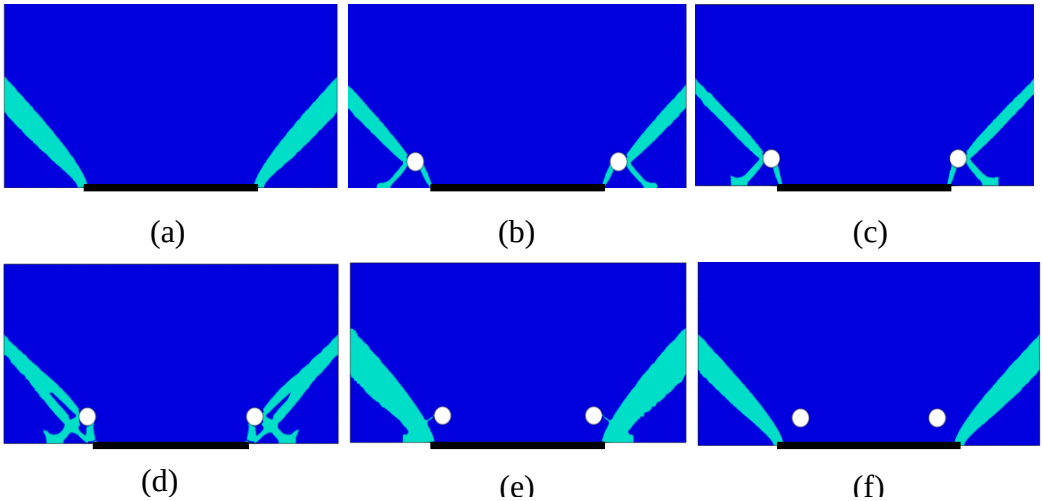

Figure 7.15 Fracture pattern at the limit state for cyclic bending moment case with different horizontal hole location (fixed vertical location $Y/a=0.3$) at: (a) without hole; (b) $X/a=0.2$;(c) $X/a=0.1$;(d) $X/a=0$;(e) $X/a=-0.1$ and (f) $X/a=-0.2$

7.5 Discussions

The above results could be explained by Figure 7.14 and Figure 7.15, which show the failure pattern at the limit state for both cyclic loading cases with various horizontal locations by keeping vertical distance constant at $\frac{Y_0}{a}=0.3$. Both cyclic loading cases have similar failure patterns at the ratchet limit state for the same horizontal location. Figure 7.14a and Figure 7.15a show that without the holes, the failure pattern appears with a 45 degree angle linking from the crack tip to the edge of the plate. When the hole is drilled at the horizontal locations $\frac{X_0}{a}=0.2$, $\frac{X_0}{a}=0.1$ and $\frac{X_0}{a}=0$ (Figure 7.14b-Figure 7.14d and Figure 7.15b-Figure 7.15d) which are within the failure area, the failure pattern at the ratchet limit state becomes discontinuous due to the presence of the holes, which weakens the plate's strength. These are the reasons why the ratchet limit boundary and normalized ratchet limit multiplier are

decreasing in these locations (Figure 7.9 and Figure 7.10). At hole location $\frac{X_0}{a} = -0.1$ (Figure 7.14e and Figure 7.15e), which is just outside the failure area, the stress concentration and stress field produced by the holes interact with that of the crack which reduces the maximum strain range, and also causes a slight reduction on the ratchet limit. When the holes are placed far from the failure area (beyond $\frac{X_0}{a} = -0.2$ in Figure 7.14f and Figure 7.15f), they cause no effect on the failure pattern. That is why the ratchet limit multiplier has the same value as that in the case of a plate without holes and so does the maximum plastic strain range.

7.6 Conclusions

In the present chapter, the effect of circular holes on maximum plastic strain range and the ratchet limit has been studied using the Linear Matching Method which was mentioned in Chapter 5. The LMM has been verified by step-by-step analysis and RIKS analysis in ABAQUS, showing that it gives very accurate ratchet limits for a plate with a centre cracked and symmetrically drilled holes under complex cyclic loading histories. Parametric studies involve holes with different diameters drilled at different locations. The optimum location where the maximum plastic strain range decreases the most with minimum effect on the ratchet limit is located at a distance 10% of the semi-cracked length from crack tip opposite the ligament for both the cyclic tensile loading and cyclic bending moment cases. And it is also observed that the location is independent of hole sizes. The most significant decrease in maximum plastic strain range is observed as 50% with 2% reduction in the ratchet limit, for the hole size D=150mm at the optimum location $\frac{X_0}{a} = -0.1$, $\frac{Y_0}{a} = 0.3$ in the cyclic tension case. For cyclic bending, this hole diameter and location gives a 72% reduction in the plastic strain range and does not reduce the ratchet limit.

The results of this chapter has shown that the LMM numerical procedure is capable to deal with the stress singularities at the crack tip and generate the ratchet limit solutions for a crack component subjected to cyclic loading condition.

CHAPTER 8. EXTENSION OF THE LINEAR MATCHING METHOD TO EVALUATE THE CYCLIC J-INTEGRAL (ΔJ) FOR CRACK COMPONENTS

8.1 Introduction

The results achieved in Chapter 7 has shown that the LMM numerical procedure can address to the stress singularity at the crack tip and can generate ratchet limit solutions for a cracked component subjected to cyclic loading condition. This leads to a one step further research on calculating the crack growth/propagation rate from Fracture Mechanics approach using the LMM numerical procedure, and this research work will be presented in this chapter.

8.1.1 Background

The existence of initial flaws arises during manufacture or heat-treatment of equipment, particularly during welding processes. These flaws cannot be avoided within structure component, since initiated cracks do not lead to instantaneous failure. Failure modes of crack-like flaws differ from industry to industry but a significant proportion of failures results from cyclic loading with high temperature often aided by environmental degradation. One of the examples is the power generation industry which is striving to meet the criteria for clean and sustainable energy production by increasing efficiency while simultaneously decreasing levels of chemical emissions and pollutants. The efficiency of conventional steam and gas turbine power plant can be significantly improved by increasing the operating temperature, leading to reduced fuel consumption and lower levels of harmful emissions. Life assessment approach needs to incorporate innovative and advanced numerical modelling in conjunction with analytical and experimental techniques to ensure operational safety and efficiency of current and future conventional or nuclear plants. With the trend towards higher operating temperatures and the competing need to extend the life of existing power plant, more accurate and reliable numerical

approaches for estimating crack propagation behaviour during a specified operation period due to creep-fatigue damage under high temperature are needed.

Continuum Damage Mechanics (CDM), developed in the last few decades, provides a framework for incorporating the effects of damage induced stiffness softening, anisotropy etc. in constitutive equations. Many CDM models can predict crack initiation and crack growth path direction for complex structures [91] However, there are drawbacks for applying these CDM models. The drawbacks include; (1) the lack of a standardised implementation meaning that careful and lengthy implementation is required; (2) the enormous computational expense required; (3) the model may require implementation of contact elements to simulate the crack closure, thus further increasing complexity; and (4) the models require a large number of material parameters and experimental determination of those parameters [92].

Another method for calculating the crack propagation rates is the Fracture Mechanics approach. Fracture mechanics is a well known approach for predicting the crack propagation and the analysis can be based on linear-elastic or more complex elastic-plastic (nonlinear) models. In 1960, Paris [93] first proposed the Linear Elastic Fracture Mechanics (LEFM) concepts to fatigue crack growth. However, LEFM becomes invalid when the plastic zone at the crack tip is significant in size compared to either the crack length or the remaining ligament of uncracked material. Elastic Plastic Fracture Mechanics (EPFM) can be used to analyze the toughness of materials with large post-yield deformation and it has been shown to better describe the fracture behaviour of ductile materials than LEFM does [71] [94]. In EPFM, the *J*-integral is a parameter that can be used to quantify both the energies consumed in the elastic and plastic deformations of a strained object [95] [96]. *J*-integral calculations have been extensively applied to creep-fatigue crack propagation at high temperatures under cyclic loading for metallic materials. The cyclic *J*-integral was first proposed and implemented by Dowling and Begley [97] as a parameter which correlates with the crack growth rate, *da/dN*. values of ΔJ plotted vs corresponding crack growth rates *da/dN*, on a double logarithmic scale, exhibited power law behaviour similar to the Paris equation [93] so that it is possible to write

$$\frac{da}{dN} = A(\Delta J)^m \tag{8.1}$$

Where A and m are constants found from the least-square regression of data.

The first objective of this chapter is to review the current state of J-integral method under cyclic loading conditions. The methods include (a) contour J-integral method (b) simplified ΔJ method and (c) the load-displacement curve & ASTM standard method. Following this review, a different ΔJ estimate scheme based on a potential energy approach using LMM is presented. This method is capable of describing the crack growth rate behaviour by considering the complete cycle accumulated effects.

This work has been published in the 13th International Conference on Pressure Vessel Technology, London, UK, 2012 [98].

8.2 Review of Δ*J* Method

8.2.1 Contour J integral

The J-integral describes the non-linear behaviour of the material ahead of a crack, and was first developed by Rice [95]. He generalized the energy release rate concept for non-linear materials and calculated it as a path independent line integral, identified as the J-integral, computed along an arbitrary contour around the crack. In [95], the path independent J-integral was defined as

$$J = \int_{\Gamma} (Wn_1 - T_m \frac{\alpha u_m}{\alpha x_1}) ds \tag{8.2}$$

where Γ is a path surrounding the crack tip which begins at the lower crack and ends at the upper face, W is the strain energy density, n_1 is the x_1 component of the outward unit normal to Γ, $T_m=\sigma_{mj}n_j$ is the traction and u_m is the displacement vector, ds is the differential arc length along Γ, and α is a partial derivative of the function u_m with respect to the x_1 coordinate direction. The value of J, obtained under elastic–plastic conditions, was shown to be numerically equal to the strain– energy release rate G (which is analogous to the stress intensity factor K) under fully elastic

conditions [94]. However, the applicability of *J*-integral to cyclic loading ΔJ was being questioned because the deformation theory of plasticity does not account for plasticity effects upon unloading. Due to the fact that the cyclic stress-strain responses related with load processes are nonlinear during Low Cycle Fatigue (LCF), in which J_{min} and J_{max} denote the *J*-integral for the minimum and maximum loading of fatigue are both related to history of loading, so the value of cyclic *J*-integral cannot be simply evaluated by the difference between J_{max} and J_{min}. Since main conceptions of Rice's *J*-integral are not applied directly to fatigue, i.e., cyclic *J*-integral parameter, which is impossibly simple extension of *J*-integral conception, needs to be newly defined. Tanaka et al [99] [100] have defined a ΔJ based on the definition of *J*-integral for monotonic loading and proved that it is independent of integral path through theory of deformation work when deformation energy may be denoted by a single-value function of strain during cyclic loading. The formulation of ΔJ from Tanaka for a standing crack subjected to a remote loading change is defined as:

$$\Delta J = \int_{\Gamma} (\Delta W n_1 - \Delta T_m \frac{\alpha \Delta u_m}{\alpha x_1}) ds \tag{8.3}$$

where Γ is the path on which ΔJ is calculated, ΔW, ΔT_m, and Δu_m, are the changes in strain energy density, traction, and displacement, respectively. However, it is unclear how to choose constitutive relation when Tanaka's ΔJ path is evaluated, and Chow and LU [101] think ΔJ path is a semi-empirical parameter with ambiguous physical reasoning. And, the analysis obtained from a path independent cyclic *J*-integral is rather laborious

8.2.2 GE/EPRI and Reference Stress Method

To obviate the complicated analysis of ΔJ for the fracture analysis of ductile material, the simple ΔJ estimation scheme (popularly known as GE/EPRI and Reference Stress Method-RSM) emerged. It was assumed that the ΔJ is the summation of elastic and fully plastic solutions. The ΔJ based on these two methods required the Ramberg-Osgood coefficient and strain hardening index as basic input to represent material tensile data. The disadvantage here is that Ramberg-Osgood

fitting of the stress-strain curve can be seriously inaccurate, leading to inaccuracy in the estimated J [102] [103]. Additionally, while applying the GE/EPRI schemes for wide variety of test data of different crack geometry with a wide range of material properties, it has been observed that GE/EPRI schemes highly over predict plastic ΔJ in the elastic to fully plastic transition region with respect to the incremental plasticity finite element solutions. Zahoor [104] first pointed out that the over-prediction of J might be as high as 3–7 times depending on the type of material. Similar observations were subsequently made by other researchers [105] [106] [107] as well. In this study, the proposed ΔJ results will be compared with the one produced by the Reference Stress Method (RSM). ΔJ estimated by the RSM for a 2-D cracked plate case in [108] is given by:

$$\Delta J = \Delta\sigma_{ref}\,\Delta\varepsilon_{ref}\,R \tag{8.4}$$

$$R = (\Delta K / \Delta\sigma_{ref})^2 \tag{8.5}$$

$$\Delta\sigma_{ref} = \sigma_y \Delta P / P_L \tag{8.6}$$

Here P_L is the limit load for the cracked geometry, and $\Delta\varepsilon_{ref}$ is the strain range corresponding to $\Delta\sigma_{ref}$ on the material cyclic stress-strain curve, which is given by the description of Ramberg-Osgood equation.

8.2.3 Load-Displacement Curve & ASTM Standard Method

Another simplified ΔJ method was introduced by Dowling and Begley [97] on A533B steels, using an approximation of the J-integral based on the area under load–displacement curves—a simplified model proposed by Rice et al. [109]. Dowling and Begley assumed that ΔJ defines the stress and strain fields near the crack tip only during the loading half of the cycle, which successfully modelled the low cycle fatigue behaviour. This simplified method was further improved by Merkle and Corten [110] and Landes et al. [111]. ΔJ values calculated from load-displacement data were used [112] [113] to correlate fatigue crack growth data in steels. ΔJ was shown to be identical to an energy rate definition similar to the original integral definition of J which can be expressed by the potential energy change with crack growth as,

$$J = -\frac{dU}{Bda} \tag{8.7}$$

Equation (8.7) converted to ΔJ is given by [112] as

$$\Delta J = -\frac{1}{B}\left(\frac{d(\Delta U)}{da}\right) \tag{8.8}$$

Where ΔU is the potential energy, B is the specimen thickness, and a is the crack length. ΔU is given by,

$$\Delta U = \int \Delta P d\delta \tag{8.9}$$

where ΔP is the loading amplitude and δ is the displacement. Thus, ΔU is an important factor in controlling fatigue crack propagation [115] [116] [117].

Sumpter and Turner [118] expanded Equation (8.7) and rewrote it in the following form:

$$J = J_e + J_p \tag{8.10}$$

J_e and J_p are the elastic and plastic components, respectively, of the total J value from monotonic case, and can be expressed by the following equations:

$$J_e = \frac{\eta_e U_e}{B(W-a)} \tag{8.11}$$

$$J_p = \frac{\eta_p U_p}{B(W-a)} \tag{8.12}$$

where U_e, and U_p are the elastic and plastic components, respectively, of the total energy, η_e, and η_p are their corresponding elastic and plastic work factors, (W-a) is the ligament length and W is the specimen width. This unconventional approach to the J-integral, based on the potential energy approach was called ASTM standard method. Equation (8.11) and (8.12) shows that J_e and J_p are a linear function of U_e and U_p.

[119] [120] [121] [122] [123] are the studies that investigated the behaviour of ΔJ with fatigue crack propagation for steels using load-displacement curves methods. It is important to notice that in all the studies mentioned above, ΔJ was calculated for each individual cycle. By adding the plastic contributions to the elastic terms the plastic contributions are calculated using the areas under load–

displacement curves. The accumulated effects over the entire cycle have not been considered numerically. One of the purposes of this chapter is to use the LMM to include these effects for calculating ΔJ.

The load–displacement curves approach (8.8) and ASTM standard methods (8.10)-(8.12) are selected in this study for the cyclic loading case, since the theoretical basis appears to be the best and permits easier processing of empirical data. Thus, the elastic–plastic cyclic *J*-integral is expressed as the summation of elastic and fully plastic solutions for various crack geometry and loading conditions which yields the following formula for estimating the total ΔJ value [102]:

$$\Delta J = \Delta J_e + \Delta J_p \tag{8.13}$$

Equation (8.8) and the form of ASTM show that ΔJ_{e} and ΔJ_{p} are functions of ΔU_{e} and ΔU_{p}, respectively. ie.

$$\Delta J_e = f(\Delta U_e) \qquad \Delta J_p = f(\Delta U_p) \tag{8.14}$$

Where ΔJ_{e} and ΔJ_{p} are the elastic and plastic portion of ΔJ, and ΔU_{e} and ΔU_{p} are elastic and plastic strain energy respectively, as shown in the hysteresis loop of Figure 8.1. Their values will be calculated from LMM by accounting for the cumulative cycle effect.

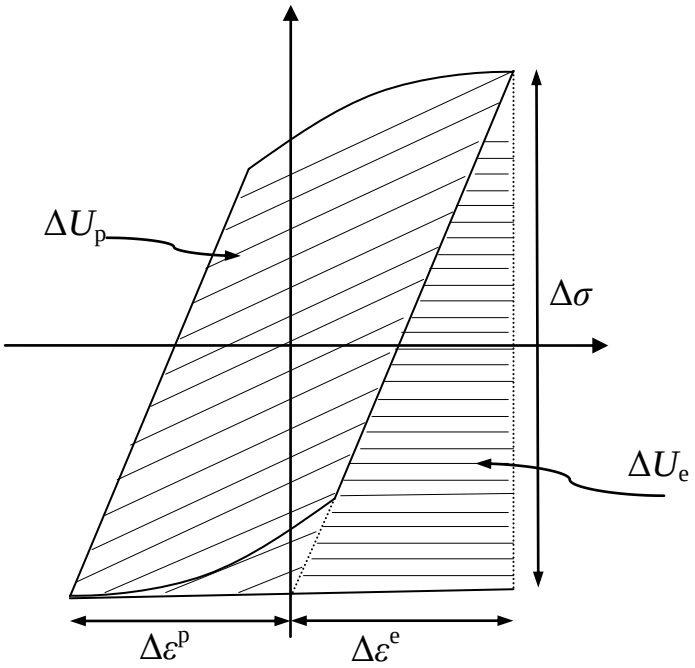

Figure 8.1 Hysteresis loop under cyclic loading case

8.2.4 Linear Matching Method (LMM)

As mentioned in pervious chapters, the LMM is distinguished from the other simplified methods by ensuring that equilibrium and compatibility are satisfied at each stage[5][20][21] [75]. In addition to the shakedown analysis method [20], the LMM has been extended beyond the range of most other direct methods by including the evaluation of ratchet limit [21]. The contribution of this chapter is to link Fracture Mechanics and Continuum Mechanics approaches to each other in order to calculate the ΔJ through the LMM numerical procedure mentioned in Chapter 3 and 5, since it has a capability to evaluate the stable cyclic response: the cyclic stresses, residual stresses, elastic & plastic strain energy and plastic strain ranges for the low cycle fatigue assessment with cyclic load history. By the use of this link, the cumulative cyclic effect of ΔJ can be solved.

In order to provide the energy form of ΔJ predictions, this chapter has been carried out on a single edge crack plate subjected to cyclic tensile and bending loading. This chapter has resulted in the formulation of a ΔJ estimation scheme using LMM which is the subject of coming sections of this chapter. The scope of this chapter was:

(a) to obtain ΔJ_e vs ΔU_e and ΔJ_p vs ΔU_p relationships, using finite element computations, for single edge crack plate under cyclic tensile and bending loading. The crack depth to plate depth ratios (a/W) used are 0.05, 0.075 and 0.1; the material models used are elastic perfectly plastic and Ramberg-Osgood model with the material work hardening exponent, n, with 5, 8 and 20;

(b) to formulate a ΔJ estimation scheme in energy form, based on the finite element results obtained in (a);

(c) to compare and validate the ΔJ estimation with the Reference Stress Method results.

8.3 Numerical Procedures for Defining Elastic and Plastic Energy (ΔU_E and ΔU_P) Through LMM

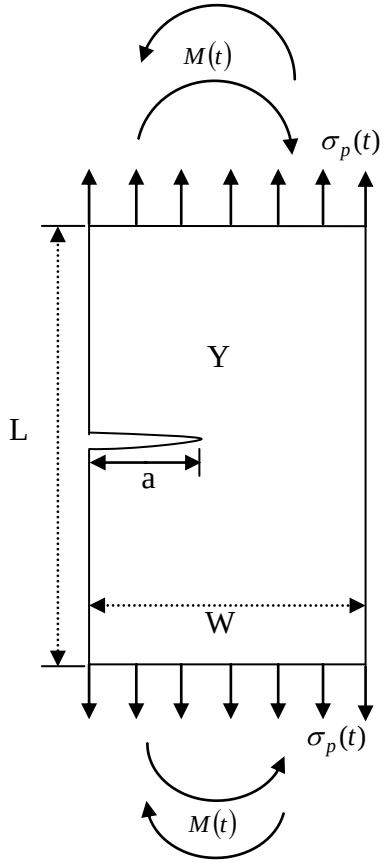

Figure 8.2 Single edge cracked plate subjected to cyclic tensile loading and cyclic bending moment

The numerical procedure in the first stage of minimization process in Chapter 5 is adopted for defining the varying residual stress field and plastic strain range.

The total internal energy range under cyclic loading is given as:

$$\Delta U = \Delta U_e + \Delta U_p \tag{8.15}$$

where ΔU_e represents the linear elastic energy range as:

$$\Delta U_e = \int_V \frac{\Delta \sigma^2}{E} dV \tag{8.16}$$

Where V corresponding to the total volume of the plate, and ΔU_p represent the plastic energy range as:

$$\Delta U_p = \int_{V_p} \Delta\sigma \Delta\varepsilon^p dV \tag{8.17}$$

Here V_p corresponding to the plastic volume of the plate and the value of $\Delta\varepsilon^p$ are obtained from Appendix II.

8.4 Numerical Example

8.4.1 Geometry and Material Model

Table 8.1 Material properties of the steel

Young's modulus E (GPa)	Poisson's ratio ν	Coefficient of thermal expansion α ($°C^{-1}$)	Yield stress σ_y (MPa)
200	0.3	1.11×10^{-5}	700

The geometrical shape and the material properties of the single edge cracked plate are shown in Figure 8.2 and Table8.1 [124], respectively. For a non-linear analysis, the elastic perfectly plastic and Ramberg-Osgood types of material model are adopted in this chapter. The following Ramberg-Osgood type stress-strain relationship for the form of monotonic loading is [80]:

$$\varepsilon = \frac{\sigma}{E} + \frac{\alpha}{E}\left(\frac{1}{\sigma_0}\right)^{n-1}\sigma^n \tag{8.18}$$

where ε is the total strain, σ is the applied stress, E is the elastic modulus, σ_0 is reference stress usually taken as 0.2% yield stress (σ_y), and α and n are the Ramberg-Osgood plastic hardening constants. This can be converted to cyclic behaviour using stress and strain ranges as:

$$\frac{\Delta\varepsilon}{2} = \frac{\Delta\sigma}{2E} + \frac{\alpha}{E}\left(\frac{\Delta\sigma}{2\sigma_0}\right)^n\sigma_0 \tag{8.19}$$

Equation (8.19) could be written as:

$$\Delta\varepsilon = \frac{\Delta\sigma}{E} + 2\frac{\alpha}{E}\left(\frac{\Delta\sigma}{2\sigma_0}\right)^n\sigma_0 \tag{8.20}$$

where $\Delta\sigma$ is the true stress range, and $\Delta\varepsilon$ is the true strain range. At the lower limit, n=1, the above equation represents linear-elastic behaviour, and at the upper limit,

$n=\infty$, it may be representing the elastic-perfectly plastic behaviour. The first term on the right-hand side of the above equation represents the elastic part and the second term represents the plastic part.

Then the plastic strain amplitude from equation (8.20) can be written as:

$$\Delta\varepsilon_p = 2\frac{\alpha}{E}\left(\frac{\Delta\sigma}{2\sigma_0}\right)^n \sigma_0 \tag{8.21}$$

and

$$\alpha = \frac{\Delta\varepsilon_p E}{2\sigma_0}\left(\frac{2\sigma_0}{\Delta\sigma}\right)^n \tag{8.22}$$

In this study the reference stress (σ_0) is taken as 0.2% yield stress (σ_y), where σ_y is defined as half the stress range that results from a strain range of 0.2% in the steady state as:

$$\sigma_y = \frac{\Delta\sigma_{0.2\%}}{2} \qquad \Delta\varepsilon_p = 0.2\% \tag{8.23}$$

From equations (8.20)-(8.22), α could be evaluated with given yield stress (σ_y) as:

$$\alpha = \frac{0.2\%E}{2\sigma_0} \tag{8.24}$$

From equation (8.23)-(8.24) it is important to note that when $\sigma_0=\sigma_y$, α is independent of the Ramberg-osgood plastic hardening constant n.

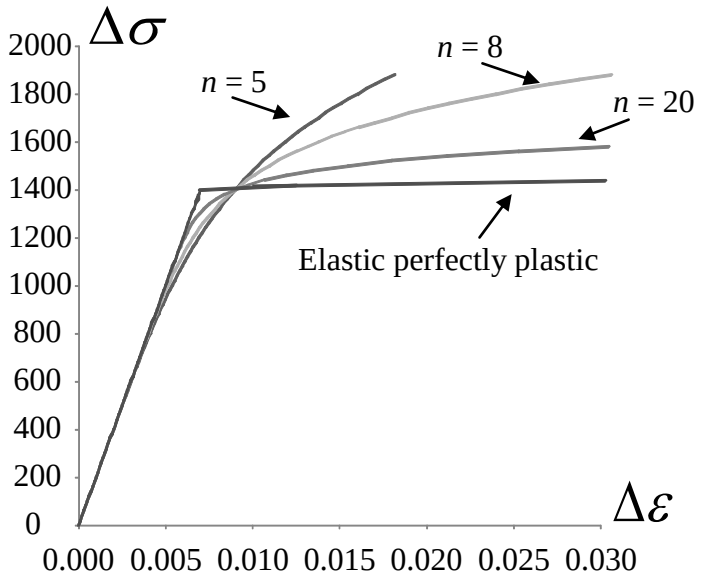

Figure 8.3 The curve of constitutive relation for elastic perfectly plastic and Ramberg-Osgood material model for different hardening n

The elastic perfectly plastic and the Ramberg-Osgood material model with power hardening exponents in equation (8.21) n=5, 8, 20, and the crack length ratio a/W=0.05, 0.075, 0.1 are used to develop the ΔJ estimation scheme and to illustrate the features of the ΔJ vs potential energy curves. All the model has an aspect ratio L/W=4. Figure 8.3 shows the curves of the above mentioned material constitutive relations.

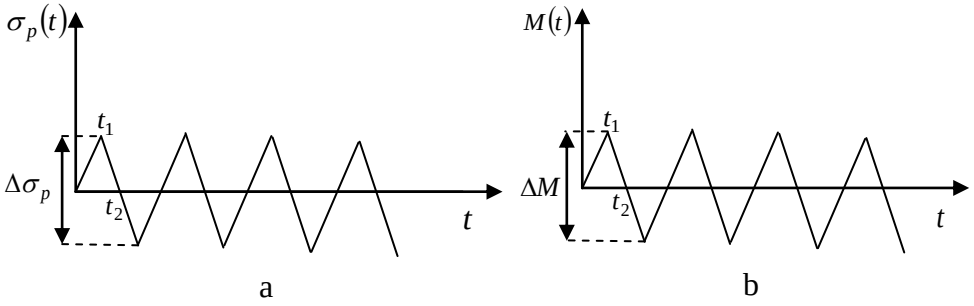

Figure 8.4 (a) The cyclic tensile loading history with tension range $\Delta\sigma_p$ (b) The cyclic bending moment history with reversed bending moment range ΔM

8.4.2 Loading

The single edge cracked plate is subjected to two different cyclic loading cases under plane strain condition. In the first case the plate is under cyclic tension loading and in the second case a cyclic bending moment with reversed bending moment range ΔM is applied to the plate. The detailed cyclic loading histories are given in Figure 8.4, which show a cyclic loading history with two load extremes during each load cycle. For the cyclic tension case (Figure 8.4a), the two extremes of loading history can be formulated as $\sigma_p(t_1)=\Delta\sigma_p/2$ and $\sigma_p(t_2)=-\Delta\sigma_p/2$, respectively, where $\Delta\sigma_p$ represents the tension range. A similar loading history has also been modelled for the cyclic bending moment case (Figure 8.4b), by replacing $\Delta\sigma_p$ with ΔM (the reversed bending moment range). The reference tensile loading range with loading magnitude equal to 100MPa is used in cyclic tension cases. A reference reversed bending moment range, ΔM=10000$N.m$, is used for the cyclic bending moment case.

8.4.3 The Global Finite Element Model

Half-model is required for both cyclic tensile loading and cyclic bending moment cases, as shown in Figure 8.5. In both cases boundary conditions are imposed in the FEM and rigid body motion for the cracked plate is prevented by restraining the two degrees of freedom of the corner node opposite the cracked face. Because the ΔJ consists of energy type terms within a relatively remote boundary encompassing the crack tip, it is not necessary to use special elements to account for the stress singularity at the crack tip. Thus, the analysis is performed using ABAQUS type CPE8R 8 node quadratic quadrilateral elements with reduced integration scheme.

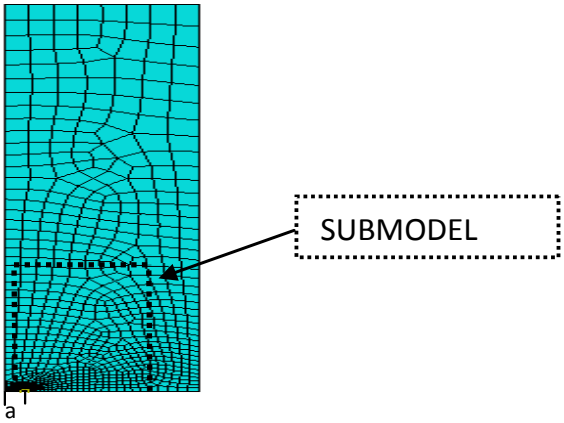

Figure 8.5 Global FEM and relative sub model

Table 8.2 Submodel Sizes

Submodel Size	A_{sub1}/A_{Global}	A_{sub2}/A_{Global}	A_{sub3}/A_{Global}	A_{sub4}/A_{Global}	A_{sub5}/A_{Global}
Cyclic Tensile Loading	0.015	0.05	0.13	0.24	1
Cyclic Bending Moment	0.05	0.1	0.15	0.25	0.5

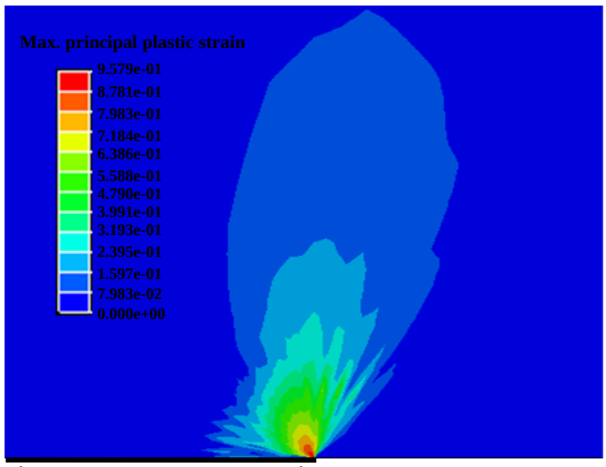

(a)

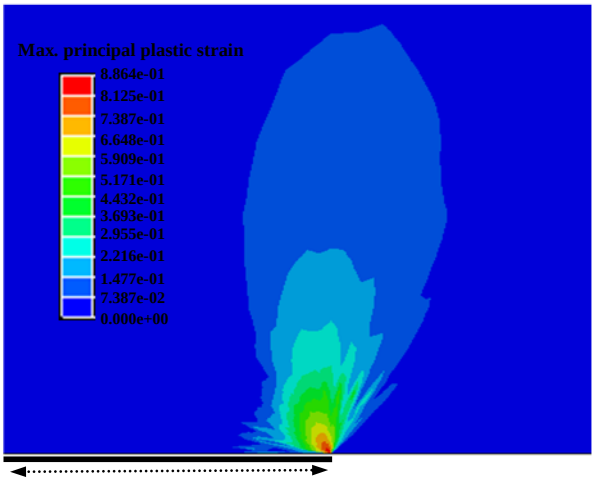

(b)

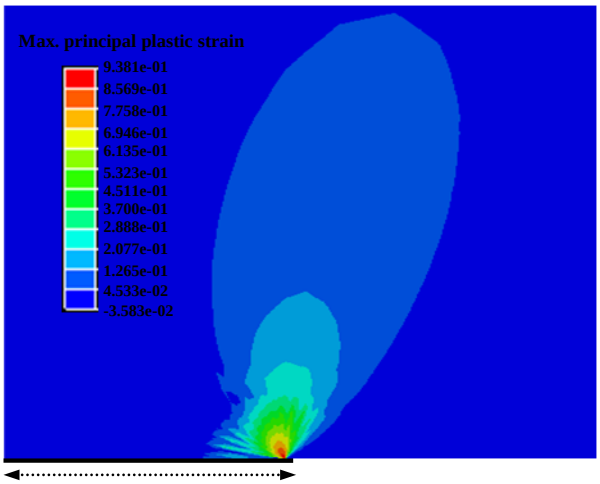

(c)

Figure 8.6 Maximum principal plastic strain for a single edge cracked plate subjected to cyclic tensile loading with $a/W = 0.075$ a)ABAQUS result from monotonic case b)ABAQUS result from step-by-step cyclic loading case c)LMM result for cyclic loading case

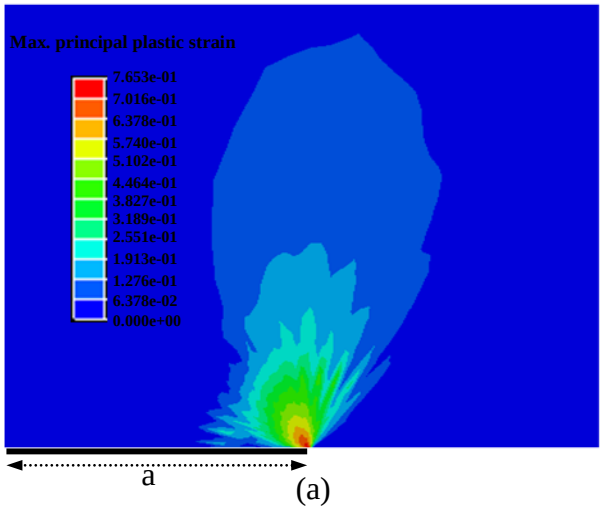

(a)

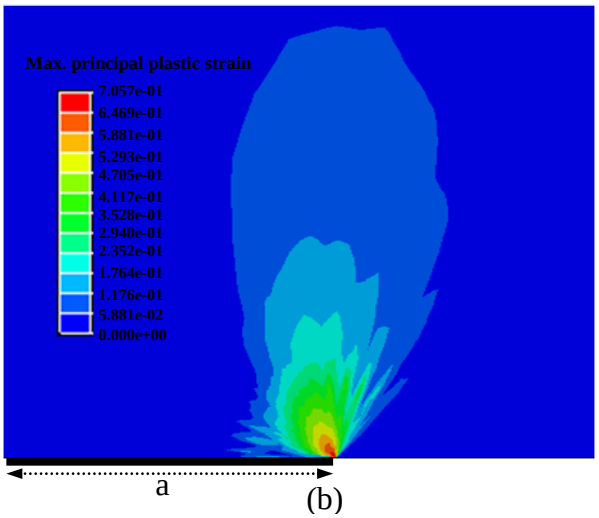

(b)

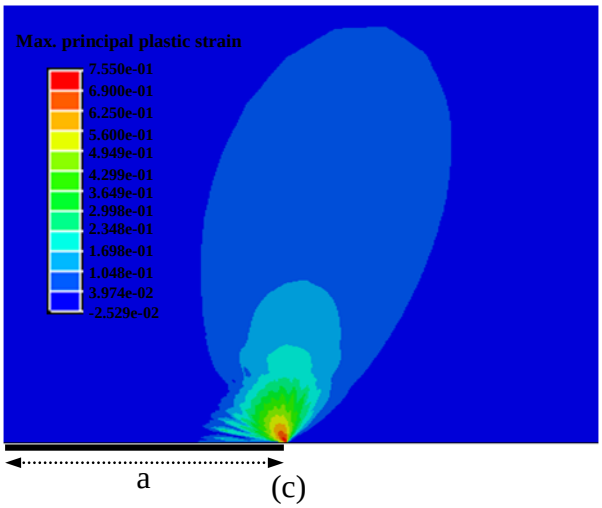

(c)

Figure 8.7 Maximum principal plastic strain for a single edge cracked plate subjected to cyclic bending moment with a/W = 0.075 a)ABAQUS result from monotonic case b)ABAQUS result from step-by-step cyclic loading case c)LMM result for cyclic loading case

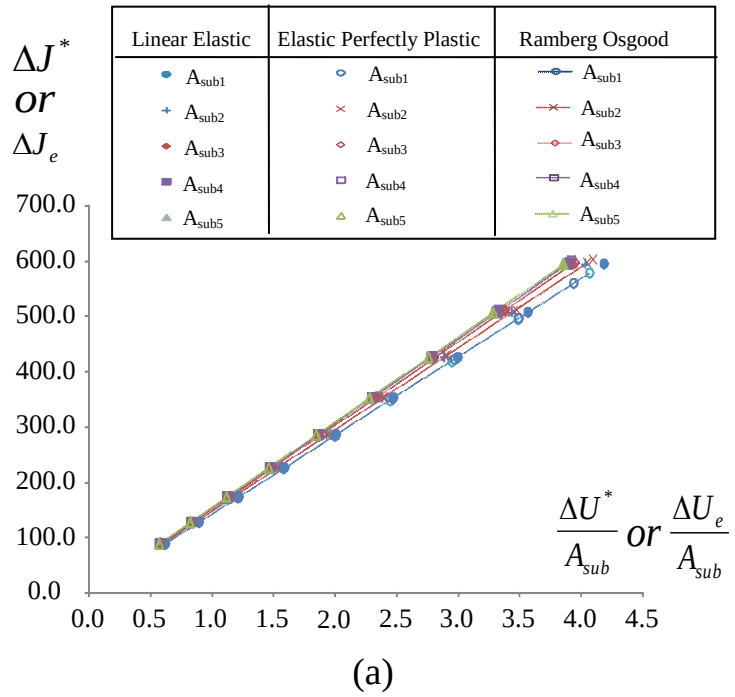

(a)

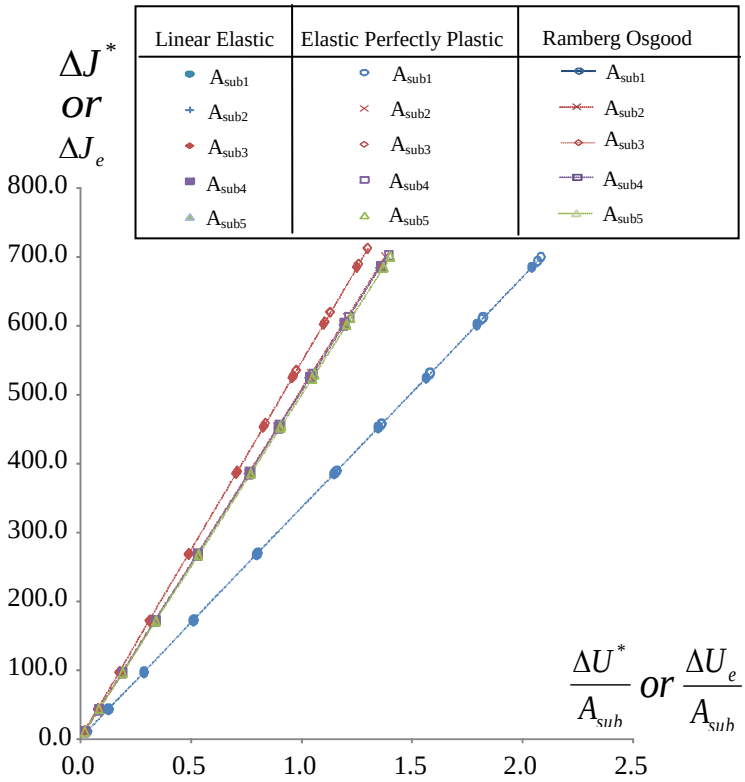

(b)

Figure 8.8 The relationship between elastic cyclic *J* and elastic energy rate with different types of material model and submodeling size ratio (a) Cyclic tensile loading case (b) Cyclic bending moment case

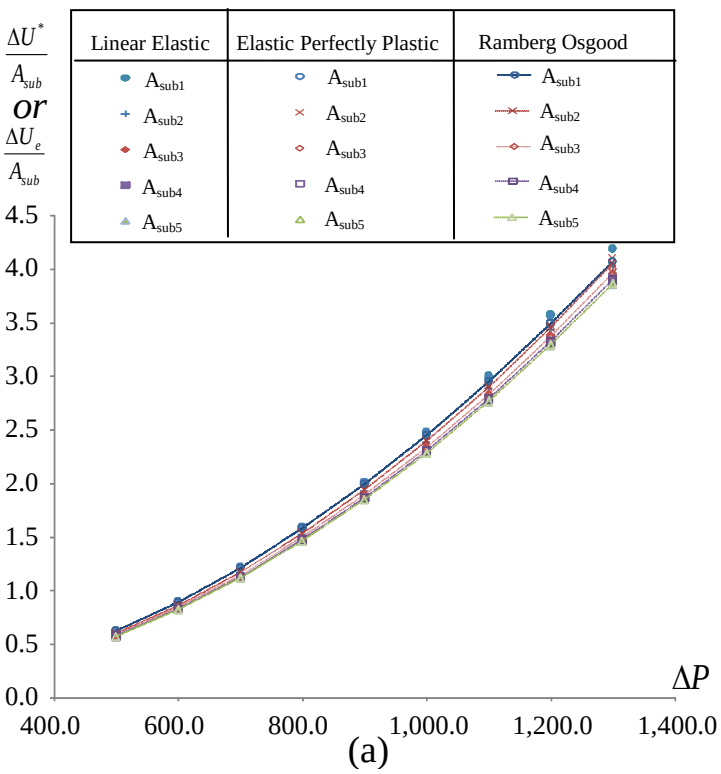

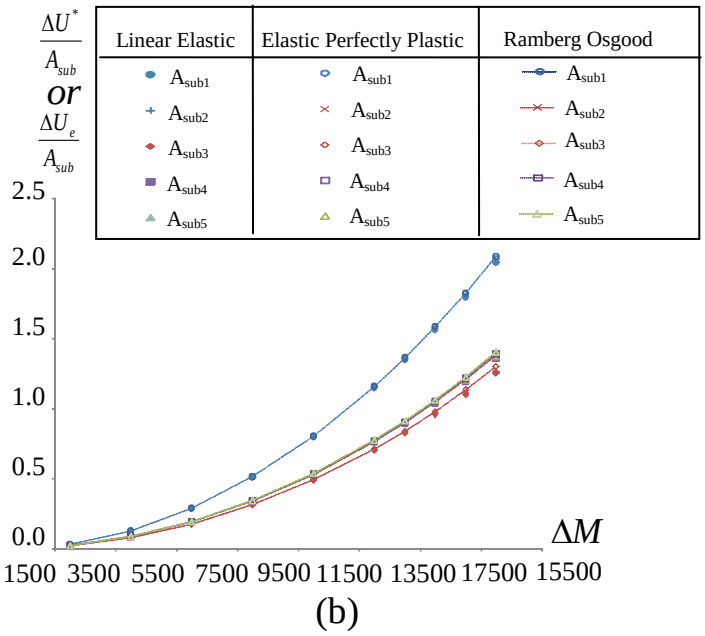

Figure 8.9 The relationship between elastic energy rate and applied loading for different types of material model and submodeling size ratios (a) Cyclic tensile loading case (b) Cyclic bending moment case

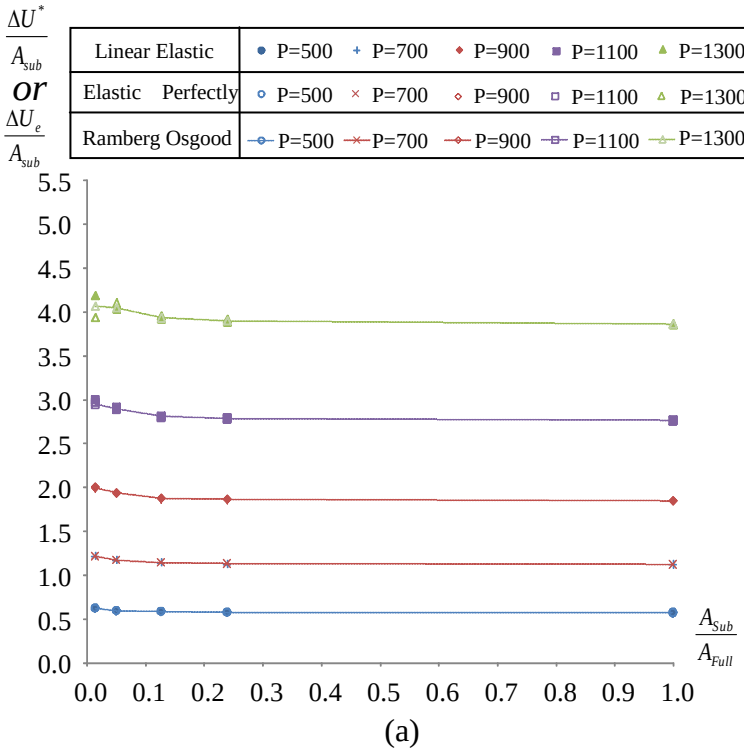

(a)

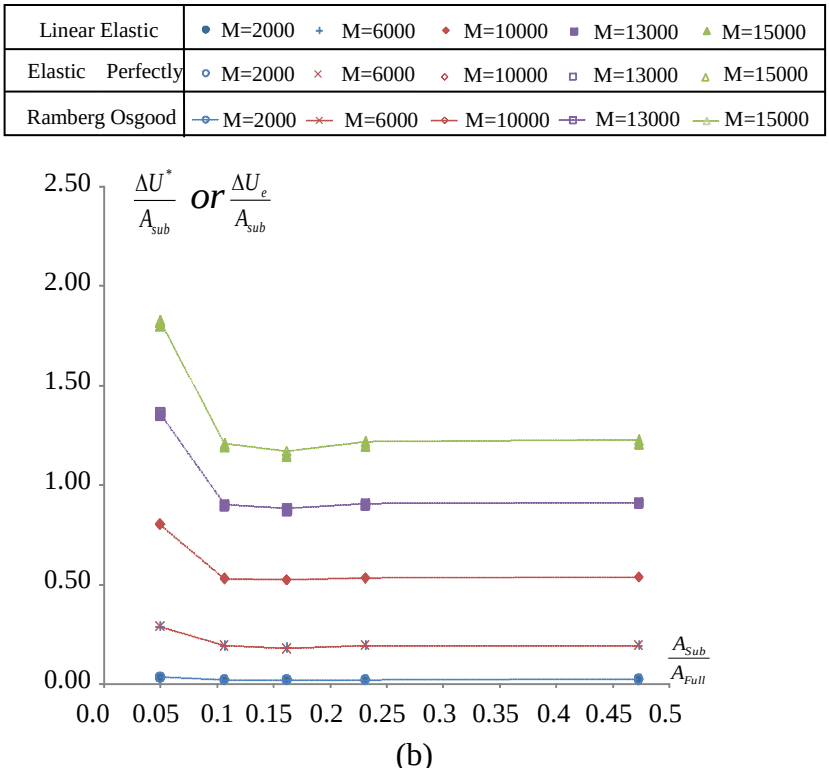

(b)

Figure 8.10 The relationship between elastic energy rate and submodelling size ratio for different types of material model with all loads up to limit load (a) Cyclic tensile loading case (b) Cyclic bending moment case

8.4.4 The Submodelling

Recently, the submodelling technique has often been used in the FE numerical analysis to study in detail an area of interest in a model. Herein, the area of interest is the region of high stress caused by the individual crack as shown in Figure 8.5. The main idea of the submodelling technique is to perform a global-local transition. This approach gives an opportunity to make a local mesh refinement. As the submodel region has a finer mesh, a submodel can provide an accurate, detailed solution. Besides better accuracy, another advantage is that one can avoid the other high stress fields caused by other stress riser, i.e. boundary conditions. In order to investigate the dependence of the cyclic *J*-integral results on the submodel size, five different submodel size ratios are considered for both cyclic loading cases (Table 8.2).

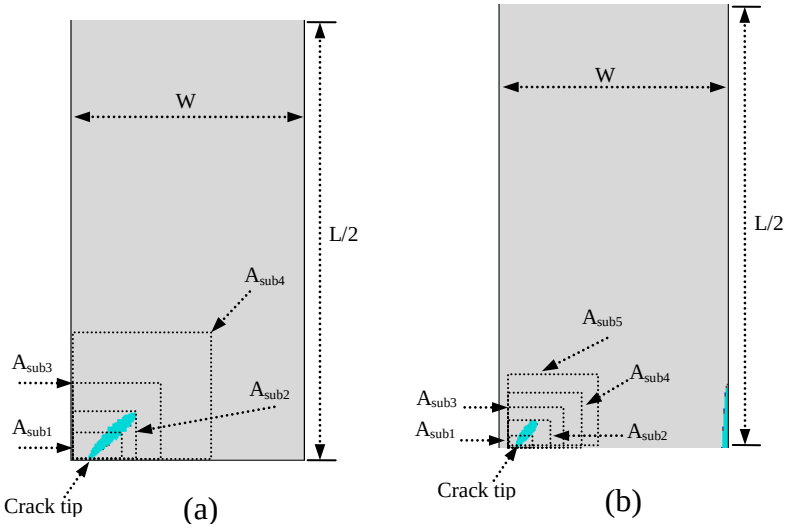

Figure 8.11 The equivalent plastic strain range with different submodelling sizes for elastic perfectly plastic material model (a) Cyclic tensile loading case at P=1100 Mpa (b) Cyclic bending moment case M=1300N.m

8.5 An Analysis of Energy Form Expression for Δ*J*

In this section the derivation of a Δ*J* expression from FEA simulations is presented. The *J* value provided from ABAQUS is composed of elastic, J_e, and plastic, J_p, parts. However, these values provided by ABAQUS are only valid for the monotonic loading case, and there is no Δ*J* value accounting for the cyclic loading

case from ABAQUS. A reasonable approximation to obtain the values of ΔJ can be achieved by performing a monotonic loading calculation, but with σ_y replaced by $2\sigma_y$ [96] [99] [125]. This conclusion was also examined by Chen at al. [76] discovering that in an un-cracked body subjected to variable loading conditions, the variations between such monotonic loading solution with an equivalent cyclic solution, measured after a reasonable number of loading cycles, is relatively small. The above assumption could be explained by Figure 8.6-Figure 8.7, which show the maximum principle strain range for cyclic tensile loading and cyclic bending moment cases with a/W=0.075 and submodel size A_{sub4}, respectively.

It is observed from Figure 8.6 and Figure 8.7 that both monotonic and cyclic loading cases have similar maximum principal plastic strain range at the crack tip when cyclic tensile loading and cyclic bending moment cases are considered. Then using such an assumption, ΔJ value for two-dimensional elastic-plastic finite element analyses under fatigue loading were then identified or replaced by the J-integral value for the monotonic loading by employing the finite element package ABAQUS.

From Figure 8.6b-Figure 8.6c and Figure 8.7b-Figure 8.7c, it is observed that when considering the monotonic loading case the LMM solutions are better results than the step-by-step cases provided from ABAQUS. The reason for the poorer result from the step-by-step inelastic analysis may be since while conducting the analysis the cyclic response values do not reach the steady cyclic state. Past investigations have revealed that the conduction of such solutions requires relatively long analysis times. From these figures, it is also observed that the LMM gives a smoother contour plot result compared to the step-by-step one. Such contor plot in Abaqus/CAE may be due to the type of element used on the crack tip. In the following sections, the relationship between ΔJ_e, ΔU_e and ΔJ_p, ΔU_p will be introduced.

8.5.1 Formulation of ΔJ_e using Submodelling

The elastic portion, ΔJ_e, can be calculated from the relationship between ΔJ^* and $\Delta U^*/A_{sub}$, where ΔJ^* and $\Delta U^*/A_{sub}$, represent the cyclic J-integral and potential energy rate from linear elastic material model, respectively.

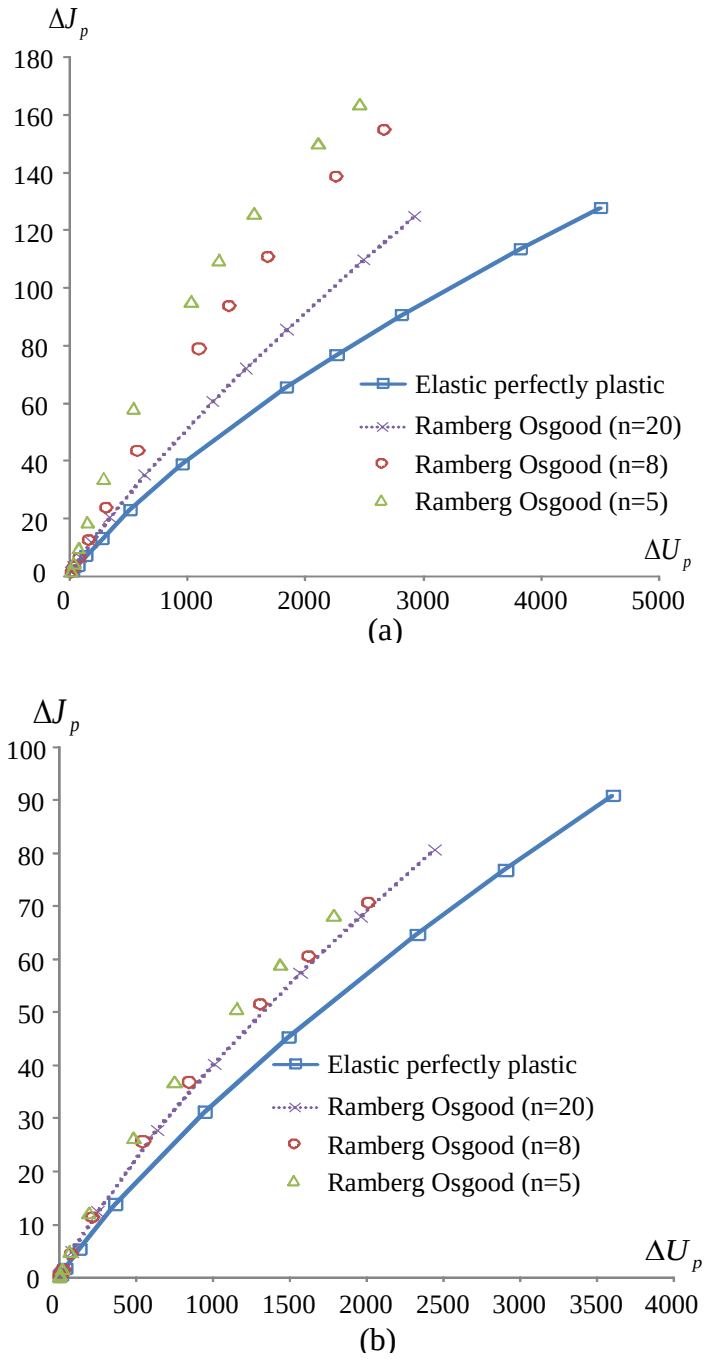

Figure 8.12 The relationship between plastic cyclic J and plastic energy for different types of material models (a) Cyclic tensile loading case (b) Cyclic bending moment case

8.5.1.1 The relationship between ΔJ* and ΔU*/Asub

It is observed from Figure 8.8 that ΔJ^* is a linear function of $\Delta U^*/A_{sub}$ for the linear elastic material model, which is independent of loading type and the submodel sizes. This relationship can be formulated as:

$$\Delta J^{*} = C\frac{\Delta U^{*}}{A_{sub}} \tag{8.25}$$

where C is the rate at which ΔJ^{*} increases with the elastic energy rate $\Delta U^{*}/A_{sub}$.

8.5.1.2 The Relationship of ΔU*/Asub and ΔUe /Asub using Submodelling

Before calculating ΔJ_e for the inelastic material model by applying the same formulation as the one used for ΔJ^{*}, the values of $\Delta U^{*}/A_{sub}$ and $\Delta U_e/A_{sub}$ are being compared with elastic perfectly plastic and Ramberg-Osgood material models, where $\Delta U_e/A_{sub}$ is the elastic potential energy rate as in the inelastic material model. The influence of applied loads on the elastic potential energy rate for both cyclic loading cases is shown in Figure 8.9 for different material models and submodel size ratios. It is observed from Figure 8.9 that the values of $\Delta U^{*}/A_{sub}$ and $\Delta U_e/A_{sub}$ are the same and are not affected by the types of material models and loadings for the same submodel size and with all load levels up to the limit load. As it may be observed from Figure 8.8-Figure 8.9 the results of the elastic portion of cyclic *J* and potential energy rate obtained by the submodel size equal to A_{sub1} deviate significantly when compared to other submodel sizes. This phenomenon could be explained by Figure 8.10 and Figure 8.11.

Figure 8.10 shows the values of $\Delta U^{*}/A_{sub}$ and $\Delta U_e/A_{sub}$ with the increasing submodel size from A_{sub1} to A_{sub5} and with different applied loading. Figure 8.11 shows the equivalent plastic strain range with different submodel sizes and with the applied loading *P*=1000Mpa and *M*=1000N.m for cyclic tensile loading and cyclic bending moment cases, respectively.

It is observed from Figure 8.10 that the results of elastic strain energy rate from the submodel sizes A_{sub1} and A_{sub2} have different values than the other submodel sizes' results. These differences become larger with the increasing applied loading when compared to the other submodel sizes. As observed from Figure 8.11, for the load levels equal to 85% of limit load, the submodel sizes equal to A_{sub1} and A_{sub2} is not sufficiently large to cover the plastic strains zone occuring on the global model for both cyclic loading cases. The values of $\Delta U^{*}/A_{sub}$ and $\Delta U_e/A_{sub}$ are stabilized for

the submodel size equal to A_{sub3}-A_{sub5} (Figure 8.10) for the load levels up to the limit load, since these sizes cover the plastic strains zone caused by the individual crack (Figure 8.11).

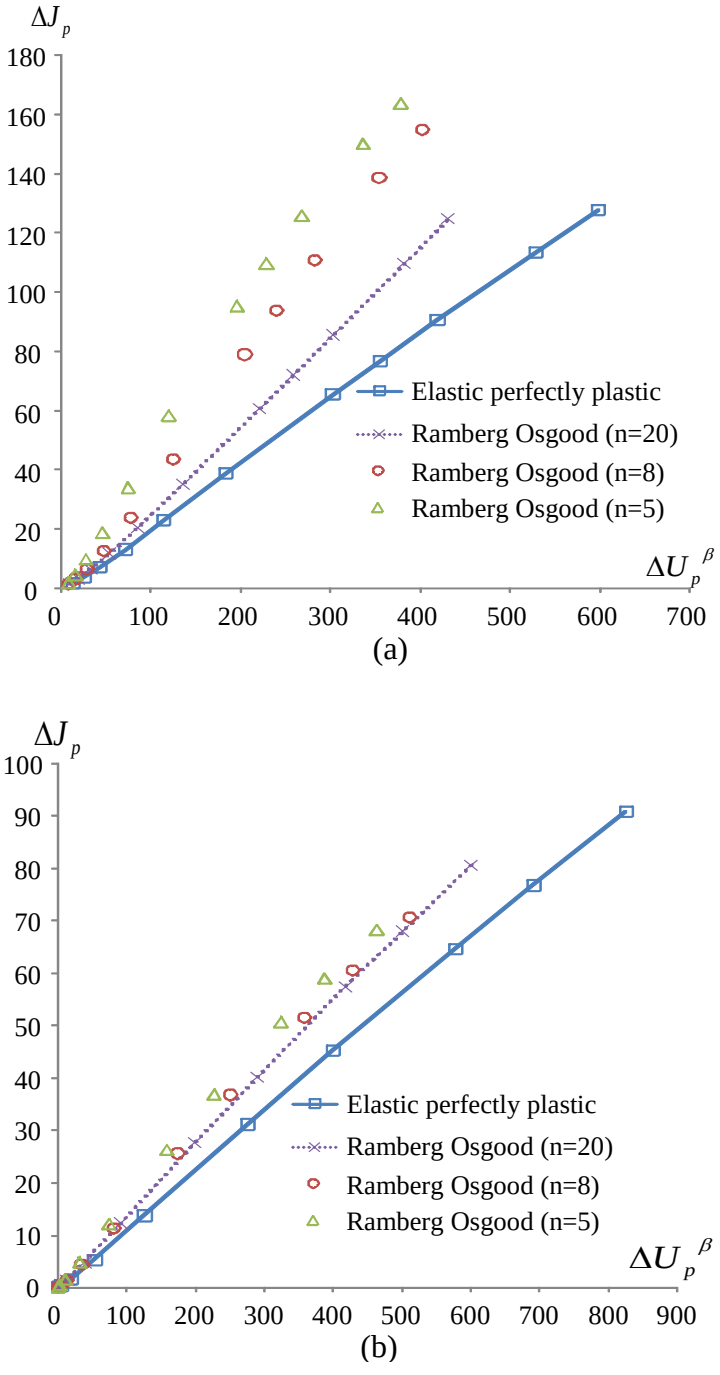

Figure 8.13 The relationship between plastic cyclic J and plastic energy for different types of material model with β=3/4 (a) Cyclic tensile loading case (b) Cyclic bending moment case

Figure 8.10a-Figure 8.11a also shows that for the cyclic tensile loading case, the elastic potential rate is stabilized for the range of submodel size ratio (A_{sub} /A_{Global}) from 0.13 to 1. However, for the cyclic bending moment case, there is no stabilization solution of the elastic potential rate for the submodel size ratio close to 1, because, as mentioned in section 8.5.4, the advantage of the submodelling is that other high stress fields caused by other stress risers can be avoided. There is a high stress concentration caused by the boundary conditions (Figure 8.11b). For more accurate solutions, a submodel size boundary should not be chosen close to 1, for the cyclic bending moment case.

8.5.1.3 The Submodelling Boundary

It can be concluded from the above results that for the single edge cracked plate under cyclic tensile loading and cyclic bending moment cases, submodel's boundaries should be taken far from the crack tip, so that the stress field in the boundary is completely unaffected by the crack. This means that selected boundary should be able to surround the plastic zone completely, ie, including the total plastic energy ΔU_p caused by the individual crack only.

8.5.1.4 The relationship between ΔJ_e and $\Delta U_e /A_{sub}$

From the relationship between $\Delta U^*/A_{sub}$ and $\Delta U_e/A_{sub}$, the elastic portion, ΔJ_e from the inelastic material model can be calculated using the linear solution C and the elastic energy ΔU_e from elastic-plastic solution as:

$$\Delta J_e = C\frac{\Delta U_e}{A_{sub}} \tag{8.26}$$

Equation (8.26) is established on the assumptions that ΔJ_e is a linear function of ΔU_e /A_{sub} (Figure 8.8), and C is the slope of the lines calculated from the linear elastic material. This equation is independent of the material model and loading type that is considered in this study.

8.5.2 Formulation of ΔJ_p

The plastic portion, ΔJ_p, can be expressed in terms of ΔJ and ΔJ_e as:

$$\Delta J_p = \Delta J - \Delta J_e \tag{8.27}$$

As described in the previous section, the submodelling boundary should include the plastic zone induced by the crack. Therefore, the value of ΔU_p for the individual crack is independent of these submodelling sizes. The variation of ΔJ_p with ΔU_p for elastic perfectly plastic and Ramberg-Osgood material model with the applied loading up to limit load is shown in Figure 8.12. It can be seen from Figure 8.12b that the curves for Ramberg-Osgood model with n=8 and n=20 are nearly coincident. Figure 8.12 also shows that, the increase in ΔJ_p values for Ramberg-Osgood and elastic perfectly plastic material models seems to have a linear variation with increasing ΔU_p. By plotting ΔJ_p against the power formulation of ΔU_p^{β} for a/W=0.075 (Figure 8.13) an approximate linear relationship is established which can be expressed as:

$$\Delta J_p = D(\Delta U_p)^{\beta} \tag{8.28}$$

where D, represents the slope of the lines in Figure 8.13. The power index β is included to form the linear relationship of ΔJ_p, and is a function of loading and material model. In Figure 8.13 β is chosen as 3/4 for all inelastic material model that are considered in this study for both cyclic loading cases. As well known, if the plastic zone size is less than about 10% of the crack length, small-scale yielding conditions exist around the crack tip. Figure 8.14 shows variation of ΔJ_p with ΔU_p^{β} (with β=1) for different inelastic material models with the plastic zone size up to 50% of the crack length for both cyclic loading cases. It is observed from Figure 8.14 that ΔJ_p is a linear function of ΔU_p^{β} (with β=1) for both cyclic loading cases for different inelastic material models. Therefore, within the region of the plastic zone with size up to 50% of the crack length equation (8.28) can be rewritten as,

$$\Delta J_p = D(\Delta U_p)^{1} \tag{8.29}$$

Equation (8.29) has the same form as equation (8.12), which is established on the assumptions that ΔJ_p is a linear function of ΔU_p.

8.5.3 Formulation of *ΔJ*

It can be concluded from the above discussion that for the single edge cracked plate under cyclic tensile loading and cyclic bending moment cases, the cyclic J integral, ΔJ, can be expressed as,

$$\Delta J = C\frac{\Delta U_e}{A_{sub}} + D(\Delta U_p)^{\beta} \tag{8.30}$$

where β=1 for plastic zone size up to 50% of the crack length

Equation (8.30) is independent of the material model, type of loading, and the submodelling sizes which boundary is cover the plastic zone induced by the crack only, that considered in this study for single edge crack plate.

The form of the general functions *C*, *D* and β will be discussed in the coming sections and their formulations are determined for a single edge crack plate subjected to cyclic tensile loading and cyclic bending moment cases.

8.6 The General Functions of *C*, *D* and β

The proposed Δ*J* equation in section 8.6 sums the elastic and plastic contributions in terms of energy. Equation (8.7)-(8.12) are the basic idea for the proposed Δ*J* equation. The investigation indicates the fact that there is a linear relationship between ΔJ_e and ΔU_e, and ΔJ_p and ΔU_p for the plastic zone size up to 50% of the crack length for 2*D* case. Further work is needed to see whether this relationship is applicable for the 3*D* case. Several form investigations were required to find the form which describes the dependence of *C* and *D*.

8.6.1 The General Form of Variables C and D

According to the ASTM standard Δ*J* should have the unit of Joules/area. Therefore, *C* is a dimensionless function, and *D* is a per unit area function which depends on the material model hardening, types of loading, and crack length ratio.

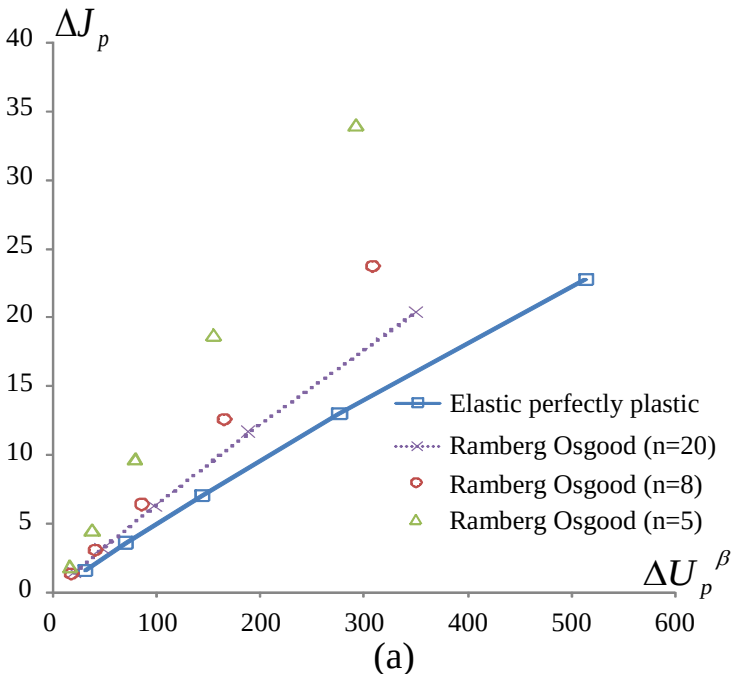

(a)

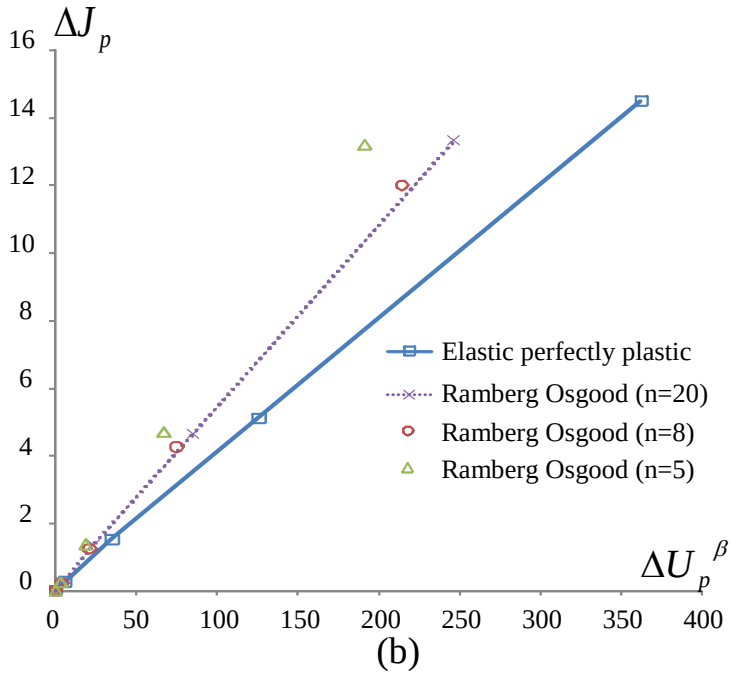

(b)

Figure 8.14 The relationship between plastic cyclic J and plastic energy for different types of material model with β=1 (a) Cyclic tensile loading case (b) Cyclic bending moment case

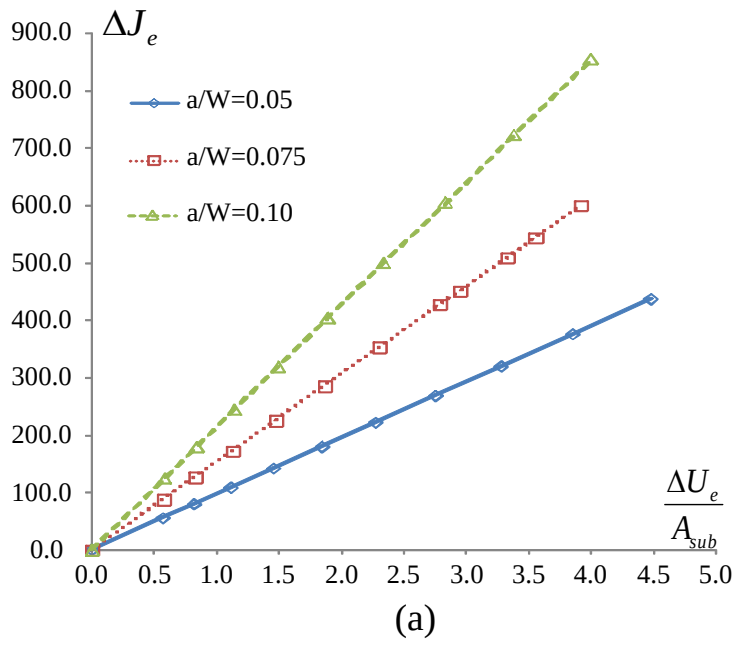

(a)

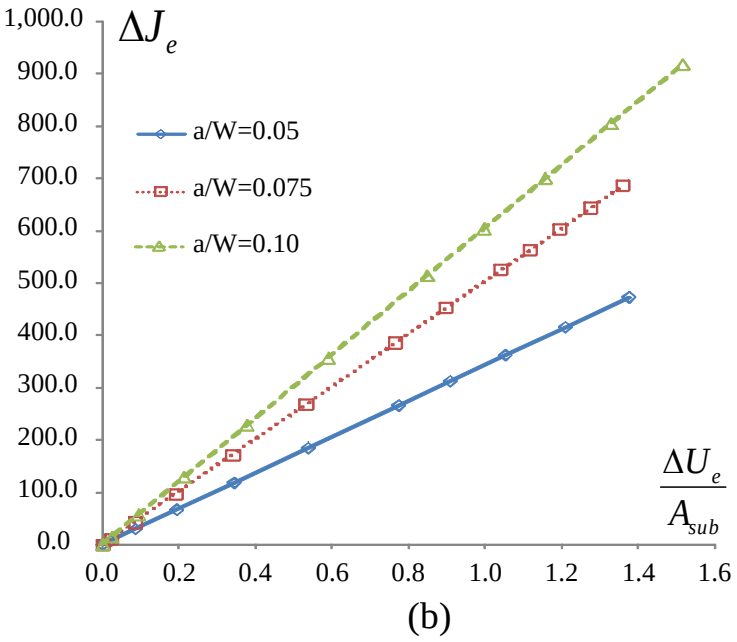

(b)

Figure 8.15 The relationship between ΔJ_e and $\Delta U_e/A_{sub}$ for elastic perfectly plastic material model with different crack size ratio (a) Cyclic tensile loading case (b) Cyclic bending moment case

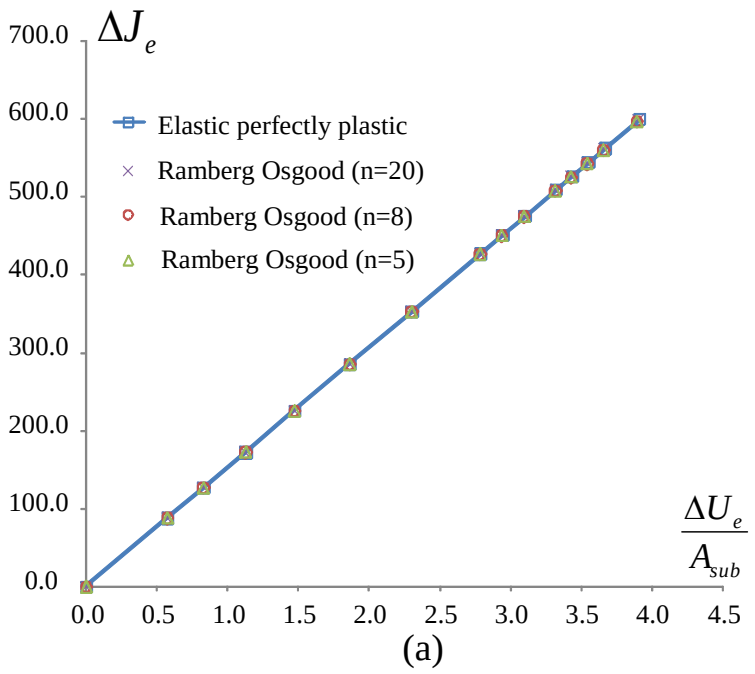

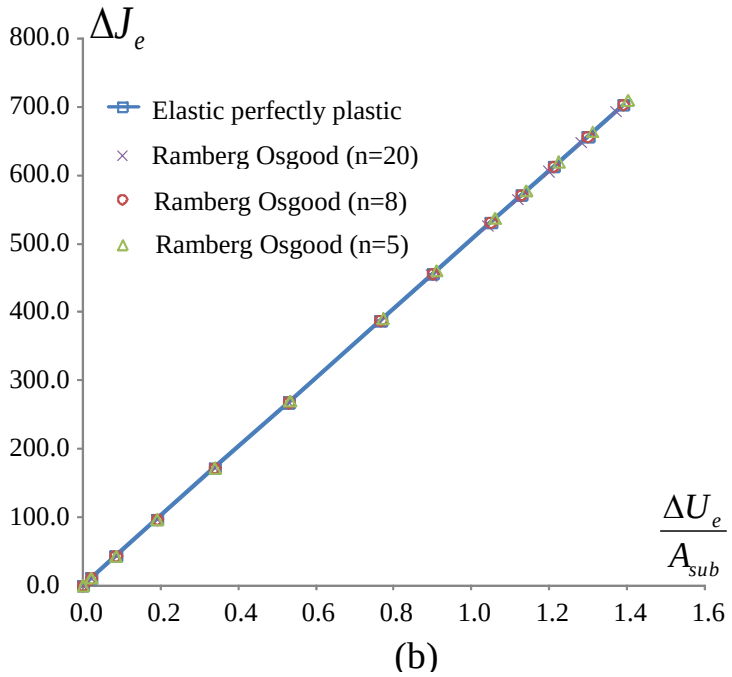

Figure 8.16 The relationship between ΔJ_e and $\Delta U_e/A_{sub}$ for different material constitutive models with a/W=0.075 (a) Cyclic tensile loading case (b) Cyclic bending moment case

8.6.2 The General Form of Variable β

β is equal to one. This will be strictly fulfilled for the small scale yielding condition in all types of 2D crack plates and even for the large scale yielding

condition when the plastic zone size is up to 50% of the crack length, under cyclic tensile loading and cyclic bending moment. β may be a function of the type of the material model when the plastic zone size is greater than 50% of crack length.

For other material types, the constants presented are not generally applicable. The procedure described in the study must be repeated to obtain values of the constants, namely C, D and β.

8.7 Proposed ΔJ Estimation for Single Edge Cracked Plate

8.7.1 Determination of C

In order to determine the formulation of function C from the ΔJ_e values, the variation of ΔJ_e with $\Delta U_e/A_{sub}$ for three a/W ratios with elastic perfectly plastic material model and for different inelastic material model with a/W=0.075 are examined by plotting ΔJ_e against $\Delta U_e/A_{sub}$ respectively as shown in Figure 8.15 and Figure 8.16. In Figure 8.15 and Figure 8.16 the size of the submodel is equal to A_{sub4} for both cyclic loading cases. It is observed from Figure 8.15 and Figure 8.16 that the dimensionless parameter C is independent of the inelastic material model, and is a function of a/W ratio and loading type only. Therefore, slope C is a function of f(a/W) and is formulated as,

$$C = f\left(\frac{a}{W}\right) \tag{8.31}$$

where $f(a/W)$ is the influence function for the crack ratio range.

In order to find this influence function, the slope of ΔJ_e is replotted in graphs of function $f(a/W)$ against a/W, for both cyclic loadings as shown in Figure 8.17. Trend lines are fitted to the data obtained from the ΔJ_e results for different crack ratios to show the influence function. Equation (8.32) is the obtained influence function for the slope C.

$$f\left(\frac{a}{W}\right)=\begin{cases}2314\left(\frac{a}{W}\right)-19.11 & (\textit{for cyclic tensile loading})\\ 5220\left(\frac{a}{W}\right)+92.16 & (\textit{for cyclic bending moment})\end{cases} \tag{8.32}$$

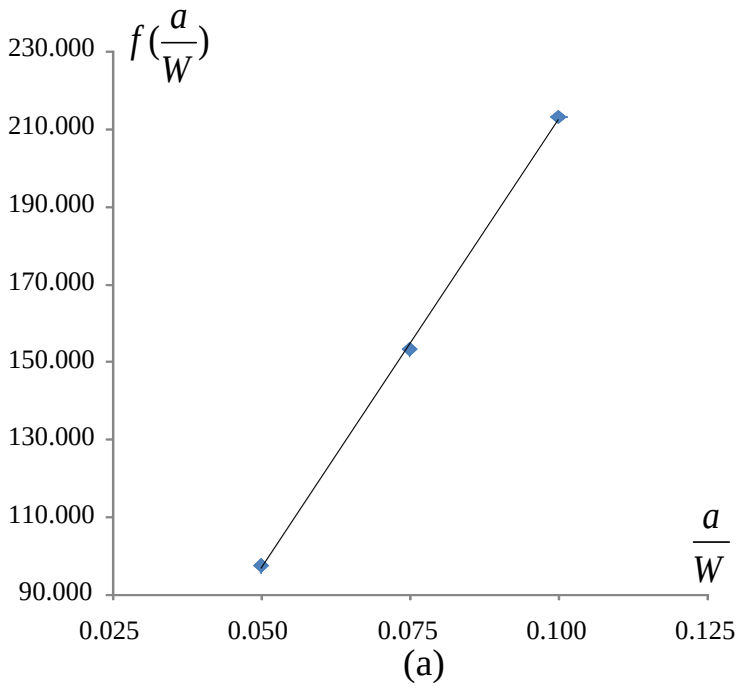

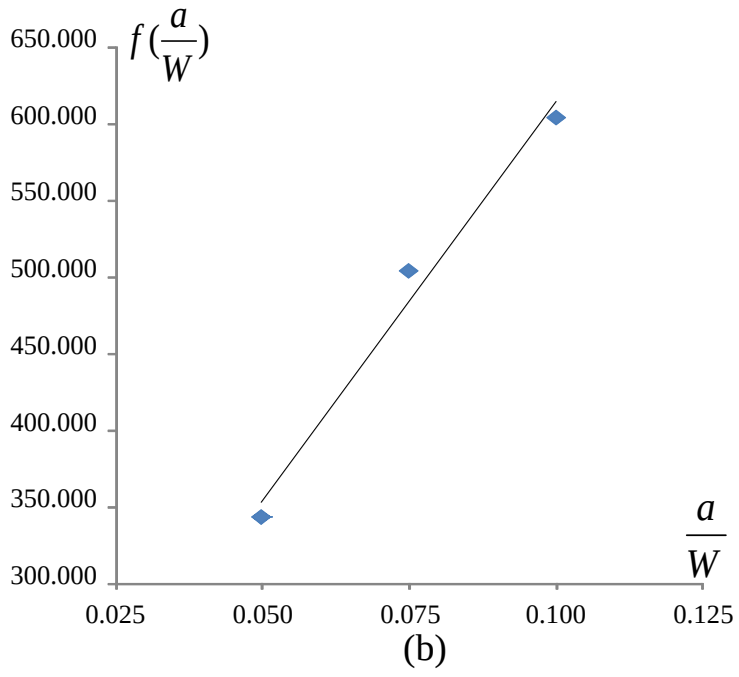

Figure 8.17 Influence function $f(a/W)$ for slope C against crack length ratio: a) cyclic tensile loading b) cyclic bending moment

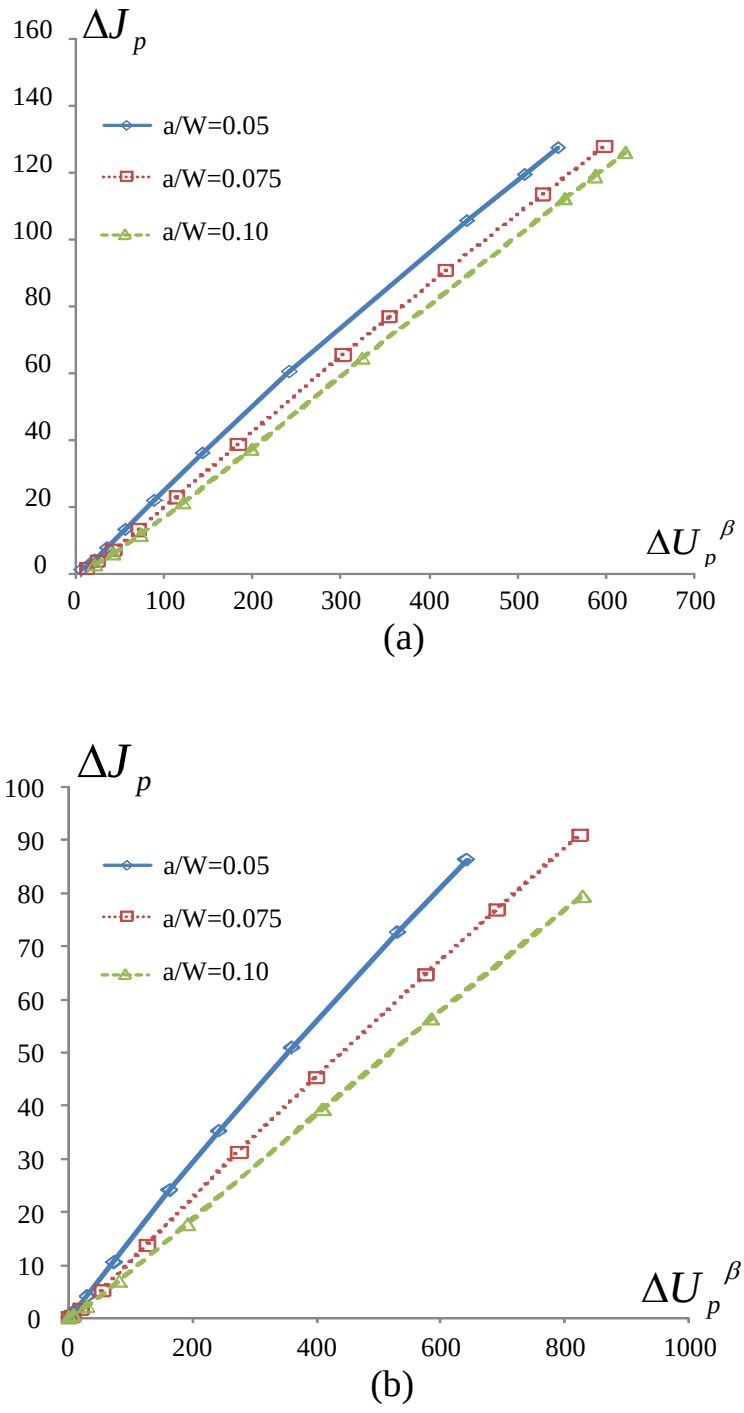

Figure 8.18 The relationship between plastic cyclic J and plastic energy for different crack length ratio with β=3/4 (a) Cyclic tensile loading case (b) Cyclic bending moment case

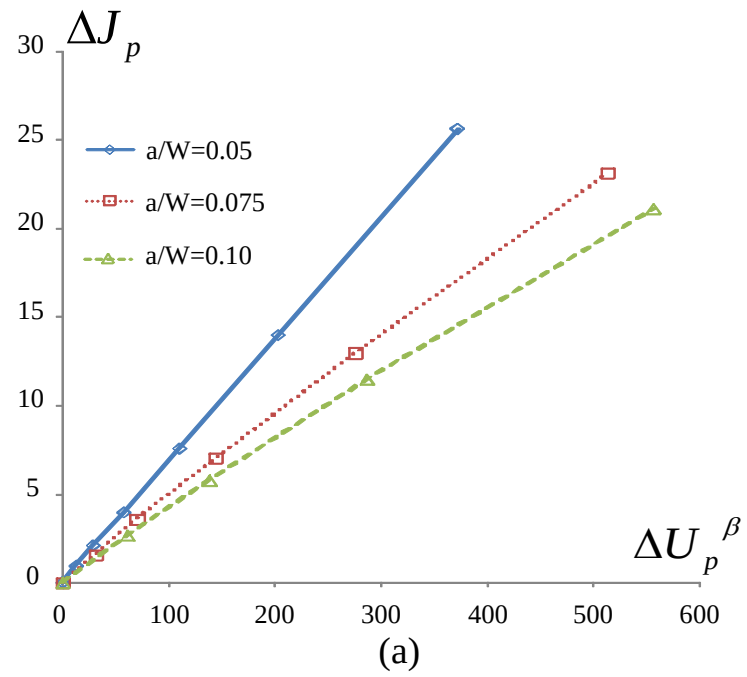

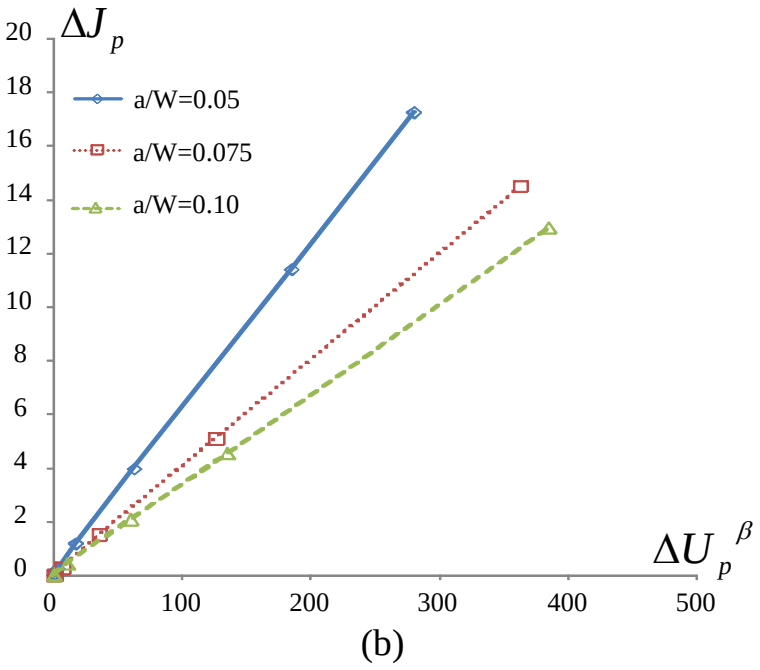

Figure 8.19 The relationship between plastic cyclic J and plastic energy for different crack length ratios with β=1 (a) Cyclic tensile loading case (b) Cyclic bending moment case

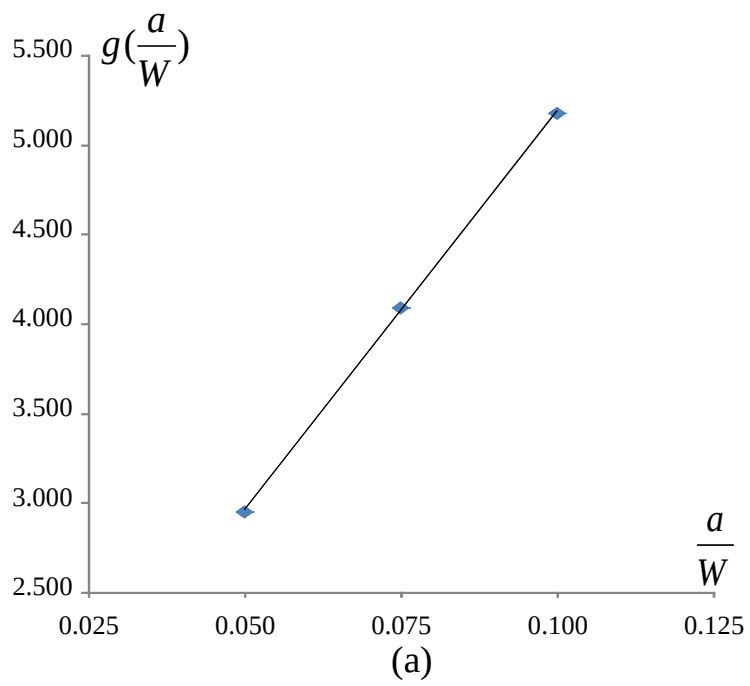

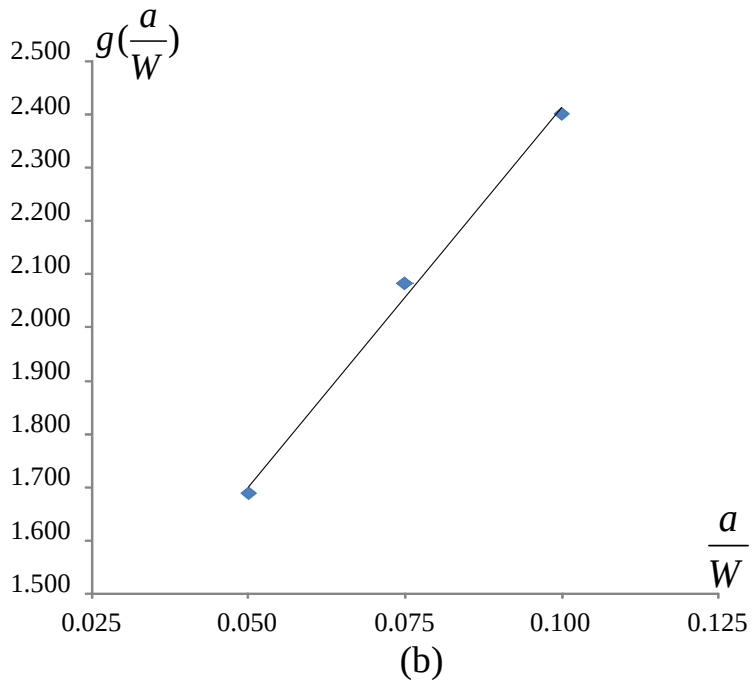

Figure 8.20 Influence function $g(a/W)$ for slope D against crack length ratio for β=3/4: a) cyclic tensile loading b) cyclic bending moment

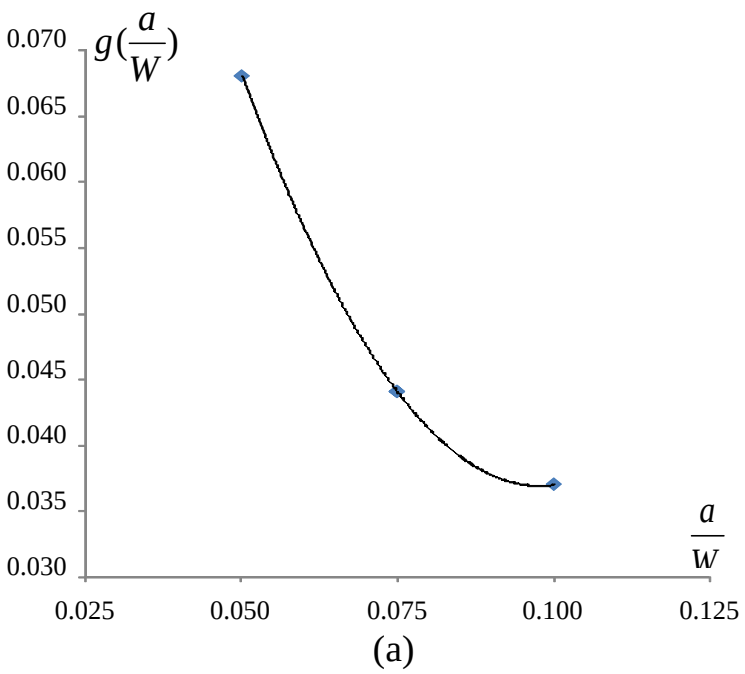

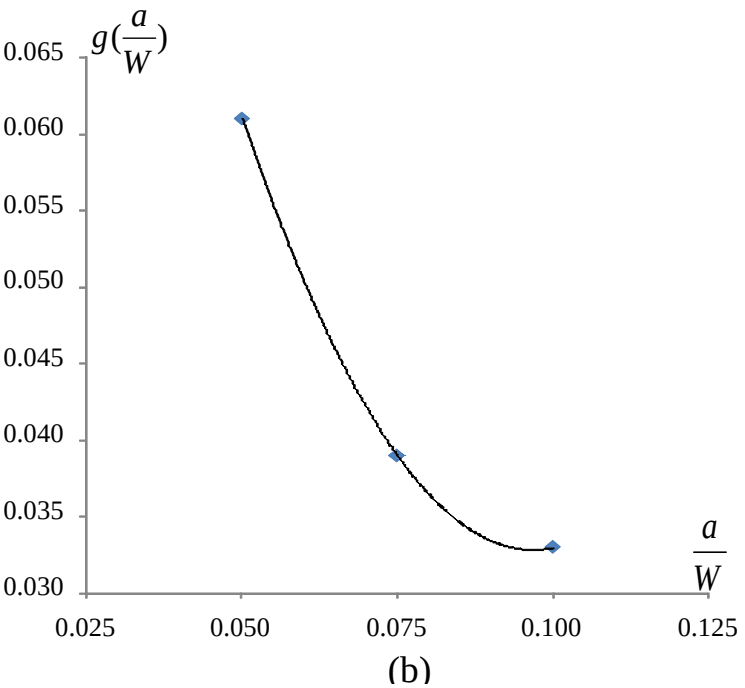

Figure 8.21 Influence function $g(a/W)$ for slope D against crack length ratio for β=1: a) cyclic tensile loading b) cyclic bending moment

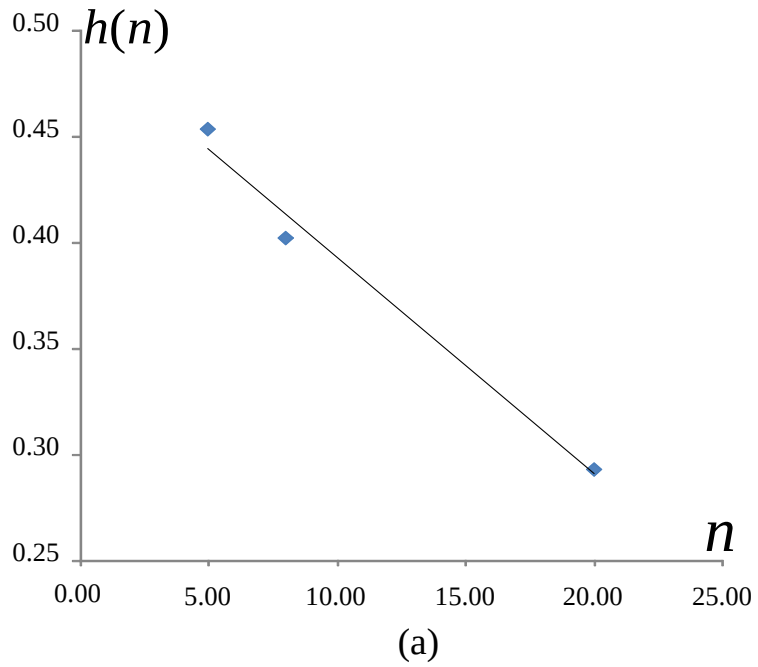

(a)

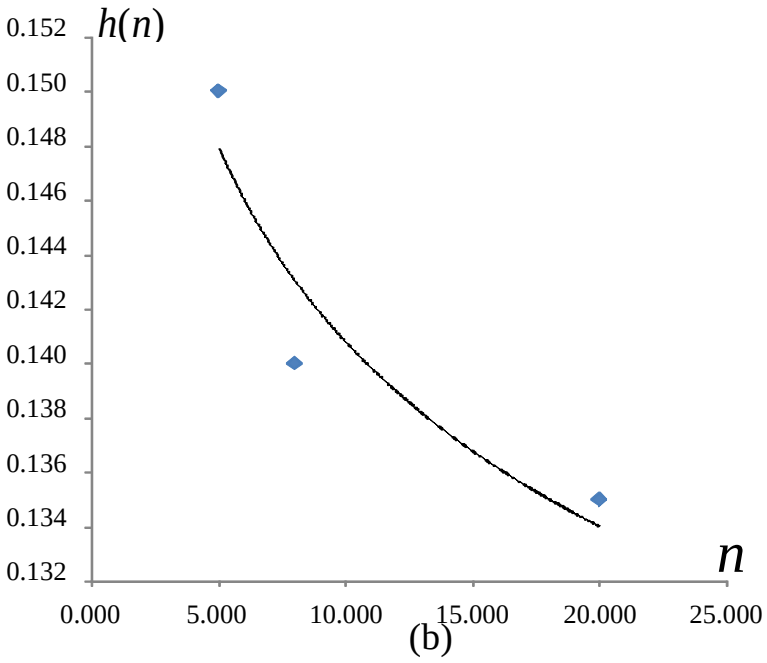

(b)

Figure 8.22 Influence function $h(n)$ for slope D against Ramberg-Osgood material hardening n with β=3/4: a) cyclic tensile loading b) cyclic bending moment

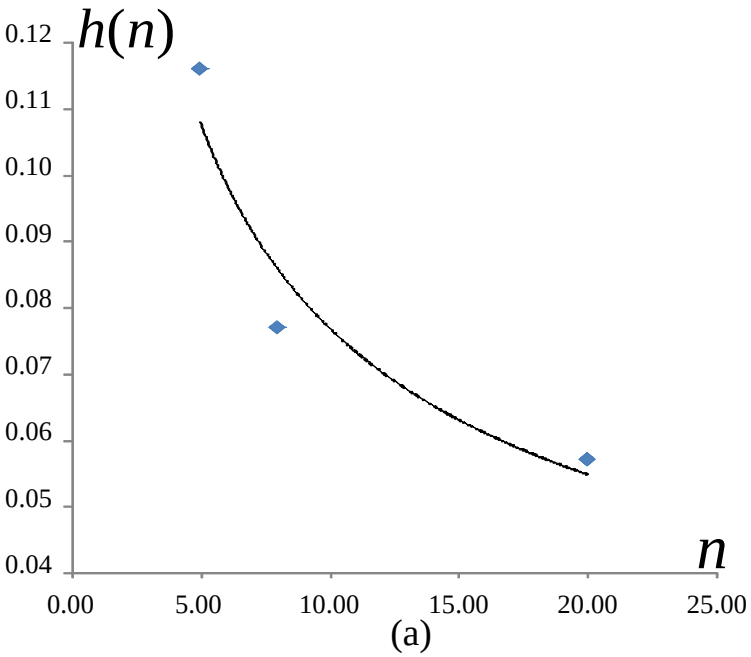

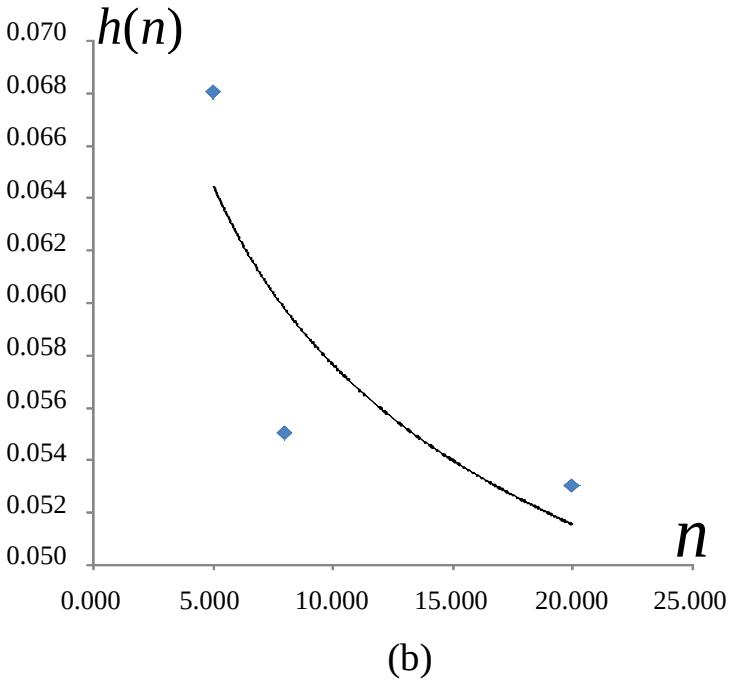

Figure 8.23 Influence function $h(n)$ for slope D against Ramberg-Osgood model material hardening n with β=1: a) cyclic tensile loading b) cyclic bending moment

8.7.2 Determination of D

In order to determine the formulation of function D from the ΔJ_p values, the variation of ΔJ_p with ΔU_p^{β} for three a/W ratios for elastic perfectly plastic material models is examined by plotting ΔJ_p against ΔU_p^{β} for β=3/4 and β=1 as shown respectively in Figure 8.18 and Figure 8.19. It is observed from Figure 8.13-Figure 8.14 and Figure 8.18-Figure 8.19 that the slope D is a function of a/W ratio, loading type, and inelastic material model for different β values. In order to simplify the formulation, slope D is assumed to be the product of two independent functions g(a/W) and h(n). Therefore, parameter D is assumed as,

$$D = \frac{g(\frac{a}{W})h(n)}{aB} \tag{8.33}$$

Where a is the crack length and B is the thickness of the plate, and $g(a/W)$, $h(n)$ are the influence functions for the crack length ratio range and the inelastic material model.

In order to find these influence functions, the results of ΔJ_p are replotted in graphs of functions g and h against a/W and n respectively as shown in Figure 8.20-Figure 8.23 for β=3/4 and β=1. Trend lines are fitted to the data obtained from the results of ΔJ_p vs ΔU_p^{β} for different crack length ratios and inelastic material model with β=3/4 and β=1 to show the influence function.

Equations (8.34) and (8.35) are the obtained influence functions for the crack length ratio range for β=3/4 and β=1, respectively. Equations (8.36)-(8.37) and (8.38) -(8.39) are the obtained influence functions for the inelastic material model range for β=3/4 and β=1, respectively.

Once C and D are defined, the cyclic J integral value is calculated for the single edge crack plate under both cyclic loadings that are mentioned in this study.

For β=3/4

$$g\left(\frac{a}{W}\right)=\begin{cases}44.5\left(\frac{a}{W}\right)+0.733 & (for\quad cyclic\quad tensile\quad loading)\\ 14.25\left(\frac{a}{W}\right)+0.987 & (for\quad cyclic\quad bending\quad moment)\end{cases} \tag{8.34}$$

For β=1

$$g\left(\frac{a}{W}\right)=\begin{cases}13.6\left(\frac{a}{W}\right)^2-2.66\left(\frac{a}{W}\right)+0.167 & (for\quad cyclic\quad tensile\quad loading)\\ 12.8\left(\frac{a}{W}\right)^2-2.48\left(\frac{a}{W}\right)+0.153 & (for\quad cyclic\quad bending\quad moment)\end{cases} \tag{8.35}$$

For β=3/4

For Ramberg Osgood parameter material n range from 5-20

$$h(n)=\begin{cases}-0.010(n)+0.495 & (for\quad cyclic\quad tensile\quad loading)\\ 0.165(n)^{-0.07} & (for\quad cyclic\quad bending\quad moment)\end{cases} \tag{8.36}$$

For elastic perfectly plastic material model

$$h(n)=\begin{cases}0.218 & (for\quad cyclic\quad tensile\quad loading)\\ 0.111 & (for\quad cyclic\quad bending\quad moment)\end{cases} \tag{8.37}$$

For β=1

For Ramberg Osgood parameter material n ranging from 5-20

$$h(n)=\begin{cases}0.236(n)^{-0.48} & (for\quad cyclic\quad tensile\quad loading)\\ 0.083(n)^{-0.16} & (for\quad cyclic\quad bending\quad moment)\end{cases} \tag{8.38}$$

For elastic perfectly plastic material model

$$h(n)=\begin{cases}0.043 & (for\quad cyclic\quad tensile\quad loading)\\ 0.039 & (for\quad cyclic\quad bending\quad moment)\end{cases} \tag{8.39}$$

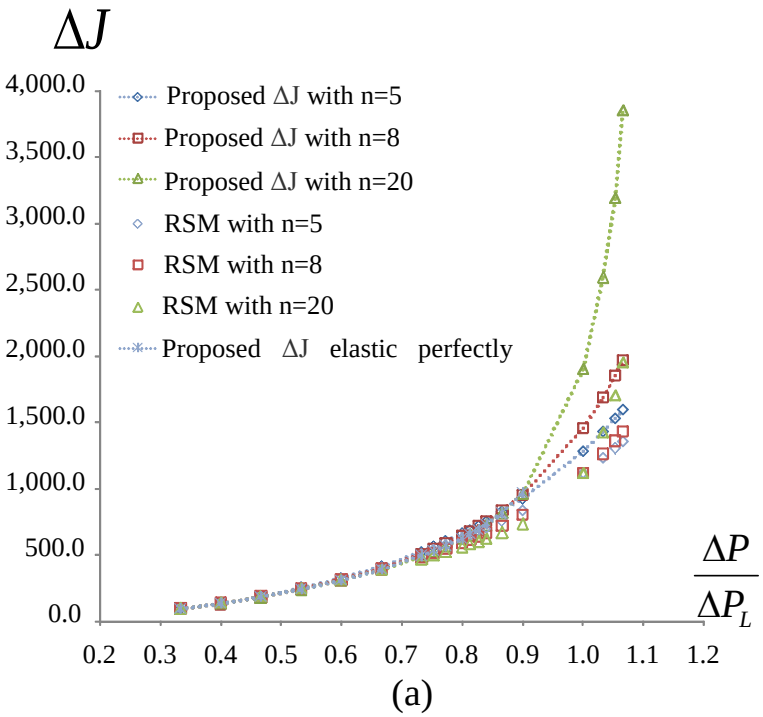

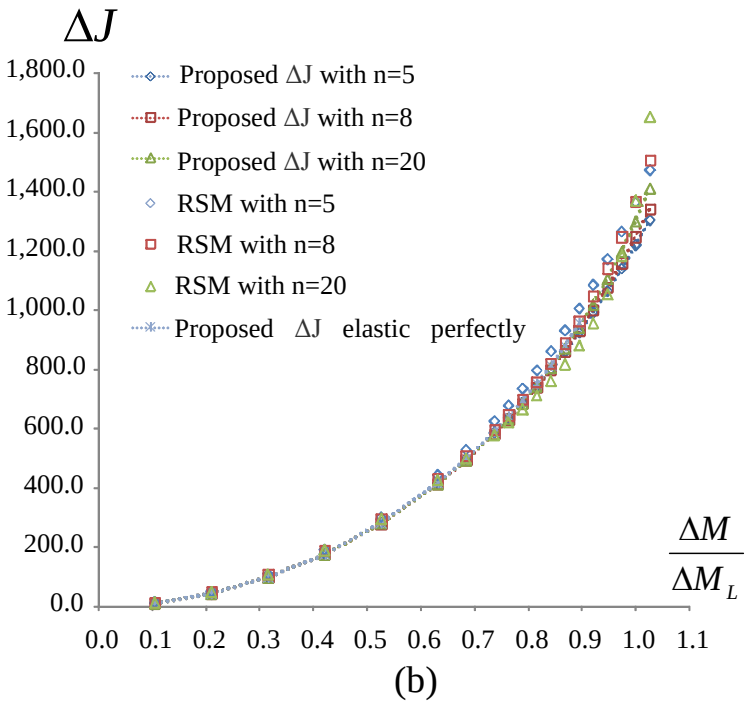

Figure 8.24 Comparison of the RSM and proposed ΔJ for different types of material models: a) cyclic tensile loading b) cyclic bending moment

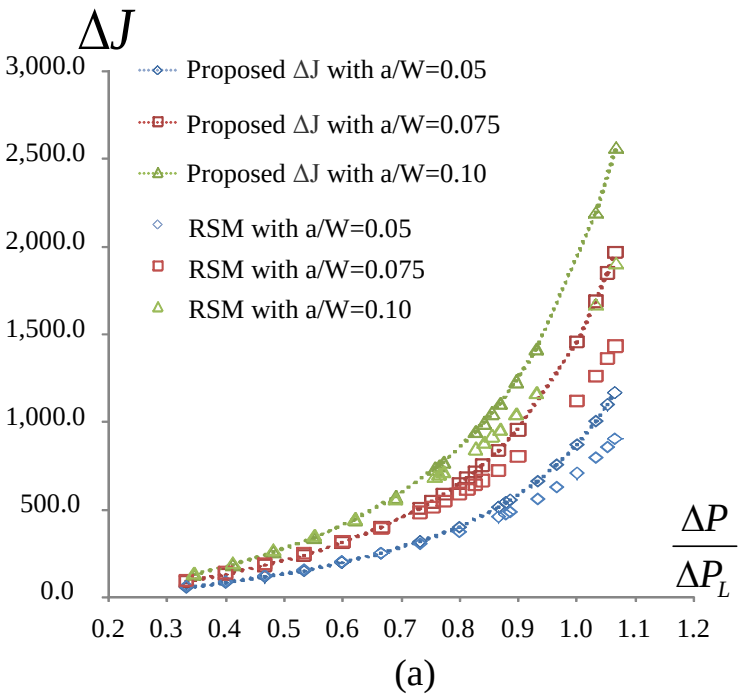

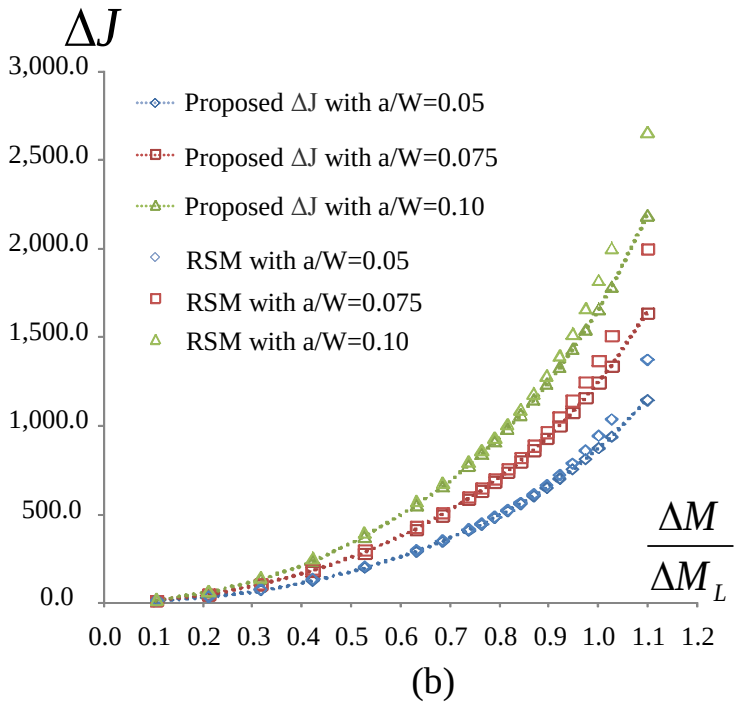

Figure 8.25 Comparison of the RSM and proposed ΔJ with different crack length ratios: a) cyclic tensile loading b) cyclic bending moment

8.8 Validation and Discussion for the Estimation Scheme

In this section we will consider first the cracked plate for different Ramberg-Osgood material constitutive relation. The ΔJ equation is obtained in section 8.7 for single edge cracked plate loaded in cyclic tension and cyclic bending moment. The results obtained from the ΔJ equation are compared graphically with Reference Stress Method for both cyclic loading cases with different Ramberg-Osgood parameter n. Figure 8.24 shows that the variation of ΔJ with Ramberg-Osgood material against load ratio $\Delta P/\Delta P_L$ and $\Delta M/\Delta M_L$, where ΔP_L, ΔM_L are the limit load range for cyclic tensile loading and cyclic bending moment respectively, with a/W=0.075. Good agreement is obtained between the proposed ΔJ equation and RSM results when the load ratio is smaller than 1.0 for both cyclic loading case. For the cyclic tensile loading case, when the load ratio is greater or equal to 1.0 the difference of ΔJ between the proposed method and RSM becomes very significant, and this difference gets larger with the increasing number of Ramberg-Osgood parameter n. However, for the bending moment case, when the load ratio is greater or equal to 1.0 the difference of ΔJ between the proposed method and RSM is not very obvious. Figure 8.24 also shows that for the load ratios smaller than 1.0, the values of ΔJ drops with increasing number of n, and for the load ratios greater or equal to 1.0, the values of ΔJ rises with increasing number of n for both proposed ΔJ method and RSM. This phenomenon can be explained by the curves of material constitutive relations shown in Figure 8.3. For the stress range less than twice of yield stress, the product of total stress-strain range is decreasing with increasing of n. And, for the stress range greater than twice of yield stress, the product of total stress-strain range is increasing with the increasing of n.

Figure 8.25 shows the variation of ΔJ against load ratio $\Delta P/\Delta P_L$ and $\Delta M/\Delta M_L$ for different crack depth with Ramberg-Osgood material n=8. Good agreement of the proposed ΔJ equation and RSM solutions is exhibited when the load ratio is smaller than 1.0 for both cyclic loading case. For load ratios greater or equal to 1.0, the results deviate significantly, for the cyclic tensile loading case.

8.9 Conclusions

In this study, a general ΔJ calculation method based on the LMM is proposed. The estimation scheme for a single edge cracked plate under cyclic tensile loading and cyclic bending moment is developed. The following conclusions can be drawn from this study:

1. The proposed ΔJ estimation, primarily derived from Fracture Mechanics concepts, is now considered from a Continuum Mechanics approach through LMM, which includes the cumulative effects over the cycle. The calculated values of ΔJ with the applied loading up to limit load are shown to correlate well with RSM under cyclic tensile loading and cyclic bending moment.

2. ΔJ_e is a linear function of $\Delta U_e / A_{sub}$, and this relation is independent of the material models and loading types that are considered in this study.

3. ΔJ_p is a linear function of ΔU_p^{β}. When β=1 this relation reduces to small scale yielding condition for the region of the plastic zone size up to 50% of the crack length.

4. The hardening constant n for the Ramberg-Osgood model has little effect on the values of ΔJ when the cyclic loading ratio ($\Delta P/\Delta P_L$) is less than 1.0.

5. A rapid procedure for predicting the values of ΔJ is provided for single edge cracked plate under cyclic tensile loading and cyclic bending moment cases.

CHAPTER 9. LINEAR MATCHING METHOD ON THE EVALUATION OF CYCLIC BEHAVIOUR WITH CREEP EFFECT

9.1 Introduction

The overall responses of mechanical structures under the combined mechanical and thermal loads without the presence of creep were discussed in previous chapters. In the coming chapters, the objective is to further unfold the current LMM for the evaluation of cyclic behaviours of mechanical structures when the effect of creep is taken into consideration.

The increasing requirements in improving the efficiency of the operation in current power plants, gas turbines, or chemical reactors, have resulted in engineering components operating at elevated temperatures. These structures often experience complex cyclic loading histories, and the main factors of structural failures for these components are creep and creep-fatigue interaction. At elevated temperatures, creep can cause within metallic components significant continuous viscoplastic strains that finally will lead to failure. The level of the creep and the time the structure will fail depend on the material, the operating temperature, the dwell period, the applied stress history and the geometry of the component. Although creep for some metals such as lead, copper and mild steel can occur at room temperatures, it is normally associated with high temperatures, typically greater than 40% of the absolute melting temperature of a metal [27].

9.1.1 Time Hardening and Steady-state Creep Law

A power law in time can be used to define the creep rate as:

$$\dot{\varepsilon}^c = B\sigma^{n^*}t^{m^*} \tag{9.1}$$

where $\dot{\varepsilon}^c$ is the uniaxial equivalent creep strain rate, σ is the von-Mises or equivalent stress, B, n^* and m^* are material creep properties, determined from creep test data. n^* is generally called the creep exponent or creep index value. One of the simplest

and most commonly used creep law relating creep strain rate to applied stress is Norton's Power Law [126],

$$\dot{\varepsilon}^c = B\sigma^{n^*} \tag{9.2}$$

This relationship describes the variation of minimum creep strain rate with applied constant stress for the secondary (steady-state) creep stage for uniaxial stress behaviour. Temperature dependence is not explicitly defined in this law and the equation is used for constant temperature conditions. However, the effect of different temperatures can be captured through the material constants *B* and *n**. For power plant applications, temperature and load remain practically constant for prolonged periods of time and the steady-state creep stage dominates the creep curve of the material, so that the use of Norton's law is valid for such analyses [25] [28].

9.1.2 Structural Response to Cyclic Loading with Creep

In the analysis of structures subjected to cyclic loading histories for an elastic plastic material without the effect of creep, the component will experience either elastic/plastic shakedown or ratchetting depending on the applied load level. The detailed explanations of the above structure's response has already been discussed in the previous chapters.

In the presence of creep, the response of the structure to cyclic loading changes significantly. The key feature of cyclic loading with creep is the synergistic interaction of plasticity and creep. One of the notable analytical treatments concerning the creep ratchetting phenomenon (or cyclically enhance creep) was given by Bree [30], which presented an analysis in which the inelastic strains developed by thermal cycling were caused by both yielding and creep. In his paper, Bree defined the phenomenon of creep ratchetting, whereby the structure may experience additional creep strain due to relaxation of the creep stresses. This definition was applied to a cylindrical tube under the action of a sustained internal pressure and cyclic temperature gradients across its wall. Bree's analysis assumes that the full stress relaxation occurs during the creep dwell. From this analysis it was found that any combination of applied steady state and cyclic loading which was above the pure elastic limit (Figure2.3) would cause creep ratchetting. To sum up, a

structure subjected to cyclic loading with creep can present different asymptotic behaviours regarding to the phenomenon of creep ratchetting [30],

1) Without creep ratchetting, no stress relaxation is taking place, therefore the accumulation of creep strain is due to primary loads only during each load cycle. Because the creep strains are driven by the primary loads alone, the situation is similar to that of monotonic loading.

2) With creep ratchetting and limited dwell time, the stress relaxation process introduces a residual stresses field so that there is a tendency for regions of the component material to yield during unloading. Thus, a closed hysteresis loop is generated even when the applied loading levels would have resulted in elastic shakedown region if creep were not present. If the applied loading level were in plastic shakedown region, additional plastic strain is formed due to the interaction of plasticity and creep which enlarges the closed hysteresis loop.

3) With creep ratchetting and large dwell time, although the effect of creep and cyclic plasticity on the residual stress field causes the cyclic stress to reset on each load cycle, the large dwell time produces increasingly large creep strain compared with plastic strain (which is limited in magnitude by the residual stress field). In other words, the appearance of the non-closed hysteresis loop would be due to creep strains, not plastic strains.

4) With creep ratchetting, where a large stress relaxation occurs despite a low level of overall creep stress, which leads to an insignificant creep strain. However, larger plastic strain occurs upon unloading due to the significant stress relaxation, thus the non-closed hysteresis loop appears due to the dominant plastic strain.

Therefore in an integrity assessment of components subjected to the cyclic load and under creep conditions, the above mechanisms need to be addressed.

Bree [46] considers the same geometry and loading condition as [30] but with only partial relaxation of stress during creep dwell. In [46] in addition to plot the stress contours through the tube wall, Bree also showed that the increase in plastic

strains caused by increasing dwell time (and thus greater stress relaxation) would reach a limit (corresponding to the complete relaxation of the creep stresses).

Situations such as the Bree cylinder which can be solved analytically are rare, and so modern analyses of more complex engineering structures use Finite Element Analysis to obtain solutions. Calculating the steady state response of structures subject to cyclic loading can require a large number of increments in full step-by-step analysis which becomes computationally expensive. As a result, the LMM has been developed to assess the stabilised response of structures subjected to cyclic loading with the effect of creep. Thus, the employed numerical procedure is the LMM, previously applied to cyclic problems without the effect of creep (Chapter 3-8), now used to generate the cyclic creep solutions.

The purpose of this chapter is to present an analysis of creep ratchetting (or cyclically enhanced creep) and creep-fatigue damage of structures through an extension of previous LMM [22]. The new method has been improved both theoretically and numerically compared to the numerical procedure mentioned in [22] by including the cyclic hardening material model, time hardening creep model, and is able to address all stable cyclic responses that are mentioned in section 9.1.2 for a structure under creep conditions by the new creep strain formulation. Cyclic stresses, residual stresses, creep strain, plastic strain range, ratchet strain and the elastic follow-up factor are calculated more efficiently and accurately by this new LMM. Firstly, the mathematical and numerical implementation of this method will be described. Secondly, in order to confirm and validate the applicability of the developed method, a benchmark example of a Bree cylinder is reanalysed in the present study through the LMM, and the results are compared with existing analytic solutions in [30]. Finally, the structural response of a plate with a central hole subjected to cyclic thermal loads and a constant uniaxial tension under high temperature is also analysed, to verify the applicability of the LMM to more general practical problems with different material and creep models.

This work has been published in the international conference of Pressure Vessels and Piping Division in Toronto, 2012.

9.2 Numerical Procedures

Considering the same problem as in Figure5.1 a structure is subjected to a general cyclic load condition. The body is subjected to a cyclic history of varying temperatures $\lambda_\theta \theta(x_i,t)$ within the volume V and varying surface loads $\lambda_p P(x_i,t)$ acting over part of the body's surface S_T, where λ_θ and λ_p are a reference load parameter. On the remainder of the surface S, denoted by S_u, the displacement satisfies $u=0$. The variation is considered over a typical cycle $0 \le t \le \Delta t$ in a cyclic state. The corresponding linear elastic stress history is denoted by $\hat{\sigma}_{ij}(x_i,t)$ as,

$$\lambda \hat{\sigma}_{ij}(x_i,t) = \lambda_\theta \hat{\sigma}^{\theta}_{ij}(x_i,t) + \lambda_p \hat{\sigma}^{p}_{ij}(x_i,t) \tag{9.3}$$

$\hat{\sigma}^{p}_{ij}$ and $\hat{\sigma}^{\theta}_{ij}$ represent the linear elastic stress history corresponding to varying surface loads $P(x_i,t)$ and temperature $\theta(x_i,t)$, respectively.

Adopting the formulation in (5.8)-(5.10), the general form of the stress solution for the cyclic problems involving changing and constant residual stress fields is given by,

$$\sigma_{ij}(x_i,t) = \lambda \hat{\sigma}_{ij}(x_i,t) + \bar{\rho}_{ij}(x_i) + \rho^{c}_{ij}(x_i,t) \tag{9.4}$$

where $\bar{\rho}_{ij}$ denotes a constant residual stress field in equilibrium with zero surface traction on S_T and corresponds to the residual state of stress at the beginning and end of the cycle. Here λ denotes a scalar load parameter. The history ρ^{c}_{ij} is the change in the residual stress during the cycle and satisfies,

$$\rho^{c}_{ij}(x_i,0) = \rho^{c}_{ij}(x_i,\Delta t) \tag{9.5}$$

For the cyclic problem defined above, the stresses and strain rates will become asymptotic to a cyclic state where;

$$\sigma_{ij}(t) = \sigma_{ij}(t+\Delta t), \qquad \dot{\varepsilon}_{ij}(t) = \dot{\varepsilon}_{ij}(t+\Delta t) \tag{9.6}$$

9.2.1 Numerical Procedure for the Varying Residual Stress Field

The numerical procedures for defining varying creep strain and residual stress is similar to the first stage in the Dual Minimization process that is described in Chapter 5.3.1 by including the load instance with creep in the cyclic histories.

The strategy of evaluating the structural responses consists of defining an appropriate class of kinematically admissible strain rate histories, $\dot{\varepsilon}_{ij}^{c}$ and a corresponding minimizing process is written as,

$$I\left(\dot{\varepsilon}_{ij}^{c},\lambda\right)=\sum_{n=1}^{N}I^{n} \tag{9.7}$$

It is assumed that plastic strains only occur at load extremes corresponding to *N* time instants, t_1, t_2, ..., t_N ,where t_n corresponds to a sequence of time points in the cyclic history, which leads to $\Delta\varepsilon_{ij}^{c}=\sum_{n=1}^{N}\Delta\varepsilon_{ij}^{n}$, where $\Delta\varepsilon_{ij}^{n}$ is the increment of plastic or creep strain that occurs at time t_n. Thus the minimization function in an incremental form is written as,

$$I^{n}\left(\Delta\varepsilon_{ij}^{n},\lambda\right)=\int_{V}\left\{\sigma_{ij}^{n}\Delta\varepsilon_{ij}^{n}-\left[\lambda\hat{\sigma}_{ij}\left(x_i,t_n\right)+\rho_{ij}\left(x_i,t_n\right)\right]\Delta\varepsilon_{ij}^{n}\right\}dV \tag{9.8}$$

and

$$\rho_{ij}\left(x_i,t_n\right)=\bar{\rho}_{ij}(x_i)+\sum_{l=1}^{n}\Delta\rho_{ij}\left(x_i,t_l\right) \tag{9.9}$$

where in (9.7) the term $\dot{\varepsilon}_{ij}^{c}$ is replaced by a sequence of increments of strain $\Delta\varepsilon_{ij}^{n}$ occurring at a sequence of *N* times t_n. The incremental minimization of $I^{n}\left(\Delta\varepsilon_{ij}^{n}\right)$ assumes that the prior history of the residual stress is known and compatibility of the total elastic and plastic strain in the increment is used. $\bar{\rho}_{ij}(x_i)$ is the constant element of the changing residual stress $\rho_{ij}\left(t_n\right)$ and represents as,

$$\bar{\rho}_{ij}^{M}=\sum_{n=1}^{N}\Delta\rho_{ij1}^{\ n}+\sum_{n=1}^{N}\Delta\rho_{ij2}^{\ n}+\cdots+\sum_{n=1}^{N}\Delta\rho_{ijM-1}^{\ n} \tag{9.10}$$

where M represents the total number of cycles. The LMM methodology requires the solution of a sequence of linear problems. From an initial estimate of the strain increment, $\Delta\varepsilon_{ij}^{n}=\Delta\varepsilon_{ijm}^{\ n}$, at *mth* cycle of iterations, a class of linear problems for a new estimate, $\Delta\varepsilon_{ij}^{n}=\Delta\varepsilon_{ijm+1}^{\ n}$, can be defined at the (*m+1*)*th* cycle of iterations.

In an iterative process, at an arbitrary integration point x_i, the repeated application of the algorithm produces a sequence of solutions for $\Delta\varepsilon_{ij}^{n}$, which converges to the

absolute minimum of the minimization function. The entire iterative procedure requires a total number of cycles, *M*, where each cycle, *m*, contains *N* iterations associated with *N* load instances, where *n*=1,2,...*N* and *m*=1,2,...*M*. If two consecutive cycles, *m* and *m+1*, are now considered, then the iterative linear coefficient $\bar{\mu}_{m+1}(t_n)$ for time instance t_n is given by the linear matching as,

$$\bar{\mu}_{m+1}(t_n) = \bar{\mu}_m(t_n)\frac{\sigma_{0m}(t_n)}{\bar{\sigma}\left(\hat{\sigma}_{ij}(t_n) + \rho_{ij}^m(t_n)\right)} \tag{9.11}$$

where $\sigma_{0m}(t_n)$ is the iterative von-Mises yield stress for Ramberg-Osgood material model or yield stress for the elastic perfectly plastic material model at load instance t_n, $\bar{\mu}_m(t_n)$ is the iterative shear modulus. The von-Mises yield stress $\sigma_{0m}(t_n)$ will be replaced by creep flow stress $\bar{\sigma}_c$ if only creep relaxation occurs at the load instance. The new distribution of the strain increment, $\Delta\varepsilon_{ijm+1}^{\ n}$, is then characterized as the solution to the following problem,

$$\Delta\varepsilon_{ij\,m+1}^{T\,n\ \prime} = \frac{1}{2\mu}\Delta\rho_{ijm+1}^{\ n\ \prime} + \Delta\varepsilon_{ijm+1}^{\ n\ \prime}, \quad \Delta\varepsilon_{kk\,m+1}^{T\,n} = \frac{1}{3K}\Delta\rho_{kk\,m+1}^{\ n} \tag{9.12}$$

$$\Delta\varepsilon_{ijm+1}^{\ n\ \prime} = \frac{1}{2\bar{\mu}_m(t_n)}\left\{\hat{\sigma}_{ij}(t_n) + \rho_{ij}^{\ m+1}(t_{n-1}) + \Delta\rho_{ijm+1}^{\ n}\right\}' \tag{9.13}$$

where the prior history of the residual stress is known as,

$$\rho_{ij}^m(t_{n-1}) = \bar{\rho}_{ij}^m + \Delta\rho_{ijm}^{\ 1} + \Delta\rho_{ijm}^{\ 2} + \ldots\ldots + \Delta\rho_{ijm}^{\ n-1} \tag{9.14}$$

The constant element of the residual stress, $\bar{\rho}_{ij}^M$ for the cyclic loading history is determined by (Appendix II),

9.2.2 Numerical Procedure for the Creep Strain and Flow Stress

Calculating the accumulated creep strain during the dwell period, $\sigma_0(t_n)$ in equation (9.11) equals to creep flow stress $\sigma_0(t_n) = \bar{\sigma}_c$, which is an implicit function of creep strain $\Delta\varepsilon^c$ and residual stress $\Delta\bar{\rho}^c$ during the creep dwell period.

We assume a time hardening creep constitutive relation as:

$$\dot{\bar{\varepsilon}}^c = B\bar{\sigma}^{n^*}t^{m^*} \tag{9.15}$$

Where $\dot{\bar{\varepsilon}}^c$ is the effective creep strain rate, $\bar{\sigma}$ is the effective von-Mises stress, *t* is the dwell time, and *B*, *m** and *n** are the creep constants of the material. When

m^*=0, the time hardening constitutive equation becomes the Norton's law (steady-state creep stage) (9.2). During the relaxation process we assume, at each point in space that an elastic follow up factor Z exists:

$$\dot{\bar{\varepsilon}}^c = -\frac{Z}{\bar{E}}\dot{\bar{\sigma}} \tag{9.16}$$

where $\bar{E} = 3E/2(1+\nu)$, E is the Young's modulus and $\dot{\bar{\sigma}} = \dot{\bar{\sigma}}(\sigma_{ij})$.

Combining (9.15) and (9.16) and integrating over the dwell time, we obtain

$$\frac{B\bar{E}\Delta t^{m^*+1}}{Z(m^*+1)} = \frac{1}{n^*-1}\left\{\frac{1}{(\bar{\sigma}_c)^{n^*-1}} - \frac{1}{(\bar{\sigma}_s)^{n^*-1}}\right\} \tag{9.17}$$

Where $\bar{\sigma}_s$ is the effective value of the start of dwell stress, $\bar{\sigma}_c$ is the effective value of the creep flow stress, and $\bar{\sigma}_c = \bar{\sigma}(\sigma_{sij} + \Delta\rho_{Cij})$. Integrating (9.16) gives the effective creep strain during the dwell period Δt as,

$$\Delta\bar{\varepsilon} = -\frac{Z}{\bar{E}}(\bar{\sigma}_c - \bar{\sigma}_s) \tag{9.18}$$

Combining (9.17) and (9.18) and eliminating $Z/\bar{E}$ gives

$$\Delta\bar{\varepsilon}^c = \frac{B(n^*-1)\Delta t^{m^*+1}(\bar{\sigma}_s - \bar{\sigma}_c)}{\left(\frac{1}{\bar{\sigma}_c^{n^*-1}} - \frac{1}{\bar{\sigma}_s^{n^*-1}}\right)(m^*+1)} \tag{9.19}$$

For the pure creep where $\bar{\sigma}_s = \bar{\sigma}_c$, the creep strain becomes:

$$\Delta\bar{\varepsilon}^c = \frac{B\bar{\sigma}_s^{n^*}\Delta t^{m^*+1}}{m^*+1} \tag{9.20}$$

The creep strain rate $\dot{\bar{\varepsilon}}^F$ at the end of dwell time Δt is calculated by (9.17) and (9.19) :

$$\dot{\bar{\varepsilon}}^F = B(\bar{\sigma}_c)^{n^*}\Delta t^{m^*} = \frac{\Delta\bar{\varepsilon}^c}{\Delta t}\frac{(m^*+1)}{(n^*-1)}\frac{\bar{\sigma}_c^{n^*}}{(\bar{\sigma}_s - \bar{\sigma}_c)}\left(\frac{1}{\bar{\sigma}_c^{n^*-1}} - \frac{1}{\bar{\sigma}_s^{n^*-1}}\right) \tag{9.21}$$

For the pure creep where $\bar{\sigma}_s = \bar{\sigma}_c$, the creep strain rate $\dot{\bar{\varepsilon}}^F$ becomes:

$$\dot{\bar{\varepsilon}}^F = B\left(\bar{\sigma}_s\right)^{n^*}\Delta t^{m^*} \tag{9.22}$$

Hence in the iterative process, we begin with current estimated $\bar{\sigma}_c^i, \bar{\sigma}_s^i$ and use equations (9.19), (9.21) or (9.22) to compute a new value of the creep stress $\bar{\sigma}_c = \bar{\sigma}_c^f$ from (9.23) to replace $\sigma_0(t_n)$ in the linear matching condition (9.11).

$$\bar{\sigma}_c = \left(\frac{\bar{\dot{\varepsilon}}^F}{B\Delta t^{m*}} \right)^{\frac{1}{n*}} \tag{9.23}$$

The above discussed numerical process could be further understood by examining the block diagram in Figure 9.1.

9.2.3 New Developments

There are three significant developments regarding the numerical procedure for the calculation of creep strain and creep stress compared to [22]. These are:

1. The numerical procedure described in [22] is based on the assumption that structural response of the steady-state hysteresis loop remain closed. This assumption means that the inelastic strain (creep strain or combination of creep and plastic strain) produced during loading is fully recovered by the reverse inelastic strain (creep strain or combination of creep and plastic strain) during unloading. In other words, the creep strain defined in [22] is bounded by the residual stress which is produced during the dwell period. However, as stated in section 9.1.2, there are more structural responses which need to be addressed. For example, as the dwell period increase, larger permanent creep strain is induced, and this permanent creep strain will become unbounded from the residual stress produced during the dwell period. Due to the limited magnitude of this residual stress, the reverse plastic strain cannot increase unlimitedly and it is not able to recover the inelastic strain (creep strain or the combination of creep and plastic strain) during loading. Thus, the assumption in [22] is not valid for larger creep strain case and should be modified. With the new numerical procedure, the calculated time dependent creep strain, defined using elastic follow up combination idea (9.19) or (9.20), is able to capture all the structural responses related to the phenomenon of creep that is described in section 9.1.2.

2. For more practical cases, the Time Hardening creep constitutive model (9.15) is considered in this study, and this model is able to reduce to Norton's law by considering m=0. In the previous study [22] the creep constitutive equation was only valid for the steady-state creep stage (Norton's law)(9.2).

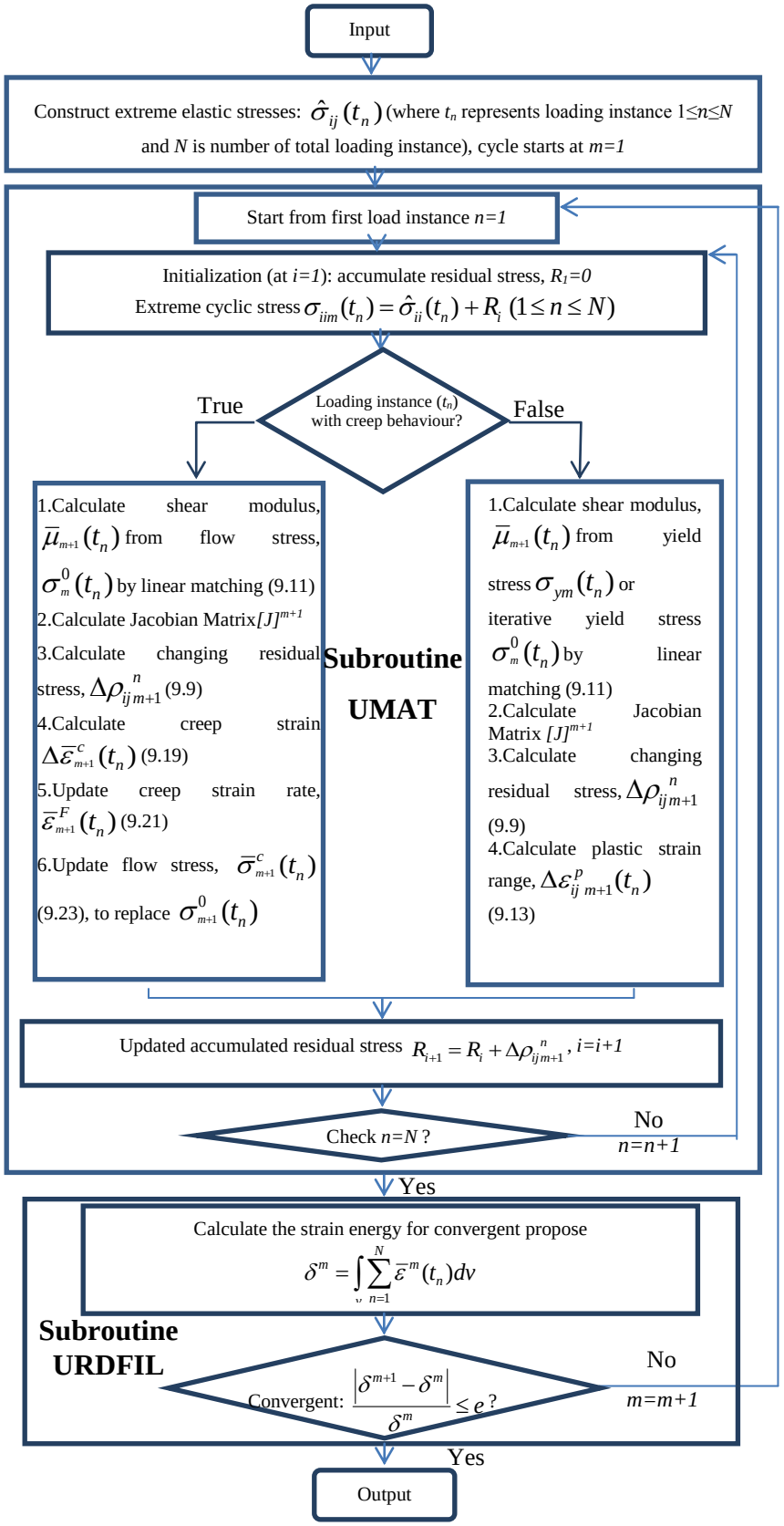

Figure 9.1Flow chart for evaluating the creep and plastic behaviour using LMM

3. For more general cases, the cyclic hardening material model (Ramberg-Osgood) is developed in this study, whereas in [22] the material model considered was only limit to elastic perfectly plastic.

The capability of these differences is shown in the numerical example of a plate with a hole.

9.3 Bree Problem

The Bree problem [30] [46] has been re-established in this section and is used to verify the results of the iterative process described above.

9.3.1 Problem Description

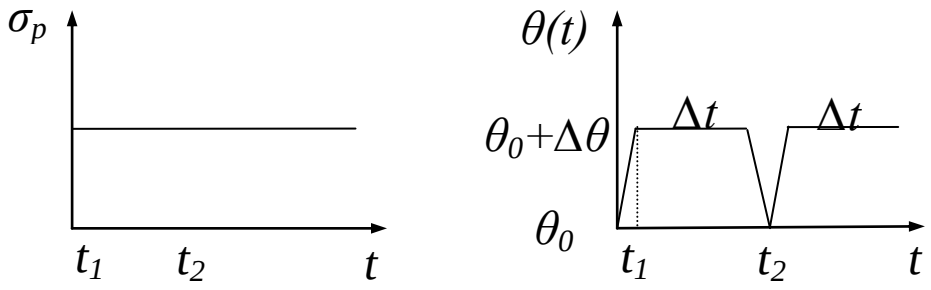

(a)

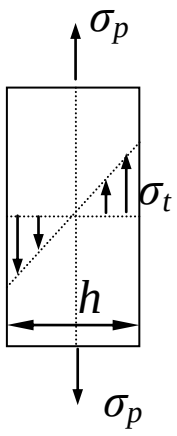

(b)

Figure 9.2 (a) Load history for constant internal pressure and cyclic temperature gradient

(b) Cross section in direction of the applied stress

The problem to be considered here is that of a cylindrical tube of mean radius R and wall thickness h that is closed at the ends [30]. The tube is subjected to an internal pressure σ_p (Figure 9.2a) and a cyclic temperature gradient across its wall. The detailed temperature history of a cylindrical tube is given in Figure 9.2a, where $\theta(t)$ varies between θ_0 and $\theta_0+\Delta\theta$. The ambient temperature θ_0 remains at $0^{\circ}C$. The temperature distribution across the wall is assumed to be linear, during the first half of each cycle (the so-called start-up) and zero during the second half of each cycle (the so-called shut down). Bree [30] made the additional assumption that, since the hoop stress is the greater of the two stresses acting, the axial stress would be ignored. Thus the problem is reduced to that of a slab with a overall stress $\sigma_p+\ \sigma_t$ acting in hoop direction only (Figure 9.2b), where the constant σ_p and cyclic σ_t is the hoop stress produced by the internal pressure and cyclic temperature distribution across the thickness, respectively.

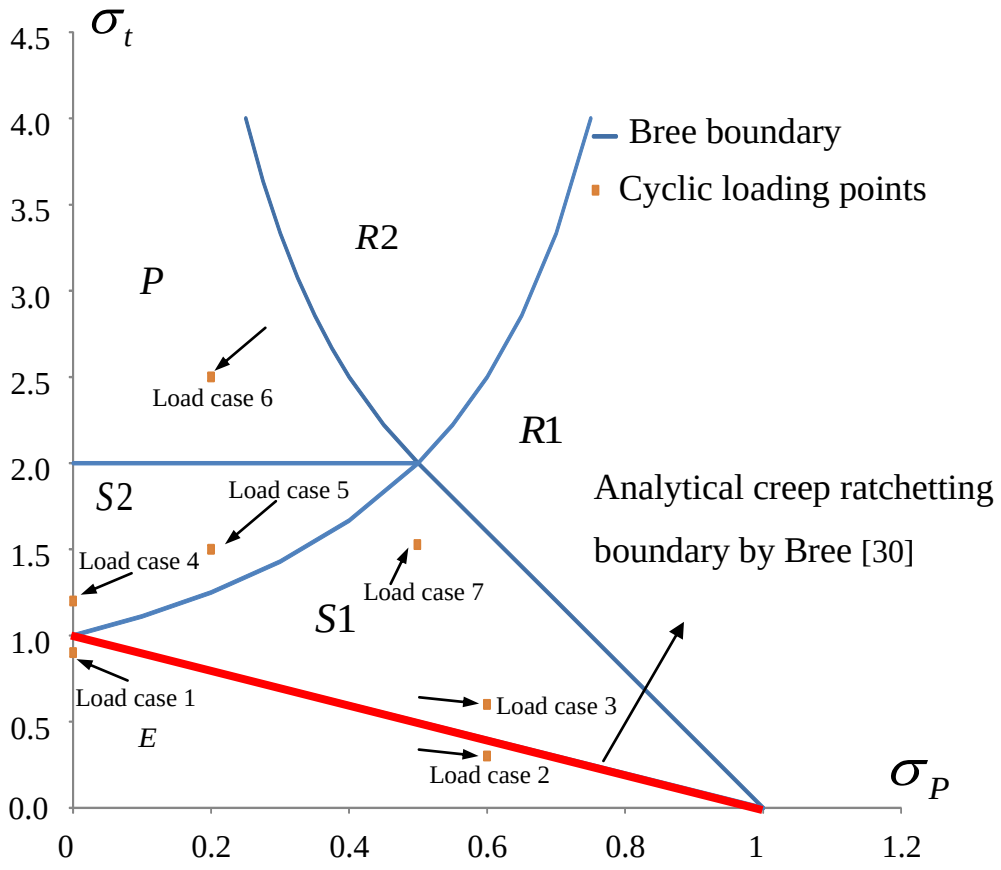

Figure 9.3 Bree diagram, showing regions of different cyclic behaviour. The axes show stress normalized by yield stress.

9.3.2 Results and Discussions

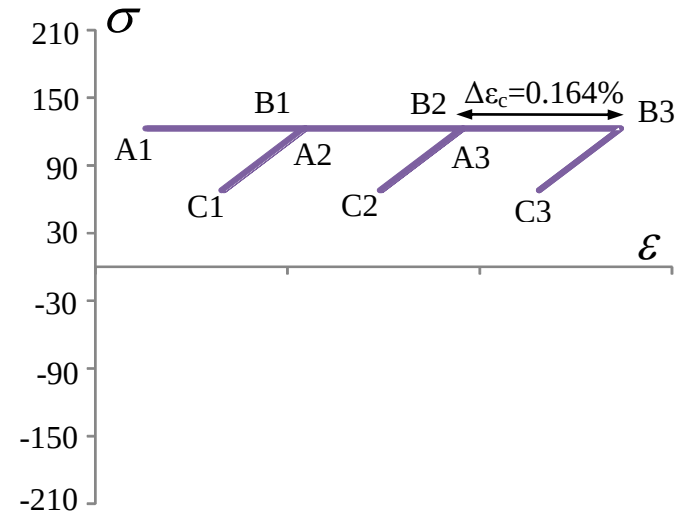

(a)

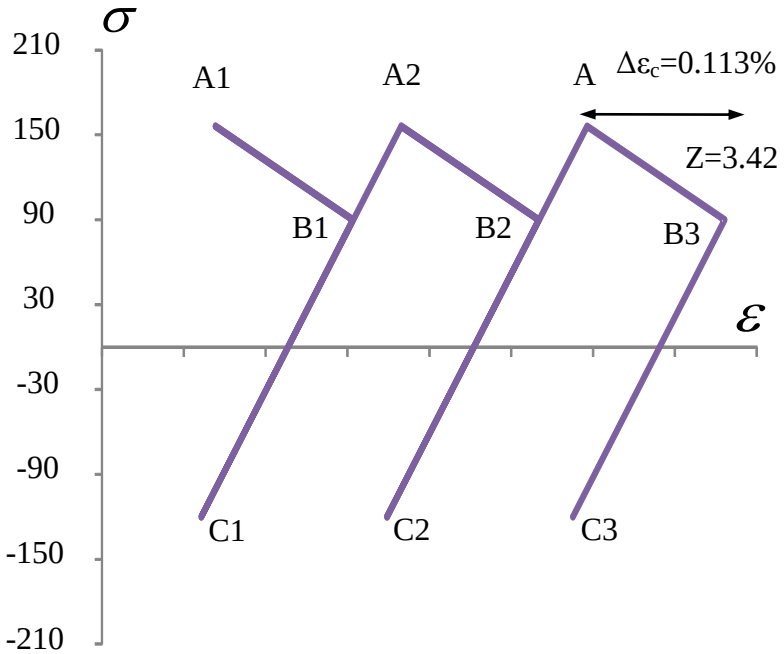

(b)

Figure 9.4 Response of the stress-strain path corresponding to the cyclic loading cases (a) 2

(b) 3

The cylindrical tube is made of 304 stainless steel with the following material properties: yield stress σ_y=205 MPa, Poisson's ratio, ν=0.3, Young's modulus, E= 200 GPa, coefficient of thermal expansion, α=1.0x10^{-5}. For the creep material data in equation (9.15) we adopt B= 5.86e-15, n*=5 and m*=0.

Figure 9.3 is the Bree [30] diagram, which illustrates the responses for the case of a pressurised cylinder subjected to cyclic through-wall thermal stress. The ordinate and abscissa give normalised values of pressure and thermal stress respectively, where the stresses have been normalised against the yield stress of the material. There are four main regions of interest. Region *E* is elastic, where pressure plus thermal stress is always less than the yield stress. Bree stated that creep ratchetting occurs if any combination of applied loading exceeds region *E*, with the assumption that the stress is fully relaxed [30]. Region *S* is the elastic shakedown. Region *P* is the reversed plasticity, where yielding occurs on every cycle, but no incremental or ratchetting strain occurs. Region *R* indicates ratchetting, where finite strain growth occurs on every cycle.

For the verification of the Bree boundary, the cyclic load cases *1*, *2*, and *3*, 4, which are just below and above the calculated elastic limit boundary (Figure 9.3), are chosen respectively. The calculated steady state stress strain path for the cyclic loadings *2* and *3,* are shown in Figure 9.4a and Figure 9.4b, respectively, where the dwell time is long enough to produce a full relaxation of creep stress. From Figure 9.4 it is observed that the calculated steady-state of stress and strain follows the path $A_1B_1C_1A_2B_2C_2A_3B_3C_3$, etc. and reaches the point A_n at the end of the nth start-up, the point B_n at the end of the nth dwell time and the point C_n at the end of the nth shutdown. Load case 2 (Figure 9.4a) exhibits a non creep ratchetting mechanism as the creep strain accumulation occurs only due to the primary stress, with no stress relaxation taking place. Load case 3 (Figure 9.4b), however, exhibits a creep ratchetting mechanism as an additional creep strain is accumulated due to stress relaxation in every cycle. Similar results are obtained from the analyses at load points 1 and 4 which confirm that the LMM can reproduce the analytical solutions of Bree [30].

For a further verification of the Bree problem with the effect of creep [46], the cyclic load case 5, which is located in the *S2* region is chosen. The calculated stress distribution obtained from Bree and LMM across the tube wall during the shutdown, start-up and dwell period processes are showed in Figure 9.5, with only partial relaxation of stress during creep dwell. It is observed From Figure 9.5 that the

calculated stress distribution from LMM correlate well with the Bree solution, which further confirm that the LMM can reproduce the analytical solution of Bree [46].

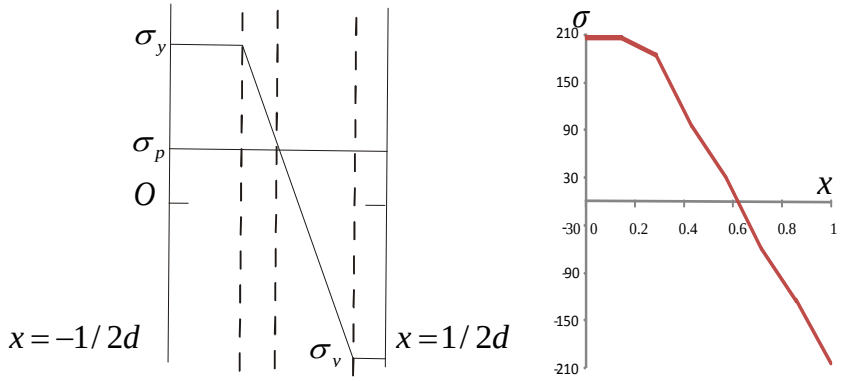

Bree solution LMM

(a)

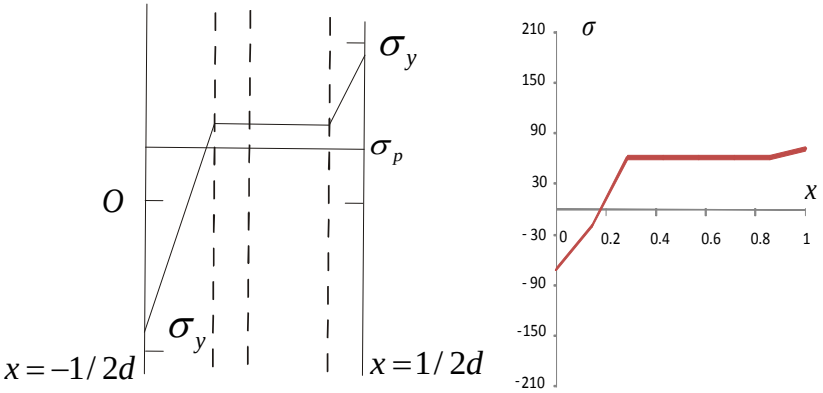

Bree solution LMM

(b)

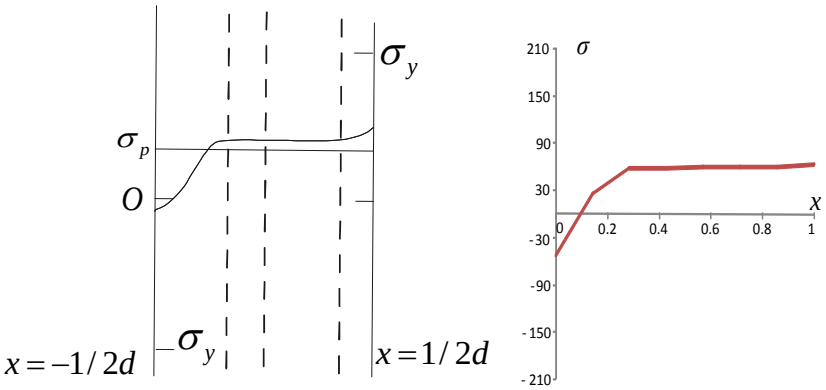

Bree solution LMM

(c)

Figure 9.5 Stress distribution across the tube wall with partial stress relaxation for the cyclic loading case 5 during (a) Shutdown (b) Start-up (c) Creep dwell, processes

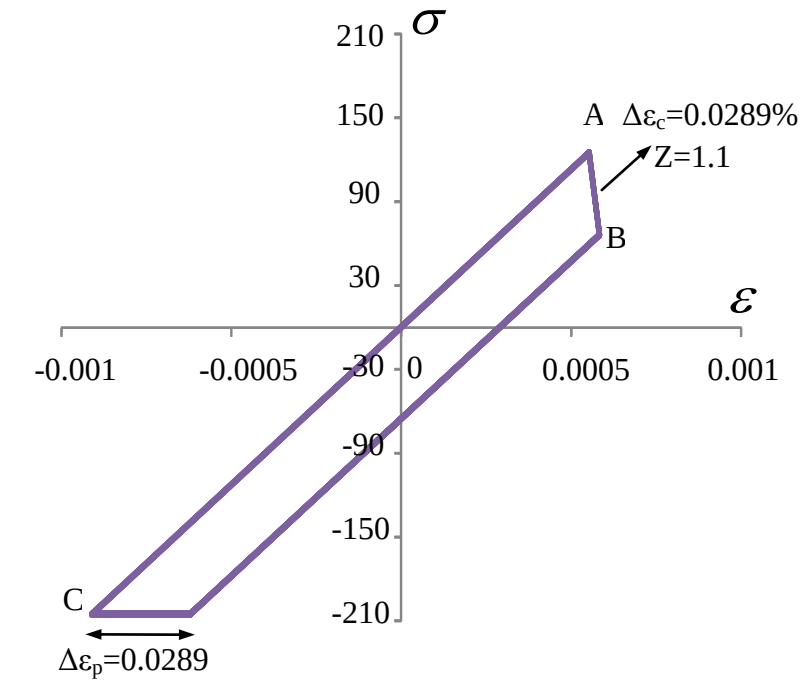

(a)

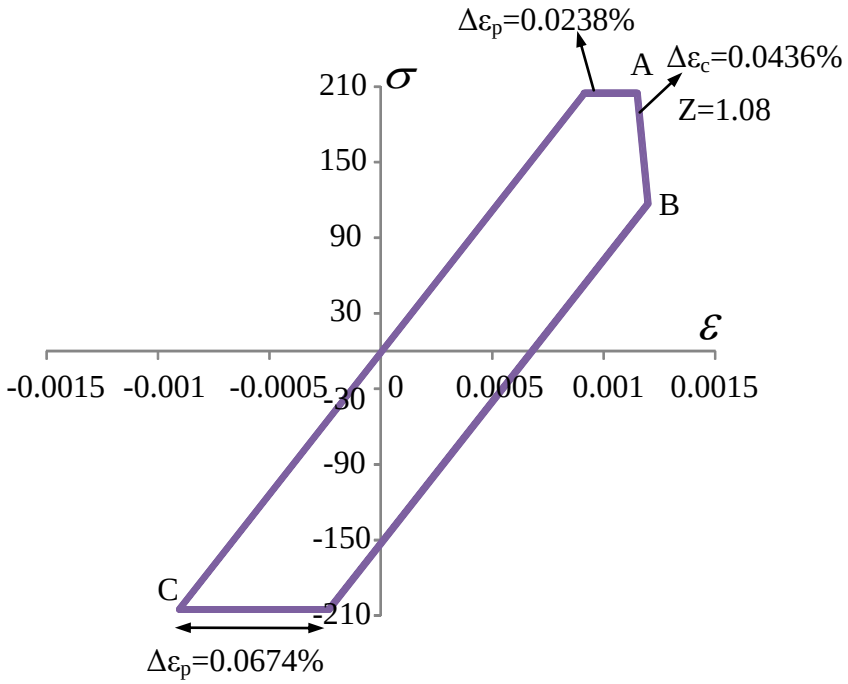

(b)

Figure 9.6 Response of the stress-strain path corresponding to the cyclic loading cases with 1 hour dwell time (a) case 5 (b) case 6

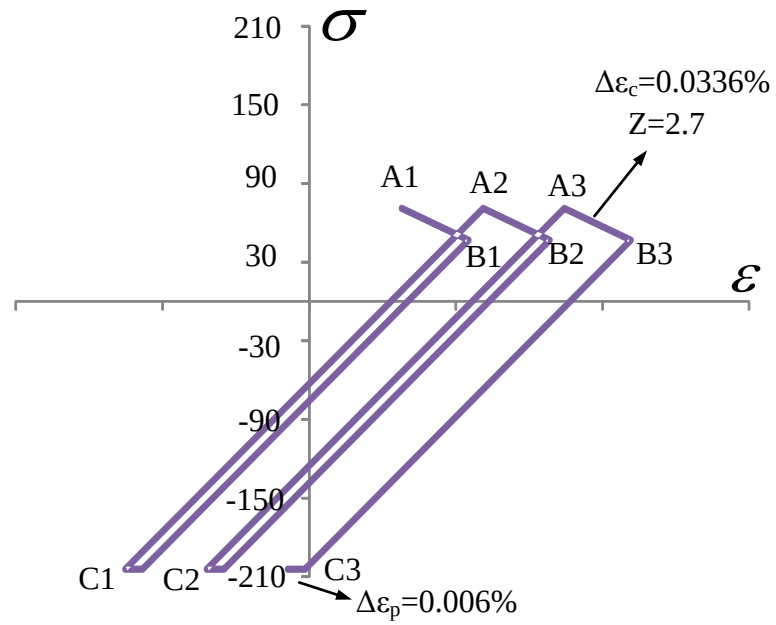

(a)

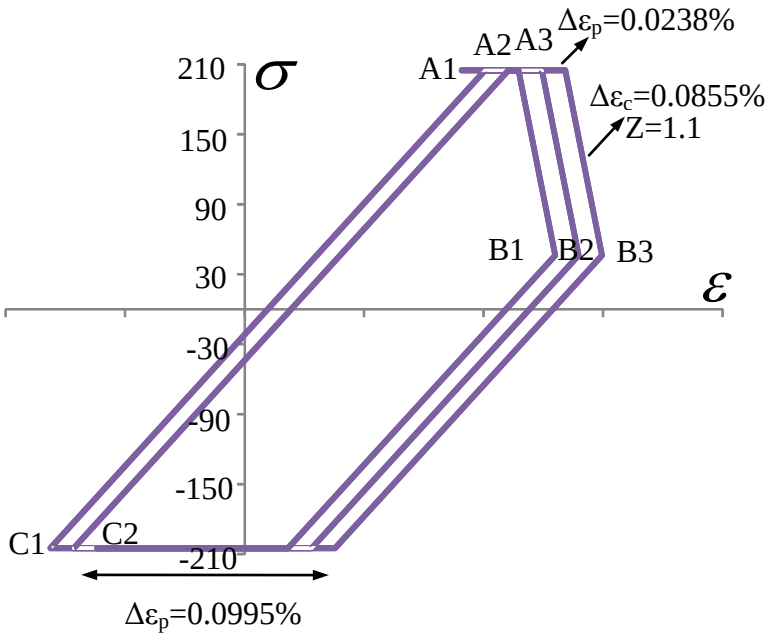

(b)

Figure 9.7 Response of the stress-strain path corresponding to the cyclic loading cases with 50 hour dwell time (a) case 5 (b) case 6

Two cyclic load points 5 and 6 (Figure 9.3), which are located in region *S2* and *P*, respectively, are chosen for investigating the other cyclic response with creep

effect beyond the creep ratchetting boundary. The steady state stress strain path for the cyclic loading points 5 and 6 with one hour and 50 hour dwell time period are shown in Figure 9.6 and Figure 9.7 respectively.

It is observed from Figure 9.6 that the steady-state stress and strain curve repeats the hysteresis loop ABC in every subsequent cycle, reaching the point A at the end of each start-up, the point B at the end of each dwell time and the point C at the end of each shut down. Due to the relaxation process the component material yields during unloading. Thus, the phenomenon of a closed hysteresis loop is generated at the cyclic load point 5 (Figure 9.6a) and at the cyclic load point 6 (Figure 9.6b) with one hour dwell time. It is observed form Figure 9.6b that there is plasticity during both the loading and unloading process for cyclic load point 6. Additional reverse plastic strains, which recover the inelastic strain due to start-up and creep dwell processes, develop due to the interaction of plasticity and creep, thus enlarging the closed hysteresis loop.

Figure 9.7 shows that the steady state responses of the structure at load points 5 and 6 no longer form a closed cycle when the creep dwell time is increased from 1 hour to 50 hours. The non-closed cycle follows the path $A_1B_1C_1A_2B_2C_2A_3B_3C_3$ showing a net accumulation of inelastic strain per cycle.

This phenomenon can be explained by the increase in dwell time causing a continuous increase in permanent creep strain. However, the reverse plastic strain, which cannot increase unlimitedly due to the limited magnitude of residual stress, is not able to recover the creep strain (Figure 9.7a) or the combination of creep strain and plastic strain during start-up (Figure 9.7b). Therefore, an open hysteresis loop is formed when the dwell time is increased.

An important parameter that is used to assess the significance of creep behaviour is the elastic follow up factor, defined as

$$Z = -\frac{\bar{E}\Delta\bar{\varepsilon}_c}{\Delta\bar{\sigma}_c} \tag{9.24}$$

Where $\bar{E} = E$ and $\bar{E} = 3E/[2(1+\upsilon)]$ denotes the effective elastic modulus with uniaxial and multiaxial case, respectively. $\Delta\bar{\sigma}_c$ is the change in effective creep stress, and $\Delta\bar{\varepsilon}_c$ is the effective creep strain during the dwell period. Z=1 corresponds to relaxation with zero change in total strain, and Z=∞ corresponds to steady state creep with no stress relaxation. With the estimated elastic follow-up factor, the creep strain can be evaluated approximately using (9.24) if a stress change during the dwell period can be measured [24]. Table 9.1 shows the values of elastic follow up factor obtained from the loading cases of 5, 6 and 7 (Figure 9.3) at the location with the highest creep strain. It can be seen that the values are sensitive to loading type. For cyclic loading case 6, which has low levels of primary loading, the increase in dwell time causes small changes in Z because the majority of the creep strain comes from stress relaxation. An increase in dwell time at load point 7 however, with larger levels of primary loading, results in a dramatic increase in Z. Although stress relaxation occurs in this situation, the primary loading results in creep strains with little relaxation, which becomes dominant at large dwell times.

Table 9.1 Values of the elastic follow-up factor Z at the location with the maximum creep strain (Figure9.3)

Load Loading Type (Figure 9.3)	Z dwell time 1h	Z dwell time 50h	Z dwell time 100h
Case 5	1.59	2.73	3.19
Case 6	1.24	1.84	1.94
Case 7	3.32	11.55	20.96

9.4 Plate with a Hole

9.4.1 Problem Description

A more practical example, a plate with a central hole and subjected to varying thermal loads and constant mechanical load is analysed using the proposed new LMM.

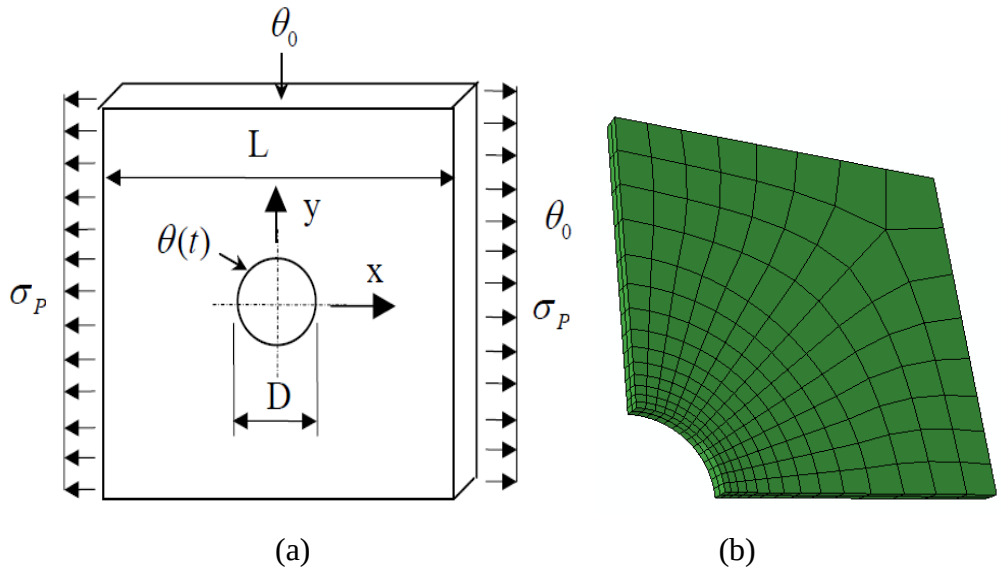

Figure 9.8 (a) Geometry of the plate with a hole subjected to varying thermal loads and its finite element mesh (D/L=0.2) (b) FEM

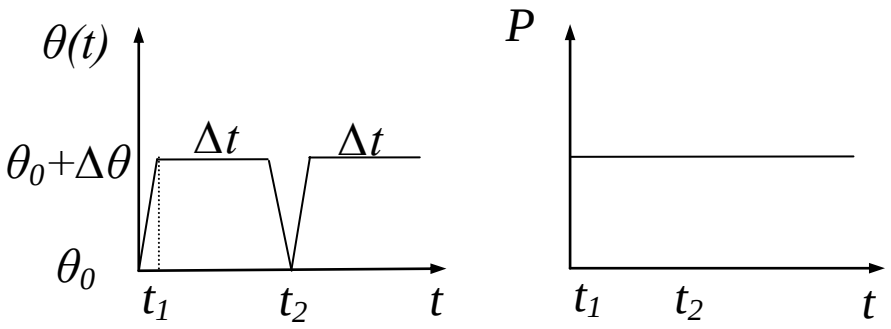

Figure 9.9 Load history with two distinct extremes (three load instances) to the elastic solution.

The geometry of the structure and its finite element mesh are shown in Figure 9.8. The 20-node solid isoparametric element with reduced integration is adopted. The ratio between the diameter D of the hole and the length L of the plate is 0.2 and the ratio of the depth of the plate to the length L of the plate is 0.05. The plate is subjected to a temperature difference $\Delta\theta$ between the edge of the hole and the edge of the plate and uniaxial tension σ_p acts along one side (Figure 9.8). The 3D plate with a hole is made of 304 stainless steel with the following material properties: yield stress σ_y=205MPa, Poisson's ratio, ν=0.3, Young's modulus, E=200 GPa, coefficient of thermal expansion, α=1.0x10^{-5}.

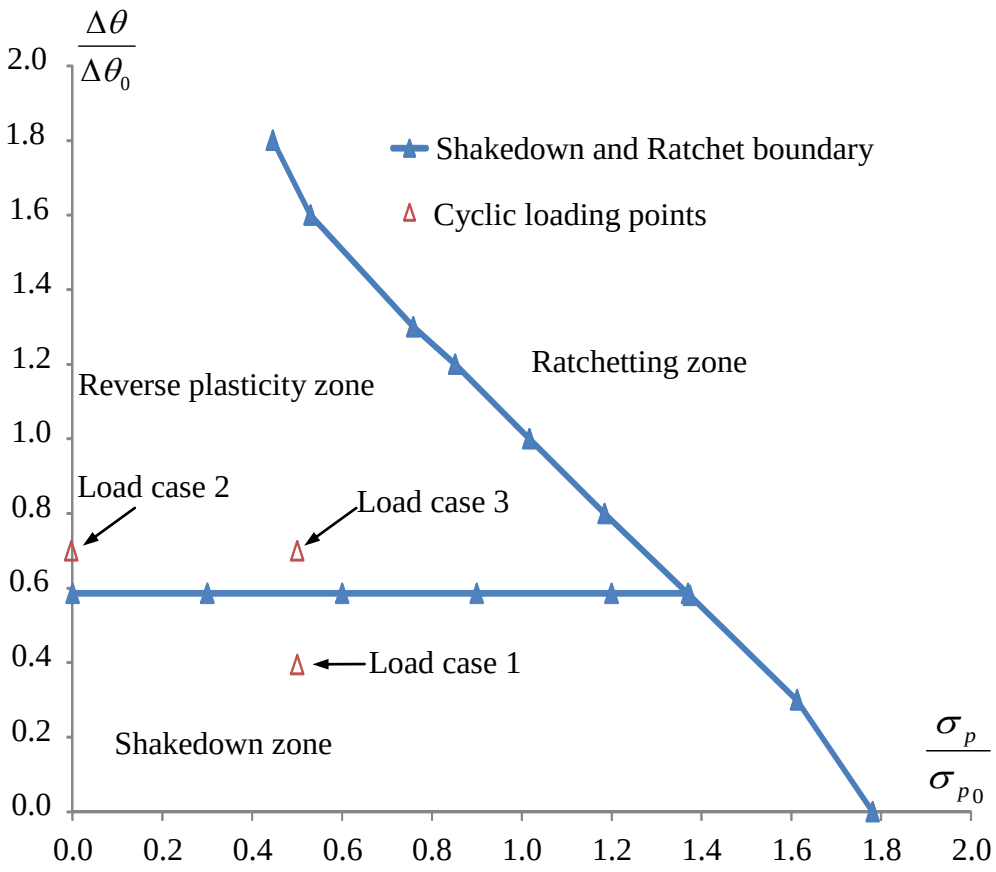

Figure 9.10 Elastic shakedown, reverse plasticity and ratchet region for the plate with a hole with constant mechanical and varying thermal load

The detailed temperature history at the inner bore of the hole is given in Figure 9.9, where $\theta(t)$ varies between θ_0 and $\theta_0+\Delta\theta$. When the ambient temperature θ_0 remains at $0^{\circ}C$, the magnitudes of the maximum thermo elastic stresses for the above thermal loading extremes can be determined by the maximum temperature difference $\Delta\theta$ between the bore of the hole and the edge of the plate. Hence the cyclic thermal load and constant mechanical load can be characterized by the maximum temperature difference $\Delta\theta$ and the uniaxial tension σ_p, respectively. The reference constant elastic mechanical stress can be calculated by the axial tension $\sigma_p=\sigma_{p0}=100MPa$ while the reference temperature difference $\Delta\theta=\Delta\theta_0=500^{\circ}C$ determines the reference cyclic elastic thermal stress. Two thermal stress extremes with three load instances are adopted for this cyclic load history:

---Load instance (1): The temperature distribution and axial tension are applied.

---Load instance (2): Both loads are sustained during a creep dwell.

---Load instance (3): The temperature load is removed (thus indicating the end of creep dwell), and the constant axial tension remains applied.

9.4.2 Results and Discussions

Figure 9.10 shows the shakedown and ratchet boundaries for the problem without the effects of creep, using the numerical procedures described in Chapters 3 and 5. In Figure 9.10 the applied uniaxial tension in the X-axis is normalized with respect to the reference uniaxial tension while the thermal load in the Y-axis is normalized by using the reference temperature difference $\Delta\theta=\Delta\theta_0=500^{\circ}C$. Three cyclic load cases 1 ($\Delta\theta=0.4\Delta\theta_0$, $\sigma_p=0.5\sigma_{p0}$), 2 ($\Delta\theta=0.7\Delta\theta_0$) and 3 ($\Delta\theta=0.7\Delta\theta_0$, $\sigma_p=0.5\sigma_{p0}$), which are located in the elastic shakedown and reverse plasticity region of the calculated boundary (Figure 9.10), are chosen to demonstrate the influence of different cyclic loading and dwell times on the cyclic response of a plate with a hole.

9.4.2.1 Verification

As mentioned in the previous section, this improved LMM has the new capability to calculate the structural response for different material and creep model. The verification of the numerical results produced by LMM and ABAQUS step-by-step analysis for elastic-perfectly plastic material model in accordance with Norton's law ("Combination Model One") and Ramberg-Osgood material model in accordance with Time Hardening law ("Combination Model Two") are shown in Figure 9.11-Figure 9.14.

For the creep material data in equation (9.15) we adopt Norton's law (steady-state creep stage) with B= 5.86e-15, n*=5 and m*=0, and the time hardening law for B= 1.01e-11, n*=2.727 and m*=-0.118 [126]

For the Ramberg-Osgood material model,

$$\frac{\Delta\varepsilon}{2}=\frac{\Delta\sigma}{2E}+\left(\frac{\Delta\sigma}{2B}\right)^{\frac{1}{\beta}} \tag{9.25}$$

we adopt E=200 GPa, B=423 and β=0.116854 [127]. All the material data are for 304 stainless steel.

The distribution of equivalent creep strain produced from LMM and step-by-step analysis for material model with Combination Model One and Two under loading case 2 (Figure 9.10) for a dwell period 10 hours are shown in Figure 9.11 and Figure 9.12, respectively. It is observed from Figure 9.11 and Figure 9.12 that the results from LMM are showing to be in a good agreement with the ABAQUS step-by-step inelastic analysis results. Similar agreement is also observed from Figure 9.13 and Figure 9.14, which show the results of equivalent creep strain distribution produced from LMM and step-by-step analysis for material model with Combination Model One and Two under loading case 3 (Figure 9.10) for dwell period of 10 hours.

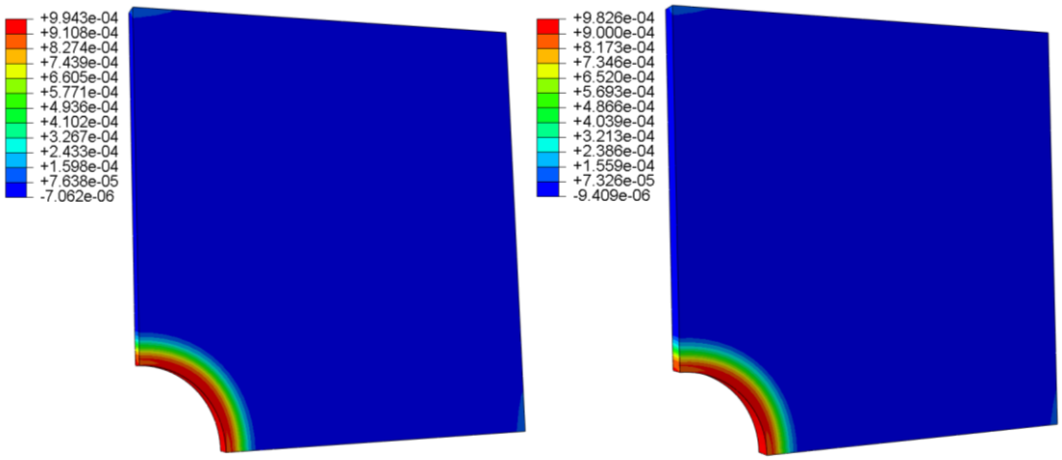

Figure 9.11 Equivalent creep strain distribution for elastic-perfectly plastic material model with Norton's law (Combination Model One) under loading case 2 after 10 hours dwell time (Figure9.10) (a) LMM (b) ABAQUS step-by-step analysis

Table 9.2 presents the values of equivalent creep and reverse plastic strain at the location with maximum creep strain produced from LMM and step-by-step analysis for different material models under loading cases 2&3 with 10 hours dwell time. It is observed form Table 9.2 that the difference for the values of maximum equivalent creep strain between LMM and step-by-step analysis is 2% and 5% for Combination Model One and Combination Model Two, respectively. Thus, the results (Figure 9.11-Figure 9.14 and Table 9.2) obtained using ABAQUS step-by-

step analysis confirm the accuracy and the capability of the results produced by the LMM.

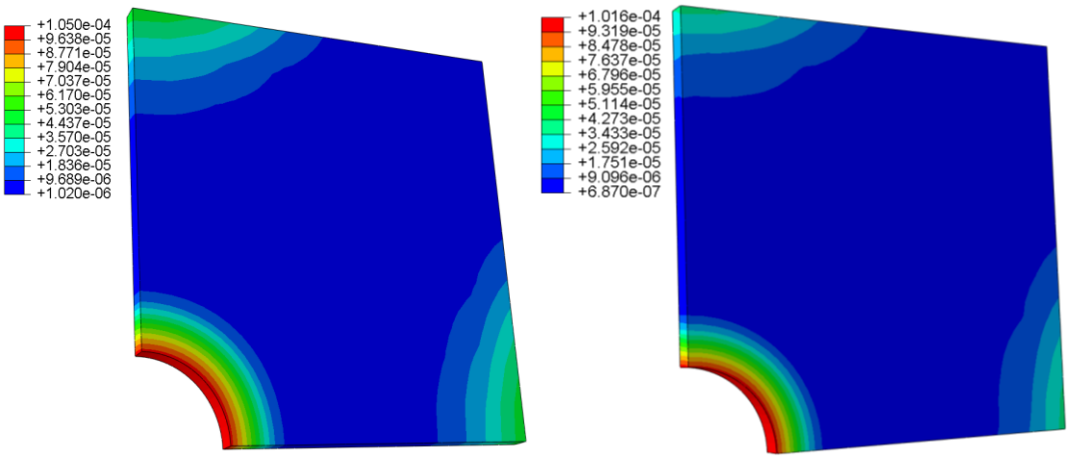

Figure 9.12 Equivalent creep strain distribution for Ramberg-Osgood material model with Time Hardening law (Combination Model Two) under loading case 2 after 10 hours dwell time (Figure9.10) (a) LMM (b) ABAQUS step-by-step analysis

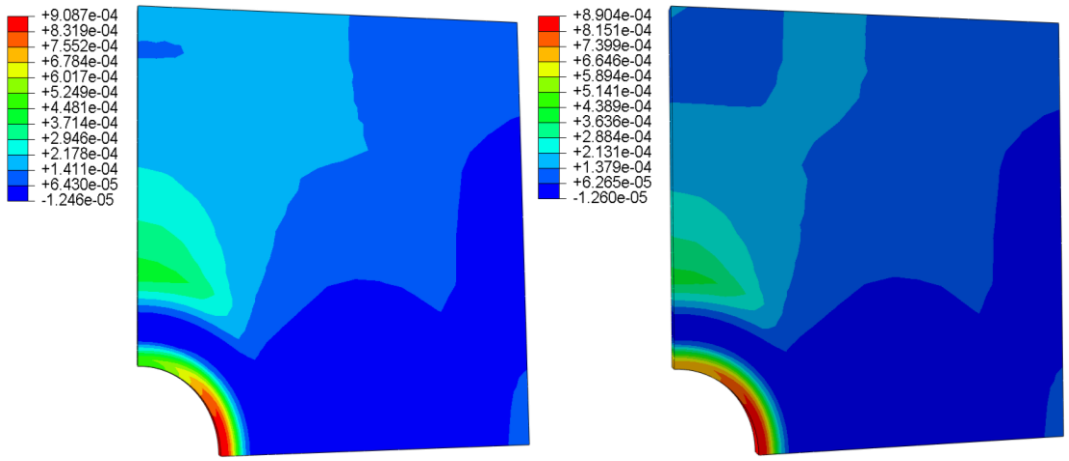

Figure 9.13 Equivalent creep strain distribution for elastic-perfectly plastic material model with Norton's law (Combination Model One) under loading case 3 after 10 hours dwell time (Figure9.10) (a) LMM (b) ABAQUS step-by-step analysis

As mentioned in Chapter 2, creep generally consists of three distinct stages, which are the primary, secondary (steady-state) and tertiary creep stage. Among these three stages, the secondary creep stage dominates each creep curve (Chapter 2) by constituting around 70% of the materials creep life. For simplification, the material model adopted in the coming sections is an elastic-perfectly plastic material model in accordance with Norton's law (Combination Model One).

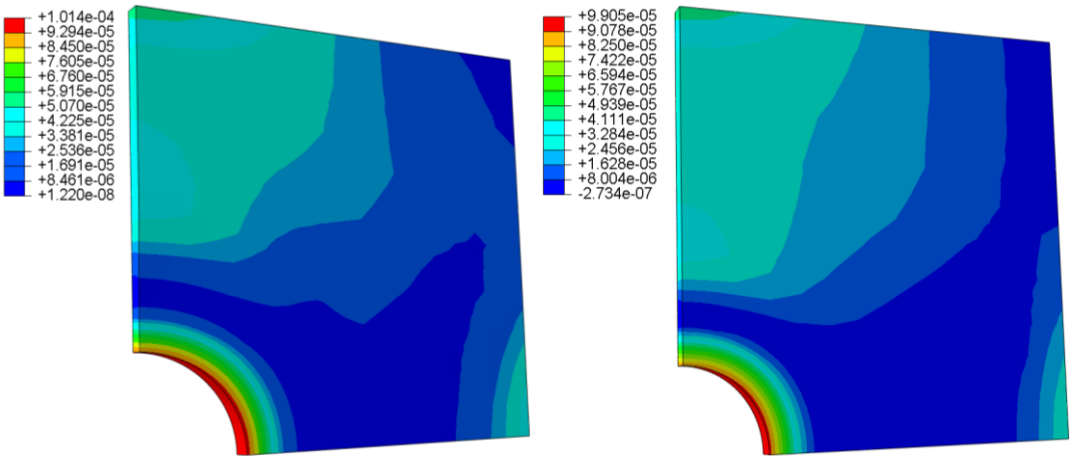

Figure 9.14 Equivalent creep strain distribution for Ramberg-Osgood material model with Time Hardening law (Combination Model Two) under loading case 3 after 10 hours dwell time (Figure9.10) (a) LMM (b) ABAQUS step-by-step analysis

Table 9.2 Values of equivalent creep and reverse plastic strain at the location with maximum creep strain for different material model under loading cases 2&3 (Figure9.10) with 10 hours dwell period produced from LMM and step-by-step analysis

Loading condition	Loading case 2		Loading case 3	
Numerical methods	Combination Model One	Combination Model Two	Combination Model One	Combination Model One
LMM (Creep Strain %)	0.0902	9.56e-3	0.086	9.132e-3
LMM (Reverser Plastic Strain %)	0.114	0.096	0.112	0.099
Step-by-step (Creep Strain %)	0.0882	9.05e-3	0.085	8.731e-3
Step-by-step (Reverser Plastic Strain %)	0.113	0.096	0.111	0.097

9.4.2.2 Locations of Maximum Creep Strain and Plastic Strain Range

The locations of maximum creep strain corresponding to different dwell period and cyclic load cases are shown in Figure 9.15 and Figure 9.16, respectively. It is observed from Figure 9.15 and Figure 9.16 that the location of maximum creep stain changes with changing dwell period and types of cyclic load cases.

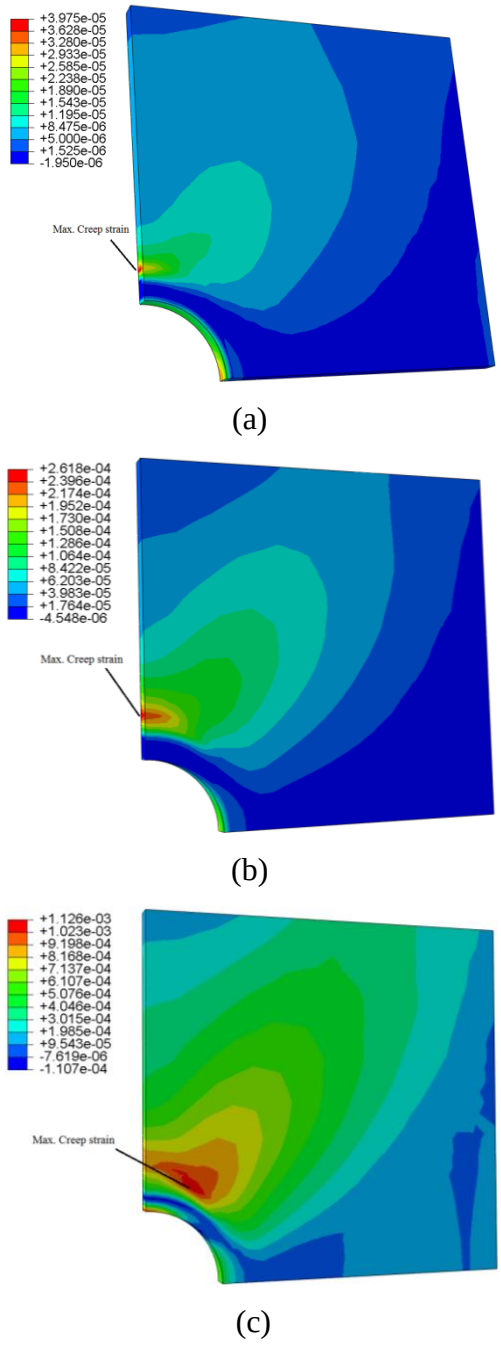

Figure 9.15 Location of maximum creep strain corresponding to the cyclic load case 1 with dwell period (a) 1 hour (b) 10 hours (c)100 hours

The locations of maximum plastic strain range corresponding to different dwell period and cyclic load cases are shown in Figure 9.17 and Figure 9.18, respectively. It is observed from Figure 9.17 and Figure 9.18 that the location of maximum plastic strain range changes with different types of cyclic load cases only, but it does not change with different dwell period.

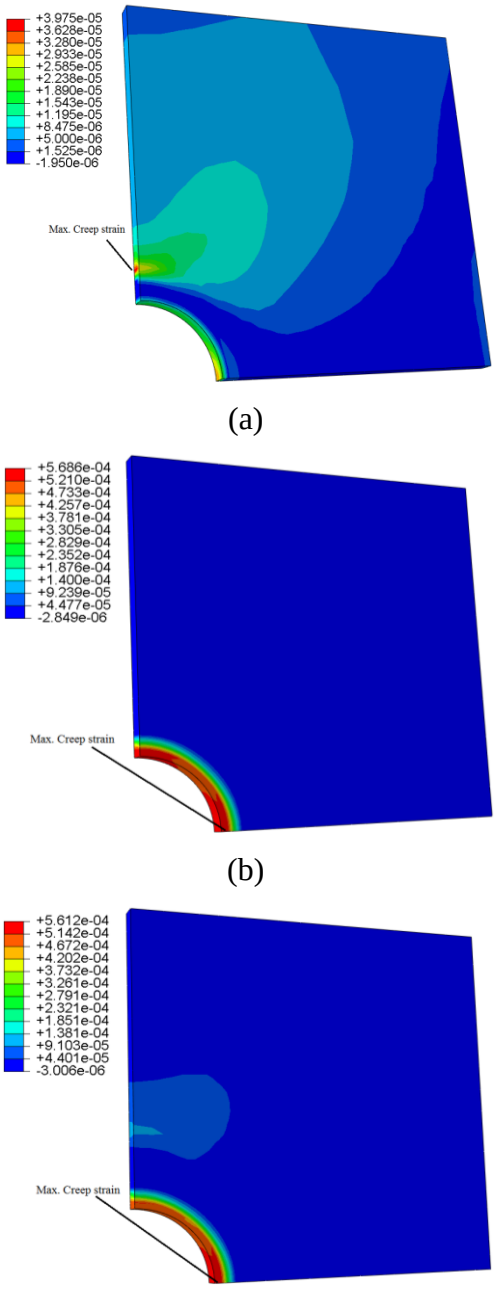

Figure 9.16 Location of maximum creep strain with 1 hour dwell period corresponding to the cyclic load (a) case 1 (b) case 2 (c) case 3

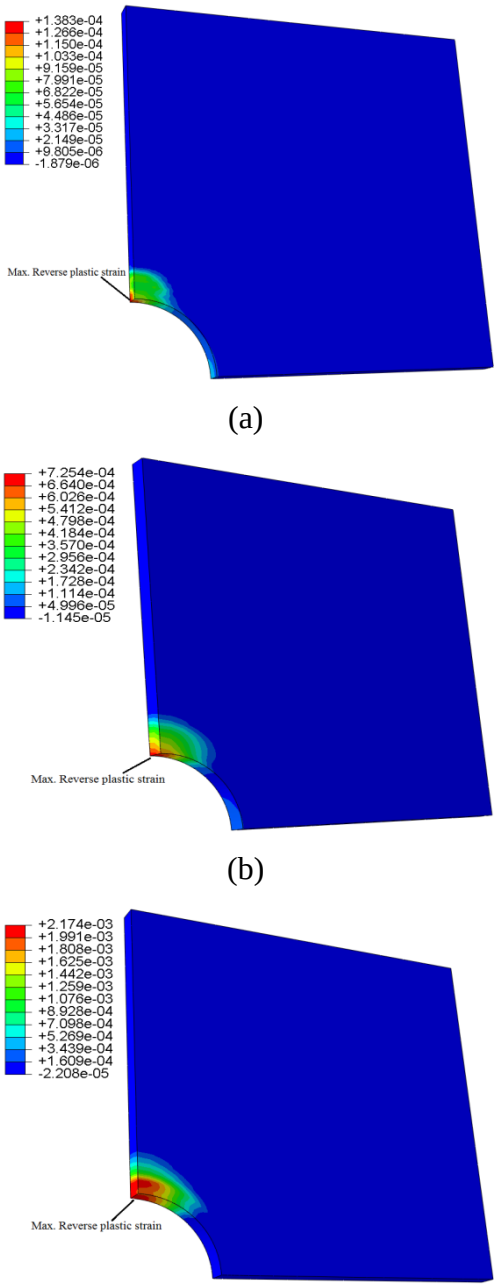

Figure 9.17 Location of maximum plastic strain range corresponding to the cyclic load case 1 with dwell period (a) 1 hour (b) 10 hours (c)100 hours

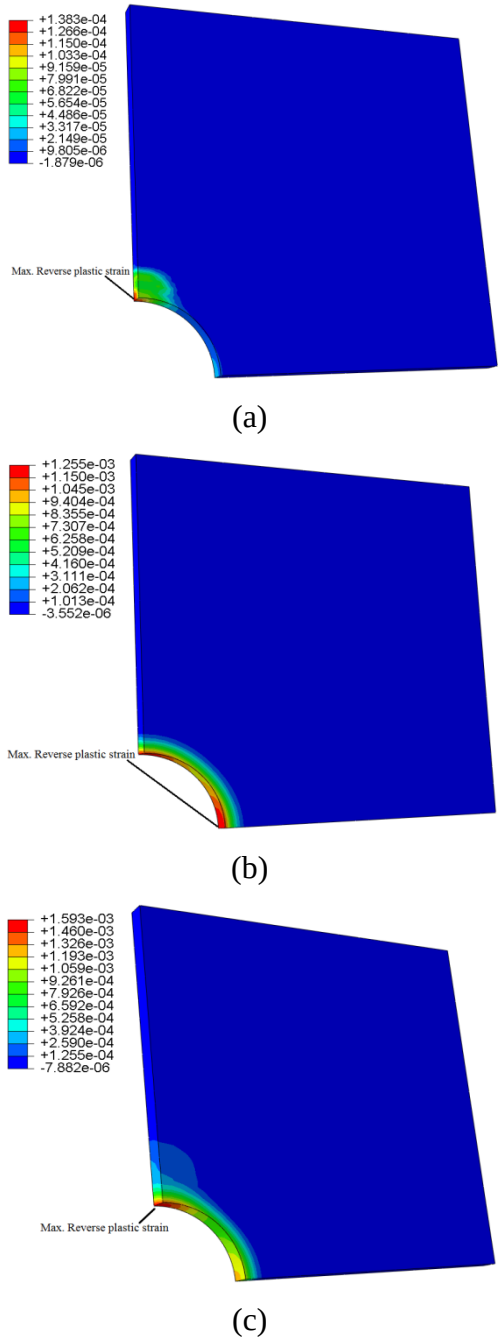

Figure 9.18 Location of maximum plastic strain range with 1 hour dwell period corresponding to the cyclic load (a) case 1 (b) case 2 (c) case 3

9.4.2.3 Cyclic Responses within Elastic Shakedown Region

The stress strain response for load case 1 at the location of maximum reverse plastic strain (Figure 9.17b) and maximum creep stain (Figure 9.15b) with dwell period of 10 hours is shown in Figure 9.19.

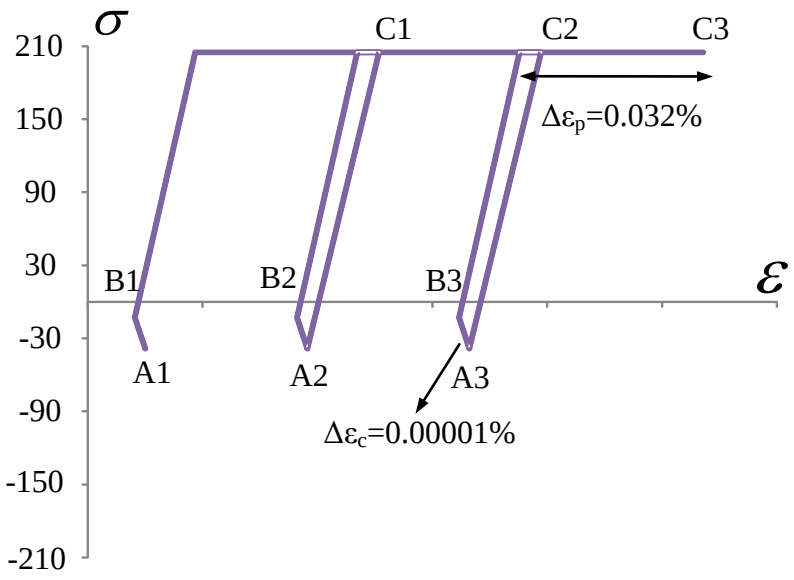

(a)

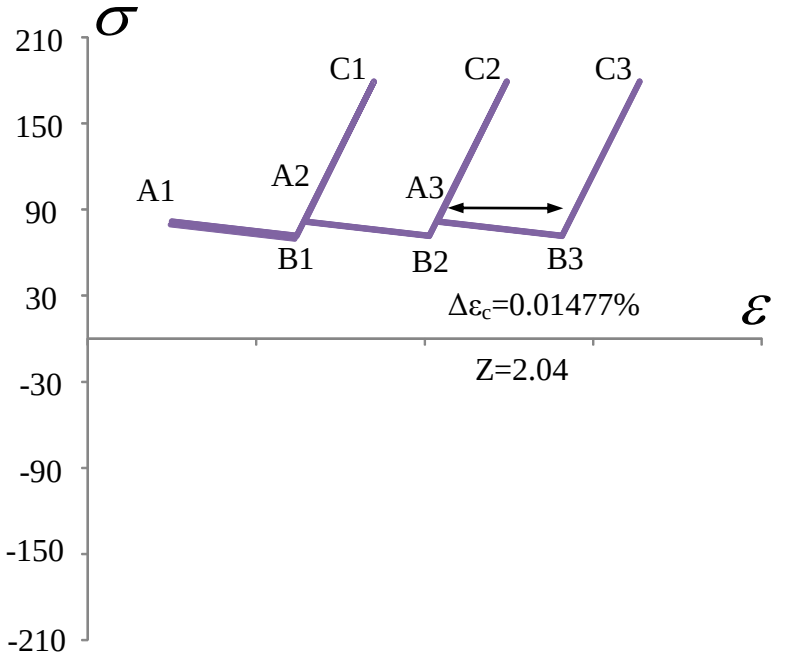

(b)

Figure 9.19 Response of the steady state stress-strain path corresponding to the cyclic load point 1(dwell period 10 hours) at the region with maximum (a) reverses plastic strain (b) creep strain

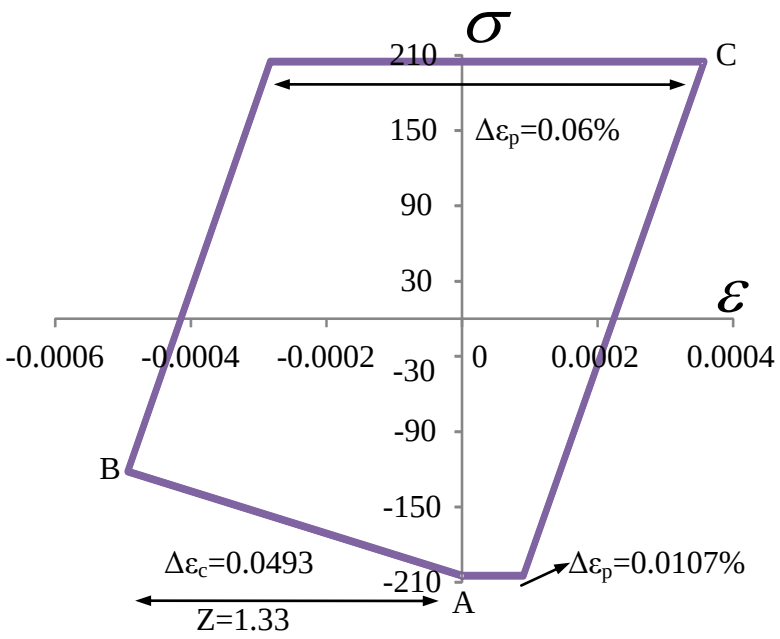

(a)

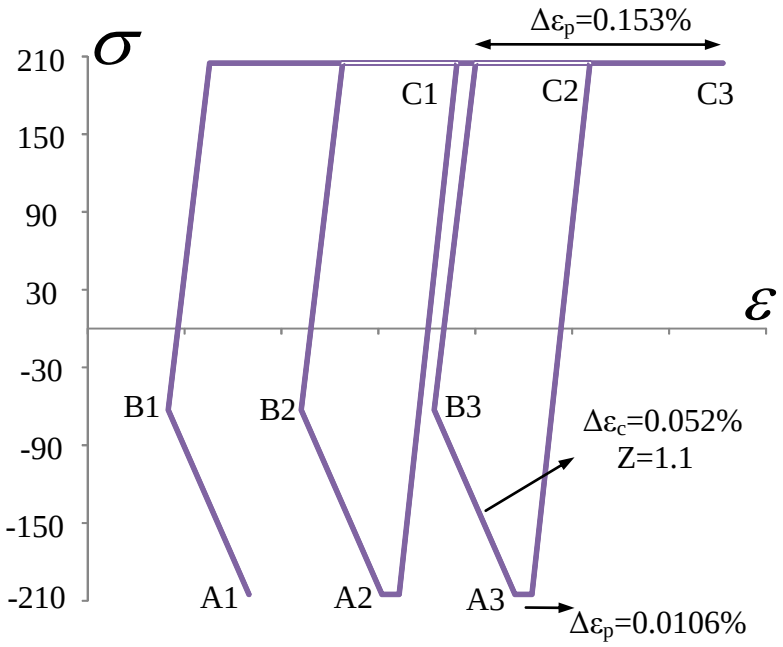

(b)

Figure 9.20 Response of the steady state stress-strain path corresponding to the cyclic load point 3 at the location with maximum reverse plastic strain with dwell period (a) 1 hour (b) 10 hours

From Figure 9.19 it is observed that the calculated steady-state of stress and strain follows the path $A_1B_1C_1A_2B_2C_2A_3B_3C_3$, etc. and reaches the point A_n at the end of the nth loading, the point B_n at the end of the nth dwell time and the point C_n at the end of the nth unloading. Both locations exhibit creep ratchetting as additional creep strain forms due to stress relaxation in every cycle.

It is observed form Figure 9.19a that the material yields during unloading due to the stress relaxation process in the structure. In Figure 9.19b the material is elastic during unloading. During loading the stress is reset to a higher value due to the formation of residual stresses in neighbouring regions. When considering possible failure mechanisms of the structure, both of these critical locations would need to be checked against different failure criteria (e.g. location at Figure 9.17b for the incremental plastic collapse and the location at Figure 9.15b for creep rupture).

9.4.2.4 The Behaviour of Cyclic Response with Changing Dwell Period

The steady state stress strain paths for the cyclic loading case 3 (Figure 9.10) at the locations of maximum reverse plastic strain with 1 and 10 hours dwell period are shown in Figure 9.20a and Figure 9.20b respectively. Figure 9.20a shows that the temperature gradient causes material to yield in compression on loading since the applied load is dominated by the compressive thermal stress. Then the creep causes the inelastic strain to increase in compression as the stresses relax. Removal of the temperature gradient causes the material to yield in tension during unloading and the reverse plastic strain recovers all the inelastic strain induced during loading and dwell time process. Therefore, the steady-state stress and strain curve (Figure 9.20a) repeats the hysteresis loop ABC with every subsequent cycle, reaching the point A at the end of each loading, the point B at the end of each dwell time and the point C at the end of each unloading. As the dwell period increases to 10 hours (Figure 9.20b), the stress relaxes further, causing the creep strain increase in compression. However, the small magnitude of creep stress causes a limited increase in creep strain. A larger reverse plastic strain is formed in tension during unloading due to the larger stress relaxation level. Thus, an opened hysteresis loop is generated and it follows the stress strain path of $A_1B_1C_1A_2B_2C_2A_3B_3C_3$.

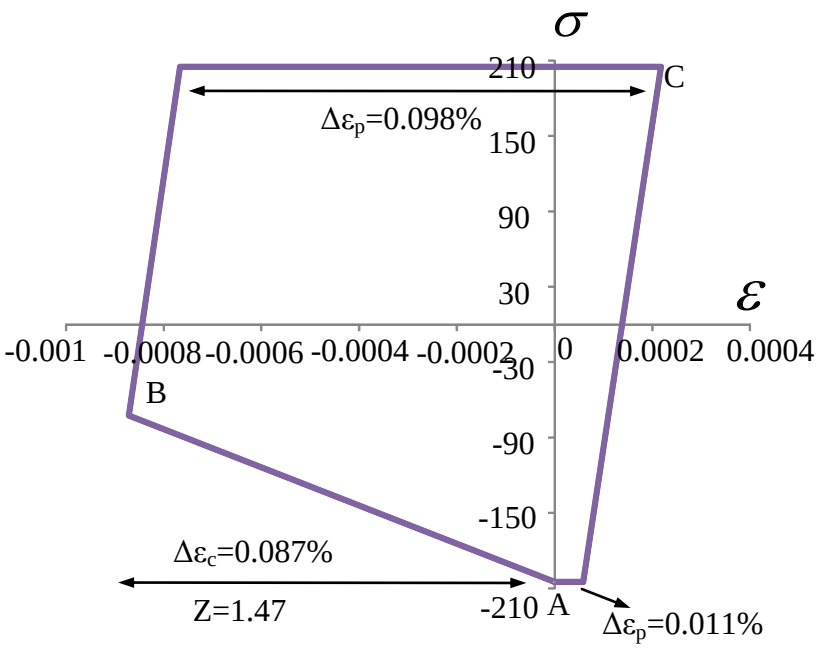

(a)

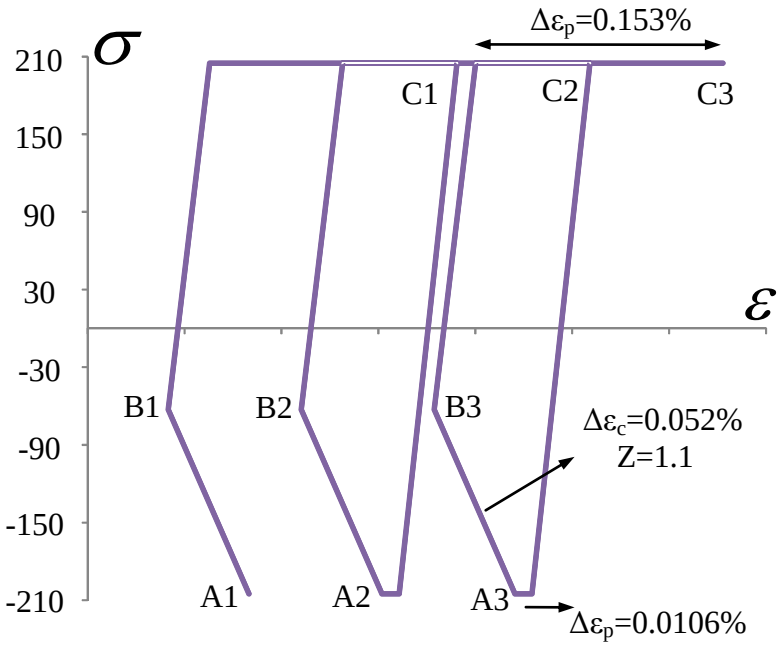

(b)

Figure 9.21 Response of the steady state stress-strain path with dwell period 10 hours at the location with maximum reverse plastic strain corresponding to the cyclic load points (a) 2 (b) 3

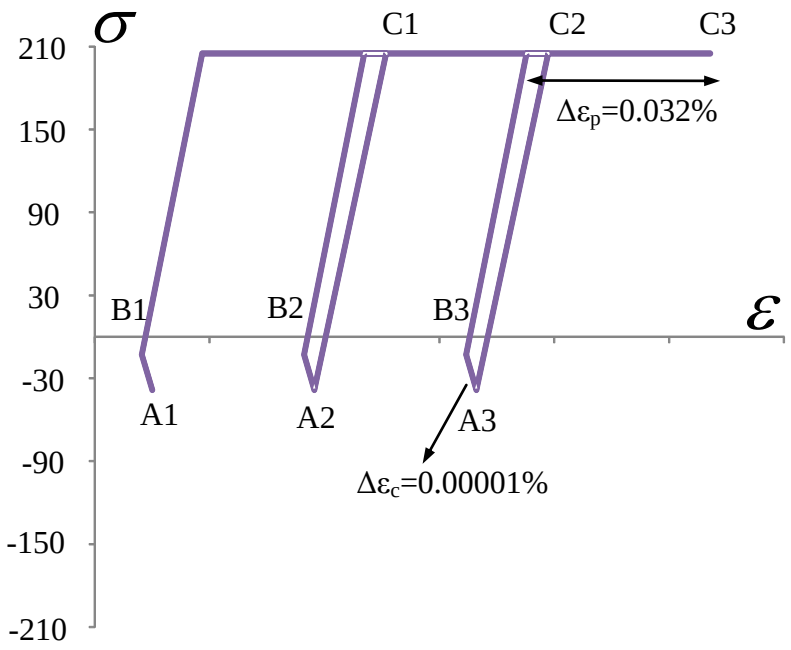

(a)

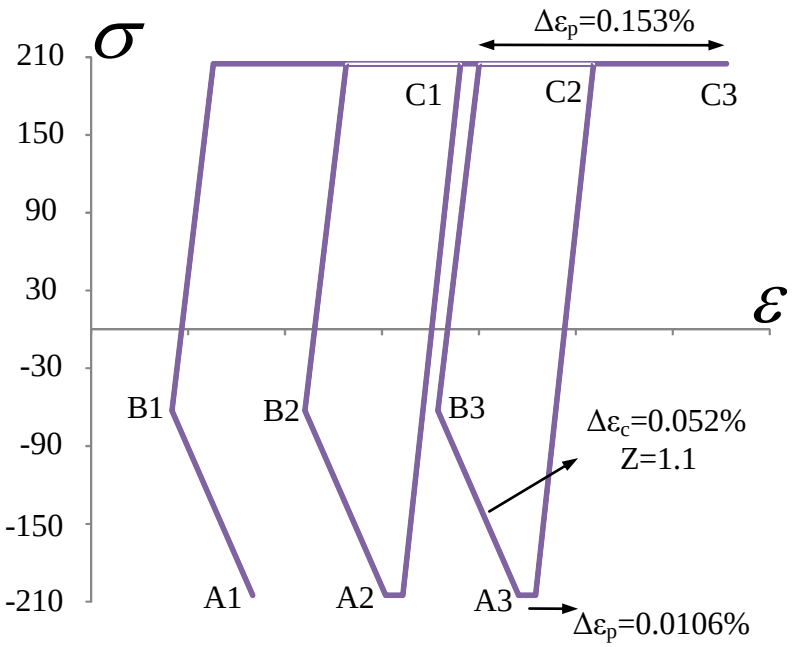

(b)

Figure 9.22 Response of the steady state stress-strain path with dwell period 10 hours at the location with maximum reverse plastic strain corresponding to the cyclic load points (a) 1 (b) 3

9.4.2.5 The Cyclic Response with Different Applied Loading

The steady state stress strain path for the cyclic loading points 2 and 3 (Figure 9.10) at the location of maximum reverse plastic strain with 10 hours dwell period are shown in Figure 9.21a and Figure 9.21b respectively. It is observed from Figure 9.21a that the steady-state stress and strain curve forms a closed hysteresis loop (ABC) when only cyclic thermal loading is applied. With an additional constant mechanical load (Figure 9.21b) applied in the tensile direction the value of stress drop becomes larger, and thus enlarges the reverse plastic strain upon unloading. Therefore, an opened hysteresis loop is created and follows the stress strain path of $A_1B_1C_1A_2B_2C_2A_3B_3C_3$.

The steady state stress strain paths for the cyclic loading points 1 and 3 (Figure 9.10) at the location of maximum reverse plastic strain with 10 hours dwell period are also compared in Figure 9.22. It shows that with the increasing cyclic thermal loads (Figure 9.22b), the higher temperature gradient causes material to yield in compression on loading. Larger creep strain is induced during stress relaxation process than that at load point 1 (Figure 9.22a). Removal of this higher temperature gradient causes a larger reverse plastic strain compared with Figure 9.22a.

Table 9.3 Values of the elastic follow-up factor Z at the location with the maximum creep strain

Load Loading Type (Figure 9.10)	Z dwell time 1h	Z dwell time 50h	Z dwell time 100h
Case 1	3.39	2.04	8.56
Case 2	1.52	1.81	1.91
Case 3	1.48	1.77	4.23

Table 9.3 shows the values of elastic follow up factor obtained from the loading cases of 1, 2 and 3 at the location with the highest creep strain. It can be seen from Table 9.3 that for cyclic loading cases 1 and 3, which has primary loading involved, the increase in dwell time causes larger changes in Z comparing to the load case without primary load (load case 2). The reason is that with the increased dwell time for the case with primary load higher creep strain occurs due to the higher stress level than the load case which has no primary load. For cyclic loading case 1, smaller

elastic follow-up factor with 10 hours dwell period is obtained comparing to the same case with 1 hour dwell period. This phenomenon can be explained by the change of the location of maximum creep strain due to the significant stress redistribution.

9.4.2.6 The Cyclic Response for a creep model occurring only at high temperature regions

In this study the main purpose is to demonstrate the capability of the extended LMM in calculating the creep-fatigue behaviour. Therefore, the above results are based on the same creep model where creep occurs at both, high and low temperature regions applied to the whole component. In reality, creep for steel occurs at temperatures which are greater than 40% of the absolute melting temperature. Thus, in the below calculation, by using LMM, the structural response for a creep model in which creep only occurs at high temperature regions will demonstrated.

The creep model [22] adopted from Norton's Power Law, is as follows:

$$\dot{\varepsilon}^c = \frac{\dot{\varepsilon}_0}{\sigma_0^{n^*}} \sigma^{n^*} \tag{9.26}$$

where $\dot{\varepsilon}_0$ is the uniaxial steady state creep rate corresponding to temperature θ and uniaxial stress σ_0. Here we adopt $\sigma_0 = \frac{\sigma_y}{2}$, n^*=5 and:

$$\dot{\varepsilon}_0 = 576.53108 \exp\left[\frac{(-19700)}{(\theta + 273)}\right] / hr \tag{9.27}$$

where the creep properties depend on temperature, typically for stainless steel. The steady state stress strain path for the cyclic loading point 2 (Figure 9.10) at the location of maximum reverse plastic strain with 10 and 1000 hours dwell periods are shown in Figure 9.23a and Figure 9.23b, respectively. It is observed from both figures that the steady-state stress and strain curves form a closed hysteresis loop (ABC) with dwell periods 10 and 1000 hours for minor stress relaxation, indicating that creep effect is insignificant under cyclic loading point 2.

Under loading case 2, the small regions where the temperature is high and the creep effect is large, are surrounded by low temperature regions (regions with insignificant creep effect). In order to maintain the self-equilibrium condition when

the structure is under the relaxation process, the stress at the high temperature regions drops slightly, and that is the reason why insignificant stress relaxation is observed in Figure 9.23.

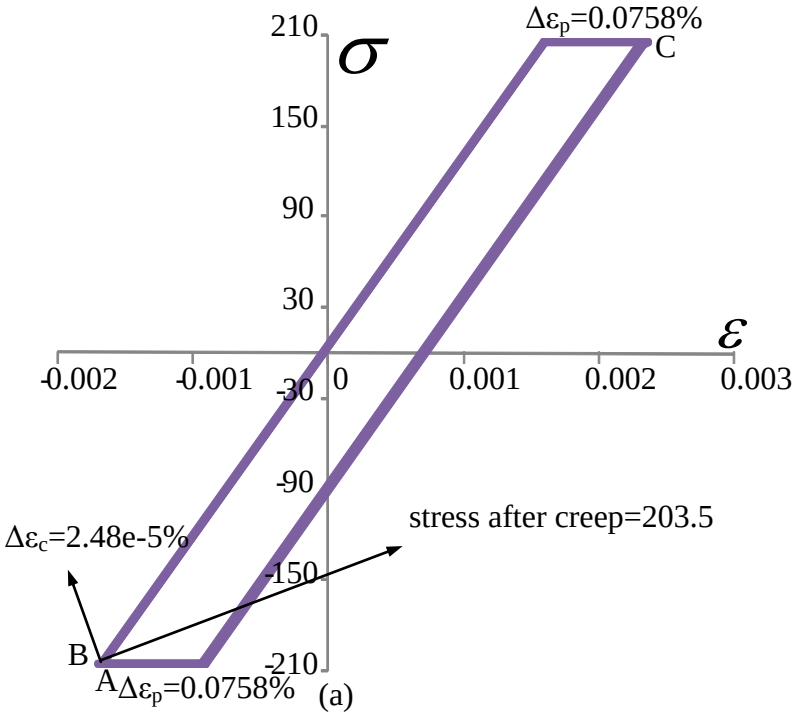

Figure 9.23 The response of the steady state stress-strain path for the creep model (mentioned in 9.4.2.6) at the location with maximum reverse plastic strain corresponding to the cyclic load point 2 with dwell periods (a) 10 hours (b) 1000 hours

9.5 Conclusions

In the present study, the structural response under cyclic loading including the effect of creep has been investigated using the LMM and the following observations have arisen:

1. The LMM has been derived and verified by the Bree problem, by being able to replicate the analytical creep ratchet limit. This method is able to evaluate the stable cyclic response (including creep and plastic strains) and elastic follow up factor. The LMM method has also been applied to a holed plate, and demonstrated its ability to determine the cyclic response and elastic follow up factor of more complex 3D structures.

2. Various cyclic responses for different loading conditions and dwell time periods have been investigated by the proposed method, which is able to address creep-fatigue damage and creep ratchetting issues.

3. It is possible for a closed cycle to form when a creep dwell occurs during the cycle where the reverse plastic strains completely recover the inelastic strain created during loading and creep dwell. However, the cycle may become non-closed if the creep strains become too large for the reverse plastic strains to recover.

4. The open hysteresis loops are either caused by the accumulation of plastic strain (ratchetting) during each load cycle (Figure 9.19a and Figure 9.20b), or determined by the accumulation of creep strain due to the cyclically enhanced creep (Figure 9.4b) or steady state creep (Figure 9.4a).

In Chapter 10, a further examination on a complex defective structure (a welded pipe) subjected to cyclic thermal load and constant internal pressure with the effect of creep will be conducted by using the numerical procedure mentioned in this chapter.

CHAPTER 10. ON THE EVALUATION OF A WELDED PIPE SUBJECTED TO CYCLIC THERMAL LOAD WITH CREEP FATIGUE INTERACTION

10.1 Introduction

Welds have critical importance in power plants and other installations. The components used in power plants operating at high temperatures are mainly complex and large in nature. Because of this, the connection of smaller components by welding is a much more common practise since forging or casting is generally much more expensive. Hence it can be said that welded joints are frequently encountered in every stage of plant operation.

10.1.1 Metallurgical and Mechanical Behaviour of Weldments

In a welding process a very hot weld metal (WM) called a weld bead is deposed, onto the cooler parent material (PM) of the components to be connected together. For large welded regions, to complete the weldment many weld beads will be laid. The PM adjacent to the weld bead, as each weld bead is laid down, is subjected to numerous heating and cooling cycles. This is producing a different structured material region compared to the PM away from the weld. This region is known as the heat-affected zone (HAZ) and its microstructure depends on the welding temperature magnitude and time it remains at this temperature, the number of heating cycles, the cooling rate, the material and the metallurgical state. Each of these different micro structural regions has its own stress, strain and rupture behaviour, which is dependent on the particular parent material, weld metal and welding conditions used for the component.

These zones generally have significantly different creep properties. For example, for low carbon steels generally the intercritical HAZ region is the weakest in terms of creep and rupture strength and has a higher ductility compared to the PM.

The WM strength and ductility can vary compared to the PM depending on material choice. e.g. [128] [129] [130]. Additionally, creep crack growth rates within different regions of the weldment can vary significantly; it may be very high in the WM region, producing a brittle mode of failure, while in regions such as the PM, crack growth is generally slow and controlled by a ductile failure mode. To effectively study creep/fatigue failure of welds it is important that all of these metallurgical and mechanical characteristics of weld behaviour are considered.

10.1.2 Numerical Analysis of A Welded Structure

The performance of power-generation components at high temperatures is generally limited by the fatigue, creep and creep-fatigue life of the weldments. For this reason, safe and reliable performance of all welded components is necessary for plants to operate effectively. However, due to the effects of material inhomogeneity of the weld, component geometry and loading, the creep, creep-fatigue interaction behaviour of welded plant structures gets complicated. As a result, since exact analytical creep solutions are not commonly available, numerical methods are usually used for specific material, geometry and loading combinations.

Conventional fusion weld geometries [131] are typically as shown in Figure 10.1, where the weld preparation angle, measured normal to the pipe or plate wall, is typically 15-30 degree. There are alternative designs [132] which specifically intended to reduce the volume of the metal present in the weldment. Such a design is referred to as Narrow Gap design, and it has a weld interface angle of around zero degree. The changes in the weld interface angle can result in major changes in the weld metal volume and may subsequently affect the stress distributions. This would mean that the failure life of the weld is also affected. Thus, an examination of the geometric effects of the pipe thickness and weld angle on the failure behaviour of a thick walled pipe weld is needed to be performed for creep and creep-fatigue conditions.

This chapter is concerned with the steady-state, creep, creep-fatigue behaviour of the heterogeneous weld-related material zones, investigating the importance of the weld and its effect on the design life. The numerical procedure of

the Linear Matching Method, as described in Chapter 9, was used to obtain the flow stress and creep strain distributions. The parametric study for the effect of failure behaviour for different size of WM and HAZ is investigated. The locations and values of the maximum creep and total strain range in the welded toe are identified and the creep fatigue lives are predicted using these maximum creep and total strain values, for a wide range of weld angles and pipe thicknesses.

10.2 Numerical Problem

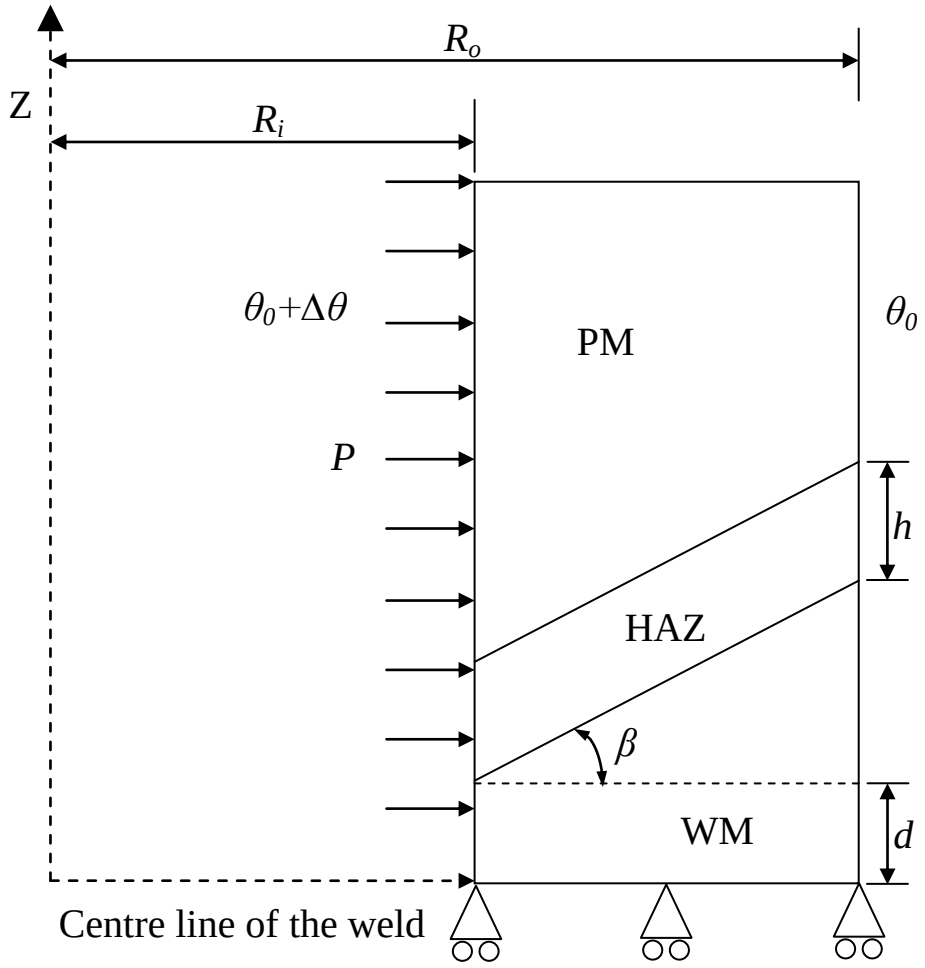

Figure 10.1 Dimensions and loading of the X20 CrMoV12-1 welded pipe

10.2.1 Geometry and Material Properties

The geometry [131] in a through thickness cross-section of a girth pipe weld subjected to varying thermal load and internal pressure is shown in Figure 10.1. The

three different material zones modelled are, the Parent Material (PM), the Weld Metal (WM), and the Heat-Affected Zone (HAZ), each of which is isotropic, elastic perfectly plastic and satisfies the von-Mises yield criterion for plastic behaviour. These regions are defined by a number of geometrical parameters. The heat-affected zone width is defined by the parameter *h*. The angle β defines the inclination of HAZ to the horizontal, the parameter *d* defines the width of weld toe. The inner radius R_i employed is 107.5mm [131], and the radius ratio R_o/R_i is 1.2. The parameter *d* and *h* employed are 6mm and 2.5mm, respectively, while the parameter, β , is varied from 0^0 to 30^0 degrees.

Table 10.1 Mechanical properties for the X20 CrMoV12-1 material at 550^0C [133]

Material	Yield stress σ_y(MPa)	Young's modulus E (GPa)	Poisson's ratio v	Coefficient of thermal expansion α ($°C^{-1}$)	Conductivity coefficient k ($Wm^{-1}°C^{-1}$)
PM	418	175253	0.3	1.246×10^{-5}	26.269
WM	520	175253	0.3	1.246×10^{-5}	26.269
HAZ	374	175253	0.3	1.246×10^{-5}	26.269

Table 10.2 Creep properties of Norton's model for the X20 CrMoV12-1 material at 550^0C [131]

Material	B	N^*
PM	2.8×10^{-17}	4.866
WM	5.266×10^{-16}	4.0
HAZ	5.6×10^{-17}	4.866

The initial residual stress in the pipe due to the welding process is considered to be zero due to post weld heat treatment [134]. And in this chapter, the Norton's law (steady-state creep stage) creep constitutive relation is adopted:

$$\dot{\bar{\varepsilon}}^c = B\bar{\sigma}^{n^*} \tag{10.1}$$

where $\dot{\bar{\varepsilon}}^c$ is the effective creep strain rate, $\bar{\sigma}$ is the effective von Mises stress, and *B*, *m* and *n** are the creep constants of the material. Table 10.1 and 10.2 show the mechanical and creep properties obtained from creep tests on X20 CrMoV12-1 material at 550^0C [131] [133], respectively.

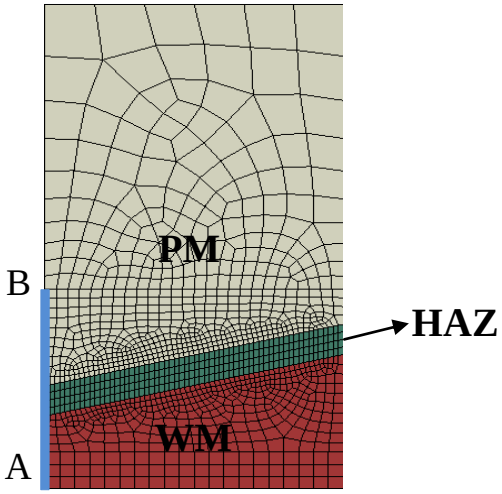

Figure 10.2 Finite element model of the X20 CrMoV12-1 welded pipe

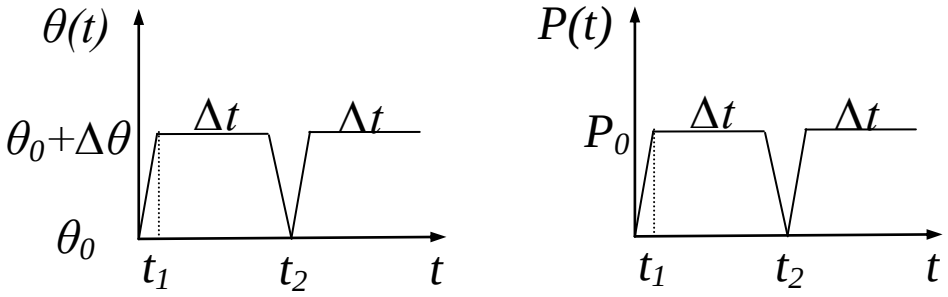

Figure 10.3 Load history with three distinct extremes (four load instances) to the elastic solution.

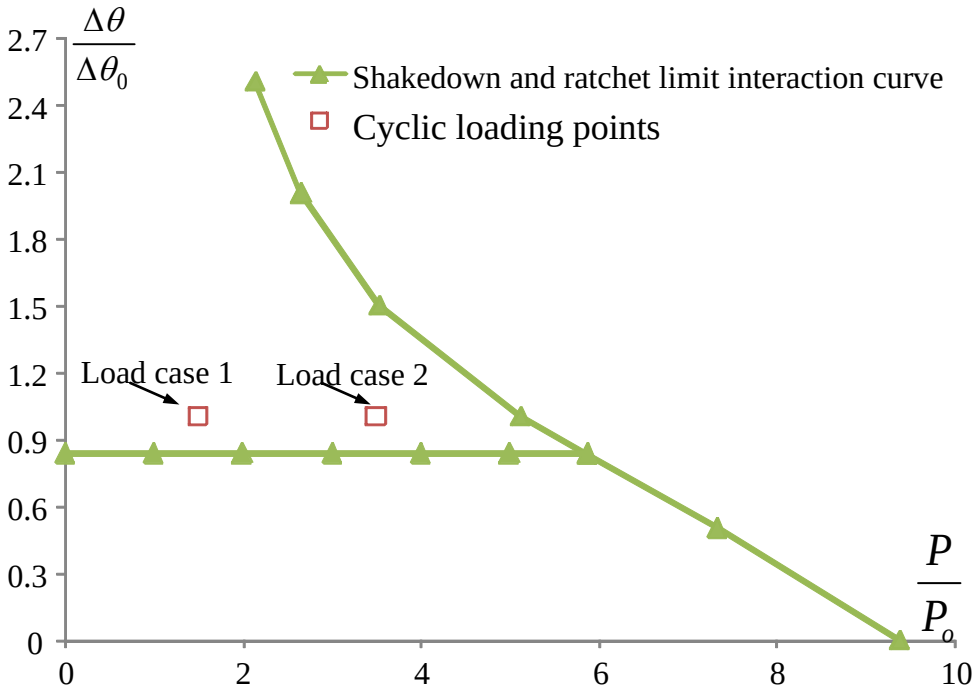

Figure 10.4 Shakedown and ratchet limit interaction curve for the welded pipe

10.2.2 Finite Element Model

Figure 10.2 shows the two dimensional axisymmetric model used in this analysis, with a symmetry condition applied in the axial direction. The free end of the pipeline is constrained in order to keep the plane section plane during loading, to simulate the expansion of a long pipe. The closed-end boundary condition is achieved by applying uniform axial thrust to the end of the pipe. The uniform axial thrust T_N induced by the internal pressure P is given by $T_N = PR_i^2/\left(R_o^2 - R_i^2\right)$. In this study, the ABAQUS type CAX8R 8-node biquadratic axisymmetric quadrilateral elements with reduced integration are used for structural analysis and DCAX8 8-node quadratic axisymmetric heat transfer quadrilateral elements with reduced integration scheme are used for the heat transfer analysis.

The detailed temperature and internal pressure history on the welded pipe is given in Figure 10.3, where $\theta(t)$ varies between θ_0 and $\theta_0+\Delta\theta$. When the ambient temperature θ_0 remains at 0^0C, the magnitudes of the maximum thermo-elastic stresses for the above thermal loading extremes can be determined by the maximum temperature difference $\Delta\theta$ between the inner surface and outer surface of the welded pipe. Hence the cyclic thermal load and the internal pressure can be characterized by the maximum temperature difference $\Delta\theta$ and the internal pressure P, respectively. The reference elastic stress induced by the internal pressure can be calculated as $P=P_0$=10MPa while the reference temperature difference $\Delta\theta=\Delta\theta_0$=550^{0}C determines the reference cyclic elastic thermal stress. Three thermal stress extremes with four load instances are adopted for this cyclic load history:

---Load instance (1): The temperature distribution and internal pressure are applied.

---Load instance (2): An internal pressure and a thermal stress occurring at the highest uniform temperature are applied due to the material mismatch.

---Load instance (3): Both thermal load and internal pressure are sustained during a creep dwell at 550^{0}C.

---Load instance (4): Both temperature load and internal pressure are removed (thus indicating the end of creep dwell)

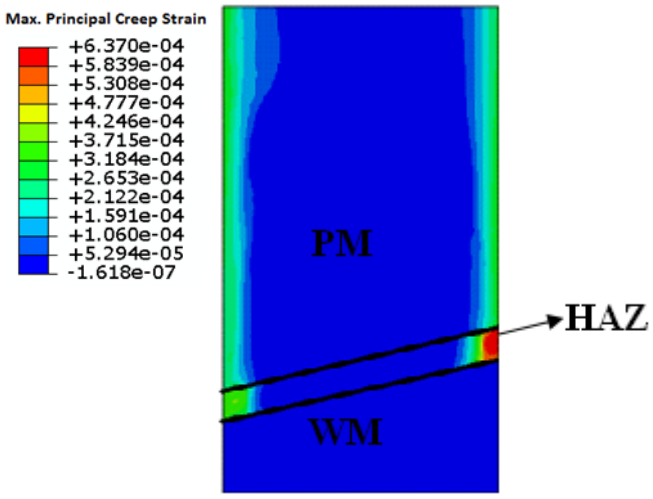

(a) 5 hours dwell period

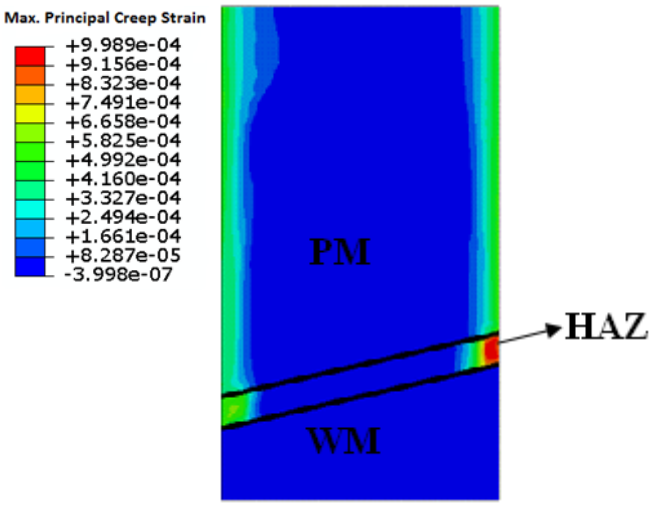

(b) 10 hours dwell period

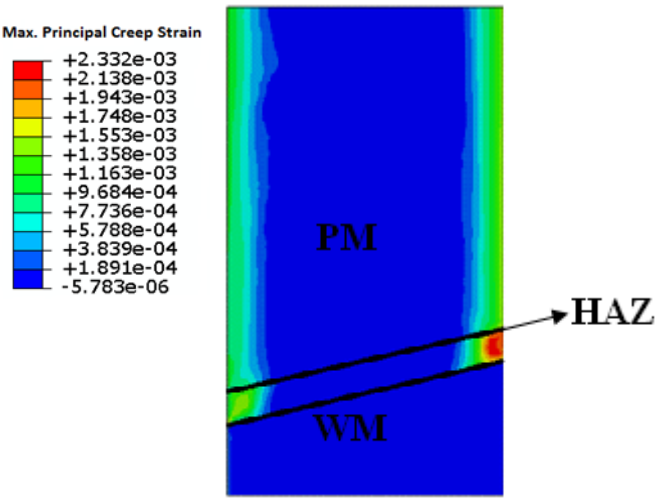

(c) 100 hours dwell period

Figure 10.5 Maximum principal creep strain for load case 1 with R_o/R_i =1.2 and β=13 after 100 load cycles from step-by-step analysis.

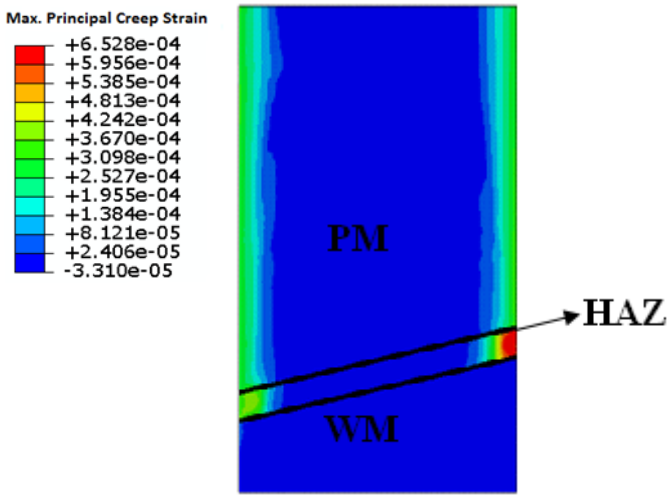

(a) 5 hours dwell period

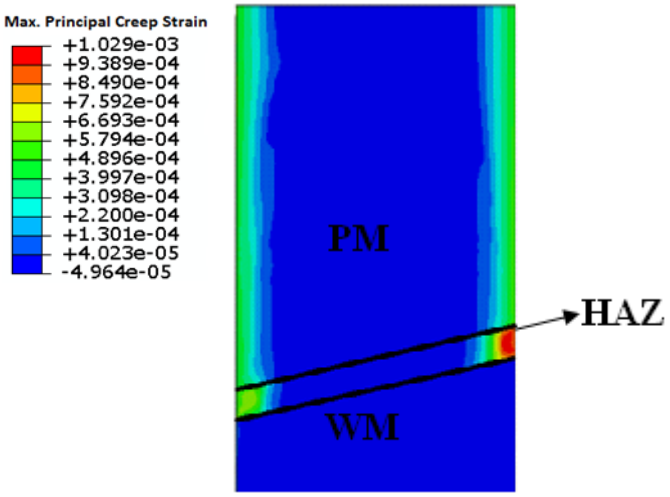

(b) 10 hours dwell period

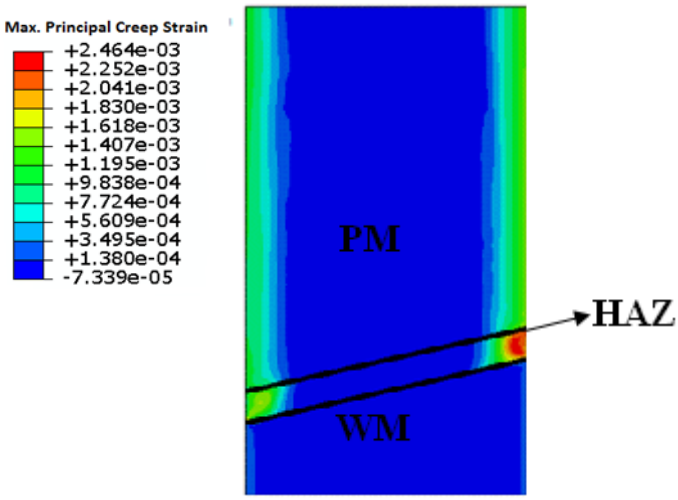

(c) 100 hours dwell period

Figure 10.6 Maximum principal creep strain for load case 1 with R_o/R_i =1.2 and β=13 by LMM

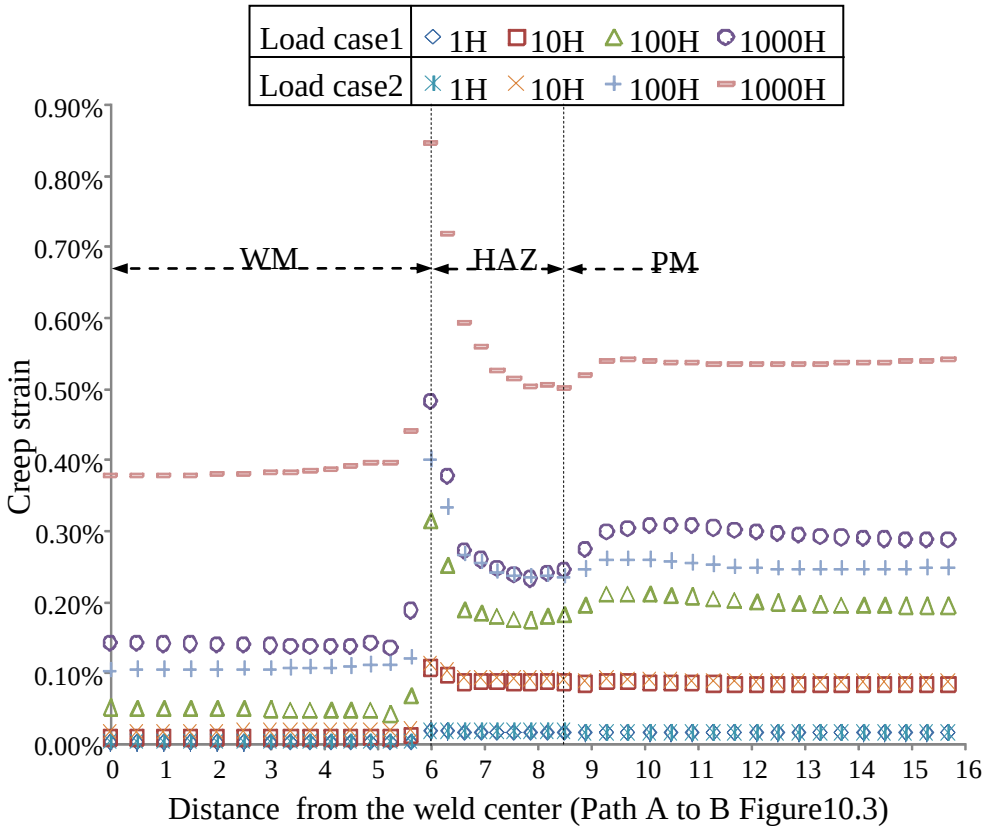

Figure 10.7 The effective creep strain distribution of the welded pipe with R_o/R_i =1.2 and β=13 for different dwell periods along the path AB in Figure 10.3.

10.3 Parametric Study

Figure 10.4 shows the shakedown and ratchet boundaries obtained from the numerical procedures described in Chapters 3&5, for the welded pipe subjected to the cyclic loading history as depicted in Figure 10.3, without the effects of creep. In Figure 10.4 the applied internal pressure in the X-axis is normalized with respect to the reference pressure (P_0=10MPa) while the thermal load in the Y-axis is normalized by using the reference temperature difference $\Delta\theta=\Delta\theta_0=550^0$C. Two cyclic load cases 1 ($\Delta\theta=\Delta\theta_0$, $P=1.5P_0$) and 2 ($\Delta\theta=\Delta\theta_0$, $P=3.5P_0$), which are located in the reverse plasticity region of the calculated boundary (Figure 10.4), are chosen to demonstrate the influence of dwell period and geometry effect on the distribution of creep and total strain of a welded pipe.

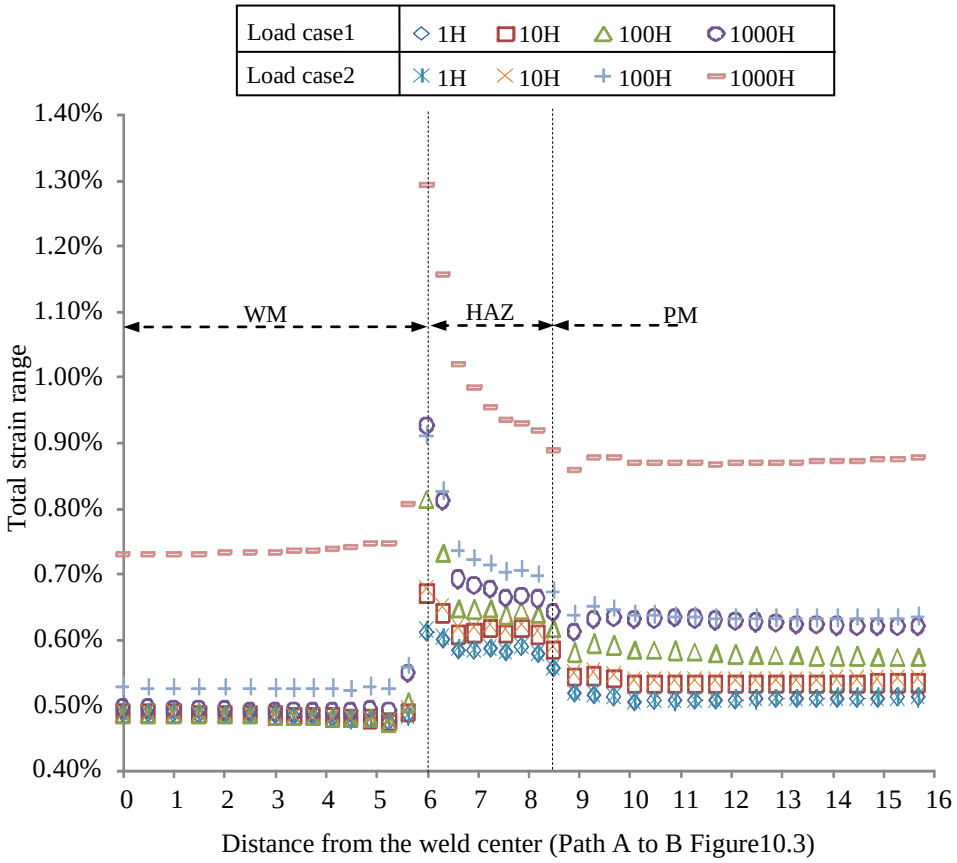

Figure 10.8 The total strain range distribution of the welded pipe with R_o/R_i =1.2 and β=13 for different dwell periods along the path AB in Figure 10.3.

In order to verify the numerical results produced by LMM, Figure 10.5 and Figure 10.6 present the accumulated creep strain after dwell period 5, 10, 100 hours for the welded pipe subjected to load cases 1 by both the ABAQUS step-by-step inelastic analyses and the LMM. The results from LMM show a good agreement with the ABAQUS step-by-step inelastic analysis results, although the values of the maximum principal creep strain produced by the LMM are slightly higher than those by ABAQUS step-by-step inelastic analyses. The reason for the smaller values of step-by-step inelastic analysis may be attributed to the cyclic response values failing to reach the steady cyclic state. In order to evaluate the structure at the steady cyclic state by step-by-step inelastic analysis, more load cycles need to be performed, which leads to slightly higher values of maximum principal creep strains.

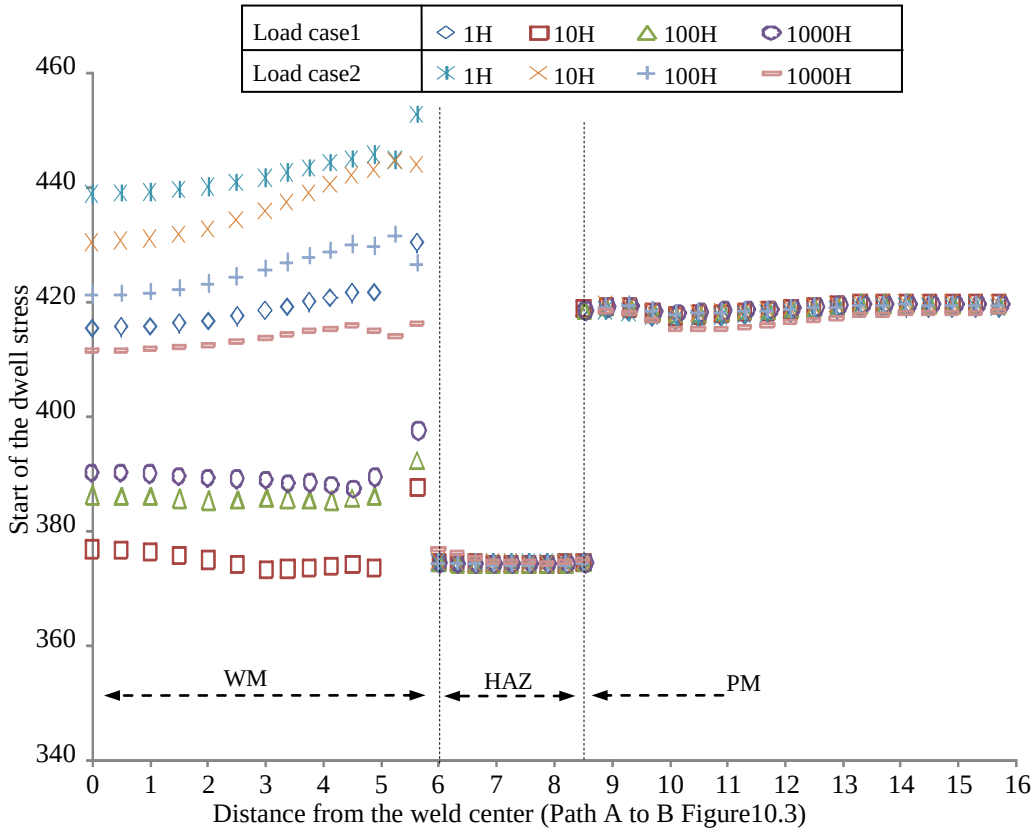

Figure 10.9 The initial stress distribution of the welded pipe with R_o/R_i =1.2 and β=13 for different dwell periods along the path AB in Figure 10.3.

10.3.1 Creep and Total Strain Distribution with Changing Dwell Time

For the loading cases 1&2, the variation of effective creep strain ε_c, and effective total strain range $\Delta\varepsilon_t$, with different dwell period along the path A to B (Figure 10.2) are shown in Figure 10.7 and Figure 10.8, respectively. It is observed that in these two figures the maximum creep strain and total strain range occur at the WM/HAZ interface within the HAZ for all the loading and dwell period cases. At this location, if we compare the loading cases 1&2, the peak creep and total strain range increase slightly when the dwell period is at 10 hours, and become increasingly significant as the dwell period rise. A similar phenomena is also observed in the PM and WM. The variation of the start of dwell stress and the flow stress (or stress state after creep) along AB are shown in Figure 10.9 and Figure 10.10, respectively. Figure 10.9 shows that within the HAZ, the variation of the start of dwell stress is

equal to the value of yield for both loading cases. After dwell period, it is observed from Figure 10.10 that within the HAZ, the larger the dwell period, the greater value of stress reduction (the greater stress relaxation).

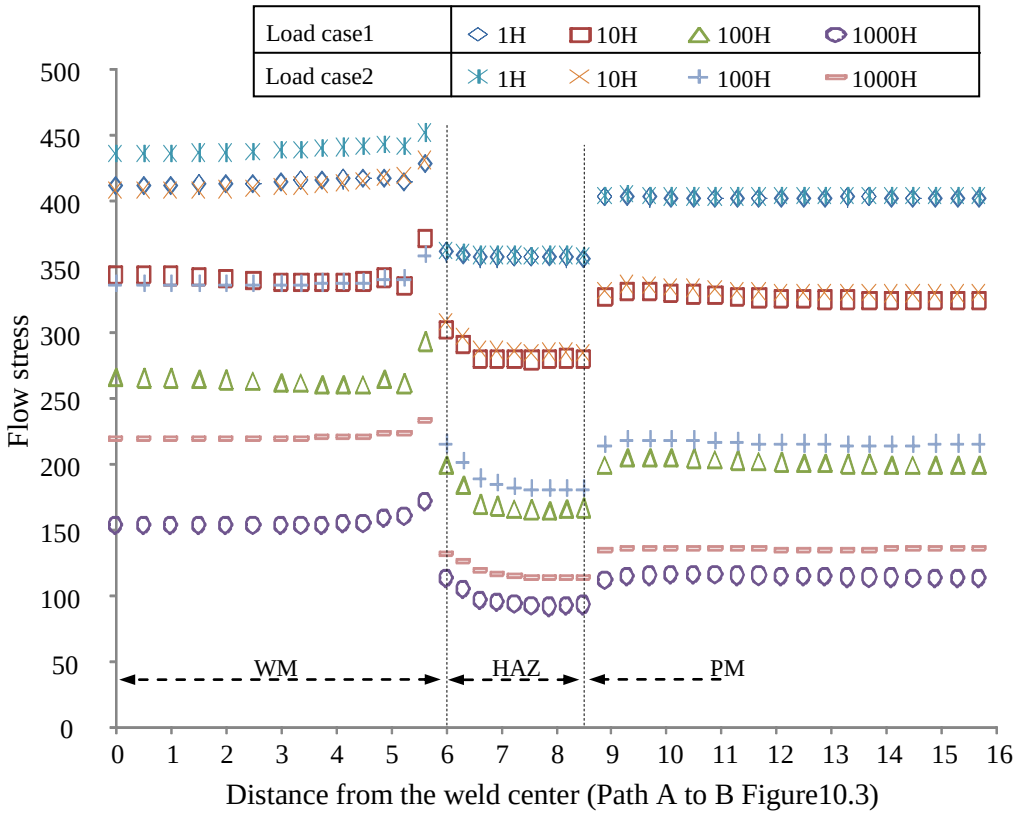

Figure 10.10 The flow stress distribution of the welded pipe with R_o/R_i =1.2 and β=13 for different dwell periods along the path AB in Figure 10.3.

10.3.2 Creep and Total Strain Distribution with Changing Welded Angle

The variations of the effective creep strain and total strain range with 100 hours dwell period and load case 1 for seven β-values, are shown in Figure 10.11 and Figure 10.12, respectively. It is observed from Figure 10.11 and Figure 10.12 that the maximum creep stain and total strain range increases with the increase of β at the location of WM/HAZ interface within the HAZ. The effective creep strain is almost independent of β in PM and WM. Similar behaviour is also observed for the distribution of the total strain range, in Figure 10.12, which shows that the total strain range is nearly independent of β within PM and WM.

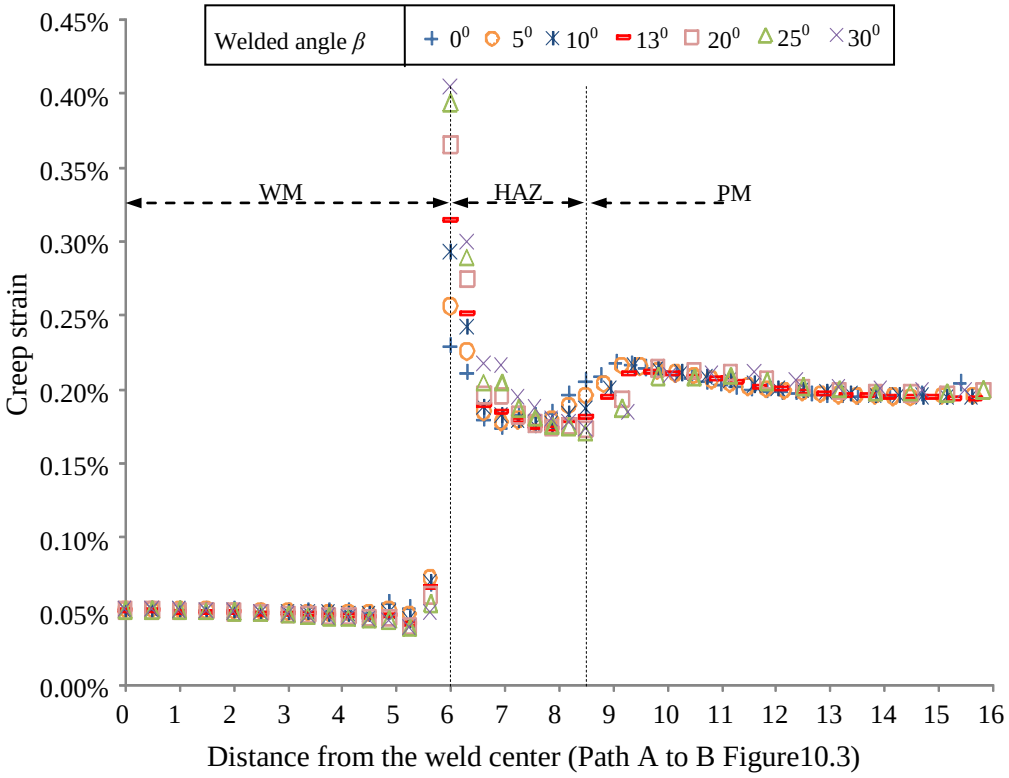

Figure 10.11 The effective creep strain distribution of the welded pipe with R_o/R_i =1.2 and dwell period=100hours for different welded angles β along the path AB in Figure 10.3.

10.3.3 Creep and Total Strain Distribution with Changing Radius Ratio R_o/R_i

Figure 10.13 and Figure 10.14 present the effects of the radius ratio R_o/R_i on the distribution of the effective creep strain and total strain range, respectively. Four different thickness ratios R_o/R_i=1.1, 1.2, 1.3, 1.4 of the welded pipe for 100 hours of dwell period with β=13 and under load case 1, were analyzed.

It is observed from Figure 10.13 that the creep strain is almost independent of the radius ratio for the location with maximum creep strain at WM/HAZ interface within the HAZ. At the same location, Figure 10.14 shows that increasing the radius ratio increases the total strain range. The increase in total strain range is caused by the increasing of the welded pipe thickness which causes higher thermal stress distribution.

Figure 10.13-Figure 10.14 also shows that the distribution of the creep strain and total strain range are changed slightly with different radius ratio R_o/R_i within PM and WM.

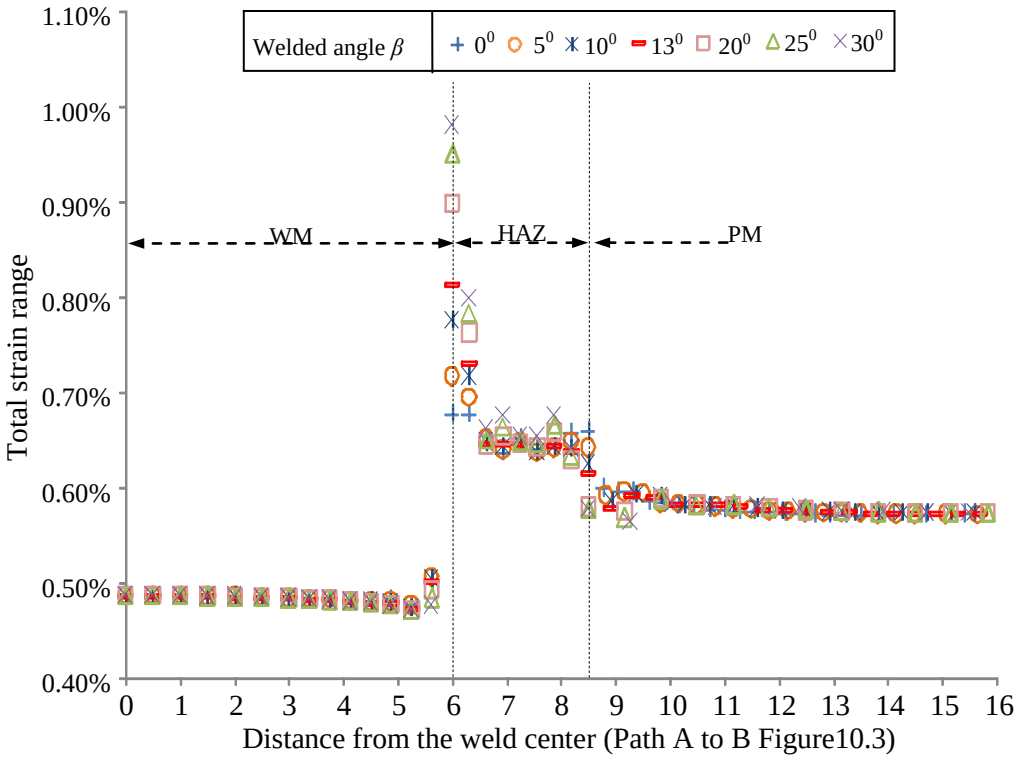

Figure 10.12 The total strain range distribution of the welded pipe with R_o/R_i =1.2 and dwell period=100hours for different welded angles β along the path AB in Figure 10.3.

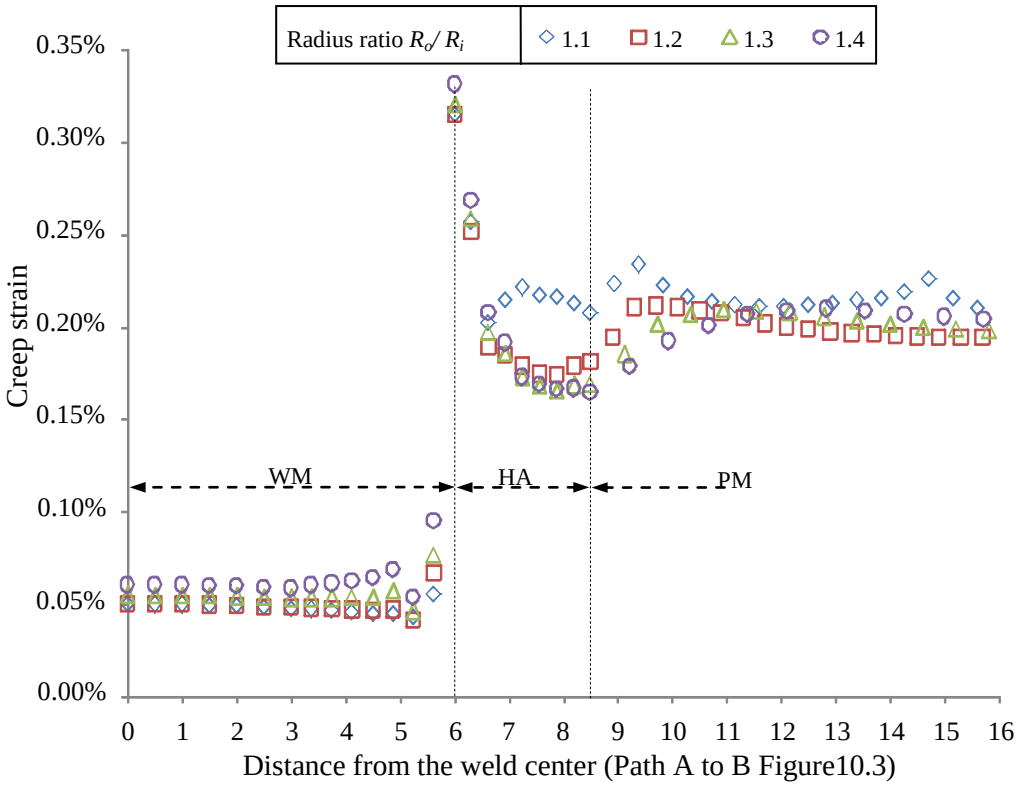

Figure 10.13 The effective creep strain distribution of the welded pipe with β =13 and dwell period=100hours for different thickness ratios R_o/R_i along the path AB in Figure 10.3.

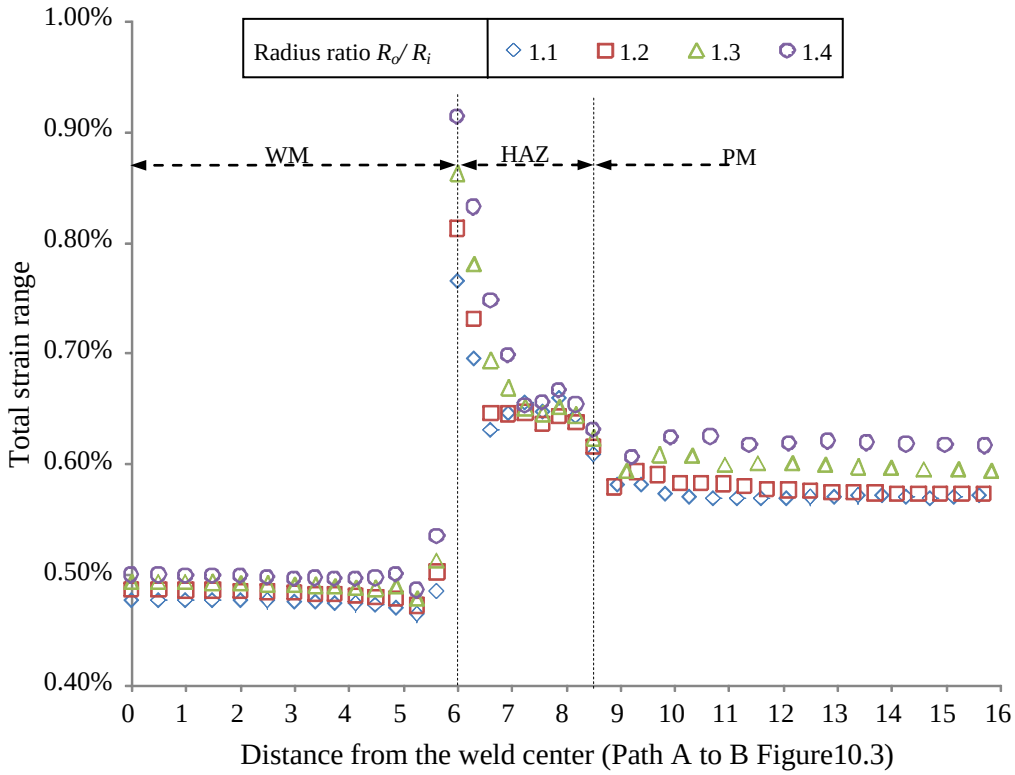

Figure 10.14 The total strain range of the welded pipe with β =13 and dwell period=100 hours for different thickness ratios R_o/R_i along the path AB in Figure 10.3.

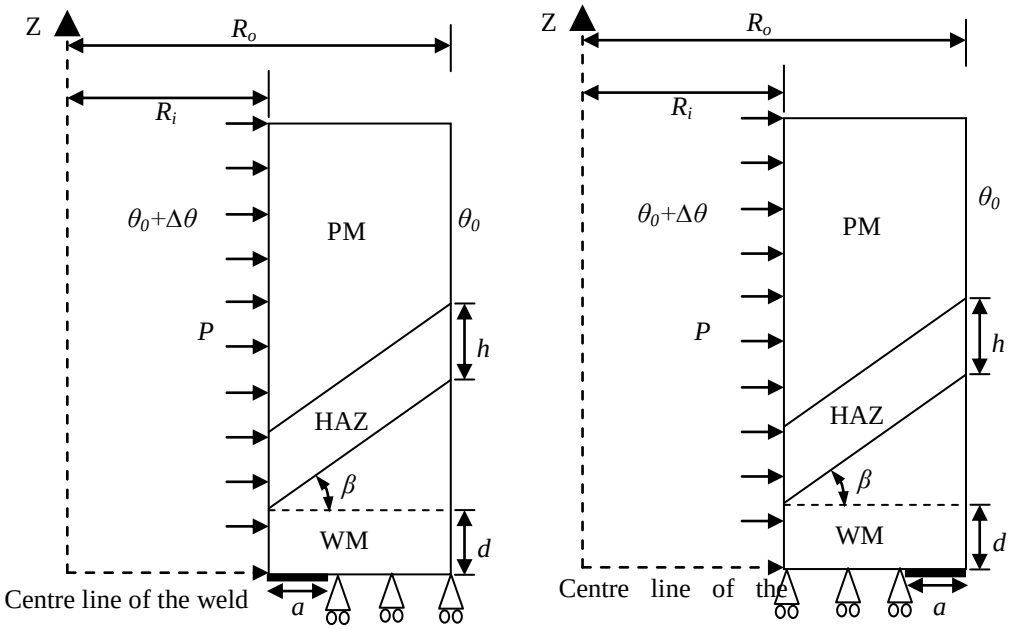

Figure 10.15 Configurations of weld cracking in the WM (a) an inner crack (b) an outer crack

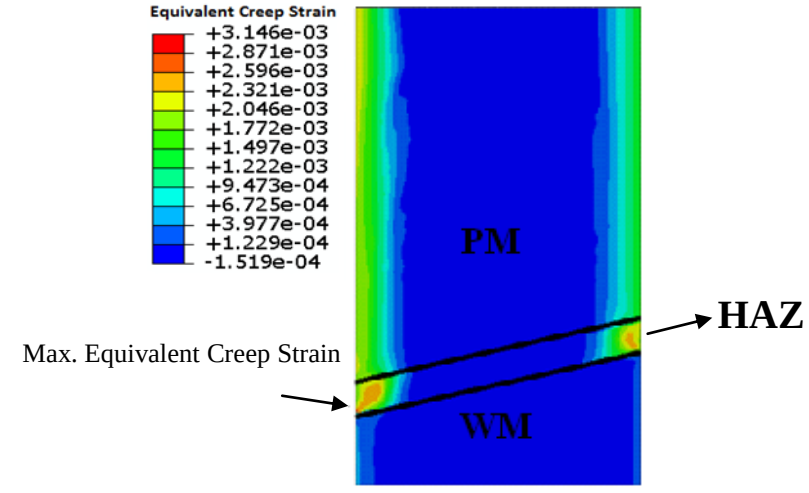

(a) Without crack

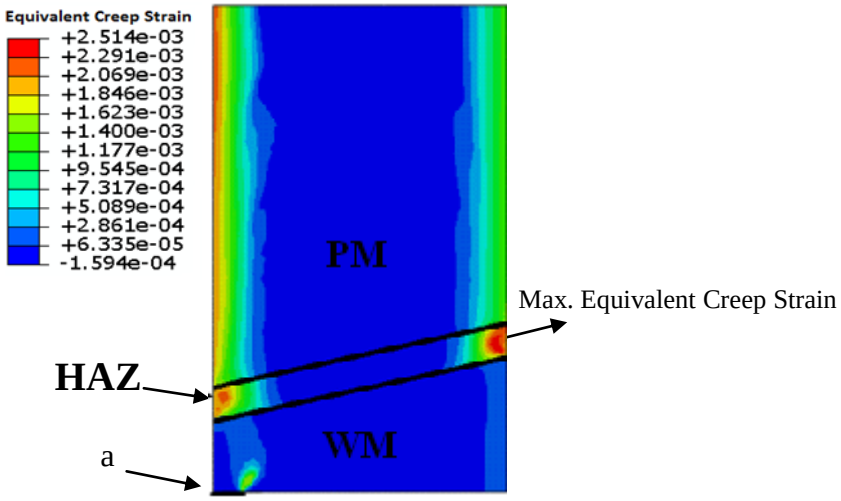

(b) Inner crack

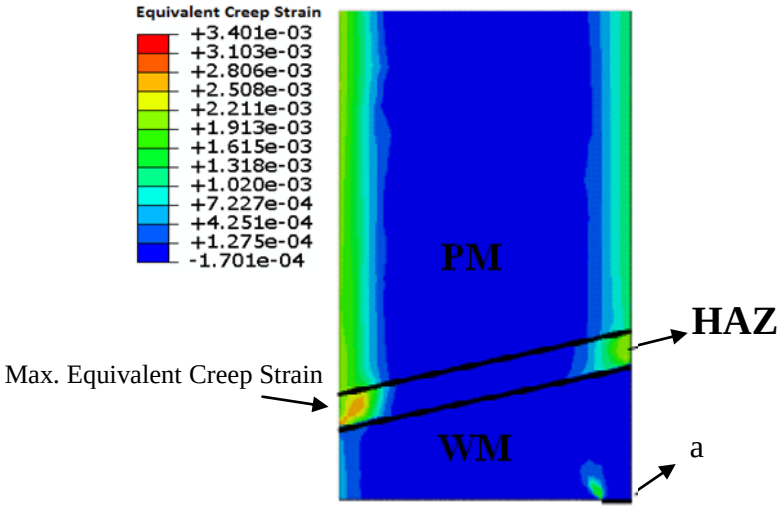

(c) Outer crack

Figure 10.16 Location of maximum creep strain with β =13, ratio R_o/R_i=1.2 and dwell period=100hours under load case 1

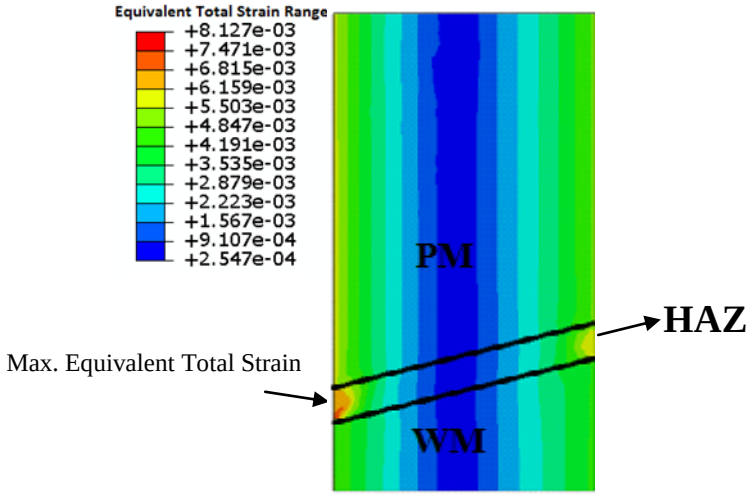

(a) Without crack

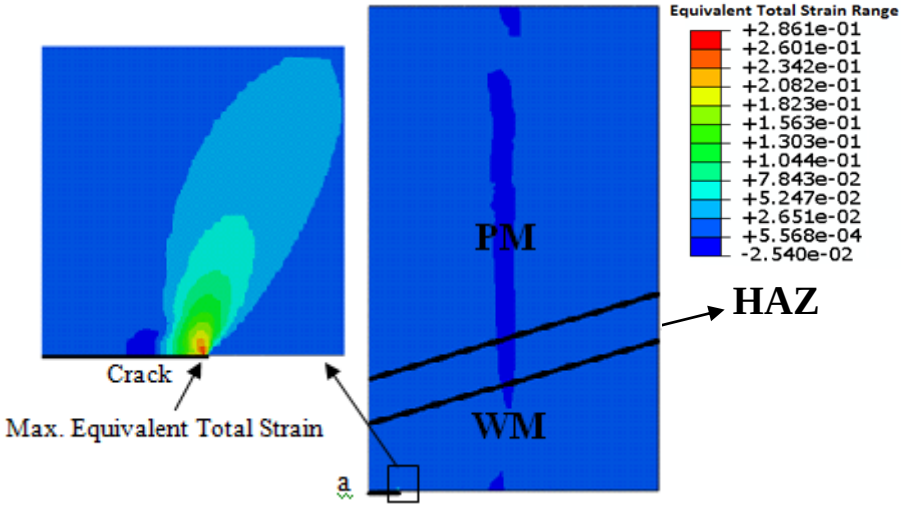

(b) Inner crack

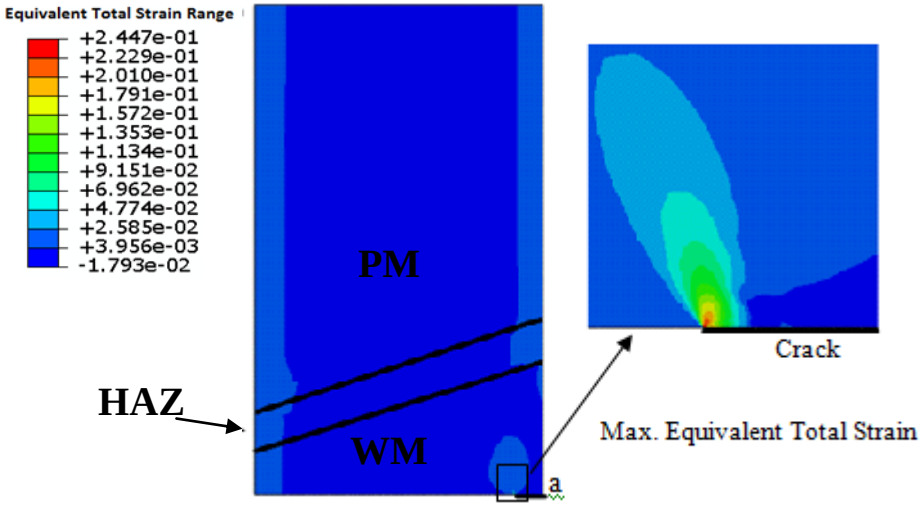

(c) Outer crack

Figure 10.17 Location of the maximum total strain range with β =13, ratio R_o/R_i=1.2 and dwell period=100hours under load case 1

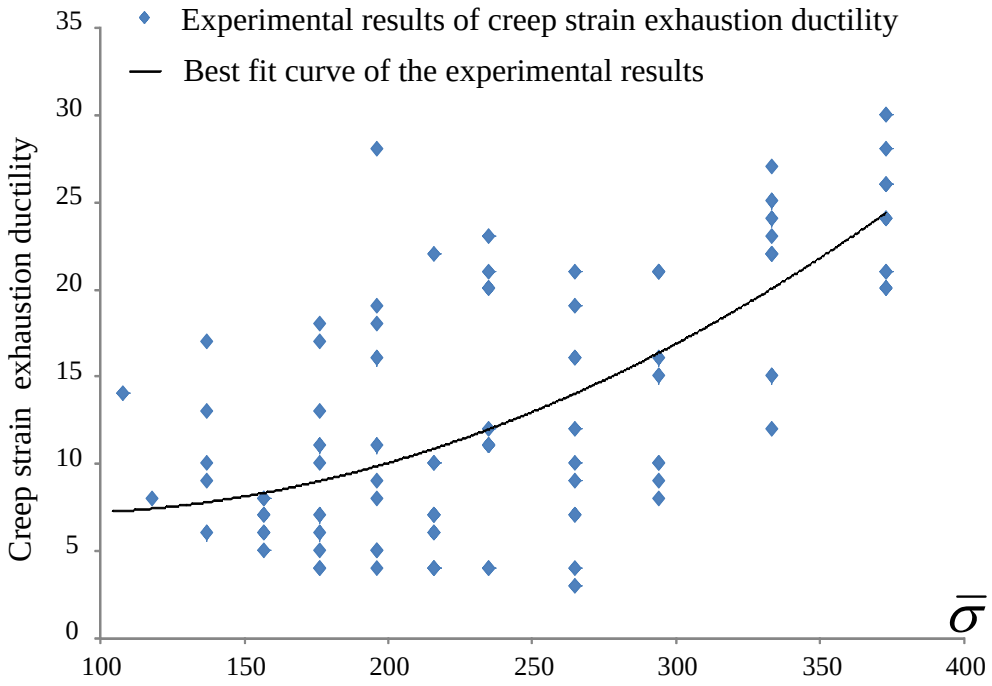

Figure 10.18 Best fit curve of the experimental results provided by [133]

10.3.4 Location of the Maximum Creep Strain and Total Strain Range in Relation to Crack Appearing within the WM

The formation of weld cracks is the primary failure mode for power plant piping under normal operating conditions. Crack initiation can be attributed to numerous cases, including poor welding practices, inadequate post weld heat treatment (PWHT), ill-designed levels of material mismatch and the accumulation of creep damage. The locations and orientations of weld cracking are normally found to initiate in the WM from the interaction of residual stresses produced from welding with the low-ductility of WM regions, thus producing circumferential 'reheat' and transverse WM cracks in the WM regions [135].

An inner crack and outer crack (with crack size $a/(R_o-R_i)=0.1$) configurations of weld cracking in the WM are shown in Figure 10.15a-b, respectively. Figure 10.16 and Figure 10.17 show the location of maximum creep strain and total strain range for $\beta=13$, $R_o/R_i=1.2$ under load case1 and for different welded pipe configurations, respectively. It can be seen from Figure 10.16a and Figure 10.17a, that for the case of a welded pipe without crack, the position of maximum creep strain and total strain

range occur at the inner pipe of WM/HAZ interface within the HAZ. While the outer crack appears (Figure 10.16c) in the WM, the maximum creep strain occurs in the same location as in the case without a crack. However, when the inner crack appears in the WM, the position of the maximum creep strain moves to the outer section of the pipe at the HAZ (Figure 10.16b). This is mainly due to the fact that there is a stress interaction between the stress concentration in the inner crack and the material mismatch area (HAZ).

Both outer crack (Figure 10.17c) and inner crack (Figure 10.17b) configurations show that the location of the maximum total strain range move to the crack tip of WM where the maximum stress occurs.

10.4 Life Estimates

10.4.1 Adopted Lifetimes Model

This section describes the mathematic model [136] used to predict the welded pipe lifetime in terms of the number of cycles to failure under creep-fatigue conditions. The number of cycles to Low Cycle Fatigue failure N^f was expressed in terms of the total strain range $\Delta\varepsilon^{total}$ in percentage [137],

$$\log\left(\Delta\varepsilon^{total}\right) = m_1 + m_2 \log\left(N^f\right) + m_3 \log\left(N^f\right)^2 \tag{10.2}$$

and the reverse relation for (10.2) is obtained as the root of square equation as [136],

$$\log\left(N^f\right) = \frac{-m_2 - \sqrt{m_2^2 - 4\,m_3\left[m_1 - \log\left(\Delta\varepsilon^{total}\right)\right]}}{2\,m_3} \tag{10.3}$$

and the fatigue damage factor per cycle,

$$\omega_{1cyc}^f = 1/N^f \tag{10.4}$$

where, the parameters m_1, m_2 and m_3 for the PM, HAZ and WM are adopted as [133], m_1=2.1349, m_2=-1.0225, m_3=0.1067

The creep endurance w_{1cyc}^c, the proportion of the creep ductility exhausted in each cycle, and N^c, the number of cycles to failure due to creep alone, are given by,

$$w_{1cyc}^{c} = \frac{\Delta\varepsilon^{c}}{\varepsilon^{*}} \quad , \quad N^{c} = \frac{1}{w_{1cyc}^{c}} \tag{10.5}$$

where, $\Delta\varepsilon^{c}$ is the accumulated creep strain during relaxation. And the creep strain exhaustion ductility, $\dot{\varepsilon}^{*}$, at 550^{0}C for these different material zones is considered as a function of creep stress level as [133] (this is the best-fit curve of the exhaustion model with experimental results provided by [133]. Figure 10.18 is a plot of the best fit curve from the experimental results provided by [133]. From this curve, the best fit function is provided as,

$$\varepsilon^{*}(\bar{\sigma}_{ave}) = 0.000199\bar{\sigma}_{ave}^{2} - 0.031466\bar{\sigma}_{ave} + 8.401515 \tag{10.6}$$

where $\bar{\sigma}_{ave}$ is the average stress during the stress relaxation process over dwell period Δt, and the estimation of the average stress could be described as follows: Considering the relaxation problem with elastic follow-up as,

$$\frac{d\bar{\varepsilon}_{c}}{dt} + \frac{Z}{\bar{E}}\frac{d\bar{\sigma}}{dt} = 0 \tag{10.7}$$

and the analytical solution for stress function in the form of (10.1) becomes,

$$\bar{\sigma}\left(t, Z, \bar{\sigma}_{0}\right) = \left[\bar{\sigma}_{0}^{1-n^{*}} - \frac{t\ \bar{E}B\left(1-n^{*}\right)}{Z}\right]^{1/(1-n^{*})} \tag{10.8}$$

where Z is the elastic follow-up factor described in Chapter 9 (9.21), and $\bar{\sigma}_{0}$ is the effective value of the start of dwell stress. B and n^{*} are the creep constants of the material described in table 10.2.

Then $\bar{\sigma}_{ave}$ is defined as a mean value of the integral function of $\bar{\sigma}\left(t, Z, \bar{\sigma}_{0}\right)$ during the dwell period as,

$$\bar{\sigma}_{ave} = \frac{1}{\Delta t}\int_{0}^{\Delta t} \bar{\sigma}\left(t, \bar{\sigma}_{0}, Z\right)dt \tag{10.9}$$

The estimate of total lifetime, corresponding to crack initiation, is given by a linear summation of fatigue and creep damage i.e. the total number of cycles to failure N^{*} is given by;

$$\frac{1}{N^{*}} = \frac{1}{N^{f}} + \frac{1}{N^{c}} \tag{10.10}$$

As the creep strain is small, its inclusion in the total strain range $\Delta\varepsilon^{total}$ has a negligible effect on fatigue damage.

Table 10.3 Life predictions evaluated at the position of maximum creep strain and total strain range with β=13^{0}C, R_o/R_i=1.2 for different dwell time

Dwell period	Load case 1			Load case 2		
	Cycle to Fatigue failure N^f (H)	Cycle to creep failure N^c (H)	Estimate of life time N^* (H)	Cycle to Fatigue failure N^f (H)	Cycle to creep failure N^c (H)	Estimate Of life time N^* (H)
1 hour	7348	140598	6983	7267	139814	6908
10 hours	5066	19175	4007	4806	18582	3818
100 hours	2697	4340	1663	1851	3646	1227
1000 hours	1836	1868	926	720	1123	438

(H)---the welded pipe failure at the WM/HAZ interface within the HAZ

Table 10.4 Life predictions evaluated at the position of maximum creep strain and total strain range with load case1, R_o/R_i=1.2, dwell period=100 hour, for different welded angles

β	Cycle to Fatigue failure N^f (H)	Cycle to creep failure N^c (H)	Estimate of life time N^* (H)
0^0	4238	4734	2236
5^0	4308	4756	2260
10^0	3015	4509	1807
13^0	2697	4340	1663
20^0	2136	4012	1394
25^0	1871	3849	1259
30^0	1726	3771	1184

(H)---the welded pipe failure at the WM/HAZ interface within the HAZ

10.4.2 Predicted Lifetimes

The variations of the failure lives, predicted by the peak effective creep strain and total strain range with β=13^0, R_o/R_i=1.2 for different dwell periods are shown in

Table 10.3. The positions where the maximum creep strain and total strain range occur are located in the HAZ. It can be seen from Table 10.3 that the failure life reduces with increasing dwell period for both loading cases. For a dwell period of 1000 hours with load case 1, the creep damage is almost equal to the fatigue damage. For dwell period less than 1000 hours the failure response is dominated by a fatigue mechanism for both loading cases.

Table 10.5 Life predictions evaluated at the position of maximum creep strain and total strain range with load case1, β =1.2, dwell period=100 hours, for different pipe thickness ratios

R_o/R_i	Cycle to Fatigue failure N^f (H)	Cycle to creep failure N^c (H)	Estimate of life time N^* (H)
1.1	3218	4282	1837
1.2	2697	4340	1663
1.3	2187	4270	1446
1.4	1859	4198	1288

(H)---the welded pipe failure at the WM/HAZ interface within the HAZ

The variations of the failure lives, predicted by the peak effective creep strain and total strain range with dwell period 100 hours, R_o/R_i=1.2 for different weld angle β under load case 1, are shown in Table 10.4. The position, where the maximum creep strain and total strain range occurs, is located in HAZ. It can be seen from Table 10.4 that the failure life reduces with increasing β.

The variations of the failure lives, predicted by the peak effective creep strain and total strain range with dwell period 100 hours, $\beta=13^0$, for different thickness ratios R_o/R_i under load case 1 are shown in Table 10.5. The position, where the maximum creep strain and total strain range occurs, is located in the HAZ. It can be seen from Table 10.5 that the failure life reduces with increasing R_o/R_i, and fatigue failure is the dominant mechanism. The reason for the fatigue domination is mainly due to the increase of the maximum plastic strain range with increasing R_o/R_i, whereas the maximum creep strain increases slightly with increasing R_o/R_i.

The variations of the failure lives, predicted by the peak effective creep strain and total strain range with dwell period 100 hours, $\beta=13^0$, $R_o/ R_i=1.2$, under load case 1 for different welded pipe configurations are shown in Table 10.6. For a welded pipe with inner and outer crack configuration, the position where the maximum creep strain and maximum total strain range occurs is located in the HAZ and in the WM, respectively. It can be seen from Table 10.6 that the failure life reduces sharply when the crack appears. The failure mechanism is dominated by the fatigue and the failure location in the WM, where the crack is located.

Table 10.6 Life predictions evaluated at the position of maximum creep strain and total strain range with load case1, β =1.2, dwell period=100 hours, R_o/R_i=1.2, for different pipe configurations

Pipe configuration	Location with maximum creep strain			Location with maximum total strain range		
	Cycle to Fatigue failure N^f	Cycle to Creep failure N^c	Estimate of life time N^*	Cycle to Fatigue failure N^f	Cycle to Creep failure N^c	Estimate Of life time N^*
Without crack	2697(H)	4340(H)	1663(H)	2697(H)	4340(H)	1663(H)
Inner crack	11868(H)	5726(H)	3862(H)	6(W)	19275(W)	6(W)
Outer crack	2177(H)	4141(H)	1426(H)	8(W)	14192(W)	8(W)

(H)---the welded pipe failure at the WM/HAZ interface within the HAZ

(W)---the welded pipe failure at the crack tip in the WM

Life comparison between the pure pipe made with material PM only and the welded pipe with $\beta=13^0$, $R_o/ R_i=1.2$, under load case 1 for different dwell periods is shown in Table 10.7. The life of welded pipe, compared to the life of the pure pipe decreases sharply. However, this difference decreases as the dwell period increases due to the significant creep effect.

Table 10.7 Life comparision between the pure pipe made with material PM and the welded pipe with β=13^{0}C, R_o/ R_i=1.2 for different dwell times under load case 1

Dwell period	Pure Pipe			Welded Pipe			
	Cycle to Fatigue failure N^f (I)	Cycle to creep failure N^c (I)	Estimate of life time N^* (I)	Cycle to Fatigue failure N^f (H)	Cycle to creep failure N^c (H)	Estimate Of life time N^* (H)	%of life reduction from pure pipe
1 hour	35206	194207	29803	7348	140598	6983	76%
10 hours	16072	28211	10239	5066	19175	4007	61%
100 hours	10217	6855	4102	2697	4340	1663	59%
1000 hours	6640	2883	2010	1836	1868	926	53%

(H)---the welded pipe failure occurs at the WM/HAZ interface within the HAZ

(I)---the failure area occurs at the inner fiber of the pure pipe

10.5 Discussions

Creep-fatigue analyses, using simplified three material axisymmetric models and Linear Matching Method, were performed for a thick walled welded pipe, with different weld angles β and thickness ratios R_o/R_i, subjected to a cyclic thermal load and internal pressure. The geometry and loading conditions are typical of the main stream pipelines observed in Denmark power plants [131]. Material data used are related to a service-aged X20 CrMoV121 weldment at 550^0C [133]. The elastic perfectly plastic relation from plastic behaviour and Norton-Bailey for stress creep relaxation is the main model assumed in this study. Failure, understood as crack initiation, is modelled as a simple linear summation of fatigue and creep damage, creep damage being included as ductility exhaustion. The distribution of effective creep strain and total strain range within the weldment and the corresponding failure lives and failure locations predicted by the maximum creep strain and total strain

range are presented to show the effects of geometry change on the creep-fatigue behaviour of the welded pipe.

For a range of weld angles between $0^0 \le \beta \le 10^0$ and $10^0 \le \beta \le 30^0$ the failure life decreases by 20% and 35%, respectively, with the increasing weld angle. It was also found that the failure life decreases up to 30% by increasing the thickness ratio R_o/R_i from 1.1 to 1.4. The failure positions for all the geometry cases (without crack) considered in this study are the same and located in the HAZ. The reason for this weak dependency change, in this particular case, is related to the fact that the HAZ creep and mechanical ductility are much lower than the WM and PM.

With the presence of the crack in the WM, the failure life decreases sharply and the failure position moves from the WM/HAZ interface to the WM. The reason for this subtle change is the high stress concentration in the crack tip.

These results are useful and provide an improved understanding of the geometry effect on the creep-fatigue interaction for the welded pipe considered in this study.

10.6 Conclusions

For the investigation of a particular X20 CrMoV121 welded pipe at 550^0C subjected to cyclic thermal and mechanical load, the following conclusions can be obtained from the current results;

1. The failure life decreases by almost 30% with the increasing welded angle β and thickness ratio R_o/R_i.

2. The failure locations of the weldment are unaffected by the geometry changes considered in this study (without crack case).

3. With the crack appearing in the WM, the failure position moves from the WM/HAZ interface to the WM.

4. It is observed from this study that although the failure mechanism is dominant mainly due to fatigue failure, 30-50% (without crack case) of life reduction is due to creep damage occurring from creep-fatigue interaction.

CHAPTER 11. CONCLUSIONS

11.1 General Conclusions

In this thesis the objective was the assessment of structural integrity and life time of mechanical components with and without the effect of creep. The numerical procedures developed in this thesis basically stem due to the requirement for more accurate and reliable numerical methods for the direct evaluation of structural response under complex cyclic loading. These procedures become even more important for structures operating at elevated temperatures with the presence of creep, especially when the economically driven environment is included as a factor.

Linear Matching Method (LMM) was used as a numerical procedure in addressing to cyclic problems of mechanical components subjected to cyclic histories of mechanical and thermal loads with or without the effect of creep. LMM is a procedure which sequentially matches the behaviours of non-linear material to that of a linear material, with the linear coefficients matching to the yield condition in plasticity or the flow equation in creep. When used within the finite element scheme, ABAQUS, the developed iterative programming algorithms, generate a monotonically reducing sequence of upper bounds that finally converges to the least upper bound shakedown loads. In addition to the implementation of the LMM to the shakedown analysis method [20], it has been extended beyond the range of most other direct methods by including the assessment of the ratchet limit and plastic strain range [21] [75][76] and steady state cyclic behaviour with creep-fatigue interaction [22]. These were the reasons that made LMM an ideal choice for this study. Following there is a summary of the results generated by the LMM in each chapter:

In Chapter 3 the application of the LMM methodology, as an iterative upper and lower bound elastic shakedown analysis method, were discussed. This numerical method was then applied to a 3D holed plate problem. The good agreement between the numerical and ABAQUS step-by-step elastic shakedown limit results, justifies

the accuracy of the methodology used. Further advantages of LMM can be observed considering the computing time necessary to generate the shakedown interactive diagram.

In Chapter 4, in order to demonstrate the efficiency and the effectiveness of the LMM for the upper and lower bound elastic shakedown limit in more complex structures, a parametric study of a composite cylinder (made of steel and aluminium) with a cross hole subjected to cyclic thermal loads and constant internal pressure is analysed. The results obtained from LMM have been verified using the step-by-step analyses, and they further proved that this method gives very accurate elastic shakedown limit results for complex structures. There are some valuable parametric results obtained in this Chapter, such as;

1. The reverse plasticity limit increases with the decreasing volume of steel with or without the presence of the cross-hole.
2. And increasing the cylinder radius ratio $\frac{R_o}{R_i}$ reduces the reverse plasticity limit and highly increases the limit load,
3. A safety shakedown envelope is created by formulating the elastic shakedown limit results of different composite material and cylinder thickness ratios with different cross-hole sizes.

The numerical procedure was further extended for the identification of the boundary between reverse plasticity and ratchetting regions, presented in Chapter 5. The LMM was then applied on the 3D square plate with a centre hole. The good correlation between the LMM and ABAQUS step-by-step ratchet limit results, justifies the accuracy of the adopted methodology. Another observation made in this chapter is that the sensitivity of the solutions to cyclic hardening, the Ramberg-Osgood type material model considered produced larger ratchet limit, when the cyclic loading is above the reverse plasticity limit compared to the elastic perfectly plastic material model. And the ratchet boundary is increasing with decreasing Ramberg-Osgood material data *n*.

In Chapter 6, LMM was implemented in a parametric study for a defective pipeline subjected to constant internal pressure and cyclic thermal gradient in order to demonstrate its efficiency and effectiveness on the ratchet limit for more complex structures. In this chapter, the effect of part-through slots on limit loading, shakedown limit, ratchet limit and maximum plastic strain range has been investigated using the proposed LMM mention in Chapters 3&5, and the numerical results has been verified by the ABAQUS step-by-step inelastic analysis, showing that it gives very accurate shakedown and ratchet limits. In this parametric study, the results showed that the axial slot configuration greatly reduces the ratchet boundary, while the small slot and circumferential slot configurations do not have any effect on the ratchet boundary. The maximum plastic strain range over the steady cycle with different cyclic loading combinations is also evaluated for a low cycle fatigue assessment in Chapter 6. It is observed from the results that the maximum plastic strain range will increase with the presence of a part-through slot. Finally, the location of the initiation of a fatigue crack for the defective pipeline with different slot configurations is determined, and it can be concluded that this location is independent of the cyclic loading types considered in this chapter.

In Chapter 7, another numerical study is conducted for a centre-cracked plate subjected to cyclic tensile loading and cyclic bending moment in order to demonstrate the effectiveness of the ratchet limit on the cracked component. The effect of circular holes on the maximum plastic strain range and the ratchet limit has been studied using the Linear Matching Method. The LMM has been verified by the step-by-step and RIKS analyses in ABAQUS. The results showed that LMM gives very accurate ratchet limit for a plate with a crack at the centre and symmetrically drilled holes under complex cyclic loading histories. The optimum hole location for reducing the crack tip plastic strain range with the least reduction in ratchet limit is identified to be located at a distance of 10% of the semi-crack length from the crack tip on the opposite the ligament. This identification was valid for both cyclic tensile loading and cyclic bending moment cases. It is also observed that the optimum location is independent of the hole size for both cyclic loading cases considered in this chapter.

Using the LMM numerical procedure in a research on calculating crack growth/propagation rate from the Fracture Mechanics approach is presented in Chapter 8. In this Chapter, a cyclic J-integral (ΔJ) model used to correlate with the crack growth rate obtained from LMM was proposed. Based on the potential energy expression for a single edge cracked plate subjected to cyclic uniaxial loading and cyclic bending moment conditions, a derivation of the cyclic J-integral (ΔJ) using LMM was presented. The study showed that the calculated value from proposed (ΔJ) model correlate well with the Reference Stress Method under cyclic tensile loading and cyclic bending moment with the applied loading up to the limit load. The proposed cyclic J-integral model indicated that ΔJ_e is a linear function of $\Delta U_e / A_{sub}$ and ΔJ_p is a linear function of ΔU_p^{β} for a small scale yielding condition and this relation is independent of the material models and loading types that are considered in this chapter.

In Chapter 9, a new approach for the direct evaluation of cyclic behaviour with the effect of creep of structures subjected to a general load condition in the steady cyclic state using LMM technique is presented. Time Hardening and Norton's law are adopted for the creep constitutive equation. The proposed method is capable to predict the stable cyclic response of a structure under creep conditions and calculate the resulting cyclic stresses, residual stresses, creep strain, plastic strain range, ratchet strain and the elastic follow-up factor. The solutions obtained from LMM have been verified by a bench mark example (Bree problem). Further investigations into the creep/fatigue behaviour for more a complex structure, a 3D plate with hole model, under variations in loading conditions and dwell periods, provided the confidence on the capability of numerical procedures.

In Chapter 10, the numerical procedure described in the previous chapter is applied on a real industrial problem in order to verify the appropriateness of LMM. A parametric study for a welded pipe subjected to cyclic thermal and mechanical load with the effect of creep is presented in this study. Good correlations were observed between the LMM and ABAQUS step-by-step inelastic analysis for the distribution of creep strain and total strain range with varying dwell period. For the investigation of a specific X20 CrMoV121 welded pipe at $550^0 C$ subjected to cyclic thermal and

mechanical load, many valuable parametric results are obtained, such as: The creep/fatigue failure life decreases with the increasing welded angle β and thickness ratio R_o/R_i , and the failure locations of the weldment are unaffected by the geometry changes considered in this study.

This thesis has shown the capabilities of utilizing the LMM in solving cyclic structural responses associated with plasticity and creep. The simplicity in its implementation as well as its accuracy in analyzing complex structures with and without the effect of creep, makes the LMM the appropriate choice as an alternative to current solution procedures (R5). In author's opinion, the methodology adopted in this thesis is a valuable tool in assessing the structural integrity of components with or without the effect of creep.

11.2 Future Work

This thesis has shown the LMM is able to address problems (it has the capability to define the cyclic structural response with or without the effect of creep) as mentioned in Chapter 1. However, there are still some areas, which need to be addressed in the future.

One particular area is the numerical developments for the LMM. For instance, one of the numerical development is for the cyclic J-integral model mentioned in Chapter 8. Since the cyclic J-integral relation is only derived for the 2D edge cracked problem, the development of the LMM needs to be extended for 3D structures to reach an overall conclusion for more practical and general examples. Another numerical development in this context is that LMM should include various cyclic hardening and creep models. In this study, the Ramberg-Osgood and elastic perfectly plastic material model with time hardening creep model are considered. For more general problems, various cyclic hardening material models and creep models (e.g. Strain Hardening creep model) should be taken under consideration.

Another area to be considered in the future work is the application of more practical parametric studies. In the parametric study mentioned in Chapter 10, for the

welded pipe under the effect of creep, only the geometric effect on the creep/fatigue behaviour of heterogeneous welded pipe under cyclic thermal and mechanical loads was investigated. However, the material effect of the heterogeneous welded pipe and the cyclic hardening model on creep/fatigue behaviour is not taken into consideration. These parametric studies may be considered as a future work. It is important to carry out the applications of the numerical procedures discussed in this thesis for other structural geometries and loading conditions since the additional investigations would further prove the efficiency and effectiveness of the LMM in addressing to cyclic structural response with or without the effect of creep.

REFERENCE

1. **Goodall, I.W., Goodman, A.M., Chell, G. C., Ainsworth, R. A., Williams, J. A.** "R5, Assessment procedures for the high temperature response of structures". *British Energy Generation Limited.* Barnett Way, Barnwood, Gloucester, GL4 3RS.

2. **Ponter, A. R. S., Carter, K. F.** "Limit state solutions, based upon linear elastic solutions with a spatially varying elastic modulus". *Computer Methods in Applied Mechanics and Engineering.* 1997, Vol. 140, pp:237-258.

3. **Ponter, A. R. S., Engelhardt, M.** "Shakedown limits for a general yield condition: Implementation and application for a von-Mises yield condition". *European Journal of Mechanics and Applied Solids.* 2000, Vol. 19, pp.423-445.

4. **Ponter, A. R. S., Chen, H. F.** "A minimum theorem for cyclic load in excess of shakedown, with application to the evaluation of a ratchet limit ". *European Journal of Mechanics and Applied Solids.* 2001, Vol. 20, pp: 539-553.

5. **Chen, H. F., Ponter, A. R. S.** "A method for the evaluation of a ratchet limit and the amplitude ofplastic strain for bodies subjected to cyclic loading ". *European Journal of Mechanics and Applied Solids.* 2001, Vol. 20, pp: 555-571.

6. **Chen, H. F., Ponter, A. R. S.** "Shakedown and limit analysesfor 3-D structures using the linear matching method'. *International Journal of Pressure Vessels and Piping.* 2001, Vol. 78, pp. 443-451.

7. **Chen, H. F., Ponter, A. R. S.** "Methods for the evaluation Of creep relaxation and the amplitude of strainsfor bodies reverse-plastic strainsfor bodies reverse-plastic subjected to cyclic loading". *Pressure Vessels and Piping, Transaction of the ASME,Cleveland, Ohio.* July 2003.

8. **ANSYS Inc.** *Southpointe, 275 Technology Drive, Canonsburg, PA 15317, (www. ansys. com).*

9. **Hibbit, Karlson and SorensenIn c.** "ABAQUSIStandard User's manual, Volumes 1,2 & 3, Version 6.1". USA, 1997.

10. **ASME.** "Boiler andpressure vessel code. Code case: Nuclear components, Case N-47-29, Class I components in elevated temperature service". Section 11, Division I, 1990.

11. **AFCEN.** "Design and construction rulesfor mechanical components ofFBR nuclear islands". *RCC-MR, AFCEN,*. Paris, 1985.

12. **Liu, YH., Carvelli, V., Maier, G.** "Integrity assessment of defective pressurized pipelines by direct simplified methods". *International Journal of Pressure Vessels and Piping.* 1997, Vol. 74, pp:49-57.

13. **Vu, D.K., Yan, A.M., Nguyen, Dang.H.** "A primal–dual algorithm for shakedown analysis of structures". *Comput. Methods Appl. Mech. Eng.* 2004, Vol. 193, pp. 4663-4674.

14. **Staat, M., Heitzer, M.** "LISA a European Project for FEM-based Limit and Shakedown Analysis". *Nuclear Engineering and Design.* 2001, Vol. 206, pp:151-166.

15. **Seshadri, R.** "Inelastic Evaluation of Mechanical and Structural components Using the Generalized Local Stress Strain Method of Analysis". *Nucl. Eng. Des.* 2005, Vol. 153, pp:287-203.

16. **Mackenzie, D., Boyle, J. T., Hamilton, R., Shi, J.** "Elastic compensation method in shell-based design by analysis". *Proceedings of the 1996 ASME Pressure Vessels and Piping Conference.* 1996, Vol. 338, pp:203-208.

17. **Mackenzie, D., Boyle, J.T., Hamilton, R.** "The elastic compensation method for limit and shakedown analysis: a review". *Trans IMechE, Journal of Strain Analysis for Engineering Design.* 2000, Vol. 35, pp:171-188.

18. **Chen, H.F., Ponter, A.R.S., Ainsworth, R.A.** "The Linear Matching Method applied to the High Temperature Life Integrity of Structures, Part 1: Assessments involving Constant Residual Stress Fields". *International Journal of Pressure Vessels and Piping.* 2006, Vol. 83 (2), pp.123-135.

19. **Chen, H.F., Ponter, A.R.S., Ainsworth, R. A.** "The Linear Matching Method applied to the High Temperature Life Integrity of Structures, Part 2: Assessments beyond shakedown involving Changing Residual Stress Fields". *International Journal of Pressure Vessels and Piping.* 2006, Vol. 83 (2), pp.136-147.

20. **Chen, H.F.** "Lower and Upper Bound Shakedown Analysis of structures With Temperature-Dependent Yield Stress". *Journal of Pressure Vessel Technology.* 2010, Vol. 132, pp. 1-8.

21. **Chen, H.F.** "A Direct Method on the Evaluation of Ratchet Limit". *Journal of Pressure Vessel Technology.* 2010, Vol. 132, 041202.

22. **Chen, H.F., Ponter, A.R.S.** "Linear Matching Method on the evaluation of plastic and creep behaviours for bodies subjected to cyclic thermal and mechanical loading". *International Journal for Numerical Methods in Engineering.* 2006, Vol. 68, pp 13-32.

23. **Tipping, D.J.** “The Linear Matching Method: A Guide to the ABAQUS User Subroutines”. *E/REP/BBGB/0017/ GEN/07, British Energy Generation.* 2007.

24. *“R5: Assessment Procedure for the High Temperature Response of Structures”.* **Ainsworth, R.A.** 2003.

25. **Boyle, J.T., Spence, J.** "Stress analysis for creep". *Butterworths, London,UK.* 1983.

26. **Coleman, M.C., Kimmins,S.T.** "The Behaviour of 1/2 Cr 1/2Mo1/4V pipe weldments in high temprature plant". *Seminar on life of welds at high temperature, IMechE, London.* 1990.

27. **Evans, R.W., Wilshire, B.** "Introduction to creep". *IOM, London. UK.* 1993.

28. **Penny, R.K., Marriott, D.L.** "Design for creep". *Second edition, Chapman and Hall, London.* 1995.

29. **Hyde, T.H., Sun, W.** "Creep of welded pipes". *Proc. of ImechE, Part E.* 1998, Vol. 212, pp.171-182.

30. **Bree, J.** “Elastic-plastic behaviour of thin tubes subjected to internal pressure and intermittent high-heat fluxes with application to fast-nuclear-reactor fuel elements”. *J. strain anal.* 1967, Vol. 2, pp. 226-238.

31. **Bree, J.** "Plastic deformation of a closed tube due to interaction of pressure stresses and cyclic thermal stresses". *Int Mech Sci.* 1989, Vols. 31 (11-12), pp. 865-892.

32. **Mohammad, Abdel Karim.** "Review Shakedown of complex structures according to various hardening rules". *International Journal of Pressure Vessels and Piping.* 2005, Vol. 82, pp. 427-458.

33. **Gruning, M.** "Die Tragfahigkeit statisch unbestimmter Tragwerke aus Stahl bei beliebig haufig wiederholter Belastung". *Berline: Springer.* 1929.

34. **Melan, E.** “Theorie Statisch Unbestimmter Systeme aus Ideal-Plastischem Bastoff. Sitzungsberichte der Akademie der Wissenschaft”. *Wien, Abtiia.* 1936, Vol. 145, pp: 195-218.

35. **Melan, E.** "Zur Plastizitat des Raumlichen Kontinuums". *Ing Arch.* 1938, Vol. 9, pp.116-126.

36. **Koiter, W. T.** "General theorems for elastic plastic soloids". *Progress in solid mechanics J.N. Sneddon and R. Hill, eds. North Holland, Amsterdam.* 1960, Vol. 1, pp:167-221.

37"Shakedown of elastic-plastic structures"*PWN- Polish Scientific Publishers, Warsaw, Elsevier, Amsterdam*

38. **Eyre, D.G., Galambos, T.V.** "Shakedown test on steel bars and beams". *J. Struct. Div., Proc. ASCE 96.* 1970, pp: 1284-1304.

39. **Puglia, A., Nerli, G.** "Experimental research on elastoplastic behaviour and collapse load of statically indetermined space tubular beams". *SMiRT-2, Berlin (West).* 1973.

40. **Egre, D.G., Galambos, T.V.** "Shakedown of grids". *J.Struct. Div., Proc. ASCE 99.* 1973, pp: 2049-2060.

41. **Grundy, P., Spencer, W.J.** "Shakedown of elastoplastic grids". *5th Australian Conf. Mech. Struct. Materials, Melbourne.* 1975, pp: 219-236.

42. **Sparacio, R.** "Prove su telai in c.'a. a collasso incrementale". *Fond. Politecn. Mezzogiorno, Univ. di Napoli.* 1967, Vol. 23.

43. **Belli, P.** "Esperienze su telai a molte iperstatiche in conglomerato armato portati al collasso incrementale". *Fond. Politecnica Mezzogiorno, Univ. di Napoli.* 1971.

44. **Ceradini, G., Gavarini, C., Petrangeli, M.P.** "Steel orthotropic plates under alternate loads". *J. Struct. Div., Proc. ASCE.* 1975, Vol. 101, pp: 2015-2026.

45. **Proctor, E., Flinders, R.F.** "Shakedown investigations on partial penetration welded nozzles in a spherical shell". *Nucl. Engrg. Des.* 1968, Vol. 8, pp: 171-185.

46. **Bree, J.** "Incremental growth due to creep and plastic yielding of thin tubes subjected to internal pressure and cyclic thermal stresses". *J. Strain Analysis.* 1968, Vol. 3, pp.122-127.

47. **Clement, G., Roche, R.** "General review of available results ofprogressive tests of structures and structural components". *In: Ratchetting in the creep range by Ponter, A. R. S., Cocks, A. C. F.,Clement, G., Roche, R., Corradi, L., & Franchi, A.,Report EUR9876EN, Directorate-General, Science Research and Development Comn-fission of the European Community, Brussels.* 1985.

48. **Cocks, A.C.F., Ponter, A.R.S.** "Computation of shakedown limits for structural components, Part II - The creep range (Brussels Diagram)". *Internal Report, University of Leicester.* 1992.

49. **kim, D.W., Chang, J., Ryu, W.** "Evaluation of the creep–fatigue damage mechanism of Type 316L and Type 316LN stainless steel". *International Journal of Pressure Vessels and Piping.* 2008, Vol. 85, pp. 378-384.

50. **Shi, D., LIu, J., Yang, X., Qi, H., Wang, J.** "Experimental investigation on low cycle fatigue and creep–fatigue interaction of DZ125 in different dwell time at elevated temperatures". *Materials Science and Engineering.* 2010, Vol. 528, pp.233-238.

51. **Maitournam, M.H., Pommier, B., Thomas, JJ.** "Determination of the asymptotic response of a structure under cyclic thermomechanical loading". *Comp Rend Mec.* 2002, Vol. 330(10), pp. 703-708.

52. **Nguyen-Tajan, TMI., Pommier, B., Maitournam, H., Houari, M., Verger, L., Du, ZZ et al.** "Determination of the stabilized response of a structure undergoing cyclic thermal–mechanical loads by a direct cyclic method". *In: ABAQUS users' conference proceedings.* 2003.

53. **Peigney, M., Claude, SC.** "An optimal control approach to the analysis of inelastic structures under cyclic loading". *J Mech Phys Solids.* 2003, Vol. 51(4), pp.575-605.

54. **Carter, P.** "Analysis of cyclic creep and rupture. Part 2: calculation of cyclic reference stresses and ratcheting interaction diagrams". *International Journal of Pressure Vessels and Piping.* 1, 2005, Vol. 82, pp. 27-33.

55. **Benoit, A., Maitournam, M.H., Rémy, L.,Oger, F.** "Cyclic behaviour of structures under thermomechanical loadings: Application to exhaust manifolds". *International Journal of Fatigue.* 2012, Vol. 38, pp. 65-74.

56. **Jones, G.L., Dhalla, A.K.** "Classification of clamp induced stresses in thick walled pipes". *In: Proc. ASME Pressure Vessels and Piping Conference, Denver,Colorado.* 1981, Vol. PVP 81, pp.17-23.

57. **Marriott, D. L.** "Evaluation of Deformation or load control of stresses under inelastic conditions using elastic finite element stress analysis". *Proc. ASME PVP Conf.Pittsburgh.* 1988, Vol. 136, pp.3-9.

58. **Mackenzie, J., Shi, J., Boyle, J.T.** "Finite element modelling for limit analysis by the elastic compensation". *Comp. Struct.* 1994, Vol. 51, pp. 403-410.

59. **Ponter, A. R. S., Carter, K. F.** "Shakedown state simulation techniques based on the linear elastic solutions". *Computer Methods in Applied Mechanics and Engineering.* 1997, Vol. 140, pp:259-279.

60. **Weichert, D., Maier, G.** "Inelastic Analysis of Structures under Variable Loads". *Theory and Engineering Applications. Kluwer Academic Publishers, Dordrecht.* 2000.

61. **Maier, G.** "Mathematical programming methods for deformation analysis at plastic collapse". *Computers and Structures.* 1977, Vol. 7, pp. 599-612.

62. **Belytschko, T., Hodge, P.G.** "Plane stress limit analysis by finite elements". *Journal of Engineering Mechanics Division.* 1970, Vol. 96, pp. 229-234.

63. **Zhang, Y.G., Zhang, P., Xue, W.M.** "Limit analysis considering initial constant loadings and proportional loadings". *Computational Mechanics.* 1994, Vol. 14, pp.229-234.

64. **Laudiero, F.** "Limit analysis of plates with piecewise linear yield surface". *Mechanica.* 1972, Vol. 7, pp.105-110.

65. **Dhalla, A.K.** "A simplified procedure to classify stresses for elevated temperature service". *Proc. ASME PVP Conf.New York.* 1987, Vol. 120, pp.177-188.

66. **Mackenzie, D., Boyle, J. T.** "A simple method of estimating shakedown loads for complex structures". *Proc. ASME PVP, Denver.* 1993, Vol. 265, pp.89-94.

67. **Martin, J. B.** "Plasticity: Fundamentals and general results". *M.I.T. Press, Boston.* 1975.

68. **Gokhfeld, D.A., Cherniavsky, O.F.** "Limit Analysis of Structures at Thermal Cycling Sijthoff and Noordhoff". *Rockville, Maryland.* 1980.

69. **Leckie, F.A., Penny, R.K.** "Shakedown loads for radial nozzles in spherical pressure vessels". *Int. J. Solids & Structures.* 1967, Vol. 3, 743-755.

70. **Carter, K.F., Ponter, A.R.S.** "The calculation of limit loads and shakedown boundaries by the effective modulus method". *Int. Conf. on Struct. Mech. in Reactor Tech., Lyon.* 1997, Vol. 1 Div 3B.

71. **Beglev, J.A., Landes, J.D.** *ASTM STP 1973.* 1973, Vol. 536, pp.246-63.

72. **Ponter, A.R.S., Chen, H. F.** "Direct methods for limits in plasticity". *Archives of Mechanics.* 57, 2005, Vols. 2-3, pp.171-187.

73. **Chen, H. F., Engelhardt, M.J., Ponter, A.R.S.** "Linear matching method for creep rupture assessment". *International Journal of Pressure Vessels and Piping.* 2003, Vol. 80, pp. 213-220.

74. **Chen, H.F., Ponter, A.R.S.** "The Linear Matching Method for shakedown and limit analyses applied to rolling and sliding point contact problems". *International Journal of Road Materials and Pavement Design.* 2005, Vol. 6, pp.9-30.

75. **Ponter, A. R. S., Chen, H. F.** "A minimum theorem for cyclic load in excess of shakedown, with application to the evaluation of a ratchet limit ". *European Journal of Mechanics and Applied Solids.* 2001, Vol. 20, pp.539-553.

76. **Chen, H. F., Ponter, A. R. S.** "A method for the evaluation of a ratchet limit and the amplitude ofplastic strain for bodies subjected to cyclic loading ". *European Journal of Mechanics and Applied Solids.* 2001, Vol. 20, pp:555-571.

77. **M. Lytwyn, H. Chen, M. Martin.** "Linear Matching Method for Ratchet Limit Prediction in Comparison to Rolls-Royce's Hierarchical Finite Element Framework". *ICPVT-13, London.* 2012.

78. **Ponter, A. R. S., Carter, K. F., Riou, B.** "Design rules for cylindrical shells subjected to axisymmetric temperature histories". *Working Group on Codes and Standards, Activity Group 2, Commission of the European Communties, Directorate General Environment, Nuclear Safety and Civil Protection, Final Report, Study Contract RA1-0224-UK,.* 1996.

79. **Calladine, C. R.** "Engineering plasticity". *Pergammon Press.* 1969.

80. **ABAQUS.** "User's manual". *Version 6.7.* 2007.

81. **Noor, Ahmed. K.** "Structures technology for future aerospace systems". *Computers and Structures.* 2000, Vol. 74, pp: 507-519.

82. **Thuis, H.G.S.J., Biemans, C.** "Design fabrication and testing of a composite bracket for aerospace applications". *Composite Structures.* 1997, Vol. 38, pp: 91-98.

83. **Makulsawatudom, P., Mackenzie, D., Hamiton, R.** "Shakedown behaviour of thick cylindrical vessels with cross-holes". *Proc. Instn Mech. Engrs.* 2004, Vol. 218, Part E: J. Process Mechanical Engineering.

84. **Camilleri, D., Mackenzie, D., Hamilton, R.** "Shakedown of a thick cylinder with a radial crosshole". *Journal of Pressure Vessel Technology.* 2009, Vol. 131 (1), 011203-1.

85. **Chen, H. F., Liu, Y. H., Cen, Z. Z., Xu B. Y.** "Numerical analysis of limit load and reference stress of defective pipelines under multi-loading systems". *International Journal of Pressure Vessels and Piping.* 1998, Vol. 75, pp:105-114.

86. **Chen, H.F., Shu, D.W.** "Lower and Upper Bound Limit Analyses for Pipeline with Multi-defects of Various Configurations". *International Journal of Pressure Vessels and Piping.* 2000, Vol. 77, pp:17-25.

87. **Grief, R., Sanders, J.** "The effect of a stringer on the stress in a cracked sheet". *J. Appl. Mech.* 1965, Vol. 32, pp.59-66.

88. **Erdogan, F., Arin, K.** "A sandwich plate with a part through and a debonding crack". *J. Eng. Fract. Mech.* 1972, Vol. 4, pp: 449-458.

89. **Thomas, S.B., Mhaiskar, M.J., Sethuraman, R.** "Stress intensity factors for circular hole and inclusion using finite element alternating method". *Theoretical and Applied Fracture Mechanics.* 2000, Vol. 33, pp: 73-81.

90. **Broek, D.** "A Similitude Criterion for Fatigue Crack Growth Modeling". *Fracture Mechanics Sixteenth Symposium, ASTM STP 868. M.F. Kanaien and A.T. Hopper. Eds. American Society for Testing and Material, Philadelphis.* 1985, pp: 347-360.

91. **Ju, S.H., Sandor, B.I., Plesha, M.E.** "Life prediction of solder joints by damage and fracture mechanics". *Journal of Electronic Packaging, Transactions of the ASME.* 1996, Vol. 118, pp.193-200.

92. **Ju, S.H., Kuskowski, S., Sandor,B.I., Plesha, M.E.** "Creep-fatigue damage analysis of solder joints". *ASTM Special Technical Publication.* 1994, pp.1-21.

93. **Paris, P., Erdogan, F.** "A critical analysis of crack propagation laws". *J. Basic Engng.* 1963, Vol. 85, pp.528-534.

94. **Begley, J.A., Landes, J.D.** "The J-integral as a fracture criterion". *Fracture toughness, proceedings of the 1971 national symposium on fracture mechanics, part II. ASTM STP 514. Philadelphia. PA: American Society for Testing and Materials.* 1972, pp.1-20.

95. **Rice, J.R.** "A path independent integral and the approximate analysis of strain concentration by notches and cracks". *J. appl. Mech.* 1986, Vol. 35, pp.379-386.

96. **Beglev, J.A., Landes, J.D.** Beglev, J.A., Landes, J.D. *ASTM STP 1972.* Vol. 514, pp.1-23.

97. **Dowling, D.E., Begley, J.A.** "Fatigue crack growth during gross plasticity and the J-integral". *ASTM-STP WI.* 1976, pp.82-103.

98 **Chen, W., Chen, H.** "On the Evaluation of Cyclic J-Integral using Linear Matching Method" *Pressure Vessels and Technology Conference, London, UK*

99. **Tanaka, K.** "The cyclic J-integral as a criterion for fatigue crack growth". *Int J Fracture.* 1983, Vol. 22(2), pp.91-104.

100. **Tanaka, K., Akiniwa, Y., Shimizu,K.** "Propagation and closure of small cracks in SiC particulate reinforced aluminum alloy in high cycle and low cycle fatigue". *Eng Fract Mech.* 1996, Vol. 55(5), pp.751-762.

101. **Chow, C. L., Lu, T. J.** "Cyclic J-integral in relation to fatigue crack initiation and propagation". *Eng Fract Mech.* 1991, Vol. 39(1), pp.1-20.

102. **Chattopadahyay, J.** "Improved J and COD estimation by GE/EPRI method in elastic to fully plastic transition zone". *Eng. Fract. Mech.* 2006, Vol. 73, pp.1959-1979.

103. **Miller, A.G., Ainsworth, R.A.** "Consistency of numerical results for power law hardening materials and the accuracy of the reference stress approximation". *Eng Fract Mech.* 1989, Vol. 32, pp.237-247.

104. **Zahoor, A.** "Evaluation of J-integral estimation schemes for flawed throughwall pipes". *Nucl Engng Des.* 1987, Vol. 100, pp.1-9.

105. **Kim Yun-Jae, Huh Nam-Su, Kim Young-Jin.** "Effect of Lu¨ders strain on engineering crack opening displacement estimations for leak before break analysis finite element study". *Fatigue Fract Engng Mater Struct.* 2001, Vol. 24, pp.617-624.

106. **Kim Yun-Jae, Huh Nam-Su, Kim Young-Jin, Choi Young-Hwan, Yang Jun-Seok.** "On relevant Ramberg–Osgood fit to engineering non-linear fracture mechanics analysis". *J Pressure Vessel Technol, ASME Trans.* 2004, Vol. 126, pp.277-283.

107. **Kim Yun-Jae, Huh Nam-Su, Kim Young-Jin.** "Enhanced reference stress-based J and crack opening displacement estimation method for leak-before-break analysis and comparison with GE/EPRI method". *Fatigue Fract Engng Mater Struct.* 2001, Vol. 24, pp.231-245.

108. **Ainsworth, R. A., Ruggles, M.B., Takahashi, Y.** "Flaw assessment guide for high temperature reactor components subject to creep fatigue loading". *Eng. Technology Divison.* 1990.

109. **Rice, J.R., Paris, P.C., Merkle, J.G.** "Some further results of J-integral analysis and estimates". *Progress in flaw growth and fracture toughness testing. ASTM STP 536. Philadelphia, PA. American Society for Testing and Materials.* 1973, pp.231-245.

110. **Merkle, J.G., Corten, H.T.** "A J-integral analysis for the compact specimen, considering axial force as well as bending effects". *J Press Vess Technol (Trans Am Soc Mech Eng).* 1974, Vol. 96, pp.286–292.

111. **Landes, J.D., Walker, H., Clarke, G.A.** "Evaluation of estimation procedures used in J-integral testing". *In: Landes JD, Begley JA,Clarke GA, editors. Elastic–plastic fracture.ASTM STP 668. Philadelphia. PA: American Society for Testing and Materials.* 1979, pp.266–287.

112. **Brose, W.R., Dowling, N.E.** "Size effects on the fatigue crack growth rate of type 304 stainless steel". *In: Landes JD, Begley JA, Clarke GA, editors. Elastic–plastic fracture. ASTM STP 668. Philadelphia, PA: American Society for Testing and Materials.* 1979, pp.720–735.

113. **Mowbray, D.F.** "Use of a compact-type strip specimen for fatigue crack growth rate testing in high-rate regime". *In: Landes JD, Begley JA, Clarke GA, editors. Elastic–plastic fracture. ASTM STP 668. Philadelphia. PA: American Society for Testing and Materials.* 1979, pp.736–752.

114. **Lambert, Y., SaiBard , P., Bathias, C.** "Application of the J concept to fatigue crack growth in large-scale yielding". *ASTM STP 969.* 1988, pp.318-329.

115. **Izumi, Y., Fine, M. E.** "Role of plastic work in fatigue crack propagation in metals". *Engineering Fracture Mechanics I1.* 1979, pp.791-804.

116. **Fine, M.E., Izumi, Y.** "Role of ductility and yield stress in fatigue crack propagation in metals". *Proc. 4th International Conference on the Strength of Metals and Alloys. Nancy, France.* 1976, Vol. 2, pp.468-472.

117. **Liaw, P. K., Kwun, S. I., Fine, M. E.** "Plastic work of fatigue crack propagation in steels and aluminum alloys". *Met. Trans.* 1981, Vol. 12A, pp.49-55.

118. **Sumpter, J.D., Turner, C.E.** *Int. J. Fract.* 1973, Vol. 9, 320.

119. **El-Haddad, M.H., Mukherjee, B.** "Elastic–plastic fracture mechanics analysis of fatigue crack growth". *In: Shih CF, Gudas JP, editors. Elastic–plastic fracture: second symposium, vol. II—fracture resistance curves and engineering applications. ASTM STP 803. Philadelphia. PA: American Society for Testing and Materials.* 1983, pp.689–707.

120. **Jolles, M.** "Effects of load gradient on applicability of a fatigue crack growth rate-cyclic J relation". *Fracture mechanics: sixteenth symposium. ASTM STP 868. Philadelphia. PA: American Society for Testing and Materials.* 1985, pp.381–91.

121. **Wang S-Z, Yang Z, Kang M-K.** "Fatigue crack growth rate under full yielding condition for 15CDV6 steel". *Engng Fract Mech.* 1983, Vol. 18(4), pp.895–902.

122. **Tanaka, K., Hoshide, T., Nakata, M.** "Elastic–plastic crack propagation under high cyclic stresses". *In: Shih CF, Gudas JP, editors. Elastic–plastic fracture: second symposium, vol. II—fracture resistance curves and engineering applications. ASTM STP 803. Philadelphia. PA: American Society for Testing and Materials.* 1983, pp.708–722.

123. **Banks-Sills L, Volpert Y.** "Application of the cyclic J-integral to fatigue crack propagation of Al 2024-T351". *Engng Fract Mech.* 1991, Vol. 40(2), pp.355–370.

124. **C. L. Lau, M. M. K. Lee, A. R. Luxmoore.** "Mythologies for predicting J-integrals under large plastic deformation-I. further developments for tension loading". 1994, Vol. 49, pp.337-554.

125. **Downling, N.E.** "Crack growth during low-cycle fatigue of smooth axial specimens". *Cyclic-stress-strain and plastic deformation aspects of fatigue crack growth.ASTM STP.* 1997, Vol. 637, pp.97-121.

126. **Norton, F.H.** "The creep of steel at high temperatures". *McGraw-Hill, London, UK.* 1929.

127. **Sorkhabi, A.H.D.S., Tahami, F.** "Experimental study of the creep behavior of parent, simulated HAZ and weld materials for cold-drawn 304L stainless steel". *Engineering Failure Analysis.* 2012, Vol. 21, pp.78-90.

128. **Cane, B.J.** "Collabrative programme on the correlation of test data for high temperature design of welded steam pipes". *Presentation and analuysis of material data, CEGB report RD/L2101N81, CEGB, UK.* 1981.

129. **Eggler, G., Ramteke, A. Coleman, M.C.,Chew, B., Peter,G., Burblies, A.,Hald,J., Jefferey, G., Rantala, J.,De Witte, M., Mohrmann, R.** "Analysis of creep in a weld 'P91' pressure vessel". *Int. J. Pres. Vess and Piping.* 1994, Vol. 60, pp.237.

130. **Hyde, T.H., Sun, W., Becker, A.A.,Williams, J.A.** "Creep continuum damage consitutive equations for the base, weld and heat-affacted zone materials of a service-age 1/2Cr1/2Mo1/4V;21/4CrlMo multi-pass weld at 640 C". *J. Strain Analysis.* 1997, Vol. 32, pp. 273-285.

131. **Storesund, J., Borggreen, K., Zang, W.** "Creep behaviour and lifetime of large welds in X20 CrMOV 121-results based on simulation and inspection". *International Journal of Pressure Vessel and Piping.* 2006, Vol. 83, pp. 875-883.

132. **Hyde, T.H., Sun, W., Becker, A.A., Williams, J.A.** "Effect of weld angle and axial load on the creep failure behaviour of an internally pressurised thick walled CrMoV pipe weld". *Int. Journal of Pressure Vessels and Piping.* 2001, Vol. 78, pp.365-372.

133. **Gandy, D.** "X20 CrMoV12-1 Steel Handbook". *Electric Power Research Institute.* 2006.

134. **Li, T., Chen, H., Chen, W., Ure, J.** "On the shakedown analysis of welded pipes". *Int. Journal of Pressure Vessels and Pipeing.* 2011, Vol. 88, pp. 301-310.

135. **Schuller, H.J., Hagn, L., Woitscheck, A.** "Cracking in the weld region of shaped components in hot steam pipelines-material invesigation". *Der Maschinenschaden.* Vol. 47, pp. 1-13.

136. **Ponter, A.R.S., Chen, H.** "Modelling of the Behaviour of a Welded Joint subjected to Reverse Bending Moment at High". *Journal of Pressure Vessel Technology*. 2007, Vol. 129 (2), pp. 254-261.

137. **Bate, S.K., Hayes, J.P., Hooton, D.G., Smith, N.G.** "Further analyses to validate the R5 volume 2/3 procedure for the assessment of austenitic weldments". *Report for British Energy Generation Ltdno. SA/EIG/11890/R002, Serco Assurance, Warrington,UK.* 2005.

APPENDIX

Appendix I

Elastic shakedown loads for temperature independent σ_y

Iteration Numbers	Upper Bound Multiplier	Lower Bound Multiplier
1	10.59089827	2.747297761
2	9.613061271	2.747297761
3	9.017467298	3.653815503
4	8.518937245	3.94125432
5	8.030861305	4.259800777
6	7.527247651	4.491835807
7	7.019241565	4.663099904
8	6.541224169	4.765882912
9	6.12997204	4.835154417
10	5.805713495	4.840631631
11	5.567101785	4.844538904
12	5.399389783	4.845106372
13	5.284165723	4.846798595
14	5.205540702	4.84693201
15	5.1512955	4.847574518
16	5.113097376	4.84761923
17	5.085724035	4.847825397
18	5.065361563	4.847840945
19	5.049389183	4.847903251
20	5.036470632	4.847913862
21	5.025474247	4.847919205
22	5.01581913	4.847924099
23	5.00727248	4.847924242
24	4.999669994	4.847924287
25	4.992889371	4.847924341
26	4.986821053	4.847924409
27	4.981383031	4.847924496
28	4.976497031	4.847924496
29	4.972100103	4.847924496
30	4.968126413	4.847924496
31	4.964525592	4.847925031
32	4.961254152	4.847925062
33	4.958276767	4.847925101
34	4.955561427	4.847925101
35	4.953080935	4.847925101
36	4.950808923	4.847925231

37	4.948724219	4.847925231
38	4.946806037	4.847925231
39	4.945035048	4.84792533
40	4.943394782	4.84792533
41	4.941871666	4.84792533
42	4.940453716	4.84792533
43	4.939130409	4.84792533
44	4.937892251	4.84792533
45	4.936730865	4.847925391
46	4.935638436	4.847925391
47	4.934608587	4.847925538
48	4.933635343	4.847925538
49	4.932713201	4.847925579
50	4.93183734	4.847925579
51	4.931003324	4.847925599
52	4.930207631	4.847925607
53	4.929447162	4.847925607
54	4.928718516	4.847925607
55	4.928019339	4.847925607
56	4.92734663	4.847925645
57	4.926698072	4.847925649
58	4.926071466	4.847925655
59	4.925465371	4.847925657
60	4.924877911	4.847925657
61	4.924307631	4.847925657
62	4.923752926	4.847925657
63	4.92321263	4.847925657
64	4.922685359	4.847925657
65	4.922169966	4.847925657
66	4.921665499	4.847925657
67	4.921171204	4.847925657
68	4.920686383	4.847925657
69	4.920210428	4.847925657
70	4.919742775	4.847925657

Elastic shakedown loads for temperature dependent σ_y

Iteration Numbers	Upper Bound Multiplier	Lower Bound Multiplier
1	10.45949136	2.747297761
2	8.374582652	2.747297761
3	8.090565028	2.747297761
4	7.364677689	2.747297761
5	6.537138227	2.747297761
6	5.683784591	2.858751263
7	5.015694961	3.274784688
8	4.584575833	3.490206883
9	4.330830205	3.618757317
10	4.185877359	3.688189936
11	4.102045127	3.730268252
12	4.051574415	3.752815667
13	4.019513324	3.767018403
14	3.99793851	3.775605465
15	3.982157819	3.781499512
16	3.969778788	3.785726667
17	3.959163027	3.789037995
18	3.950114452	3.79187327
19	3.942257086	3.794288215
20	3.93541429	3.796382887
21	3.929435621	3.798209267
22	3.924176004	3.799804201
23	3.919522228	3.801207131
24	3.915390747	3.802448532
25	3.911714727	3.803550315
26	3.908434696	3.804529882
27	3.905504957	3.805406179
28	3.902880529	3.806187655
29	3.900522283	3.806887678
30	3.898395512	3.807516732
31	3.896473482	3.808083778
32	3.894731082	3.808596757
33	3.893149122	3.809061546
34	3.891708407	3.809483536
35	3.890394267	3.809866415
36	3.889192202	3.810218412
37	3.888089397	3.810539001
38	3.887073451	3.810832828
39	3.886134841	3.811104224
40	3.885265037	3.811354599

41	3.884456681	3.811586621
42	3.883703168	3.811802251
43	3.882998746	3.812003251
44	3.882338228	3.812191158
45	3.88171709	3.812367353
46	3.881131125	3.812533045
47	3.880576972	3.812689353
48	3.880051329	3.812837176
49	3.879551263	3.812977357
50	3.879074101	3.813110727
51	3.878618105	3.813238063
52	3.878181137	3.813359715
53	3.877761401	3.813476063
54	3.877357415	3.813587867
55	3.876967619	3.813695874
56	3.876590633	3.813799673
57	3.87622572	3.813900129
58	3.875871712	3.813997517
59	3.875527623	3.814092197
60	3.875192504	3.814183902
61	3.874865599	3.81427312
62	3.874546045	3.814360713
63	3.874233207	3.814445949
64	3.873926553	3.814529312
65	3.873625632	3.814611087
66	3.87333003	3.814691351
67	3.873039387	3.814770203
68	3.872753372	3.814847718
69	3.872471692	3.814923997
70	3.872194075	3.814999117

Appendix II

Iteration procedures for changing residual stress field

The entire iterative procedure requires a number of cycles, where each cycle contains N iterations associated with N load instances. The first iteration is to evaluate the changing residual stress $\Delta\rho_{ij}^{1}$ associated with the elastic solution $\hat{\sigma}_{ij}^{\Delta}(t_1)$ at the first load instance. Defined $\Delta\rho_{ijm}^{n}$ as the evaluated changing residual stress for *nth* load instance at *mth* cycle of iterations, where n=1,2,...N and m=1,2,...M. At each iteration, the above changing residual stress $\Delta\rho_{ijm}^{n}$ is calculated. The entire iterative procedure is shown as follows:

At cycle m=1 of iterations:

Iteration 1: Solved $\Delta\rho_{ij1}^{1}$ form the elastic solution $\hat{\sigma}_{ij}^{\Delta}(t_1)$ at the first load instance.

Iteration 2: Solved $\Delta\rho_{ij1}^{2}$ from $\hat{\sigma}_{ij}^{\Delta}(t_2)+\Delta\rho_{ij_1}^{1}$

Iteration N: Solved $\Delta\rho_{ij1}^{N}$ from $\hat{\sigma}_{ij}^{\Delta}(t_N)+\Delta\rho_{ij_1}^{1}+\Delta\rho_{ij_1}^{2}+\ldots+\Delta\rho_{ij_1}^{N-1}$

At cycle m=2 of iterations:

Iteration N+1: Solved $\Delta\rho_{ij2}^{1}$ from $\hat{\sigma}_{ij}^{\Delta}(t_1)+\Delta\rho_{ij_1}^{1}+\Delta\rho_{ij_1}^{2}+\ldots+\Delta\rho_{ij_1}^{N}$

Iteration N+1: Solved $\Delta\rho_{ij2}^{2}$ from $\hat{\sigma}_{ij}^{\Delta}(t_2)+\Delta\rho_{ij_1}^{1}+\Delta\rho_{ij_1}^{2}+\ldots+\Delta\rho_{ij_1}^{N}+\Delta\rho_{ij_2}^{1}$

Iteration 2N: Solved $\Delta\rho_{ij2}^{N}$ from $\hat{\sigma}_{ij}^{\Delta}(t_N)+\Delta\rho_{ij_1}^{1}+\Delta\rho_{ij_1}^{2}+\ldots+\Delta\rho_{ij_1}^{N}+\Delta\rho_{ij_2}^{1}+\Delta\rho_{ij_2}^{2}+\ldots+\Delta\rho_{ij_2}^{N-1}$

At cycle m=M of iterations:

Iteration MN-N+1: Solved $\Delta\rho_{ijM}^{1}$ from $\hat{\sigma}_{ij}^{\Delta}(t_1)+\sum_{n=1}^{N}\Delta\rho_{ij_1}^{n}+\ldots+\sum_{n=1}^{N}\Delta\rho_{ij_{M-1}}^{n}$

Iteration MN-N+2: Solved $\Delta\rho_{ijM}^{2}$ from $\hat{\sigma}_{ij}^{\Delta}(t_2)+\sum_{n=1}^{N}\Delta\rho_{ij_1}^{n}+\ldots+\sum_{n=1}^{N}\Delta\rho_{ij_{M-1}}^{n}+\Delta\rho_{ij_M}^{1}$

Iteration MN: Solved $\Delta\rho_{ijM}^{N}$ from $\hat{\sigma}_{ij}^{\Delta}(t_N)+\sum_{n=1}^{N}\Delta\rho_{ij_1}^{n}+\ldots+\sum_{n=1}^{N}\Delta\rho_{ij_{M-1}}^{n}+\sum_{n=1}^{N-1}\Delta\rho_{ij_M}^{n}$

When the convergence occurs at the Mth cycle of iterations, the summation of changing residual stress at N time points must approach to zero due to the stable cyclic response.

$$\sum_{n=1}^{N} \Delta\rho_{ijM}^{\ n} = 0$$

Hence the constant residual stress $\bar{\rho}_{ij}^{M}$ over the cycle can also be determined by

$$\bar{\rho}_{ij}^{M} = \sum_{n=1}^{N} \Delta\rho_{ij1}^{\ n} + \sum_{n=1}^{N} \Delta\rho_{ij2}^{\ n} + \cdots + \sum_{n=1}^{N} \Delta\rho_{ijM-1}^{\ n}$$

And the converged accumulated residual stress at the time instant t_n, is given by,

$$\rho_{ij}(t_n) = \bar{\rho}_{ij}^{M} + \sum_{k=1}^{n} \Delta\rho_{ijM}^{\ k}$$

The corresponding plastic strain range occurring at time instant t_n is calculated by,

$$\Delta\varepsilon_{ij}^{p}(t_n) = \frac{1}{2\bar{\mu}_n}\left[\hat{\sigma}_{ij}^{\Delta'}(t_n) + \rho_{ij}^{'}(t_n)\right]$$